BEILSTEIN JOURNAL OF NANOTECHNOLOGY

Hybrid nanomaterials: from the laboratory to the market

Edited by Andreas Taubert, Fabrice Leroux, M. Pierre Rabu and Veronica de Zea Bermudez

Imprint

Beilstein Journal of Nanotechnology
www.bjnano.org
ISSN 2190-4286
Email: journals-support@beilstein-institut.de

The *Beilstein Journal of Nanotechnology* is published by the Beilstein-Institut zur Förderung der Chemischen Wissenschaften.

Beilstein-Institut zur Förderung der Chemischen Wissenschaften
Trakehner Straße 7–9
60487 Frankfurt am Main
Germany
www.beilstein-institut.de

BEILSTEIN JOURNAL OF NANOTECHNOLOGY

Hybrid nanomaterials: from the laboratory to the market

Verónica de Zea Bermudez[*1], Fabrice Leroux[*2], Pierre Rabu[*3] and Andreas Taubert[*4]

Editorial

Open Access

Address:
[1]Department of Chemistry and CQ-VR, University of Trás-os-Montes e Alto Douro, 5000-801 Vila Real, Portugal, [2]Institute of Chemistry, ICCF – UMR CNRS 6296, University Clermont Auvergne, 24 av. des Landais, BP 80026, Aubière 63171, France, [3]Université de Strasbourg, CNRS, Institut de Physique et Chimie de Matériaux de Strasbourg, F-67034 Strasbourg, France and [4]Institute of Chemistry, University of Potsdam, D-14476 Potsdam, Germany

Email:
Verónica de Zea Bermudez[*] - vbermude@utad.pt; Fabrice Leroux[*] - Fabrice.leroux@uca.fr; Pierre Rabu[*] - Pierre.Rabu@ipcms.unistra.fr; Andreas Taubert[*] - ataubert@uni-potsdam.de

* Corresponding author

Keywords:
hybrid nanomaterials

Beilstein J. Nanotechnol. **2017,** *8,* 861–862.
doi:10.3762/bjnano.8.87

Received: 15 March 2017
Accepted: 22 March 2017
Published: 13 April 2017

This article is part of the Thematic Series "Hybrid nanomaterials: from the laboratory to the market".

Editor-in-Chief: T. Schimmel

Materials, in all forms, are one of the mainstays of human development. The Stone Age would not have happened the same way without the ability of early humans to process stone into tools that could be used to their advantage. Similar observations can be made for every major step in human development up to the modern computer age where a whole zoo of different materials in very different amounts and very different forms is necessary to achieve the performance of countless devices that are ubiquitous today.

Along with active materials development by mankind, nature has developed highly complex, advanced materials with properties that are often superior to those made by humans. In this context, complexity is one of the keywords: biological materials are often highly complex, highly structured with well-defined hierarchy, with complex chemical compositions, often composed of a combination of organic and inorganic components, and therefore, they often have specifically adapted micro- and macroscopic properties and emergent phenomena. Materials from the natural world offer extraordinary features, such as self-healing, miniaturization, reconfigurability, and defect tolerance. Moreover, their synthesis typically takes place at roughly ambient conditions – often presenting a challenge to chemists, biologists, physicists, and engineers in its full complexity.

In spite of these challenges, we nowadays have a basic understanding of how (desired) material properties are related to material composition and structure. One of the key observations in this context is that the most desirable properties typically do not arise from a single material or chemical composition. Rather, these highly sought after properties, such as specific magnetic, optical, electrical, biological, or mechanical properties, arise from a delicate interplay of several material components of different origin, composition, and individual chemical and physical properties. As a result, some of the most attractive materials for modern technology are materials composed of at least two (and often more) different components – these are known as hybrid materials.

Indeed, biological high-performance materials such as bone or teeth are organic/inorganic hybrid materials of multiscale hierarchical structure and chemical composition perfectly matched to their respective task. As a result, hybrid materials have been explored for essentially all applications possible. Their chemical composition has been studied throughout the entire periodic table; countless organic molecules and polymers have been studied for their effects on structure, physical properties, and processability. Often, a "shotgun approach" towards the synthesis of new materials has been successful, and by serendipity, many interesting and useful materials have been found.

The recent past, however, has seen two developments that are key to the development and application of new, high-performance hybrid materials: (i) a new level of rational design has been reached − many molecular and supramolecular principles of hybrid material organization are not only known and quantified, but there are also strategies available to exploit these principles for materials design and materials production and (ii) the rapid development of computational and materials analysis tools, which provide much better insight into materials structure and properties than what was possible 15 or 20 years ago. As a result, we now understand some aspects of the interplay between chemical and physical properties much better, for example, between the chemical components and the macroscopic behavior of these materials. Consequently, it is also possible to make materials that have vastly improved properties by combination of carefully selected components with well-known individual properties.

As a result, there are many advanced hybrid materials available, some on a fairly large scale. Nevertheless, one of the remaining challenges is the transfer of these fascinating materials into large-scale applications in fields that are relevant to our modern society. Examples are healthcare, energy, environment, safety and security, but also less obvious are fields like arts and restoration. This clearly shows that, beyond developing new hybrid materials, there is a need to bring the most promising materials to the market for the benefit of the entire world.

This Thematic Series "Hybrid nanomaterials: from the laboratory to the market" was inspired by a series of symposia on advanced hybrid materials held at the E-MRS Spring Meetings in 2010, 2012, 2014, and 2016. From the beginning, the goal of the symposia was to foster discussion and exchange between groups active in this exciting yet very challenging field. The Thematic Series presents highlights from virtually all subfields of hybrid materials research. As the guest editors, we invite you to browse the issue, find among the many creative ideas presented here the ones that are most appealing to you, and to develop your own strong program in research, development, and application of advanced hybrid materials.

We would also like to thank the staff at the *Beilstein Journal of Nanotechnology*, along with all contributors and referees for making this exciting Thematic Series possible.

Verónica de Zea Bermudez, Fabrice Leroux, Pierre Rabu, and Andreas Taubert

Vila Real, Aubière, Strasbourg and Potsdam, March 2017

License and Terms

BEILSTEIN JOURNAL OF NANOTECHNOLOGY

Prediction of the mechanical properties of zeolite pellets for aerospace molecular decontamination applications

Guillaume Rioland[1], Patrick Dutournié[*1,§], Delphine Faye[2], T. Jean Daou[*1,¶] and Joël Patarin[1]

Full Research Paper

Open Access

Address:
[1]Université de Strasbourg (UDS), Université de Haute-Alsace (UHA), CNRS, Equipe Matériaux à Porosité Contrôlée (MPC), Institut de Science des Matériaux de Mulhouse (IS2M), UMR 7361, 3 bis rue Alfred Werner, F-68093 Mulhouse, France and [2]Service Laboratoires & Expertise, Centre National d'Etudes Spatiales (CNES), 18 avenue Edouard Belin, 31401 Toulouse Cedex 9, France

Email:
Patrick Dutournié[*] - patrick.dutournie@uha.fr;
T. Jean Daou[*] - jean.daou@uha.fr

* Corresponding author
§ Phone: +33 3 89 33 67 52, Fax: +33 3 89 33 68 85
¶ Phone: +33 3 89 33 67 39, Fax: +33 3 89 33 68 85

Keywords:
design of experiments methodology; mechanical performance; molecular decontamination; operating optimums; zeolite pellets

Beilstein J. Nanotechnol. **2016,** *7,* 1761–1771.
doi:10.3762/bjnano.7.169

Received: 15 June 2016
Accepted: 20 October 2016
Published: 18 November 2016

This article is part of the Thematic Series "Hybrid nanomaterials: from the laboratory to the market".

Guest Editor: A. Taubert

Abstract

Zeolite pellets containing 5 wt % of binder (methylcellulose or sodium metasilicate) were formed with a hydraulic press. This paper describes a mathematical model to predict the mechanical properties (uniaxial and diametric compression) of these pellets for arbitrary dimensions (height and diameter) using a design of experiments (DOE) methodology. A second-degree polynomial equation including interactions was used to approximate the experimental results. This leads to an empirical model for the estimation of the mechanical properties of zeolite pellets with 5 wt % of binder. The model was verified by additional experimental tests including pellets of different dimensions created with different applied pressures. The optimum dimensions were found to be a diameter of 10–23 mm, a height of 1–3.5 mm and an applied pressure higher than 200 MPa. These pellets are promising for technological uses in molecular decontamination for aerospace-based applications.

Introduction

Molecular contamination is of great concern in aerospace-based applications. Once satellites are in orbit, molecules contained in paints, adhesives or glues can outgas and form films or droplets on the surface of mirrors, lenses, solar cells or thermal detectors. The National Aeronautic and Space Administration (NASA) has investigated the chemical nature of these mole-

cules; hydrocarbons and plasticizers were identified as the most important of the outgassed molecules [1,2]. The surface of all the on-board equipment such as the thermal captor or optics could become covered by molecules, leading to a deterioration of these tools.

Porous alumina, silica, zeolites and charcoal have been tested to solve the molecular contamination issue, and zeolites have been selected as the best candidates. At very low concentration, zeolites are able to trap water and volatile organic compounds thanks to their great adsorption abilities [3]. The French Space Agency (CNES) studied zeolites for the adsorption of volatile organic compounds in satellites [4-8].

Zeolites are aluminosilicate materials with micropores. They are the result of a combination of AlO_4 and SiO_4 tetrahedra. Zeolites are often used in adsorption and catalytic applications due to their high thermal stability and interesting adsorption properties [9-15]. Today, 231 different zeolite structures have been discovered, but only some of them are currently used in industry [16-19].

In most applications, and for more convenience (i.e., handling, transport), zeolites cannot be used in powder-form. For space-based applications, particulate contamination has to be avoided. However, binders are necessary to improve the mechanical properties and to allow for the compression of powders. In the literature, significant amounts of binder is used to shape zeolites, leading to objects (e.g., cylinders, beads) with high mechanical resistance and optimal dimensions [20-24]. In the literature, the use of a hydraulic press to form zeolite pellets is not common, although some articles have been published [24,25]. Moreover, the mechanical resistance (compression tests) is either low (between 1 and 10 MPa) or the amount of binder is very high (more than 20 wt %) [20-25]. In our previous work, a hydraulic press was used to make zeolite pellets with very good mechanical resistance (about 100 MPa) and with a very small amount of methylcellulose or sodium metasilicate as binder (5 wt %) [8]. Because vibrations or impact upon satellites launch could cause the destruction of these bodies and contaminate on-board equipment, improved mechanical performance of zeolite materials is highly sought after. In order to use zeolite pellets for space-based applications, they must have both good mechanical properties and adhere to size limitations (e.g., volume, diameter, height and number of pellets).

Recently, Lai et al. developed a new empirical model able to predict the mechanical properties (ultimate compressive strength) of a binary mixture pellet based on the volume fraction of HZSM-5 (MFI) zeolite in the binary pellet, the hold time and elastic rebound [26].

In this paper, we propose two other models able to predict the ultimate compressive strength of zeolite pellets regardless of dimension. These models (used in many fields) are based on a design of experiments (DOE) methodology [27-29]. Thus, the optimum dimensions will be linked to the best mechanical resistance, leading to an optimum pellet able to trap pollutants without being damaged by impact or vibrations.

Experimental

Materials

Two hydrophilic and two hydrophobic zeolites have been chosen to make zeolite pellets:

- FAU 13X powder with a crystal size of 3–5 µm and a Si/Al molar ratio of 1.2 was purchased from Sigma-Aldrich.

- Na-LTA powder with a crystal size of 3–5 µm and a Si/Al molar ratio of 1.1 was purchased from CECA.

- MFI Sicade-2 powder with a crystal size of 3–5 µm and an infinite Si/Al molar ratio was purchased from Zephir Alsace.

- BEA powder with a crystal size of 3–5 µm and a Si/Al molar ratio of 136 was synthesized according to the protocol described below.

The gel preparation and hydrothermal synthesis were performed using a polypropylene bottle. First, 1.5 g of hydrofluoric acid (Sigma-Aldrich, 40% in water) was poured on 11 g of tetraethylammonium hydroxide (Sigma-Aldrich, 40% in water) used as structure-directing agent. 0.12 g of BEA zeolite germs are added and blended under vigorous mixing (700 rpm). 6 g of silica (Zeosil® 1165 MP, Rhodia) were finally added, giving the following gel molar composition: 1:0.3:0.3:4.17 $SiO_2/(C_2H_5)_4NOH/HF/H_2O$. The homogenization is carried out with a Teflon® rod.

The gel was introduced into PTFE-lined stainless-steel autoclaves and heated at 150 °C for 2 days. After synthesis the product was filtered, washed with deionized water several times and dried overnight at 100 °C. The organic compounds were finally removed by calcination at 550 °C for 8 h in air (ramp at 1 °C·min^{-1}).

Methylcellulose (MC) was purchased from Acros Organics. Anhydrous sodium metasilicate (Na_2SiO_3) was purchased from Fluka Chemicals.

Characterization techniques

The ultimate compressive strength of the consolidated pellets was determined by uniaxial and diametric compression tests.

The stress and displacement were recorded until the pellets crack by applying a displacement rate of 0.5 mm/min with an Instron 4505 Zwick dynamometer. To obtain a statistically significant data distribution, three identical pellets were analyzed for each parameter.

Preparation of zeolite pellets

In a recent paper, the preparation of MFI-type zeolite pellets was described [8]. The pelletization apparatus is divided into two parts: a manual hydraulic press (Atlas 15T Manual Hydraulic Press, Specac) and a pellet die where the powder is incorporated. The zeolite pellets were prepared from a mixture of binder, 1:4 zeolites (FAU, BEA, LTA and MFI-types) to water. First, distilled water was mixed with a certain amount of binder (5 wt % of the pellet for optimized conditions). This amount of water was optimized: if too much water is added, the mixtures cannot be pelletized (the mixture is liquid). On the other hand, with too little binder, cracks appear after the ejection of pellets. Then, zeolite is added. Water improves the diffusion of binder in zeolite powder and allows the formation of a MC or Na_2SiO_3 gel which acts as glue that holds particles together. The mixture was stirred and put in the pellet die for pelletization. A definite compression load was applied during 5 min in order to form a pellet. The pellets were finally dried at 70 °C during 24 h.

Calculation and experimental section

To predict the mechanical resistance of zeolite pellets of various dimensions, it is necessary to know the ultimate compressive strength applied to a mixture composed of one to four zeolites (FAU, BEA, LTA and MFI-types) and 5 wt % of binder (methylcellulose or sodium metasilicate).

This ultimate compressive strength depends on some factors, such as the compression load and the dimensions of the pellet. These dimensions are linked to the amount of the mixture introduced in the pellet die. The mechanical properties of two different formulations compacted with the same compression loads and the same diameter will be different because the pellet height is not the same. The pressure applied to the mixture is assumed as the applied force (weight) divided by the surface of the pellet. The ultimate compressive strength was determined by uniaxial and diametric compression tests.

To analyse the influence of the three studied parameters on the mechanical properties, a parametric study of the ultimate compressive strength was conducted by using DOE. This methodology allows the maximum information to be obtained about the operating parameter influencing the process while minimizing the number of experimental tests [30]. In this case, the influence of three parameters (diameter, height and applied pressure) on the ultimate compressive strength of the final pellet is studied.

Table 1 shows the experimental tests that have been used for conception of our mathematical models. The studied range is e = 1 to 7 mm (height), Ø = 10 to 32 mm (diameter) and P = 29.5 to 277.5 MPa (applied pressure).

The studied parameters of each test are chosen to optimize the pertinence and the relevance of the experimental tests. These parameters are normalized to compare the effects and the influence of the studied function. A rotatable central composite design was used and consists of three distinct sets of experimental runs: a set of central points, a full factorial design (orthogonal) and a set of axial points identical to the central point except for one parameter (values outside the studied range) [28,31]. All the experimental tests are systematically repeated 3 times.

To explore relationships between the studied function and the operating parameters a surface response methodology was used. A second-degree polynomial equation including interactions was used to approximate experimental results. A set of 105 equations (corresponding to the experimental trials) with 10 coefficients was statically solved by minimizing a quadratic criterion.

Results and Discussion

Uniaxial compression tests

This test is carried out along the y-axis as shown in Figure 1. Experimental, ultimate compressive strengths were investigated by using the DOE methodology [32]. As mentioned before, the studied parameters have been described.

The first model is estimated from results of the uniaxial compression tests by minimizing the quadratic criterion between experimental and numerical results. The obtained model is:

$$Y(\mathrm{MPa}) = 42.96 + 24.28P' - 19.26e' + 15.54\varnothing' + 2.84P'^2 + 14.97e'^2 - 3.09\varnothing'^2 - 13.26P'e' + 6.95P'\varnothing' + 5.18e'\varnothing' \quad (1)$$

where Y is the ultimate compressive strength (MPa) and P', e', Ø' are the values of the applied pressure (MPa), the height (mm) and the diameter (mm) of the pellet, respectively, normalized in the range (−1,1).

The maximal error calculated with the 105 experimental tests is less than 12 MPa and it is less than the maximal experimental error (13 MPa) observed for the repeated tests.

Table 1: Experimental tests (3 or 6 repeated tests) to study the influence of three parameters (diameter, height and applied pressure) on the ultimate compressive strengths of the final pellets. *Y* is the uniaxial ultimate compressive strength and *Z* is the diametric ultimate compressive strength.

Dimensions (diameter × height) (mm × mm)	Applied pressure, *P* (MPa)	*Y* (MPa)	*Z* (MPa)
13.0 × 1.0	153.5	70.0, 50.0, 60.0	0.80, 0.82, 0.81
13.0 × 2.0	110.0	44.0, 48.0, 41.0	0.70, 0.75, 0.71
	230.0	75.0, 71.0, 78.0	0.90, 0.85, 0.86
13.0 × 4.0	29.5	5.0, 4.5, 6.5	0.10, 0.08, 0.07
	150.0	21.0, 21.0, 17.0	0.39, 0.45, 0.44
	153.5[a]	20.0, 18.0, 22.0, 23.5, 20.5, 22.5	0.59, 0.65, 0.66, 0.61, 0.69, 0.70
	270.0	45.0, 50.0, 53.0	1.10, 1.05, 1.09
	277.5[a]	45.0, 50.0, 42.0, 51.0, 50.0, 45.0	1.10, 1.09, 1.05, 1.10, 1.08, 1.07
13.0 × 6.0	110.0	14.0, 11.0, 12.0	0.48, 0.55, 0.44
	230.0	21.0, 23.0, 19.0	0.99, 0.91, 0.90
13.0 × 7.0	153.5[a]	11.0, 9.0, 10.0, 8.0, 7.0, 8.0	0.60, 0.64, 0.68, 0.60, 0.69, 0.69
10.0 × 2.5	29.5 [a]	7.5, 7, 5.5, 5, 7.0, 8.0	0.25, 0.34, 0.21, 0.28, 0.30, 0.31
	91.5 [a]	15.0, 14.0, 18.0, 15.0, 17.0, 18.0	0.70, 0.67, 0.68, 0.71, 0.69, 0.64
	215.5	45.0, 41.0, 37.0	1.30, 1.35, 1.25
10.0 × 5.5	29.5	2.5, 2.8, 2.0	0.15, 0.18, 0.11
	91.5[a]	4.5, 5.0, 5.0, 3.5, 3.0, 5.5	0.30, 0.37, 0.38, 0.38, 0.36, 0.40
	215.5	8.0, 9.0, 11.0	1.10, 1.15, 1.05
32.0 × 2.0	110.0	60.0, 58.0, 63.0	0.18, 0.15, 0.20
	230.0	120.0, 111.0, 123.0	0.45, 0.51, 0.55
32.0 × 2.5	91.5	45.0, 50.0, 55.0	0.12, 0.11, 0.13
	215.5[a]	95.0, 90.0, 85.0, 100.0, 90.0, 95.0	0.40, 0.37, 0.35, 0.41, 0.38, 0.41
32.0 × 4.0	150.0	56.0, 60.0, 61.0	0.18, 0.22, 0.20
32.0 × 5.5	91.5[a]	40.0, 38.0, 30.0, 40.0, 35.0, 48.0	0.10, 0.10, 0.08, 0.11, 0.07, 0.09
	215.5	80.0, 85.0, 80.0	0.29, 0.24, 0.31
32.0 × 6.0	110.0	45.0, 40.0, 41.0	0.15, 0.19, 0.16
	230.0	84.0, 90.0, 80.0	0.34, 0.36, 0.35
32.0 × 7.0	230.0	91.0, 95.0, 88.0	0.24, 0.26, 0.21

[a]For some conditions, 6 mechanicals tests have been carried out.

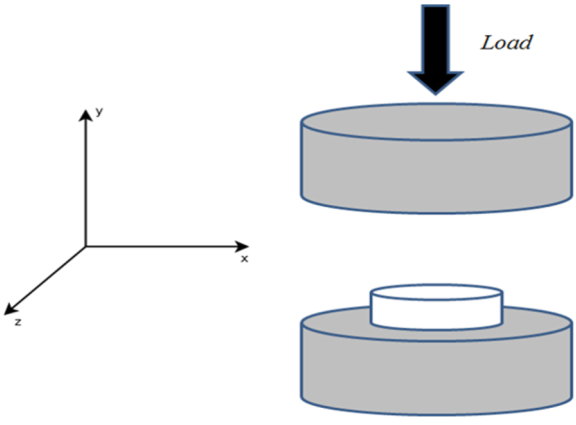

Figure 1: Schematic of uniaxial compression test of a zeolite pellet along the *y*-axis.

This equation shows that the ultimate compressive strength linearly depends on the applied pressure and the diameter. Indeed, quadratic terms of the diameter and the applied pressure are small compared to the linear parameters. The pertinence of the mathematical approximation is investigated for three series of six experimental tests. The results are summarized in Table 2.

Each series corresponds to a particular pellet diameter (10, 13 and 32 mm, respectively). The observed maximal error is all the more significant as the pellet diameter is increased. The average experimental ultimate compressive strengths are 16.2 ± 2.2 MPa, 47.2 ± 5.2 MPa and 38.5 ± 9.5 MPa for pellet diameters of 10, 13 and 32 mm, respectively. The average experimental values are very close to the calculated values obtained by using Equation 1 (16.7, 47.2 and 39.0, respectively).

Table 2 confirms that the model can be used for these zeolite pellets: the calculated ultimate compressive strengths fit with the experimental ultimate compressive strengths, even when the applied pressures are out of the domain previously selected. The approximation model is now confirmed with the different experimental pellets and can be used for any operating conditions

Table 2: Experimental and calculated ultimate compressive strengths for 3 series of 6 experimental tests (uniaxial compression tests). Y_{exp} is the experimental and Y the calculated ultimate compressive strengths of the pellets, respectively.

Series 1 (Ø = 10 mm, P = 91.5 MPa, e = 2.4 ± 0.1 mm)						
Y_{exp} (MPa)	15	14	18	15	17	18
Y (MPa)			16.7			
Series 2 (Ø = 13 mm, P = 277.5 MPa, e = 4.1 ± 0.2 mm)						
Y_{exp} (MPa)	45	50	42	51	50	45
Y (MPa)			47.2			
Series 3 (Ø = 32 mm, P = 91.5 MPa, e = 5.5 ± 0.4 mm)						
Y_{exp} (MPa)	40	38	30	40	35	48
Y (MPa)			39.0			

included in the studied range for predictive calculations. Figure 2 shows the ultimate compressive strength function of the pellet diameter and the applied pressure for a pellet height equal to 4.5 mm. These results show that the ultimate compressive strength increases when diameter and the applied pressure increase.

The results obtained with Equation 1 for different pellet heights are shown in Figure 3 for a pellet diameter of 21 mm. The ultimate compressive strength is maximal for thin pellets and pelletized at high pressure. Small-height and large-diameter pellets compacted at high pressures show the best mechanical properties in terms of uniaxial compression resistance.

These results can be partially explained by the inhomogeneity of the density in the thickness of the material, especially for thicker pellets. Figure 4 shows the pellet density for different pellet heights and diameter. The diameter of the studied pellets are 10, 13 and 32 mm for applied pressures of 215.5, 153.5 and 277.5 MPa, respectively.

The density is higher for thin pellets and decreases with the pellet size. This rapid density depletion for thin pellets (height between 1 and 3 mm) seems to level off for thick pellets. This observation can be explained by the formation of two dense layers on both sides of the pelletized material, creating a density gradient in the material. This can also explain the results presented in Figure 3. Indeed, the ultimate compressive strength is higher for thin pellets because they are denser materials [33].

To confirm this observation, different measures of densities are shown in Figure 5 as a function of the applied pressure. The density of pellets pelletized at 277.5 MPa are higher than those pelletized at 153.5 MPa (for the same diameter and height). The

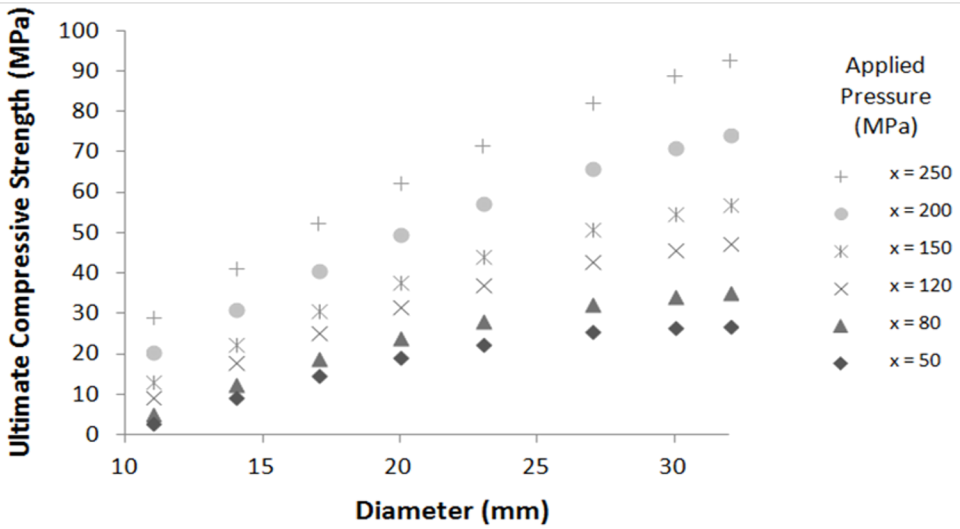

Figure 2: Ultimate compressive strength calculated by using Equation 1 for different pellet diameters and applied pressures (pellet height = 4.5 mm).

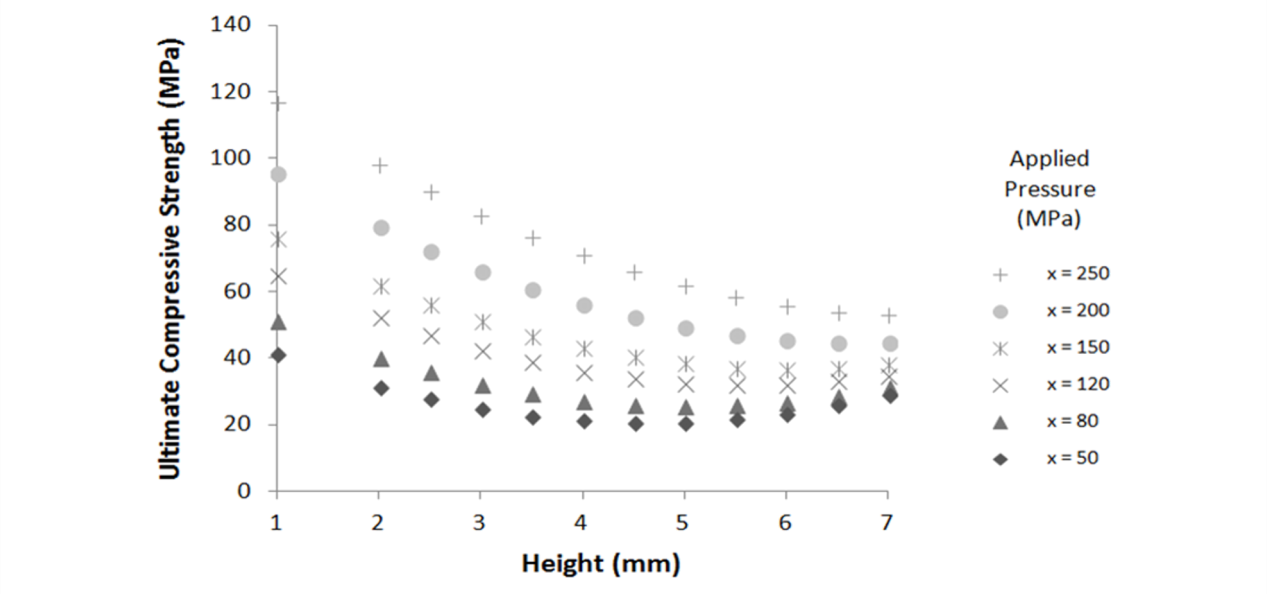

Figure 3: Ultimate compressive strength calculated by using Equation 1 for different pellet heights and applied pressures (pellet diameter = 21 mm).

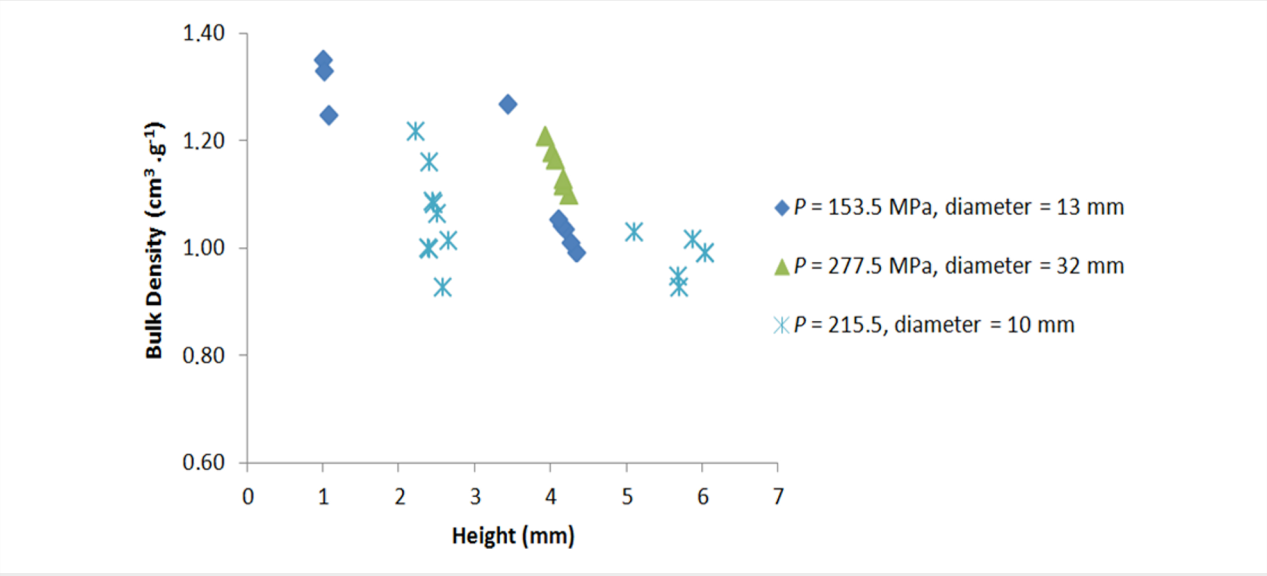

Figure 4: Bulk pellet density as a function of pellet height for different applied pressures. The diameters of the studied pellets are 10, 13 and 32 mm for applied pressures of 215.5, 153.5 and 277.5 MPa, respectively.

correlation between samples size (diameter and height) and mechanical properties makes physical sense. Indeed, when the applied pressure (compression load) increases, the bulk density of the pellet increases. For example, the pellet height decreases from 3.2 to 2.8 mm when the applied pressure increases from 75 to 600 MPa with the same mass of zeolite (0.4 g, diameter = 13 mm). This behavior is linear up to 400 MPa (studied range) and after 400 MPa the density of the pellet levels off (1050 $kg \cdot m^{-3}$). This can be explained by a density gradient along the pellet height. The thicker the pellet, the higher the density gradient is in the material [33].

Diametric compression tests

A second mechanical test was performed to enhance the knowledge about the pellet mechanical stability [32]. This test is carried out along the *y*-axis as shown in Figure 6, where the pellet is now shown on its edge. This test is commonly called the "Brazilian test". Experimental ultimate compressive strengths are studied according to pellet size and the applied pressure.

As this was performed for uniaxial compression tests, experimental results of diametric compression tests are numerically

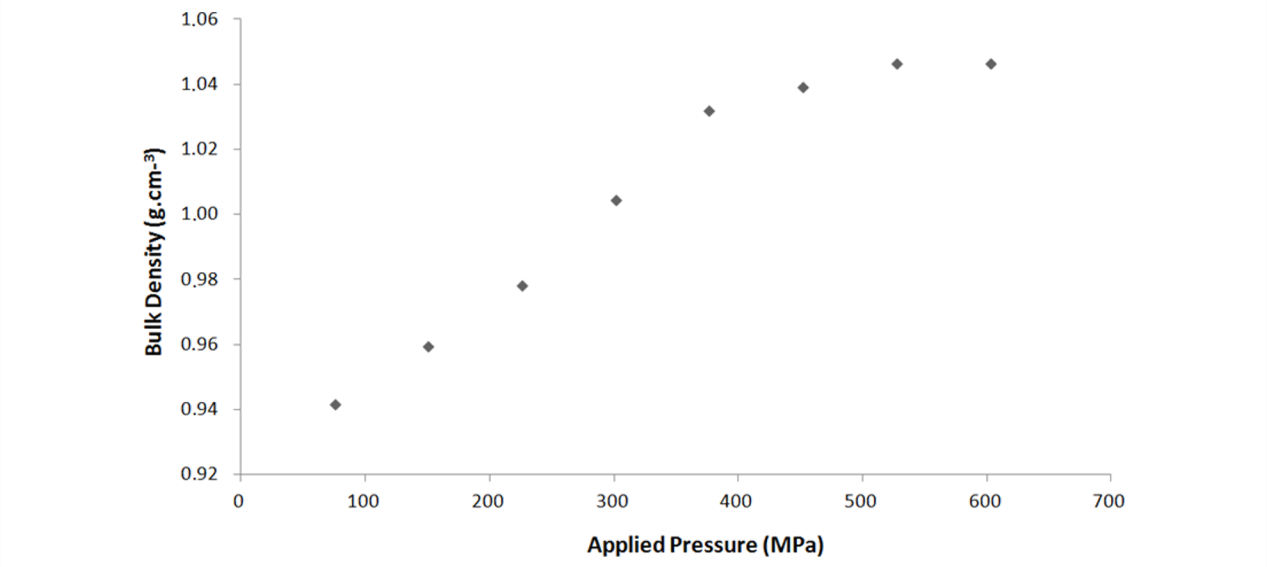

Figure 5: Bulk density as a function of the pressure applied to the mixture for 13 × 3 mm^2 pellets made with 5 wt % of binder. The pellets may be comprised of one to four zeolites.

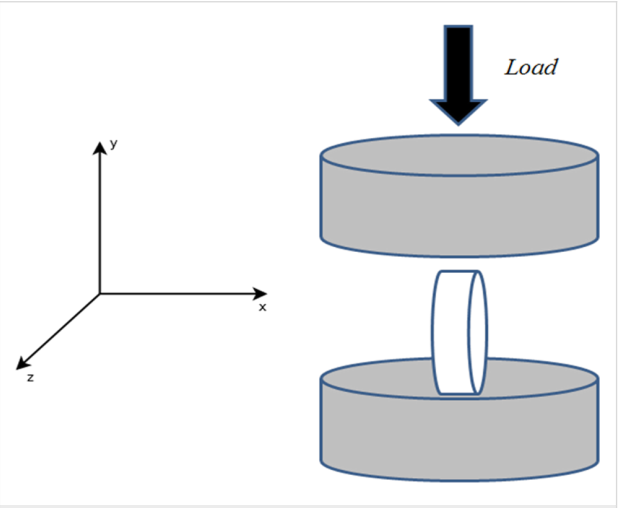

Figure 6: Schematic of diametric compression test of a zeolite pellet along the *y*-axis.

approximated by a second order equation according to the DOE methodology. The best-fit parameters are obtained by minimizing a quadratic criterion. The obtained model is:

$$Z(\mathrm{MPa}) = 0.16 + 0.27P' - 0.14e' - 0.21\varnothing' + 0.03P'^2 + 0.20e'^2 + 0.14\varnothing'^2 - 0.05P'e' - 0.10P'\varnothing' + 0.01e'\varnothing' \quad (2)$$

where Z is the ultimate compressive strength (MPa) and P', e', Ø' are the values of the applied pressure (MPa), the height (mm) and the diameter (mm) of the pellet, respectively, normalized in the range (−1,1).

The investigation is performed with 105 experimental tests and the maximal error was less than 0.14 MPa. The pertinence of the mathematical approximation is investigated for three series of 6 experimental tests. The results are summarized in Table 3.

Each series corresponds to a particular pellet diameter (10, 13 and 32 mm, respectively). The observed maximal error is all the more significant as the pellet is larger in diameter (Series 3). The average experimental ultimate compressive strengths are 0.69 ± 0.05 MPa, 1.08 ± 0.03 MPa and 0.09 ± 0.02 MPa for pellet diameters of 10, 13 and 32 mm, respectively. Nevertheless, given the low strength values, the experimental relative error is significant (around 22% for Series 3). The calculated values obtained by using Equation 2 give a good approximation of experimental results in the studied range.

The analysis of the estimated parameters (coefficients of Equation 2) shows that the highest mechanical strengths are obtained for thin and compact pellets pelletized at high pressure. These results exhibit the same trend as the previous ones; indeed, the best mechanical properties are obtained with dense pellets. Figure 7 shows the calculated ultimate strength function of pellet height and applied pressure for a pellet of 10 mm diameter. The ultimate compressive strength increases when the applied pressure increases and when the pellet height decreases.

These outcomes confirm that the model can be used for a predictive purpose to simulate the mechanical strength of zeolite pellets. The calculated ultimate compressive strengths fit with the experimental ultimate compressive strengths in the studied range for diametric compression operations.

Table 3: Experimental and calculated ultimate compressive strengths for 3 series of 6 experimental tests (diametric compression tests). Z_{exp} is the experimental and Z the calculated ultimate compressive strengths of the pellets, respectively.

Series 1 (Ø = 10 mm, P = 91.5 MPa, e = 2.4 ± 0.2 mm)						
Z_{exp} (MPa)	0.70	0.67	0.68	0.71	0.74	0.69
Z (MPa)			0.68			
Series 2 (Ø = 13 mm, P = 277.5 MPa, e = 4.1 ± 0.1 mm)						
Z_{exp} (MPa)	1.10	1.05	1.09	1.10	1.05	1.09
Z (MPa)			1.06			
Series 3 (Ø = 32 mm, P = 91.5 MPa, e = 5.6 ± 0.2 mm)						
Z_{exp} (MPa)	0.09	0.10	0.08	0.11	0.07	0.09
Z (MPa)			0.05			

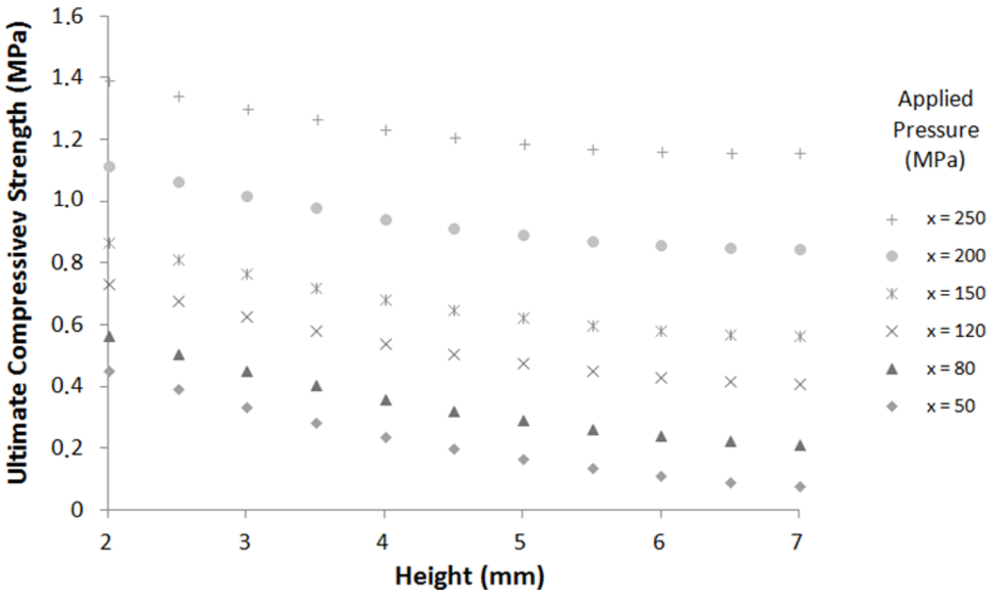

Figure 7: Ultimate compressive strength calculated by using Equation 2 as a function of pellet height for different applied pressures (pellet diameter = 10 mm).

Simultaneous analysis of mechanical tests and operating optimums

In order to use zeolite pellets for space-based applications, both mechanical properties and size limitations (volume, diameter, height and number of pellets) must be met. Therefore, each mechanical test was separately described by a three-dimensional equation of degree two as follows:

$$Y \text{ and } Z\,(\text{MPa}) = a0 + a1P' - a2e' + a3\varnothing' + a4P'^2 + a5e'^2 - a6\varnothing'^2 - a7P'e' + a8P'\varnothing' + a9e'\varnothing' \quad (3)$$

where Y and Z are the ultimate compressive strengths (MPa) and P', e', Ø' are the values of the applied pressure (MPa), the height (mm) and the diameter (mm) of the pellet, respectively, normalized in the range (−1,1).

The parameter analyses performed in previous sections (uniaxial and diametric compression tests) have shown the optimal pelletization conditions to have the best mechanical properties with respect to compression tests. With these two equations, the optimal dimensions and conditions can be found in order to form pellets with the highest mechanical properties (in terms of uniaxial and diametric compression tests). Figure 8

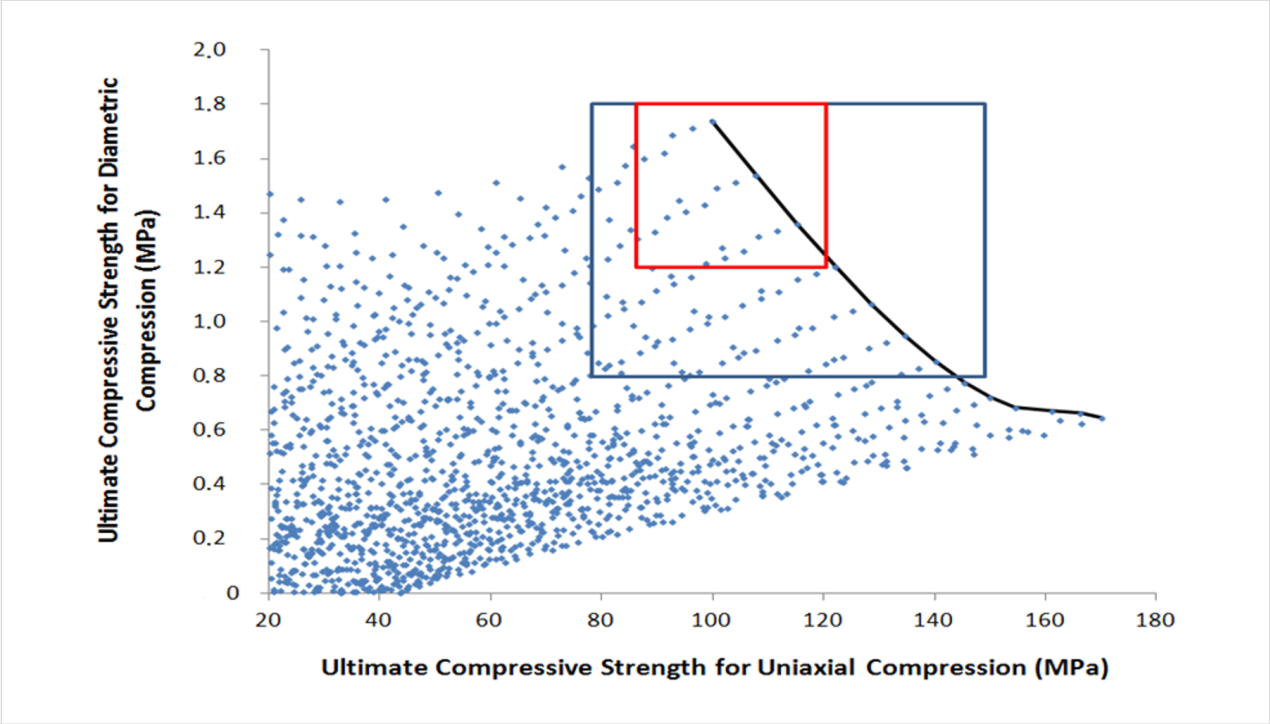

Figure 8: Operating points in a Y (MPa) vs Z (MPa) diagram. $Y(Z)$ is the ultimate compressive strength for diametric (uniaxial) compression. The black curve is called the Pareto curve. The red square is the selection of the best pellets; $Y \geq 90$ MPa and $Z \geq 1.2$ MPa. The blue square represents a larger selection of the optimum pellets; $Y \geq 80$ MPa and $Z \geq 0.8$ MPa.

shows all the operating points calculated by Equation 1 and Equation 2 in a diametric ultimate compression strength vs uniaxial ultimate compression strength diagram.

The optimal operating points (Pareto curve) are depicted by the black curve. This curve is the result of the best couples (Y,Z) [34]. These theoretical results are interesting but exclude an interesting part of the operating points from a spatial application point of view. Moreover, a part of the curve leads to low mechanical properties in terms of diametric compression tests. To have a better selection of pellets, two different scenarios are studied. The first one (red square) is the selection of the best pellets; $Y \geq 90$ MPa and $Z \geq 1.2$ MPa. A second selection (blue square) represents a larger selection of the optimum pellets; $Y \geq 80$ MPa and $Z \geq 0.8$ MPa. These two scenarios ensure high mechanical strength pellets with a wide range of pellet sizes at the same time.

These results have independently shown that the best mechanical performance is reached for high applied pressures and thin pellets. On the contrary, the pellet diameter improves uniaxial mechanical properties but weakens the pellet during diametric compression tests. To estimate the optimal range of the pelletization conditions, Equation 1 and Equation 2 are simultaneously used to calculate parameters relative to the selection of operating points.

Figure 9 shows the operating parameters (diameter, height and applied pressure) corresponding to the best operating point (red square).

The operating optimums are obtained for high applied pressure, thin pellets (less than 1.7 mm) with a diameter less than 16 mm. The largest selection of operating conditions is obtained for pellet diameters between 12 and 14 mm. As previously observed, the most dense and compact pellets have the best mechanical properties. Figure 10 shows the operating parameters (diameter, height and applied pressure) corresponding to the best operating points of scenario 2 (blue square).

Many options of pellet sizes (height and diameter) are possible. The operating optimums are obtained for high applied pressure, thin pellets (up to 3.5 mm) and in a wide range of diameters (from 10 to 23 mm).

Conclusion

Two empirical models were developed allowing the estimation of the mechanical properties of all zeolite pellets made with 5 wt % binder (methylcellulose or sodium metasilicate). Two mechanical tests were carried out: uniaxial and diametric compressions. The optimum pellet dimensions are a diameter in the range of 10–23 mm, a height of 1–3.5 mm and an applied pressure higher than 200 MPa. Experimental values

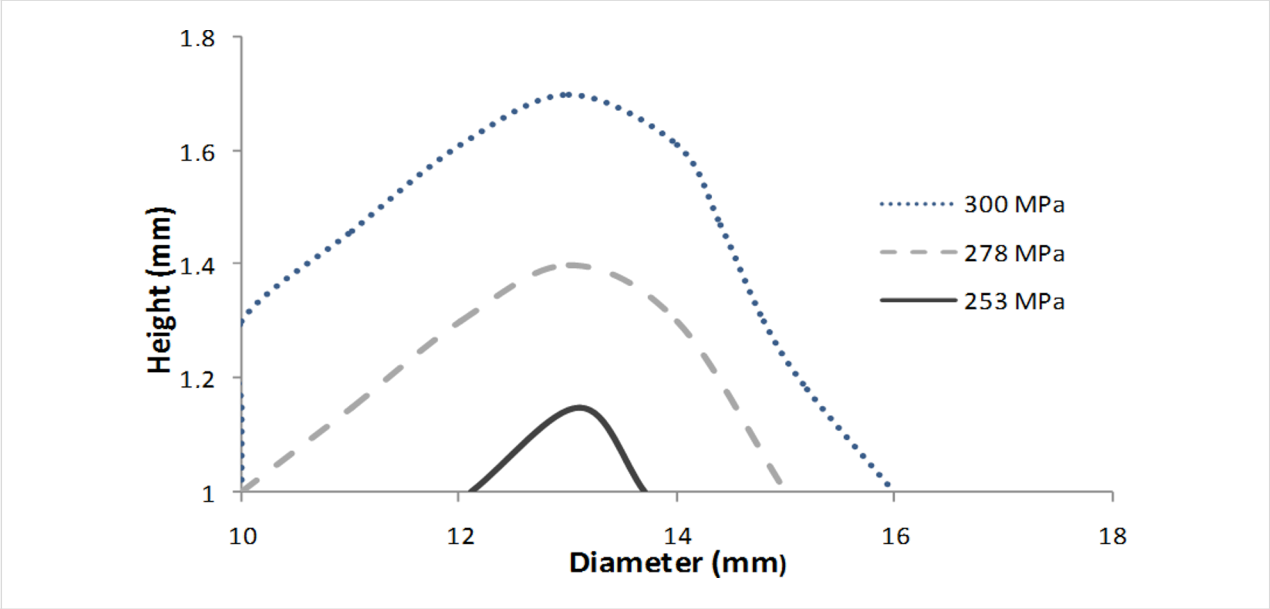

Figure 9: Pellet size and applied pressure for the best mechanical properties; scenario 1 (red square in Figure 8) is the selection of the best pellets with $Y \geq 90$ MPa and $Z \geq 1.2$ MPa.

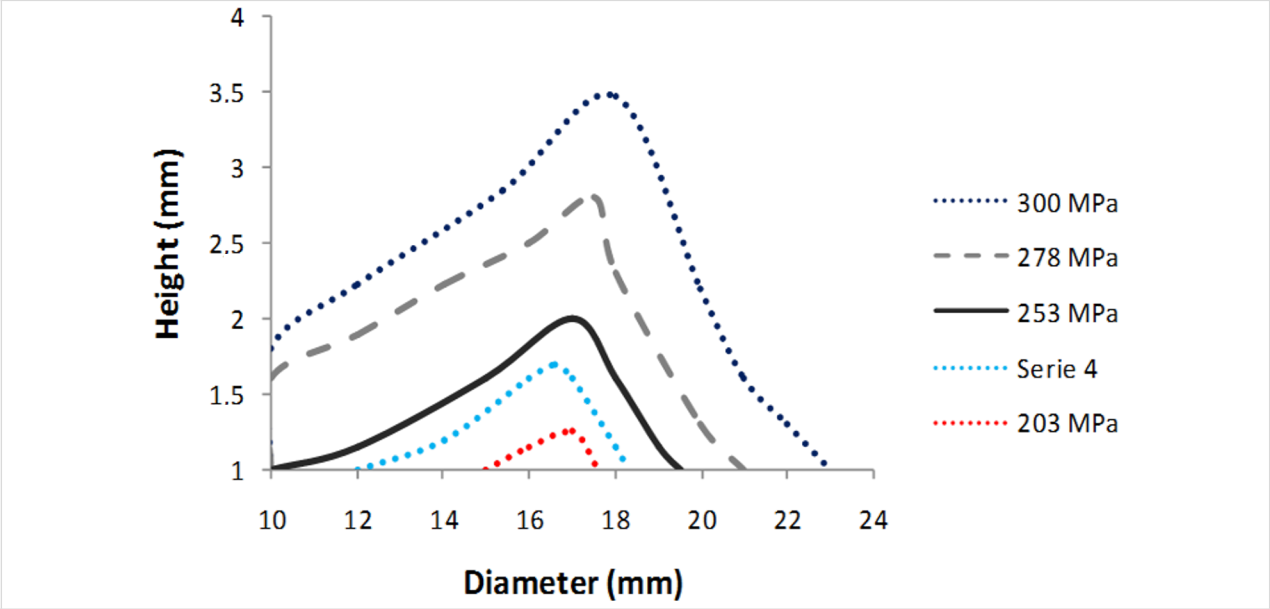

Figure 10: Pellet size and applied pressure for the best mechanical properties; scenario 2 (blue square in Figure 8) is the selection of the best pellets with $Y \geq 80$ MPa and $Z \geq 0.8$ MPa.

may of course be out these defined domains but the presented model will not predict the mechanical properties of them.

These pellets can be used in molecular decontamination applications, especially in the aerospace field where the dimensions are very important. Indeed, the available space inside a satellite is limited, and the dimensions of any adsorbent bodies have to be controlled to avoid increased costs of the satellite. This methodology allows the various dimensions of pellets while respecting technical constraints and at the same time ensuring good mechanical properties. The adsorption properties of the zeolite pellets were also preserved [8].

Acknowledgements

We thank Gautier Schrodj for his assistance with the mechanical tests. We acknowledge the financial support from the French Space Agency (CNES) and the Region Alsace.

References

1. Perry, J. L. *NASA/TM* **1995,** *NASA-TM-108497,* 4–9.
2. Chen, P.; Hedgeland, R.; Montoya, A.; Roman-Velasquez, J.; Dunn, J.; Colony, J.; Petitto, J., Eds. *The changing Testing Paradigm,* 20th Space Simulation Conference, Annapolis, MD; 1999.
3. Barengoltz, J. B.; Moore, S.; Soules, D.; Voecks, G. *JPL Publ.* **1994,** *94,* 1–48.
4. Kirsch-Rodeschini, H. Ph.D. Thesis, University of Haute-Alsace, 2006.
5. Lauridant, N.; Daou, T. J.; Arnold, G.; Soulard, M.; Nouali, H.; Patarin, J.; Faye, D. *Microporous Mesoporous Mater.* **2012,** *152,* 1–8. doi:10.1016/j.micromeso.2011.12.012
6. Lauridant, N.; Daou, T. J.; Arnold, G.; Nouali, H.; Patarin, J.; Faye, D. *Microporous Mesoporous Mater.* **2013,** *172,* 36–43. doi:10.1016/j.micromeso.2013.01.017
7. Daou, T. J.; Lauridant, N.; Arnold, G.; Josien, L.; Faye, D.; Patarin, J. *Chem. Eng. J.* **2013,** *234,* 66–73. doi:10.1016/j.cej.2013.08.103
8. Rioland, G.; Daou, T. J.; Faye, D.; Patarin, J. *Microporous Mesoporous Mater.* **2016,** *221,* 167–174. doi:10.1016/j.micromeso.2015.09.040
9. Davis, M. E. *Nature* **2002,** *417,* 813–821. doi:10.1038/nature00785
10. Wong, S.; Ngadi, N.; Abdullah, T. A. T.; Inuwa, I. M. *Ind. Eng. Chem. Res.* **2016,** *55,* 2543–2555. doi:10.1021/acs.iecr.5b04518
11. Kabalan, I.; Rioland, G.; Nouali, H.; Lebeau, B.; Rigolet, S.; Fadlallah, M.-B.; Toufaily, J.; Hamiyeh, T.; Daou, T. J. *RSC Adv.* **2014,** *4,* 37353–37358. doi:10.1039/C4RA05567E
12. Zhao, H.; Ma, J.; Zhang, Q.; Liu, Z.; Li, R. *Ind. Eng. Chem. Res.* **2014,** *53,* 13810–13819. doi:10.1021/ie502496v
13. Zeng, Y.; Maghadam, P. Z.; Snurr, R. Q. *J. Phys. Chem. C* **2015,** *119,* 15263–15273. doi:10.1021/acs.jpcc.5b03156
14. Silva, J. A. C.; Ferreira, A.; Mendes, P. A. P.; Cunha, A. F.; Gleichmann, K.; Rodrigues, A. E. *Ind. Eng. Chem. Res.* **2015,** *54,* 6390–6399. doi:10.1021/acs.iecr.5b01608
15. Rioland, G.; Bullot, L.; Daou, T. J.; Simon-Masseron, A.; Chaplais, G.; Faye, D.; Fiani, E.; Patarin, J. *RSC Adv.* **2016,** *6,* 2470–2478. doi:10.1039/C5RA23258A
16. Bartholomew, C. H.; Farrauto, R. J. *Fundamentals of Industrial Catalytic Processes;* Wiley: New York, 2006.
17. Corma, A. *Chem. Rev.* **1995,** *95,* 559–614. doi:10.1021/cr00035a006
18. Čejka, J.; Centi, G.; Perez-Pariente, J.; Roth, W. J. *Catal. Today* **2012,** *179,* 2–15. doi:10.1016/j.cattod.2011.10.006
19. Liu, Z.; Wang, Y.; Xie, Z. *Chin. J. Catal.* **2012,** *33,* 22–38. doi:10.1016/S1872-2067(10)60299-9
20. Sánchez, P.; Dorado, F.; Fúnez, A.; Jiménez, V.; Ramos, M. J.; Valverde, J. L. *J. Mol. Catal. A: Chem.* **2007,** *273,* 109–113. doi:10.1016/j.molcata.2007.03.076
21. Jasra, R. V.; Tyagi, B.; Badheka, Y. M.; Choudary, V. N.; Bhat, T. S. G. *J. Am. Chem. Soc.* **2003,** *42,* 3263–3272. doi:10.1021/ie010953l
22. Chandrasekar, G.; Hartmann, M.; Murugesan, V. *J. Porous Mater.* **2009,** *16,* 175–183. doi:10.1007/s10934-007-9182-7
23. Topka, P.; Karban, J.; Soukup, K.; Jirátová, K.; Šolcová, O. *Chem. Eng. J.* **2011,** *168,* 433–440. doi:10.1016/j.cej.2010.12.079
24. Itani, L.; Valtchev, V.; Patarin, J.; Rigolet, S.; Gao, F.; Baudin, G. *Microporous Mesoporous Mater.* **2011,** *138,* 157–166. doi:10.1016/j.micromeso.2010.09.011
25. Hasan, F. A.; Xiao, P.; Singh, R. K.; Webley, P. A. *Chem. Eng. J.* **2013,** *223,* 48–58. doi:10.1016/j.cej.2013.02.100
26. Lai, Z. Y.; Goh, S. M. *Fuel* **2015,** *150,* 378–385. doi:10.1016/j.fuel.2015.02.021
27. Dutournié, P.; Salagnac, P.; Glouannec, P. *Drying Technol.* **2006,** *24,* 953–963. doi:10.1080/07373930600776050
28. Valencia, P.; Espinoza, K.; Ceballos, A.; Pinto, M.; Almonacid, S. *Process Biochem. (Oxford, U. K.)* **2015,** *50,* 589–597. doi:10.1016/j.procbio.2014.12.028
29. Lam, J.; Carmichael, S. T.; Lowry, W. E.; Segura, T. *Adv. Healthcare Mater.* **2015,** *4,* 534–539. doi:10.1002/adhm.201400410
30. Hinkelmann, K.; Kempthorne, O. *Design and Analysis of experiments, Introduction to experimental design;* Wiley: New Jersey, 2008.
31. NIST / SEMATECH Engineering Statistics Handbook, e-handbook. http://www.itl.nist.gov/div898/handbook/. Accessed 2003.
32. Proulx, T. *Dynamic behavior of materials, Annual Conference on Experimental and Applied Mechanics;* 2011.
33. Kadiri, M. S. Ph.D. Thesis, INP Toulouse, 2014.
34. Anderson, M. J.; Whitcomb, P. J. *Practical tool for effective experimentation;* CRC Press: New York, 2015.

License and Terms

The definitive version of this article is the electronic one which can be found at: doi:10.3762/bjnano.7.169

BEILSTEIN JOURNAL OF NANOTECHNOLOGY

Effective intercalation of zein into Na-montmorillonite: role of the protein components and use of the developed biointerfaces

Ana C. S. Alcântara[1,2], Margarita Darder[*1], Pilar Aranda[*1] and Eduardo Ruiz-Hitzky[1]

Full Research Paper

Open Access

Address:
[1]Instituto de Ciencia de Materiales de Madrid, CSIC, Cantoblanco, 28049-Madrid, Spain and [2]present address: Universidade Federal do Maranhão, Departamento de Química – PPGQuim, LIM-Bionanos, 65080-805, São Luís, MA, Brazil

Email:
Margarita Darder[*] - darder@icmm.csic.es;
Pilar Aranda[*] - aranda@icmm.csic.es

* Corresponding author

Keywords:
biohybrids; biointerfaces; bionanocomposites; montmorillonite; zein

Beilstein J. Nanotechnol. **2016,** *7,* 1772–1782.
doi:10.3762/bjnano.7.170

Received: 27 July 2016
Accepted: 02 November 2016
Published: 18 November 2016

This article is part of the Thematic Series "Hybrid nanomaterials: from the laboratory to the market".

Guest Editor: A. Taubert

Abstract

Biohybrid materials based on the intercalation of zein, the major storage protein in corn, into sodium-exchanged montmorillonite were prepared following two synthesis strategies. The first one made use of zein dissolved in 80% (v/v) ethanol/water solution, the usual solvent for this protein, while the second method is new and uses a sequential process that implies the previous separation of zein components in absolute ethanol. This treatment of zein with ethanol renders a soluble yellow phase and an agglomerate of insoluble components, which are able to intercalate the layered silicate when an aqueous dispersion of montmorillonite is added to the ethanol medium containing both phases. The diverse steps in this second route were investigated individually in order to understand the underlying mechanism that drives to the intercalation of this complex hydrophobic biomacromolecule into the hydrophilic interlayer space of sodium-exchanged montmorillonite. In addition to physicochemical characterization of the resulting materials, these biohybrid interfaces were also evaluated as biofillers in the preparation of diverse ecofriendly nanocomposites.

Introduction

Organic–inorganic hybrids are composed of organic and inorganic units that interact at the molecular scale, and the characteristics of these subunits determine a broad range of properties of the hybrid relevant for many applications [1]. Particularly, biological species can be employed in the preparation of these materials, giving rise to biohybrids, which represent a growing field of research addressed to produce advanced functional materials [2]. Many studies have demonstrated that even large molecules, such as polypeptides and proteins, intercalate into montmorillonite and other smectite clay minerals, producing biohybrid materials [2]. Montmorillonite is a 2:1 phyllosilicate characterized by a colloidal particle size, high specific surface

area and large cation exchange capacity (CEC) around 70–100 milliequivalents/100 g of clay. Structurally each silicate layer is formed by the repetition of a central octahedral alumina sheet sandwiched by two tetrahedral silica sheets [3]. Isomorphic substitutions in the octahedral and, partially, in the tetrahedral sheets result in a net negative charge of the layers that is compensated by cations (typically Na^+ and Ca^{2+}) located in the interlayer region [3]. These interlayer cations are exchangeable by treatment with diverse cationic species, being the reason of its extensive use in the development of hybrid materials by ion-exchange intercalation reactions. Since 1950 when Talibudeen reported on the intercalation of gelatin into montmorillonite [4], other biohybrids also based on the assembly of smectite clays and proteins (e.g., bovine serum albumin, gelatin, casein or soy) have been vastly studied [5-10]. However, protein adsorption on montmorillonite clay can be considered a complex process in which the structural stability of the protein, the ionic strength, the pH value as well as the surface properties can influence the affinity of the biomolecule toward the inorganic interface. In addition to the particular characteristics of each protein, the structural size and proportion of hydrophobic residues may be also a key factor in order to achieve their intercalation in montmorillonite [11,12]. Thus, depending on the type of protein involved, it is possible to obtain different interaction mechanisms between the clay and the biomacromolecule, generating the need to investigate possible interactions that can occur in less-studied proteins.

Zein is the major storage protein of corn and an important source of protein in the human diet either through direct consumption or through consumption of animals whose feed is based on corn, such as poultry or swines [13]. Although zein is known since 1821 [14,15], there is only recent interest in this protein focusing on its potential technological use [16,17]. Zein is insoluble in water but soluble in aqueous ethanol (60–95% (v/v)), aqueous solution at pH > 11, some organic polar solvents (e.g., propylene glycol and acetic acid) and certain anionic detergents [16,18,19]. The solubility is attributed to the nonpolar amino acid residues of the protein, such as valine, leucine, proline, isoleucine, alanine, and phenylalanine, which confer a hydrophobic character to the protein [16]. Therefore, a good knowledge of structural and solubility properties of zein becomes essential for the preparation of materials based on this protein. In this sense, there are reports on zein–montmorillonite composite materials prepared by thermo-plasticization and blown-extrusion techniques [20,21], or from protein solved in ethanol/water mixtures [22]. However, in these examples, organoclays containing alkylammonium surfactant species [20,22] or polyethylene glycol as plasticizer [21] were required to produce the zein-based materials. Nevertheless, the process of formation of zein–montmorillonite biohybrids making use of sodium-exchanged montmorillonite (Na-montmorillonite) and the possible mechanism that leads to them have not been described so far. With regard to this, the complex structure of zein and the role of the amino acids in its composition have to be considered, as well as the specific conformation of this protein, in order to understand a mechanism that may drive to the biohybrid formation.

In this paper, a systematic study on the preparation of zein–montmorillonite biohybrids is reported, focusing on the control of solubilized zein for an effective intercalation of the protein into Na-montmorillonite. In order to investigate the underlying mechanism of zein intercalation, the structure and features of the synthesized biohybrids were also analyzed. Zein-based biohybrids were further tested as reinforcing fillers of other biopolymer matrixes to probe their usefulness in the development of "fully" ecofriendly bioplastics. In fact, organoclays prepared by intercalation of biomolecules such as lipids or proteins have been recently reported [23-26], resulting in so-called bio-organoclays useful as fillers in the preparation of bionanocomposites or as biointerfaces for adsorption of biological species. In the present case, the incorporation of the biofillers intends to improve their compatibility with the polymer matrix, while keeping the biocompatible character of the material, and additionally incorporating interesting properties, such as barrier properties, as reported for other bio-organoclays used in reinforced bioplastics [25,27,28].

Results and Discussion

Characterization of zein in (80% v/v) ethanol solution and absolute ethanol

Zein is not soluble in water or pure alcohol. Ethanol/water mixtures of 80% (v/v) are the most commonly used solvent. However, it was observed in this work that a separation process of different components of zein in a soluble phase (EXT) and a precipitate (PCT) occurs in pure ethanol (Figure 1A), as detailed in the Experimental section. These phases show different textural characteristics as observed by FE-SEM (Supporting Information File 1, Figure S1). Colorimetric tests using a ninhydrin spray solution as revealing agent confirmed the presence of protein in the extracted liquid phase, showing a purplish color resulting from reaction between ninhydrin and free amino groups from amino acids of solubilized zein (Supporting Information File 1, Figure S2).

The molecular weight of the protein was investigated by electrophoresis (SDS-PAGE) as presented in Figure 1B. Zein solubilized in 80% v/v ethanol solution (Figure 1B, lane a) gives rise to two bands at approximately 23 and 25 kDa indicative of the α-zein conformation, which correspond to Z19 and Z22 proteins, respectively [29]. This SDS-PAGE gel also shows bands

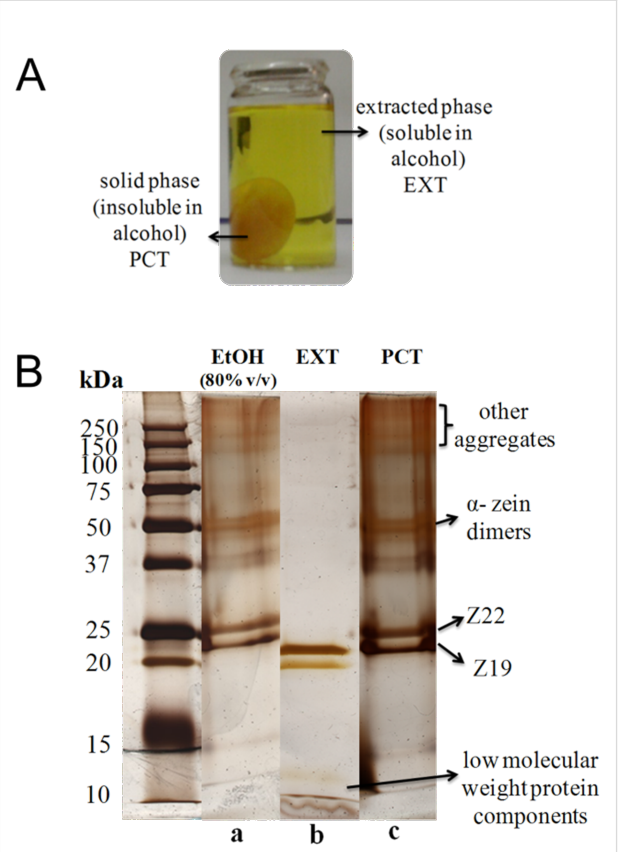

Figure 1: (A) Picture showing the separation phenomenon observed when zein protein is dispersed in absolute ethanol, and (B) SDS-PAGE of zein in 80% (v/v) ethanol/water solution (a) and of the EXT (b) and PCT (c) zein fractions separated in absolute ethanol. PCT was dissolved in 80% (v/v) ethanol/water for the analysis. The electrophoretic gel was silver stained.

around 50 kDa that reveal the presence of α-zein dimers [30,31], as well as bands at higher molecular mass (around 150 and 250 kDa) corresponding to other protein aggregates, such as trimers, tetramers and/or oligomers.

Electrophoresis measurements conducted in the PCT and EXT phases revealed that the protein pattern of PCT (Figure 1B, lane c) is very similar to that of neat zein (Figure 1B, lane a), with bands of α-zein and its dimers at approximately 21–25 kDa and 50 kDa, respectively. An intense band set of protein aggregates is also observed between 150 kDa and 250 kDa. The SDS-PAGE of the EXT phase presents a band at around 10 kDa together with those corresponding to α-zein (Figure 1B, lane b). This 10 kDa band, also reported by other authors [31], could be related to ethanol-soluble protein components associated with the xanthophyll pigments responsible for the yellow color of zein, such as lutein and zeaxanthin, which are located in the core of the triple-helical segments strongly linked to the Z19 monomer [32].

The FTIR spectra in the 4000–500 cm^{-1} region of zein, EXT and PCT (Supporting Information File 1, Figure S3A) show the bands of amide A (3600–3100 cm^{-1}), amide I (1665–1655 cm^{-1}), and amide II (1540–1530 cm^{-1}) of the protein. The spectrum of PCT (Supporting Information File 1, Figure S3A, spectrum c) is very similar to that of EXT (Supporting Information File 1, Figure S3A, spectrum b), except that the latter shows more evidently the presence of a shoulder at 1742 cm^{-1} attributed to the $\nu_{C=O}$ vibrations of carboxylic groups present in the protein structure [33]. CP-MAS ^{13}C NMR (Supporting Information File 1, Figure S3B) spectra of zein and the two fractions separated from ethanol are complex and very similar to each other, presenting signals between 173–175 ppm due to carbonyls present in the peptide groups in both the main chain and the protein side chains. The signals at 128 ppm, those from 45 to 70 and those from 15 to 45 ppm are assigned to amino acid aromatic side chains, α-carbons linked to amino groups, and carbons from the amino acid aliphatic side chains, respectively [33].

Thus, these studies indicate that although zein cannot be dissolved in pure ethanol, a separation process of different components of the protein occurs in this medium corresponding to the soluble (EXT) and insoluble zein fractions (PCT), where EXT phase is composed mainly by monomers and other protein components of low molecular weight, while PCT phase is formed by protein fractions of higher molecular mass.

Zein–montmorillonite biohybrids

A protocol that uses zein in its usual solvent, 80% (v/v) ethanol/water, and the clay dispersed in the same medium was firstly tried for the preparation of zein–montmorillonite biohybrids (synthesis 1). In an alternative synthetic approach (synthesis 2) the clay was dispersed in water, favoring the formation of a swollen phase, and zein was treated with pure ethanol to provoke its segregation in two phases. Then both systems were mixed until reaching a content of 80% (v/v) ethanol/water and left to evolve to equilibrium. The amount of zein adsorbed on montmorillonite (MMT) through these two synthetic procedures starting from systems with variable amounts of zein in contact with a defined amount of clay was deduced by CHNS chemical analysis and the results are summarized in Table 1. The values of zein adsorption on MMT prepared by synthesis 2 are almost two times higher than those resulting from synthesis 1, which suggests a different adsorption mechanism in each procedure. In both cases the adsorption increases rapidly at low protein concentration, and then reaches a constant value of approximately 11.0 g and 40.0 g of adsorbed zein per 100 g of MMT in synthesis 1 and 2, respectively. This plateau region at zein equilibrium concentration above 0.25 and 2.0 $g{\cdot}L^{-1}$ in each case can be better observed from the two adsorption curves in

Table 1: Biohybrids of the Z-MMT_S1 and Z-MMT_S2 series, prepared by adsorption of zein from 80% (v/v) ethanol/water solution and from zein segregated phases in absolute ethanol, respectively. The protein content was determined by CHNS chemical analysis.

mass of zein (in g) in contact with clay (100 g clay)	Z-MMT_S1 biohybrids codes	adsorbed zein (g zein/100 g MMT)	Z-MMT_S2 biohybrids codes	adsorbed zein (g zein/100 g MMT)
10.0	Z-MMT_S1-7	7.74	Z-MMT_S2-9	9.25
20.0	Z-MMT_S1-9	9.13	Z-MMT_S2-14	14.0
40.0	Z-MMT_S1-9.5	9.52	Z-MMT_S2-20	20.3
66.6	Z-MMT_S1-10	10.3	Z-MMT_S2-26	26.2
100.0	Z-MMT_S1-11	10.8	Z-MMT_S2-35	35.5
166.0	Z-MMT_S1-14	14.6	Z-MMT_S2-37	37.5
333.3	Z-MMT_S1-20	20.8	Z-MMT_S2-40	39.5
500.0	Z-MMT_S1-27	27.4	Z-MMT_S2-46	46.6

Figure S4 (Supporting Information File 1). At higher equilibrium concentration, the amount of adsorbed zein increases rapidly, probably because in highly concentrated solutions zein is present as aggregates that adsorb on the silicate, as observed in biohybrids of zein and fibrous clays [25].

The XRD patterns of the Z-MMT_S1 biohybrid materials with low adsorbed protein content show the (001) reflection peak at a 2θ value close to that of pristine MMT (Figure 2a). The diffractogram of Z-MMT_S1-27, with the highest zein content, shows two reflections at low 2θ angles, one corresponding to a d_{001} value of 1.18 nm, similar to that of MMT, and a second broad peak centered at 1.55 nm that can be related to the presence of an intercalated phase. Taking into account the thickness of the silicate layer of 0.96 nm [34], the interlayer distance (Δ_{dL}) gives a value of 0.59 nm, which is lower than the dimensions of the zein monomer, considering that the α-helix monomer of zein has a thickness of approximately 1.2 nm [35]. A possible explanation could be related to a partial intercalation of zein, affecting only the edges of the clay particles via ion-exchange reaction of Na^+ by protonated glutamine groups in the loops of α-helix zein molecules. Anyway, the presence of two (001) reflections in the diffractogram suggests the presence of mixed phases in the materials prepared under these synthesis conditions. The resulting biohybrids are probably formed with most of the protein molecules situated just at the external surface of

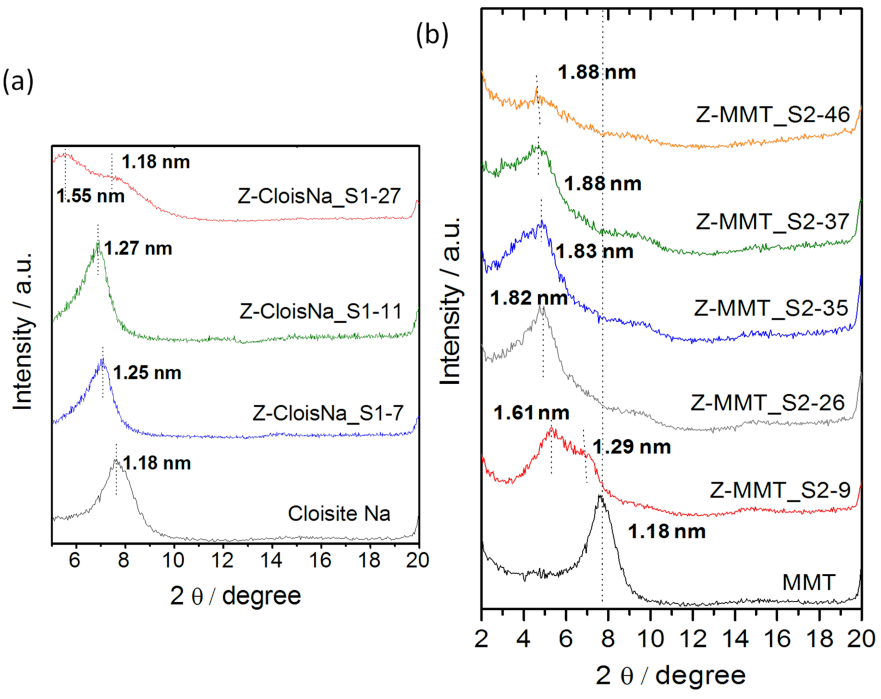

Figure 2: XRD patterns of (a) Z-MMT_S1 and (b) Z-MMT_S2 biohybrids.

the sodium montmorillonite, concluding that zein cannot be intercalated effectively in MMT by this method, as already reported by Park and co-authors in studies on zein–montmorillonite biohybrids processed by electrospinning [36].

On the other hand, the XRD patterns of Z-MMT_S2 biohybrids (Figure 2b) confirm the intercalation of zein in the clay interlayer space by the shift of the 001 peak towards lower 2θ values. Although the XRD pattern of Z-MMT_S2-9 shows a broad peak, it is possible to evidence two peaks corresponding to basal spacings of 1.61 and 1.29 nm, which suggest mixed phases with and without intercalated protein, respectively. The value of d_{001} increases with zein content and can reach a value of around 1.88 nm for zein contents higher than 25 g of protein per 100 g of MMT. The increase of the interlayer distance can be estimated to about 0.92 nm for Z-MMT_S2-37 and Z-MMT_S2-46 biohybrids, this latter having the highest content in zein. In this case, the intercalated protein is probably distorting its structure to become accommodated in the interlayer region. Similar results were reported for other proteins intercalated in sodium montmorillonite, such as bovine serum albumin (BSA) [5]. Therefore, the new route 2 seems more effective to achieve the incorporation of zein molecules into the intracrystalline space of sodium montmorillonite.

The infrared spectra of pristine MMT, zein, and Z-MMT_S2 biohybrids which contain 9.25, 26.2 and 46.6 g of protein per 100 g of MMT, respectively, are shown in Figure 3. The IR bands at 3634, 1648 and 1045 cm^{-1} are assigned to ν_{OH} modes of Al,Mg(OH) and δ_{HOH} modes of water molecules in the clay and characteristic $\nu_{Si-O-Si}$ vibration modes of the aluminosilicate, respectively (Figure 3a). Other bands that can be attributed to the intercalated protein are also observed in the spectra of the biohybrids. The frequency of the band corresponding to the ν_{CO} vibration mode of amide I that appears at 1658 cm^{-1} in pristine zein (Figure 3e) is shifted toward higher frequency values, reaching wavenumber values of 1664 cm^{-1} in the biohybrids (Figure 3b–d). This shift may be a consequence of the perturbation introduced in the amide group by interactions between the involved protonated amino groups and the negatively charged sites in the clay structure. Similar results involving changes in the amide-I band of zein were reported by Ozcalik and Tihminlioglu [37] in bionanocomposites based on organomodified montmorillonite. The band ascribed to the ν_{NH} vibration mode of the amide-A groups in zein also appears at higher wavenumber in the biohybrids, where the frequency depends on the amount of intercalated protein. This observation points out to the existence of hydrogen bonding interactions between such groups of zein and the interlayer water molecules in the clay [38]. The presence of interactions between the protein and the MMT clay is also confirmed by the displacement to lower wavenumbers of the ν_{CN} amide-II band of zein at 1538 cm^{-1}, appearing in the biohybrids at 1533 cm^{-1}.

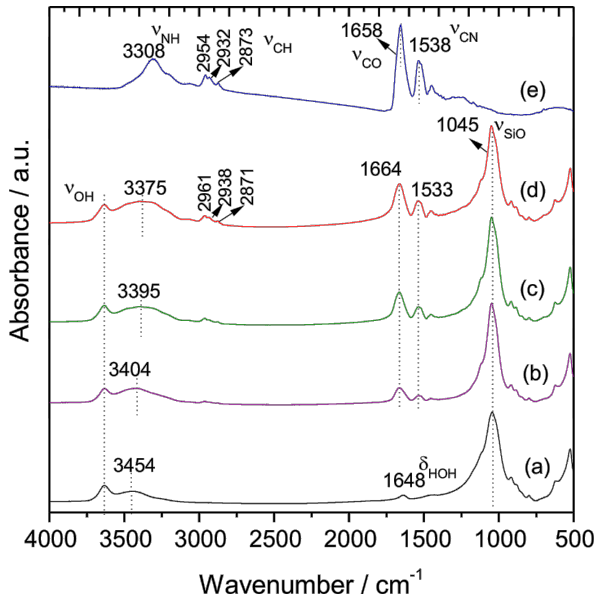

Figure 3: FTIR spectra in the 4000–500 cm^{-1} region of (a) starting MMT, (b) Z-MMT_S2-9, (c) Z-MMT_S2-26 and (d) Z-MMT_S2-46 biohybrid materials, and (e) pristine zein.

The Z-MMT_S2-46 intercalation compound, with the highest content in zein, was chosen for characterization by TEM microscopy (Figure 4). These images show the presence of the characteristic platelets of montmorillonite tactoids, which confirm that the intercalation of zein does not affect the intrinsic organization of the layered clay. By a calculation using an average of seven sheets (measurement performed by the microscope software, Figure 4b), it was found a basal spacing average of 1.7 nm in this TEM image, close to that deduced from the XRD patterns that clearly confirms the intercalation of the protein.

Intercalation mechanism of zein in MMT from protein segregated phases in absolute ethanol

In order to understand the mechanism underlying the intercalation process in synthesis 2, the interaction of MMT with each zein phase segregated in absolute ethanol was investigated individually (Figure S5a, Supporting Information File 1). Thus, the extracted phase (EXT), after removal of the precipitate fraction (PCT), was used to prepare biohybrids by addition of an aqueous clay suspension, resulting in a series of materials denoted as EXT–MMT biohybrids (Supporting Information File 1, Figure S5a, route 1). On the other hand, biohybrids based on PCT and MMT were prepared by directly mixing the MMT aqueous suspension and PCT re-suspended in pure

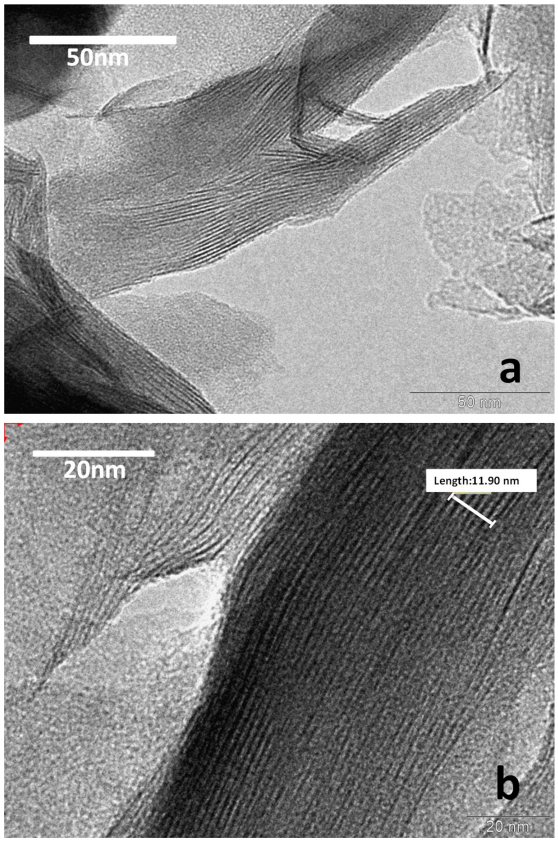

Figure 4: TEM images of the Z-MMT_S2-46 biohybrid sample. In b) the region used to estimate the basal space distance is signaled (seven sheets).

ethanol, obtaining the so-called PCT–MMT biohybrids (Supporting Information File 1, Figure S5a, route 2). In both cases, the biohybrids were formed in a final liquid phase of 80:20 (v/v) ethanol/water, i.e., similar to that used in synthesis 2.

These EXT and PCT phases were obtained from three different initial amounts of zein in pure ethanol: 20, 100 and 500 g of protein per 100 g of MMT. The amount of protein adsorbed on MMT in each case, determined by CHNS chemical analysis, was 3.32, 10.2, and 15.8 g per 100 g of MMT in the EXT–MMT biohybrids, and 18.0, 43.2, and 65.5 g per 100 g of MMT in the PCT–MMT materials. These results reveal that the biohybrids based on EXT show a lower amount of adsorbed protein than those prepared from PCT. This fact may be related to the adsorption of zein oligomers present in the PCT fraction, as shown by SDS-PAGE (Figure 1B). Adsorption of the components from EXT on MMT is confirmed from analysis by UV–vis spectroscopy of the supernatant separated after formation of the EXT–MMT biohybrids (Supporting Information File 1, Figure S6), which shows clearly the decrease of intensity in the bands ascribed to protein and carotenoid components with respect to those in the EXT phase.

The X-ray diffractograms of the EXT–MMT samples (Figure 5a) show a progressive increase of the interlayer distances as the amount of adsorbed protein increases, reaching a basal spacing value of 1.63 nm for the EXT-MMT16 sample. On the other hand, the d_{001} values determined in the PCT–MMT biohybrids range between 1.26 and 1.33 nm (Figure 5b), indi-

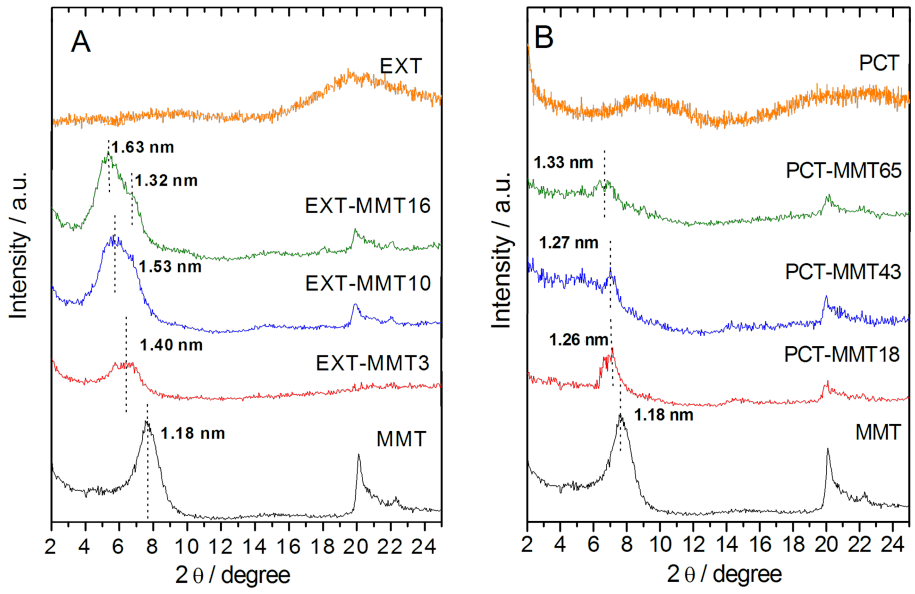

Figure 5: XRD patterns of the biohybrids prepared from (A) the extracted (EXT) and (B) the precipitate (PCT) fractions separated from different amounts of zein in pure ethanol.

cating that only a negligible intercalation took place in this case. The protein adsorbed from the PCT phase is rather located at the external surface of the clay.

The key to understanding such differences in the adsorption behavior from these two zein phases is the nature of each protein fraction. Natural zein shows two reflections at approximately 2θ = 9.3° and 20.4° in its XRD pattern, attributed to interhelix packing structure and zein α-helix backbone, respectively [21]. The EXT phase shows only a reflection around 2θ = 20.4° (Figure 5a), indicating the absence of interhelix packing, probably because the arrangement in molecular aggregates is not favored in pure ethanol, as shown by SDS-PAGE (Figure 1B, lane b). This would favor the intercalation of this phase in MMT. Conversely, in addition to a broad signal at 2θ = 20–25° that reveals the presence of zein α-helix structure, the diffractogram of the PCT phase (Figure 5b) shows a peak at 2θ = 9.3° ascribed to interhelix-packing domains [21], as also corroborated by SDS-PAGE (Figure 1B, lane c). The presence of these molecular aggregates in the PCT fraction, due to interhelix packing, could hinder the incorporation of zein molecules between the MMT layers, as shown in Figure 5b.

Considering that the EXT phase seems to play a significant role in the mechanism of zein intercalation between the layers of montmorillonite, EXT–MMT biohybrids (in aqueous dispersion) were employed as substrate for the incorporation of the PCT phase (in pure ethanol) giving rise to a series of biohybrids named as EXT–MMT/PCT (Supporting Information File 1, Figure S5b). The XRD patterns of these biohybrids are displayed in Figure 6. As observed, the characteristic 001 rational order peak in the starting EXT-MMT16 material containing 15.8 g of zein per 100 g of MMT (Figure 6a) is shifted towards lower 2θ values in the EXT–MMT/PCT biohybrids (Figure 6b–d). These basal spacing values slightly increase as the PCT content increases in the dispersion, reaching a maximum value of 1.88 nm (Figure 6d). This basal spacing value is similar to that of the Z-MMT_S2-46 biohybrid (1.88 nm), which is the biohybrid prepared by synthesis 2 route using the highest amount of zein (Figure 2b). These results are in agreement with those reported by Weiss [11], which revealed that intercalation of several proteins, such as salmin, serum and egg albumin, generally never surpasses a basal spacing of about 1.8 nm, independently of the initial protein concentration. However, in this case, although the intercalation of PCT moiety in the EXT-MMT16 hybrid can be confirmed by XRD studies, it cannot be ruled out that some PCT fractions could be also adsorbed at the external surface of the mineral. Thus, it can be inferred from this study that the mechanism of zein intercalation in MMT from the zein phases separated in ethanol could be associated with two main stages: i) the formation of a bio-organoclay based on MMT and ethanol-soluble components of zein, i.e., monomers and other protein components of low molecular weight, which can be more easily incorporated into the water-swollen MMT; ii) the intercalation of PCT constituents into the clay interlayer space possibly ascribed to the cooperative role of the already adsorbed components of zein in the biohybrid. This proposed mechanism could explain the ability of the hydrophobic protein to penetrate into the interlayer region of sodium montmorillonite following the “synthesis 2” approach proposed in this work.

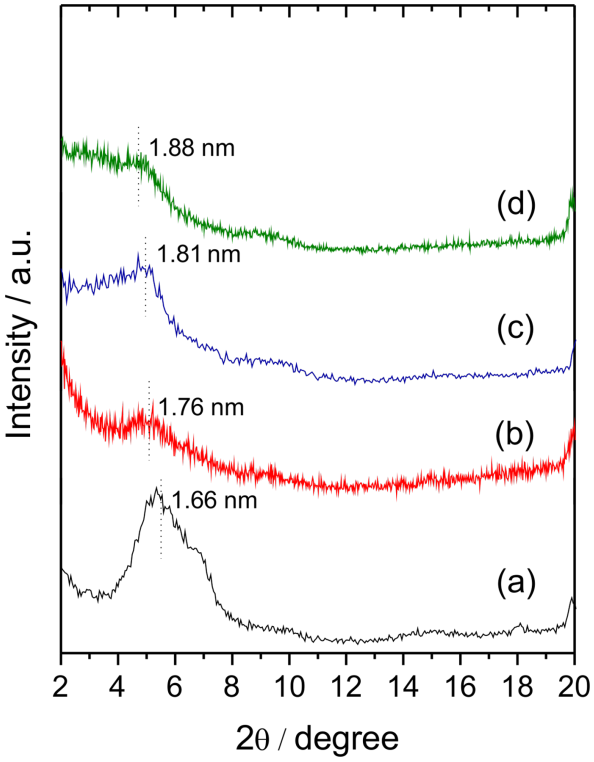

Figure 6: XRD patterns of (a) EXT-MMT16 biohybrid and the EXT–MMT/PCT biohybrids prepared with different PCT phases recovered from (b) 0.06, (c) 0.3 and (d) 1.5 g of zein in 80 mL of pure ethanol.

Zein-layered clays as nanofillers in biopolymer films

The biocompatible character of the developed bio-organoclays makes them an environmentally friendly alternative to alkylammonium-based organoclays for the use as nanofiller of bioplastics. Thus, the intercalation compound Z-MMT_S2-46 was tested as biofiller of zein (Z) and starch (STH) matrices and compared to neat MMT. Bionanocomposite films with 1.25 and 3.50% of biofiller and pure biopolymer films were prepared by casting methods (Figure 7). For this it is necessary to add a certain amount of glycerol as plasticizer component in the blank films to reduce their high brittleness. The light transmittance of

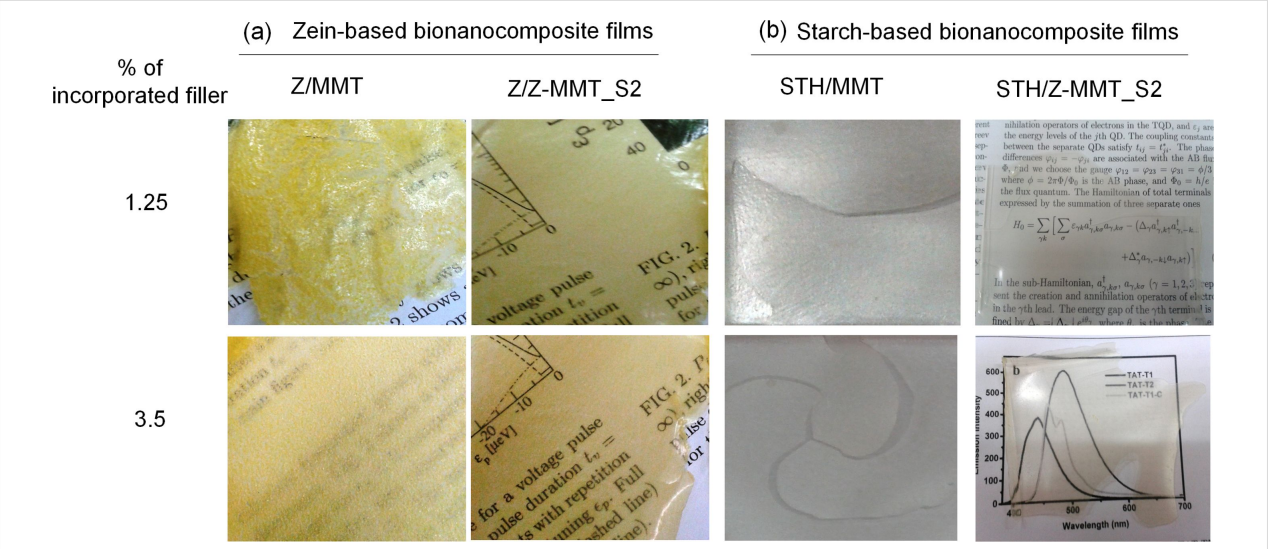

Figure 7: Photographs of (a) zein and (b) starch bionanocomposite films loaded with pure MMT or Z-MMT_S2-46 biohybrid.

zein bionanocomposites was higher for films containing Z-MMT_S2, but in the starch materials its effect was similar to that of MMT (Supporting Information File 1, Figure S7). Self-standing MMT-modified zein films show great opacity and an inhomogeneous aspect ratio (Figure 7a), due to a poor compatibility between the hydrophilic clay and the hydrophobic zein matrix. In contrast, Z/Z-MMT_S2 bionanocomposite films present a higher homogeneity and transparency (Figure 7a), confirming a good dispersion of the biohybrid within the zein matrix. Interestingly, all the bionanocomposite films based on starch appear very homogenous (Figure 7b), but those loaded with neat MMT are very brittle and exhibit fractures. This behavior is likely due to the absence of plasticizer, commonly used to increase the flexibility of the resulting material. Conversely, starch films loaded with 1.25% (w/w) of Z-MMT_S2 biohybrid do not exhibit fractures even without the addition of plasticizer, indicating the good compatibility of the biohybrid and the polysaccharide matrix.

Tensile-stress studies were carried out for the zein and starch bionanocomposite films. Those films loaded with neat MMT and 3.5% (w/w) Z-MMT_S2 biohybrid were excluded from this study due to their high brittleness. Similar behavior was observed for pure zein and starch films, and in these cases glycerol was added as plasticizer in order to use them as reference.

The Young´s modulus of the Z/Z-MMT_S2 film is 1.2 GPa, about 2.5 times higher than that of the unmodified film of zein (0.5 GPa), being analogous to that reported by Nedi et al. [21] in thermoplastic zein films modified with 5 wt % of MMT and using 25 wt % poly(ethylene glycol) as plasticizer. This loading of Z-MMT_S2 seems to act simultaneously as reinforcing filler and plasticizer in the zein matrix, reducing its brittleness even in the absence of glycerol. Similar results were observed in the STH/Z-MMT_S2 film, showing a Young's modulus of 0.5 GPa, around twice that of the pristine starch film (0.2 GPa). This value is slightly higher than those reported for thermoplastic starch matrices reinforced by cationic starch-modified montmorillonite [27], probably because the addition of plasticizers was avoided in the current work. In contrast to the zein-based films, the positive effect of zein-based fillers on starch cannot be attributed to the compatibility between both systems, but it might be due to their plasticizing effect.

The elongation-at-break values of the bionanocomposites Z/Z-MMT_S2 and STH/Z-MMT_S2 were 2.0% and 1.98%, respectively, lower than those measured for neat zein and starch films (3.1% and 10.7%, respectively). These higher values in the blank biopolymer films are due to the glycerol plasticizer, as commented above, which increases flexibility and stretchability of the biopolymer matrix. In the bionanocomposite films, a reduced mobility of the zein and starch chains after incorporation of the biofiller can take place, as observed in other clay-reinforced polymer nanocomposites [39].

Although this preliminary study would require optimization for the preparation of bionanocomposites with better properties, these results point out to the promising use of zein-based biohybrids as an ecological alternative to conventional alkylammonium-modified clays usually employed as reinforcing agent.

Conclusion

A new insight about the formation of biohybrids from the intercalation of zein protein in Na-montmorillonite clay was

afforded comparing two methodologies of synthesis: the direct adsorption of zein from 80% (v/v) ethanol/water solution and the adsorption of the zein phases previously segregated in absolute ethanol to which is added a water suspension of the clay (80% (v/v) ethanol/water in the final system). Only the latter was more effective in achieving the incorporation of zein molecules into the intracrystalline space of Na-montmorillonite. A systematic study of the individual steps of intercalation of zein into the layered clay evidences that once zein phases are separated in ethanol, the ethanol-soluble components of zein first intercalate into Na-montmorillonite, being followed by a subsequent cooperative process in which the protein present in the biohybrid favors further adsorption of other zein components.

The obtained biohybrids were evaluated as bio-organoclays for the incorporation in zein and starch biopolymer films, which exhibited good compatibility, homogeneity and mechanical properties, and made it possible to avoid the addition of compatibilizers or plasticizers. These results suggest that these new biohybrid materials could be associated with other polymers of different nature, being a promising ecological alternative to common organoclays based on alkylammonium cations. Other fields of applying the biohybrids could be the use as biointerfaces of various biological species.

Experimental

Starting materials and reagents

A natural Wyoming sodium montmorillonite (MMT), commercialized as Cloisite®Na^+, was purchased from Southern Clay Products (USA). Zein (Z) and starch from corn were purchased from Sigma-Aldrich, absolute ethanol from Panreac, and ninhydrin spray reagent 0.1% for chromatography from Merck. Deionized water (resistivity of 18.2 MΩ·cm) was obtained with a Maxima Ultrapure Water from Elga.

Synthesis of zein–montmorillonite biohybrids

For the preparation of zein–montmorillonite biohybrids (Z-MMT) two synthetic routes were explored.

Synthesis 1 (Z-MMT_S1 materials)

A MMT suspension (6 $g \cdot L^{-1}$) was prepared in aqueous 80% (v/v) ethanol solution by vigorous stirring in a shear mixer (G2 model, Lomi) in order to properly disperse the clay. Solutions of zein (80% (v/v) ethanol/water) with different content in protein (30–1500 mg) were prepared in 50 mL, in order to achieve different weight proportions of zein with respect to montmorillonite in the biohybrid materials. Each zein solution was added to 50 mL of the MMT dispersion and the resulting mixture was stirred for 48 h at room temperature. Then, the solid product was isolated by centrifugation and dried overnight at 40 °C.

Synthesis 2 (Z-MMT_S2 materials)

In this synthesis, 300 mg of MMT were firstly swollen in 20 mL of water. Different amounts of zein (30–1500 mg) were added to 80 mL of ethanol. Zein was not completely dissolved in pure ethanol, but a separation process of different components of the protein took place, yielding an extracted phase (soluble in alcohol, denoted as EXT) and a solid or precipitate phase (insoluble in alcohol, denoted as PCT), resulting from the agglomeration of the insoluble components (Figure 1A). The aqueous clay suspension was then added to this system with the two phases of zein in absolute ethanol. The solid phase of the protein began to solubilize as the liquid phase reached a 80:20 ethanol/water ratio, forming at this point a homogeneous Z-MMT suspension. The system was kept under magnetic stirring for 48 h at room temperature, and then the solid was separated by centrifugation and dried overnight at 40 °C.

Use of zein–montmorillonite as biofiller in bionanocomposites preparation

The biohybrid Z-MMT_S2_46 (i.e., containing 46 g of zein per 100 g clay) was used in the preparation of zein and starch films with different biofiller content (0, 1.25 and 3.50% with respect to the biopolymer mass). In the case of zein films loaded with zein–montmorillonite (Z/Z-MMT_S2), 2.5 g of zein were solubilized in 45 mL of aqueous ethanol solution (80% (v/v)), under vigorous magnetic stirring and kept at 80 °C. Then, 5 mL of zein–montmorillonite dispersion in water were added to the zein solution at 80 °C forming a single batch that was kept under stirring for approximately 30 min to reach room temperature. After total homogenization, the resulting dispersion was placed in a methacrylate mould, and dried at room temperature. The starch films based on zein–montmorillonite biohybrids (STH/Z-MMT_S2) were prepared similarly to the zein films discussed above, but starch was dissolved in pure water at 80 °C.

For comparison, zein and starch films containing MMT (Z/MMT and STH/MMT, respectively) were also prepared under the same conditions than those used for the preparation of the bionanocomposite films filled with biohybrids. Blank films of zein (Z) and starch (STH) were prepared by dissolving 2.5 g of zein or starch in 50 mL of ethanol solution at 80% (v/v) or pure water, respectively. In both systems it was necessary to add 0.5 g of glycerol as plasticizer, keeping the mixtures under magnetic stirring at 80 °C until complete homogenization of the components.

Characterization

Fourier transform infrared (FTIR) spectra of samples in film form or diluted in KBr as pellets were recorded from 4000 to 250 cm^{-1} (2 cm^{-1} resolution) with a FTIR spectrophotometer BRUKER IFS 66v/S. CHNS elemental chemical microanalysis

of samples was determined in a Perkin-Elmer 2400 analyzer. Solid-state CP-MAS ^{13}C NMR spectra of samples spun at 10 kHz were obtained in a Bruker Avance 400 spectrometer, using a contact time of 2 ms and a period between successive accumulations of 5 s. The number of scans was 800 and chemical shift values were referenced to tetramethylsilane. The qualitative analysis of protein fractions (λ = 250–600 nm) and the UV–vis transmittance (λ = 200–800 nm) of bionanocomposite films (rectangular shape, 2 cm × 4 cm) were determined using a Shimadzu UV-1201 spectrophotometer. Surface morphology was observed with a FE-SEM equipment FEI-NOVA NanoSEM 230, which allowed semi-quantitative analysis of elements. The equipment allows for the direct observation of samples adhered on a carbon tape without requirement of any conductive coating on the surface. For the TEM images (Philips Tecnai 20, operating at 200 kV), the biohybrids were previously embedded in epoxy resin and then cut in very thin sections using an ultramicrotome (LEICA EM UC6) equipped with a diamond blade.

SDS-PAGE

SDS-PAGE was performed according to Cabra and co-workers [29], where aliquots of 7.5 µL containing approximately 30 µg of zein solubilized in 80% (v/v) ethanol/water or those zein fractions obtained from pure ethanol were re-suspended in equal volumes of deionized water and buffer (0.125 M Tris-Cl, 4% SDS, 20% glycerol, 10% 2-mercaptoethanol (BME), and bromphenol blue 0.01%, pH 6.4). The EXT phase was directly used after separation in absolute ethanol, while the PCT phase was firstly solubilized in 80% (v/v) ethanol/water. The polyacrylamide gels at 20% were silver-stained for band visualization.

Mechanical properties

The mechanical properties, Young's modulus (E) and elongation at break, of the bionanocomposite film samples were evaluated (in three replicates) with a Model 3345 Instron Universal Testing Machine (Instron Engineering Corporation Canton, MA, USA) according to the ASTM standard method D 882-88. Rectangular samples (ca. 60 mm × 15 mm) were mounted between the grips with an initial separation of 50 mm, and the cross-head speed was set at 2 mm·min^{-1}.

Supporting Information

Supporting Information File 1

Additional experimental data.
[http://www.beilstein-journals.org/bjnano/content/supplementary/2190-4286-7-170-S1.pdf]

Acknowledgements

This work was supported by the MINECO (Spain) projects MAT2012-31759 & MAT2015-71117-R and the EU COST Action MP1202. A.C.S.A. acknowledges CSIC for a JAE-Predoc fellowship. The authors also thank Mr. A. Valera and Mr. C. Sebastián for technical assistance in the FE-SEM study, and Mr J. González Casablanca (CAT URJC) for the TEM images.

References

1. Sanchez, C.; Belleville, P.; Popall, M.; Nicole, L. *Chem. Soc. Rev.* **2011,** *40,* 696–753. doi:10.1039/c0cs00136h
2. Ruiz-Hitzky, E.; Darder, M.; Aranda, P. An introduction to bio-nanohybrid materials. In *Bio-inorganic Hybrid Nanomaterials - Strategies, Syntheses, Characterization and Application;* Ruiz-Hitzky, E.; Ariga, K.; Lvov, Y. M., Eds.; Wiley-VCH: Weinheim, 2008; pp 1–40. doi:10.1002/9783527621446.ch1
3. Brigatti, M. F.; Galán, E.; Theng, B. K. G. Structures and mineralogy of clay minerals. In *Handbook of Clay Science;* Bergaya, F.; Theng, B. K. G.; Lagaly, G., Eds.; Elsevier Science Ltd.: Amsterdam, 2006; pp 19–86. doi:10.1016/S1572-4352(05)01002-0
4. Talibudeen, O. *Nature* **1950,** *166,* 236. doi:10.1038/166236a0
5. De Cristofaro, A.; Violante, A. *Appl. Clay Sci.* **2001,** *19,* 59–67. doi:10.1016/S0169-1317(01)00047-3
6. Darder, M.; Ruiz, A. I.; Aranda, P.; Van Damme, H.; Ruiz-Hitzky, E. *Curr. Nanosci.* **2006,** *2,* 231–241. doi:10.2174/157341371060203023l
7. Chen, P.; Zhang, L. *Biomacromolecules* **2006,** *7,* 1700–1706. doi:10.1021/bm050924k
8. Lin, J.-J.; Wei, J.-C.; Juang, T.-Y.; Tsai, W.-C. *Langmuir* **2007,** *23,* 1995–1999. doi:10.1021/la062013h
9. Fernandes, F. M.; Ruiz, A. I.; Darder, M.; Aranda, P.; Ruiz-Hitzky, E. *J. Nanosci. Nanotechnol.* **2009,** *9,* 221–229. doi:10.1166/jnn.2009.J002
10. Tran, A. T. T.; James, B. J. *Colloids Surf., A* **2012,** *414,* 104–114. doi:10.1016/j.colsurfa.2012.08.066
11. Weiss, A. In *Organic Geochemistry;* Eglinton, G.; Murphy, M. T. J., Eds.; Springer Verlag: Berlin, Germany, 1969; pp 737–781. doi:10.1007/978-3-642-87734-6_38
12. Chao, V. W.-K.; Hsu, C.-C.; Lu, W.-M.; Chen, W.-J.; Naveen, B.; Tsai, T.-Y. *RSC Adv.* **2015,** *5,* 10936–10943. doi:10.1039/C4RA13334J
13. Bicudo, R. C.; Bicudo, T. C.; Forato, L. A.; Colnago, L. A.; Lanças, F. M. *Comun. Tec. - EMBRAPA, Cent. Pesqui. Agropecu. Trop. Umido* **2006,** *77,* 1–3.
14. Lawton, J. W. *Cereal Chem.* **2002,** *79,* 1–18. doi:10.1094/CCHEM.2002.79.1.1
15. Anderson, T. J.; Lamsal, B. P. *Cereal Chem.* **2011,** *88,* 159–173. doi:10.1094/CCHEM-06-10-0091
16. Shukla, R.; Cheryan, M. *Ind. Crops Prod.* **2001,** *13,* 171–192. doi:10.1016/S0926-6690(00)00064-9
17. Paliwal, R.; Palakurthi, S. *J. Controlled Release* **2014,** *189,* 108–122. doi:10.1016/j.jconrel.2014.06.036
18. Li, Y.; Li, J.; Xia, Q.; Zhang, B.; Wang, Q.; Huang, Q. *J. Phys. Chem. B* **2012,** *116,* 12057–12064. doi:10.1021/jp305709y
19. Sun, C.; Dai, L.; He, X.; Liu, F.; Yuan, F.; Gao, Y. *Food Hydrocolloids* **2016,** *58,* 11–19. doi:10.1016/j.foodhyd.2016.02.014
20. Luecha, J.; Sozer, N.; Kokini, J. L. *J. Mater. Sci.* **2010,** *45,* 3529–3537. doi:10.1007/s10853-010-4395-6

21. Nedi, I.; Maio, E. D.; Iannace, S. *J. Appl. Polym. Sci.* **2012,** *125,* E314–E323. doi:10.1002/app.36860
22. Alcântara, A. C. S.; Aranda, P.; Darder, M.; Ruiz-Hitzky, E. In *Proceedings of the ACS Division of Polymeric Materials: Science & Engineering,* 241st National Meeting and Exposition of the American-Chemical-Society (ACS), Anaheim, CA, March 27–31, 2011; pp 114–115.
23. Wicklein, B.; Darder, M.; Aranda, P.; Ruiz-Hitzky, E. *Langmuir* **2010,** *26,* 5217–5225. doi:10.1021/la9036925
24. Yang, L.; Phua, S. L.; Teo, J. K. H.; Toh, C. L.; Lau, S. K.; Ma, J.; Lu, X. *ACS Appl. Mater. Interfaces* **2011,** *3,* 3026–3032. doi:10.1021/am200532j
25. Alcântara, A. C. S.; Darder, M.; Aranda, P.; Ruiz-Hitzky, E. *Eur. J. Inorg. Chem.* **2012,** *2012,* 5216–5224. doi:10.1002/ejic.201200582
26. Phua, S. L.; Yang, L.; Toh, C. L.; Huang, S.; Tsakadze, Z.; Lau, S. K.; Mai, Y.-W.; Lu, X. *ACS Appl. Mater. Interfaces* **2012,** *4,* 4571–4578. doi:10.1021/am300947b
27. Chivrac, F.; Pollet, E.; Dole, P.; Avérous, L. *Carbohydr. Polym.* **2010,** *79,* 941–947. doi:10.1016/j.carbpol.2009.10.018
28. Alcântara, A. C. S.; Darder, M.; Aranda, P.; Ayral, A.; Ruiz-Hitzky, E. *J. Appl. Polym. Sci.* **2016,** *133,* 42362. doi:10.1002/app.42362
29. Cabra, V.; Arreguin, R.; Galvez, A.; Quirasco, M.; Vazques-Duhalt, R.; Farres, A. *J. Agric. Food Chem.* **2005,** *53,* 725–729. doi:10.1021/jf048530s
30. Esen, A. *J. Cereal Sci.* **1987,** *5,* 117–128. doi:10.1016/S0733-5210(87)80015-2
31. Sessa, D. J.; Eller, F. J.; Palmquist, D. E.; Lawton, J. W. *Ind. Crops Prod.* **2003,** *18,* 55–65. doi:10.1016/S0926-6690(03)00033-5
32. Momany, F. A.; Sessa, D. J.; Lawton, J. W.; Selling, G. W.; Hamaker, S. A.; Willett, J. L. *J. Agric. Food Chem.* **2006,** *54,* 543–547. doi:10.1021/jf058135h
33. Forato, L. A.; Bicudo, T. C.; Colnago, L. A. *Biopolymers* **2003,** *72,* 421–426. doi:10.1002/bip.10481
34. Theng, B. K. G.; Newman, R. H.; Whitton, J. S. *Clay Miner.* **1998,** *33,* 221–229. doi:10.1180/000985598545589
35. Wang, Q.; Crofts, A. R.; Padua, G. W. *J. Agric. Food Chem.* **2003,** *51,* 7439–7444. doi:10.1021/jf0340658
36. Park, J. H.; Park, S. M.; Kim, Y. H.; Oh, W.; Lee, G. W.; Karim, M. R.; Park, J. H.; Yeum, J. H. *J. Compos. Mater.* **2012,** *47,* 251–257. doi:10.1177/0021998312439221
37. Ozcalik, O.; Tihminlioglu, F. *J. Food Eng.* **2013,** *114,* 505–513. doi:10.1016/j.jfoodeng.2012.09.005
38. Ruiz-Hitzky, E.; Aranda, P.; Serratosa, J. M. Clay-organic interactions: Organoclay complexes and polymer-clay nanocomposites. In *Handbook of Layered Materials;* Auerbach, S. M.; Carrado, K. A.; Dutra, P., Eds.; Marcel Dekker: New York, 2004; pp 91–154. doi:10.1201/9780203021354.ch3
39. Alexandre, M.; Dubois, P. *Mater. Sci. Eng., R* **2000,** *28,* 1–63. doi:10.1016/S0927-796X(00)00012-7

License and Terms

BEILSTEIN JOURNAL OF NANOTECHNOLOGY

In situ formation of reduced graphene oxide structures in ceria by combined sol–gel and solvothermal processing

Jingxia Yang[1,2], Johannes Ofner[3], Bernhard Lendl[3] and Ulrich Schubert[*1]

Full Research Paper

Open Access

Address:
[1]Institute of Materials Chemistry, Vienna University of Technology, Getreidemarkt 9, 1060 Wien, Austria, [2]permanent address: College of Chemistry and Chemical Engineering, Shanghai University of Engineering Science, LongTeng Road 333, 201620 Shanghai, P. R. China and [3]Institute of Chemical Technologies and Analytics, Vienna University of Technology, Getreidemarkt 9, 1060 Wien, Austria

Email:
Ulrich Schubert* - Ulrich.Schubert@tuwien.ac.at

* Corresponding author

Keywords:
ceria; CO oxidation; graphene oxide; sol–gel processing

Beilstein J. Nanotechnol. **2016,** *7,* 1815–1821.
doi:10.3762/bjnano.7.174

Received: 23 August 2016
Accepted: 10 November 2016
Published: 23 November 2016

This article is part of the Thematic Series "Hybrid nanomaterials: from the laboratory to the market".

Guest Editor: A. Taubert

Abstract

Raman and IR investigations indicated the presence of reduced graphene oxide (rGO)-like residues on ceria nanoparticles after solvothermal treatment in ethanol. The appearance of such structures is closely related to cerium *tert*-butoxide as precursor and ethanol as solvothermal solvent. The rGO-like residues improve the catalytic CO oxidation activity. This was also confirmed by introduction of "external" graphene oxide during sol–gel processing, by which the rGO structures and the catalytic activity were enhanced.

Introduction

Ceria (CeO_2) has been widely studied as catalyst or catalyst support for redox reactions owing to its high oxygen storage and release capacity. It is mostly used together with other components, such as noble metals or transition metal oxides, such as NiO or Co_3O_4, because synergistic effects improve the catalytic properties. Graphene-modified CeO_2 greatly enhances the performance in electrochemical devices (supercapacitors, fuel cells or batteries) [1-7] or (photo-)catalysts [8-16]. The property enhancements are mainly due to the charge transfer between graphene and CeO_2. For the preparation of graphene–CeO_2 composites external graphene oxide (GO) is usually added to the ceria precursor or pre-synthesized ceria particles followed by reduction to reduced graphene oxide (rGO) [1-16].

In a previous study, we have synthesized CeO_2 [17] from cerium *tert*-butoxide by combined sol–gel and solvothermal processing. The kind of post-synthesis treatment of the gels proved to be crucial for the specific surface area, the Ce^{3+} proportion and, as a consequence, the CO oxidation activity of the obtained materials, which were composed of 3.5–5.5 nm ceria nanoparticles. CeO_2 solvothermally treated with EtOH had

the highest surface area and showed better CO oxidation activity than the hydrothermally treated samples. A weight loss of ca. 12% was observed in TGA after solvothermal treatment of the gels with ethanol. This was not the case after hydrothermal treatment (only ca. 4%). We interpreted the high weight loss in the former samples to the presence of residual organic groups partly originating from EtOH and possibly associated with the high Ce^{3+} proportion (12%). We now show that the organic residues contain graphene-like structures. Furthermore, external graphene oxide was introduced into the system, to investigate how the graphene-like structures influence the properties and structure of the ceria–graphene composites.

Ceria or its composites are often prepared by solvothermal synthesis using various alcohols. In some reports organic residues on the surface of the ceria particles were noticed, even if ceria was prepared from $(NH_4)_2[Ce(NO_3)_6]$, and alkoxide or carboxylate groups were identified [18]. Graphene-like structures, however, were never mentioned.

Experimental

Synthesis of rGO-modified CeO_2

The procedure for the preparation of the ceria–rGO composites was the same as previously reported for that of pure ceria [17] (or Co_3O_4-modified CeO_2 [19]) with the difference that varying proportions of GO were added to the precursor mixture. Graphene oxide (GO) was synthesized by the modified Hummer method [20,21]. All steps involving Ce(O*t*-Bu)$_4$ were carried out under moisture-free argon using standard Schlenk or glove box techniques.

Ce(O*t*-Bu)$_4$ (5 mmol) was dissolved in 1,2-dimethoxyethane (10 mL), followed by the addition of acetaldoxime (10 mmol) and stirring for 30 min, addition of the surfactant F127 (0.025 mmol) and additionally stirring for 1 h. No water was added during this stage. Different proportions of GO (0–0.2 g) were then added. The mixture was stirred for 30 min, ultrasonically treated for at least 2 h and then deposited onto glass sheets (20 × 30 cm^2), which had been cleaned with 10% KOH, isopropanol and acetone and dried at 100 °C. The deposited films were exposed to ambient humidity at room temperature for 24 h (for hydrolysis and condensation along with solvent evaporation). The solid films were then scraped off with a razor blade to get a gel powder. The gel from 5 mmol Ce(O*t*-Bu)$_4$ was transferred into a 60 mL autoclave with 30 mL EtOH, which was sealed, heated to 200 °C for 6 h and then cooled to room temperature by means of cold water. The solid was separated by centrifugation, washed at least three times with EtOH and H_2O and then dried at 105 °C overnight. The samples were named rGO(x)-CeO_2 (rGO was used to indicate GO after solvothermal treatment), where x is the mass of added GO in grams. For the sake of consistency, the sample with organic residues, but without externally added rGO is thus labelled rGO(0)–CeO_2.

Characterization

Raman spectra and maps were collected on a Horiba Jobin Yvon Micro-Raman spectrometer (LabRam 800 HR) equipped with an integral Olympus BX 41 microscope (20× objective) and a Peltier-cooled CCD detector, using the 632 nm line of a HeNe laser (1.5 mW) for excitation. A 600 line grating was used for obtaining the Raman spectra. The Raman–Stokes spectra were recorded in the range of 2500–300 cm^{-1} at 1.3 cm^{-1} spectral resolution. The spectrograph was calibrated using the 520 cm^{-1} Raman band of a Si wafer. Raman mapping was performed using a 10× magnification objective and a 300 line grating; a 532 nm (frequency doubled Nd:YAG) DPSS laser was used. An area of 500 × 500 μm^2 with a lateral resolution of 5 μm was mapped by scanning each pixel three times for 1 s.

X-ray powder diffraction (XRD) measurements were performed on a Philips X'Pert diffractometer using Cu Kα radiation (λ = 1.5406 Å). High-resolution transmission electron micrographs (HRTEM) were recorded on a TECNAI F20 operated at 200 kV. Before the measurements, the samples were ultrasonically dispersed in EtOH for 30 min, and then deposited on copper grids covered with carbon films. FTIR spectra with 4 cm^{-1} resolution were recorded on a Bruker Tensor 27 equipped with an ATR Micro Focusing MVP-QL with a ZnSe crystal, using OPUS 4.0 software for analysis.

Thermogravimetric analysis (TGA) was performed on a Netzsch Iris TG 209 C in a platinum crucible in synthetic air with a heating rate of 10 °C/min. Nitrogen sorption measurements were performed on an ASAP 2020 (Micromeritics). The samples were degassed in vacuum at room temperature for at least 5 h prior to measurement. The total surface area was calculated according to Brunauer, Emmett and Teller (BET), and the pore size distribution (from the desorption branch) according to Barrett, Joyner and Halenda (BJH).

CO oxidation was performed in a continuous-flow fixed-bed quartz reactor under atmospheric pressure. A sample amount of 20 mg was loaded into the reactor and pretreated with synthetic air (30 mL/min) at 200 °C for 40 min (heating rate 10 °C/min). Then the sample was cooled to 30 °C in flowing synthetic air, and a mixture of 5 vol % CO, 10 vol % O_2 and 85 vol % He (total flow 50 mL/min) was introduced. The system was then heated to 650 °C with a ramping rate of 5 °C/min. The concentrations of CO and CO_2 in the outlet streams were monitored by gas chromatography with a HP-PLOT Q column and a flame ionization detector. For temperature-programmed reduction of

CO (CO-TPR) the samples were exposed, after cooling, to a mixture of 5 vol % CO and 95 vol % He (total flow 50 mL/min) at room temperature. Then the system was ramped up to 900 °C at a heating rate of 10 °C/min. The gas stream was analyzed by an online quadrupole mass spectrometer (QMS) (Prisma Plus QMG 220, Pfeiffer Vacuum) equipped with a Faraday detector.

Results and Discussion

In order to shed light on the nature of the organic residues formed when the ceria gels were supercritically treated with ethanol [17], we performed extensive Raman studies. The sample (named rGO(0)–CeO_2 according to the labelling scheme used in this article) surprisingly showed Raman bands that are attributed to the D- (1388 cm^{-1}) and the G- (1577 cm^{-1}) band of graphene (Figure 1f). As amorphous carbon shows no D-band [22,23], the organic residues have a graphene-like structure, indicating graphene-like structures in the organic residue. Furthermore, the F_{2g} band of CeO_2 was also observed at 461 cm^{-1}.

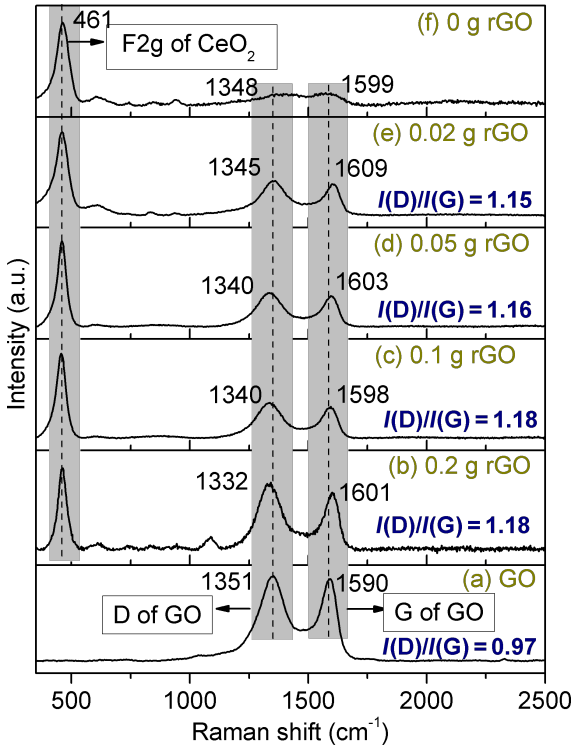

Figure 1: Raman spectra of GO (a); of CeO_2 with rGO-like organic residues (sample rGO(0)–CeO_2) (f); and of rGO–CeO_2 composites with different proportions of added rGO (b–e) after solvothermal treatment in ethanol.

The D-band is related to a breathing mode of κ-point photons of A_{1g} symmetry, and the G-band can be attributed to the splitting of the E_{2g} stretching mode of graphite, which reflects the proportion of the sp^2-hybridized carbon atoms [24]. The intensity ratio I(D)/I(G) represents the degree of disorder in a graphite layer. The GO synthesized in this study showed the typical D- and G-band at 1351 cm^{-1} and 1590 cm^{-1}, respectively, with an intensity ratio I(D)/I(G) of 0.97. Generally, the G- and D-bands slightly shift to lower values when GO is reduced to graphene [25,26].

No D- and G-band were observed in the Raman spectra (Supporting Information File 1, Figure S1) when (1) H_2O was used instead of EtOH for solvothermal treatment or (2) cerium ammonium nitrate $(NH_4)_2[Ce(NO_3)_6]$ was used as precursor instead of cerium *tert*-butoxide (identical preparation conditions in all cases). We did not check cerium alkoxides, $Ce(OR)_4$, with other groups R. This indicates that the appearance of residues with rGO-like structures is closely related to cerium *tert*-butoxide (or possibly $Ce(OR)_4$ in general) as precursor and ethanol as the solvothermal solvent. The alcohol acts as a reductant for GO.

In this study, varying proportions of pre-synthesized graphene oxide (GO) were introduced into the ceria gel to investigate its dispersion and its effect on structure and properties of the sol–gel ceria. Raman spectra showed that the D-bands of all rGO–CeO_2 composites were shifted to lower values (Figure 1), indicating that the GO had been reduced to graphene (rGO) during solvothermal processing in EtOH. The G-bands, however, were slightly shifted to higher values compared with that of GO. This can be attributed to the increased number of defects caused by stress from the oxygen states [16,27,28] as indicated by the intensity ratio I(D)/I(G). I(D)/I(G) values for all rGO–CeO_2 composites were larger than that of GO, indicating that the number of defects in the graphene layer increased during the reduction of GO [29,30]. Anchoring of CeO_2 on rGO also caused an intensity decrease and up-shifting of the G-band because of the electron transfer [9,16].

The distribution of rGO was investigated by Raman mapping. Only the mappings for the samples with 0.2 g, 0.05 g and 0.02 g rGO are reproduced in Figure 2, because the Raman intensity for GO proportions of 0.1 and 0.05 g were almost the same. For a GO proportion of 0.05 and 0.02 g, the Raman mapping showed no obvious phase separation, indicating that rGO and CeO_2 were homogeneously dispersed. However, when the GO proportion was 0.2 g, phase separation (agglomeration of rGO) was observed by partial disappearance of the CeO_2 signal and the enhancement of the rGO signal in the corresponding area. In this case, GO apparently cannot disperse well enough after solvothermal treatment.

The IR spectra of all rGO–CeO_2 composites (Figure 3) were almost the same, and only the peak intensities were somewhat

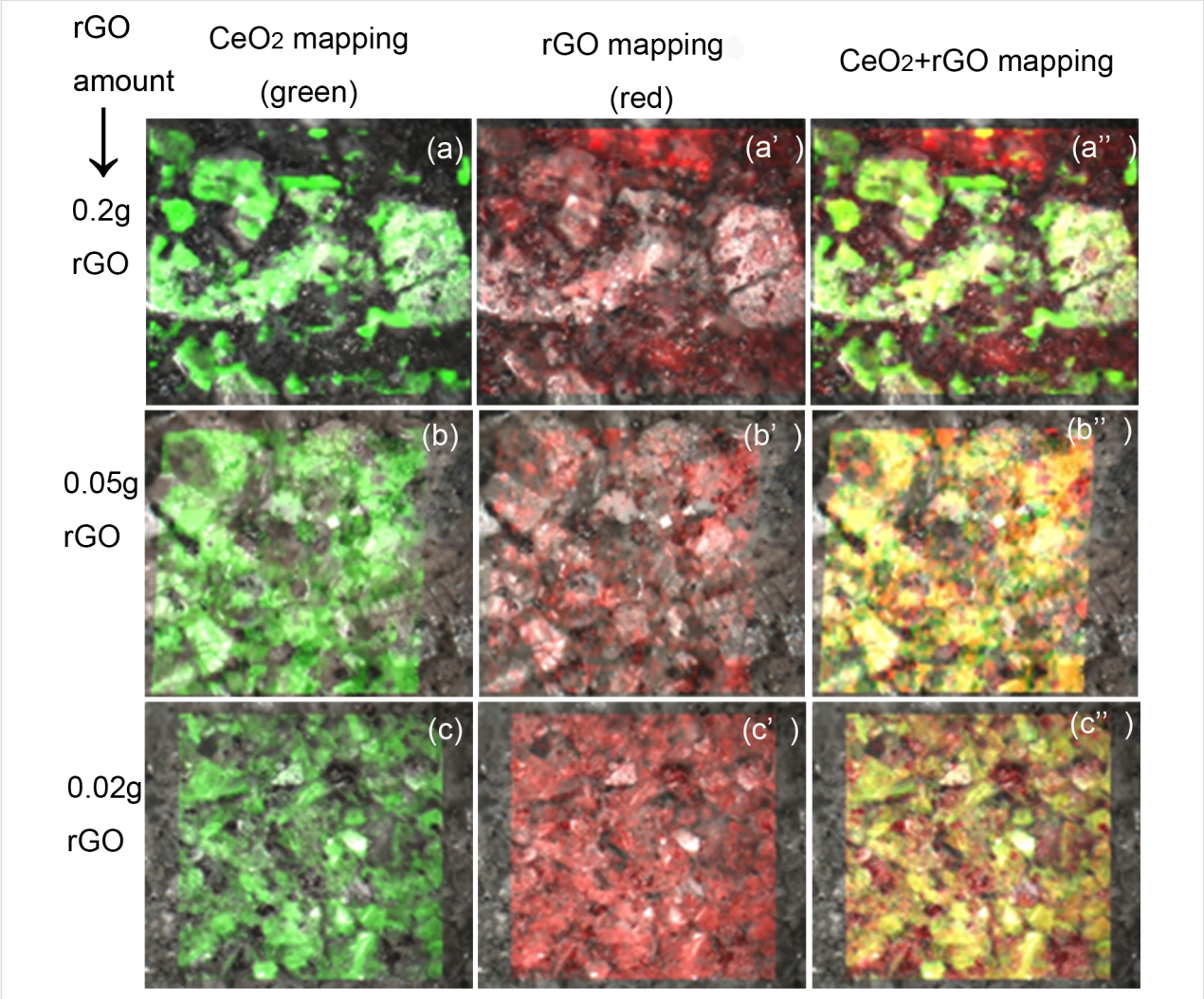

Figure 2: Raman mapping of rGO–CeO_2 composites with different proportions of rGO after solvothermal treatment in ethanol (mapping area: 500 × 500 μm^2).

different. They also showed a clear transition from GO to rGO. GO has strong bands in the range of 3000–3500 cm^{-1} and 1000–1750 cm^{-1}, which correspond to OH and COO/CO groups, respectively. After the solvothermal treatment, the intensity of OH (3000–3500 cm^{-1}) and C–O (1042 cm^{-1}) vibrations decreased while the intensity of COO (1250–1700 cm^{-1}) increased, indicating that part of the defects were repaired and rGO was formed. Compared with the COO groups of GO (Figure 3b), the positions of C=O bands shifted from 1719 cm^{-1} to 1492 cm^{-1}. The shifts are most likely caused by coordination of graphene to CeO_2 through the residual COO groups. The IR spectrum of the sample prepared without addition of rGO was similar to that of 0.02 g rGO. Part of the COO bands is most probably due to ceria-bound acetate groups, formed from ethanol either during the formation of CeO_2 [18] or the reduction of GO. They cannot be distinguished spectroscopically from graphene-bound COO groups.

In the absence of externally added rGO, the TGA curve had only one shoulder at 150–250 °C, corresponding to a weight loss of 12.3%, as reported earlier [17]. The rGO-containing samples had an additional shoulder at 300–400 °C, which is probably due to the formation of rGO (Supporting Information File 1, Figure S2). The weight loss generally increased with increasing rGO proportion [12.4% for rGO(0.02)-CeO_2, 16.5% for rGO(0.05)-CeO_2, 19.1% for rGO(0.1)-CeO_2, and 26.3% for rGO(0.2)-CeO_2]. All weight losses were larger than the amount of added GO due to the organic residues after solvothermal treatment (ca. 11%). Thus, the formed rGO originates from both added GO and the organic residues.

Varying the proportion of GO (from 0 to 0.2 g) did not influence the CeO_2 crystallite size (1.9–2.6 nm, calculated from Scherrer's equation based on the strongest peak at 28.7°) to a large extent (Supporting Information File 1, Figure S3). The

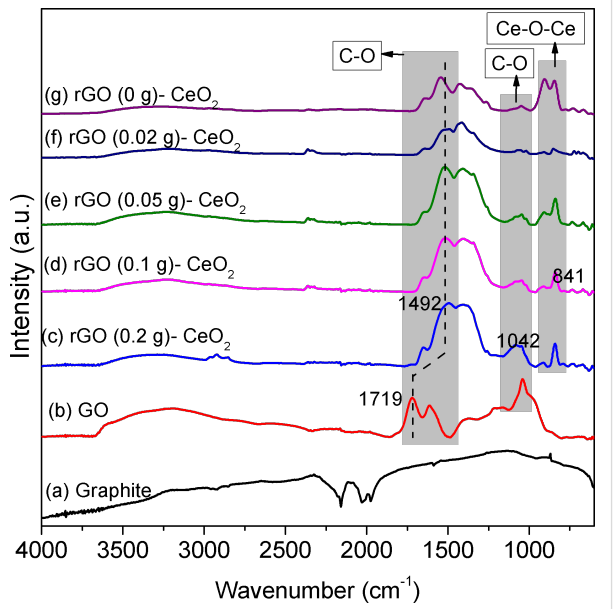

Figure 3: IR spectra of graphite (a); GO (b); CeO_2 with rGO-like organic residues (sample rGO(0)–CeO_2) (g); rGO–CeO_2 composites with different proportions of added rGO (c–f) after solvothermal treatment in ethanol.

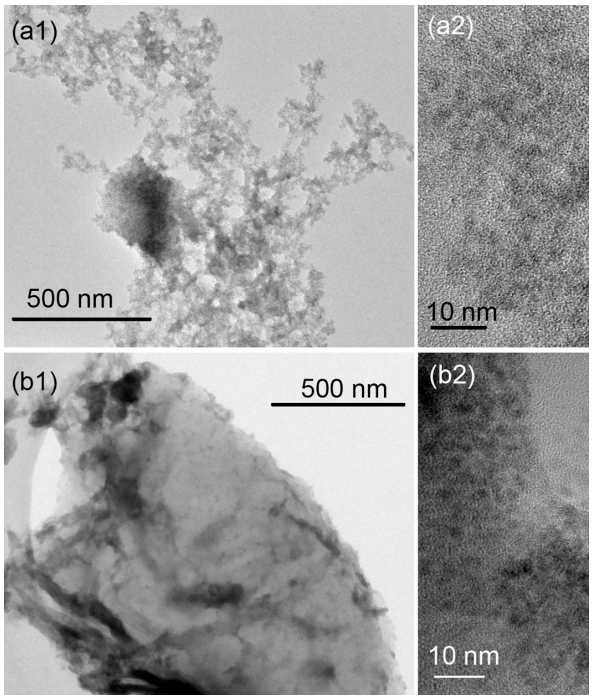

Figure 4: Morphologies of rGO(0)–CeO_2 (a1: TEM, a2: HRTEM) and rGO(0.05)–CeO_2 (b1: TEM, b2: HRTEM).

particle size of the undoped sample was 1.9 nm, and changed to 1.9–2.2 nm upon addition of 0.02–0.1 g GO. Only the sample rGO(0.2)–CeO_2 had a slightly larger CeO_2 crystallite size (2.6 nm).

The TEM (Figure 4) were consistent with the XRD results and showed that rGO(0)–CeO_2 and rGO(0.05)–CeO_2 are formed by 2–4 nm ceria particles. The rGO sheets can be easily observed in rGO(0.05)–CeO_2, and CeO_2 particles were attached to the rGO sheets.

N_2 adsorption–desorption results for the rGO–CeO_2 composites with different proportions of rGO after solvothermal treatment are shown in Figure 5, left. Only rGO(0.2)–CeO_2 is mesoporous, according to the IUPAC classification, while the others contain mainly micropores and a small portion of mesopores. This can also be seen from the pore size distribution (Figure 5, right). rGO(0.2)–CeO_2 has an average pore size of 4.8 nm, while the other samples have smaller pore size in the range of

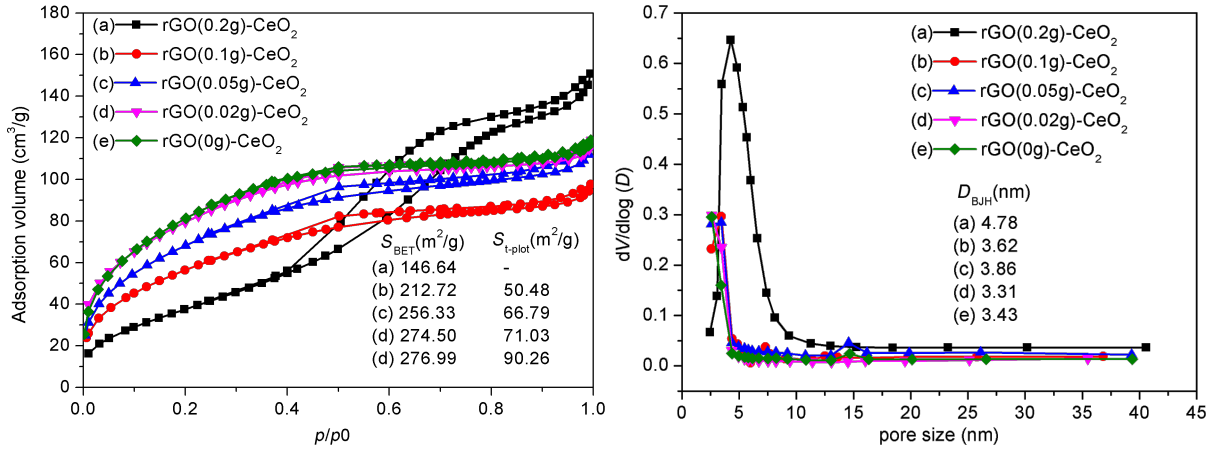

Figure 5: N_2 adsorption–desorption isotherms (left) and pore size distributions (right) for CeO_2 with rGO-like organic residues (rGO(0)–CeO_2) (e) and rGO–CeO_2 composites (a–d) with different proportions of rGO after solvothermal treatment with ethanol.

3.3–3.8 nm. The surface area increased with decreasing rGO proportion, from 147 m^2/g with 0.2 g rGO to 275 m^2/g with 0.02 g rGO. rGO(0)–CeO_2 and rGO(0.02)–CeO_2 processed almost the same surface area.

The influence of the rGO proportion on the catalytic activity for CO oxidation was tested for rGO(0.05)–CeO_2 compared to rGO(0)–CeO_2 under the same conditions (Figure 6). The catalytic activity of rGO(0.05)–CeO_2 was higher than that of rGO(0)–CeO_2. Both samples were also calcined at 500 °C for 2 h to remove rGO and the organic residues (samples marked with AC). After calcination, the surface area of rGO(0.05)–CeO_2 was reduced from 256.3 to 55.5 m^2/g and that of rGO(0)–CeO_2 from 276.9 to 88.9 m^2/g. The activity of rGO(0.05)–CeO_2–AC is somewhat lower than that of rGO(0.05)-CeO_2 at the same temperature, but still higher than that of rGO(0)–CeO_2–AC. For example, $r_{250\ °C}$ (the reaction rate at 250 °C per gram catalyst) for rGO(0.05)–CeO_2 during first heating is $1.19 \cdot 10^{-5}$ changed to $8.77 \cdot 10^{-6}$ mol/s·g for rGO(0.05)–CeO_2–AC. This decrease is possibly caused by the removal of graphene and reduction of the surface area.

The advantage of the rGO(0.05)–CeO_2 composite can also be seen from the CO temperature-programmed reduction (CO-TPR) (Figure 7). Both CO_2 and H_2 evolution showed signals at lower temperatures (ca. 100 °C) for rGO(0.05)–CeO_2 than for rGO(0)–CeO_2. Similar to rGO(0)–CeO_2, rGO(0.05)–CeO_2 also showed three features: removal of surface lattice oxygen (below 300 °C), water-gas shift between CO and surface OH groups (300–500 °C), and extraction of bulk oxygen (above 500 °C), respectively, as discussed previously [17].

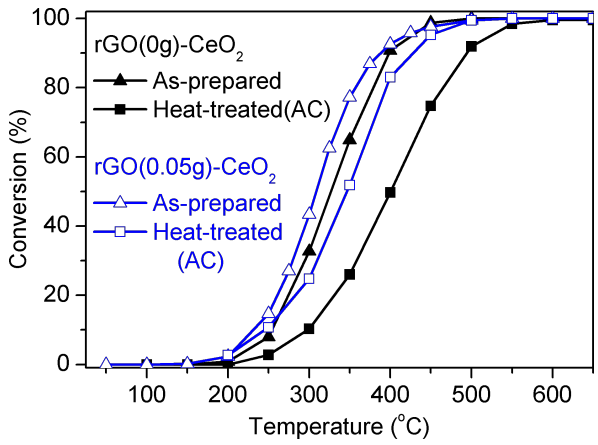

Figure 6: CO oxidation at different temperatures for CeO_2 with rGO-like organic residues (rGO(0)–CeO_2) and the rGO(0.05)–CeO_2 composite.

Conclusion

We have shown in this article that the organic residues generated upon solvothermal treatment of ceria gels, obtained by sol–gel processing of cerium *tert*-butoxide, in ethanol as solvent [17] contain reduced graphene oxide (rGO)-like structures. The appearance of rGO-like structures can be associated with cerium *tert*-butoxide (or possibly cerium alkoxides in general) as precursor and ethanol as solvothermal solvent, and may also explain the higher catalytic activity (compared with, for example hydrothermally treated samples). This was also confirmed by introduction of "external" graphene oxide during sol–gel processing, by which the rGO structures and the catalytic activity were enhanced. The previously observed higher catalytic CO

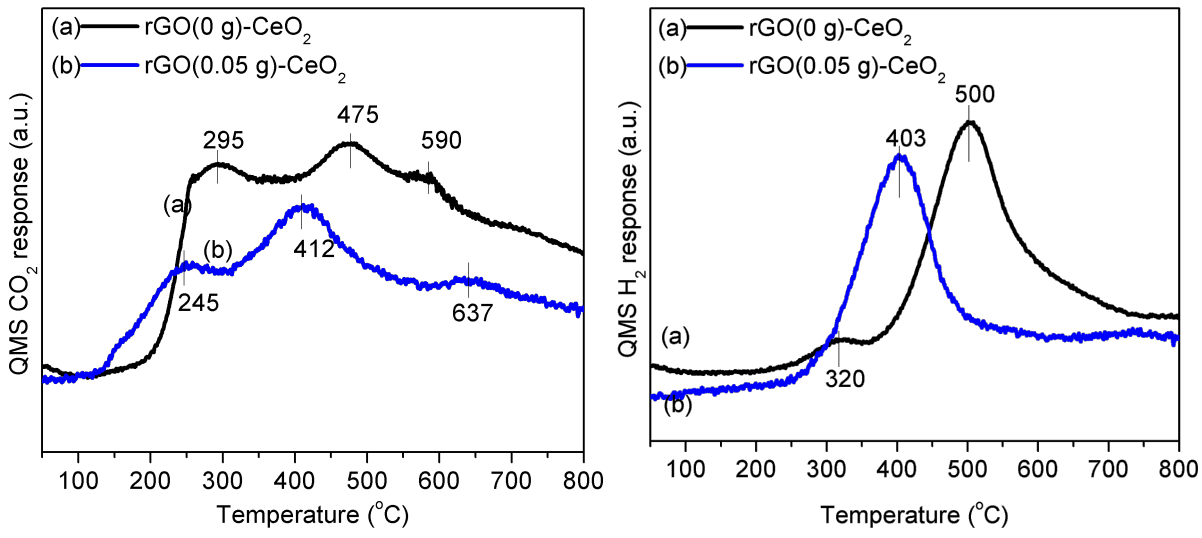

Figure 7: CO_2 (left) and H_2 (right) evolution during CO-TPR over rGO(0)–CeO_2 and rGO(0.05)–CeO_2.

oxidation activity of ceria samples solvothermally treated in ethanol can therefore be traced back to the presence of rGO structures [17].

Supporting Information

Supporting Information File 1

Additional experimental data.
[http://www.beilstein-journals.org/bjnano/content/supplementary/2190-4286-7-174-S1.pdf]

Acknowledgements

This project was supported by the Austrian Science Funds (FWF) in the framework of the Doctoral School Building Solids for Function (Project W1243). The authors thank Christine Artner for the XRD measurements, and Liliana Lukashuk and Karin Föttinger for the access to and help for catalytic measurements.

References

1. Yan, T.; Li, R.; Zhu, H.; Li, Z. *Mater. Res. Bull.* **2016,** *78,* 163–171. doi:10.1016/j.materresbull.2016.02.024
2. Vanitha, M.; Keerthi; Cao, P.; Balasubramanian, N. *J. Alloys Compd.* **2015,** *644,* 534–544. doi:10.1016/j.jallcom.2015.03.221
3. Dezfuli, A. S.; Ganjali, M. R.; Norouzi, P.; Faridbod, F. *J. Mater. Chem. B* **2015,** *3,* 2362–2370. doi:10.1039/C4TB01847H
4. Su, Q.; Chang, L.; Zhang, J.; Du, G.; Xu, B. *J. Phys. Chem. C* **2013,** *117,* 4292–4298. doi:10.1021/jp312169j
5. Wang, G.; Bai, J.-T.; Wang, Y.-H.; Ren, Z.-Y.; Bai, J.-B. *Scr. Mater.* **2011,** *65,* 339–342.
6. Yu, X.; Kuai, L.; Geng, B. *Nanoscale* **2012,** *4,* 5738–5743. doi:10.1039/c2nr31765f
7. Kuila, T.; Mishra, A. K.; Khanra, P.; Kim, N. H.; Lee, J. H. *Nanoscale* **2013,** *5,* 52–71. doi:10.1039/C2NR32703A
8. Xiao, X.; Sheng, Z.; Yang, L.; Dong, F. *Catal. Sci. Technol.* **2016,** *6,* 1507–1514. doi:10.1039/C5CY01228G
9. Yang, Y.; Tian, C.; Sun, L.; Lü, R.; Zhou, W.; Shi, K.; Kan, K.; Wang, J.; Fu, H. *J. Mater. Chem. A* **2013,** *1,* 12742–12749. doi:10.1039/c3ta12399e
10. Kakaei, K.; Rahimi, A.; Husseindoost, S.; Hamidi, M.; Javan, H.; Balavandi, A. *Int. J. Hydrogen Energy* **2016,** *41,* 3861–3869. doi:10.1016/j.ijhydene.2016.01.013
11. Jiang, L.; Yao, M.; Liu, B.; Li, Q.; Liu, R.; Lv, H.; Lu, S.; Gong, C.; Zou, B.; Cui, T.; Liu, B.; Hu, G.; Wågberg, T. *J. Phys. Chem. C* **2012,** *116,* 11741–11745. doi:10.1021/jp3015113
12. Srivastava, M.; Das, A. K.; Khanra, P.; Uddin, M. E.; Kim, N. H.; Lee, J. H. *J. Mater. Chem. A* **2013,** *1,* 9792–9801. doi:10.1039/c3ta11311f
13. Ji, Z.; Shen, X.; Xu, Y.; Zhu, G.; Chen, K. *J. Colloid Interface Sci.* **2014,** *432,* 57–64. doi:10.1016/j.jcis.2014.06.045
14. Kumar, S.; Ojha, A. K.; Patrice, D.; Yadav, B. S.; Materny, A. *Phys. Chem. Chem. Phys.* **2016,** *18,* 11157–11167. doi:10.1039/C5CP04457J
15. Ji, Z.; Shen, X.; Li, M.; Zhou, H.; Zhu, G.; Chen, K. *Nanotechnology* **2013,** *24,* 115603. doi:10.1088/0957-4484/24/11/115603
16. Ling, Q.; Yang, M.; Rao, R.; Yang, H.; Zhang, Q.; Liu, H.; Zhang, A. *Appl. Surf. Sci.* **2013,** *274,* 131–137. doi:10.1016/j.apsusc.2013.02.129
17. Yang, J.; Lukashuk, L.; Li, H.; Föttinger, K.; Rupprechter, G.; Schubert, U. *Catal. Lett.* **2014,** *144,* 403–412. doi:10.1007/s10562-013-1162-8
18. Slostowski, C.; Marre, S.; Babot, O.; Toupance, T.; Aymonier, C. *Langmuir* **2012,** *28,* 16656–16663. doi:10.1021/la303265t
19. Yang, J.; Lukashuk, L.; Akbarzadeh, J.; Stöger-Pollach, M.; Peterlik, H.; Föttinger, K.; Rupprechter, G.; Schubert, U. *Chem. – Eur. J.* **2015,** *21,* 885–892. doi:10.1002/chem.201403636
20. Hummers, W. S., Jr.; Offeman, R. E. *J. Am. Chem. Soc.* **1958,** *80,* 1339. doi:10.1021/ja01539a017
21. Kovtyukhova, N. I.; Ollivier, P. J.; Martin, B. R.; Mallouk, T. E.; Chizhik, S. A.; Buzaneva, E. V.; Gorchinskiy, A. D. *Chem. Mater.* **1999,** *11,* 771–778. doi:10.1021/cm981085u
22. Ferrari, A. C.; Robertson, J. *Philos. Trans. R. Soc. London, Ser. A* **2004,** *362,* 2477–2512. doi:10.1098/rsta.2004.1452
23. Schwan, J.; Ulrich, S.; Batori, V.; Ehrhardt, H.; Silva, S. R. P. *J. Appl. Phys.* **1996,** *80,* 440–447. doi:10.1063/1.362745
24. Ferrari, A. C.; Basko, D. M. *Nat. Nanotechnol.* **2013,** *8,* 235–246. doi:10.1038/nnano.2013.46
25. Stankovich, S.; Dikin, D. A.; Piner, R. D.; Kohlhaas, K. A.; Kleinhammes, A.; Jia, Y.; Wu, Y.; Nguyen, S. T.; Ruoff, R. S. *Carbon* **2007,** *45,* 1558–1565. doi:10.1016/j.carbon.2007.02.034
26. Lambert, T. N.; Chavez, C. A.; Hernandez-Sanchez, B.; Lu, P.; Bell, N. S.; Ambrosini, A.; Friedman, T.; Boyle, T. J.; Wheeler, D. R.; Huber, D. L. *J. Phys. Chem. C* **2009,** *113,* 19812–19823. doi:10.1021/jp905456f
27. Joung, D.; Singh, V.; Park, S.; Schulte, A.; Seal, S.; Khondaker, S. I. *J. Phys. Chem. C* **2011,** *115,* 24494–24500. doi:10.1021/jp206485v
28. Lee, J.; Novoselov, K. S.; Shin, H. S. *ACS Nano* **2011,** *5,* 608–612. doi:10.1021/nn103004c
29. Fu, Y.; Wang, X. *Ind. Eng. Chem. Res.* **2011,** *50,* 7210–7218. doi:10.1021/ie200162a
30. Fan, Z.-J.; Kai, W.; Yan, J.; Wei, T.; Zhi, L.-J.; Feng, J.; Ren, Y.-m.; Song, L.-P.; Wei, F. *ACS Nano* **2011,** *5,* 191–198. doi:10.1021/nn102339t

License and Terms

BEILSTEIN JOURNAL OF NANOTECHNOLOGY

Controlled supramolecular structure of guanosine monophosphate in the interlayer space of layered double hydroxide

Gyeong-Hyeon Gwak[‡1], Istvan Kocsis[‡2], Yves-Marie Legrand[‡2], Mihail Barboiu[*2] and Jae-Min Oh[*1]

Full Research Paper

Open Access

Address:
[1]Department of Chemistry and Medical Chemistry, College of Science and Technology, Yonsei University, Wonju, Gangwondo, 26493, Republic of Korea, and [2]Adaptive Supramolecular Nanosystems Group, Institut Européen des Membranes, University of Montpellier/ENSCM/CNRS 5635, Pl. Eugène Bataillon, CC 047, 34095 Montpellier, Cedex 5, France

Email:
Mihail Barboiu[*] - mihail-dumitru.barboiu@univ-montp2.fr;
Jae-Min Oh[*] - jaemin.oh@yonsei.ac.kr

* Corresponding author ‡ Equal contributors

Keywords:
guanosine monophosphate; hydrogen bond; layered double hydroxide; ribbon structure; supramolecular assembly

Beilstein J. Nanotechnol. **2016,** *7,* 1928–1935.
doi:10.3762/bjnano.7.184

Received: 28 July 2016
Accepted: 11 November 2016
Published: 06 December 2016

This article is part of the Thematic Series "Hybrid nanomaterials: from the laboratory to the market".

Guest Editor: A. Taubert

Abstract

Guanosine monophosphates (GMPs) were intercalated into the interlayer space of layered double hydroxides (LDHs) and the molecular arrangement of GMP was controlled in LDHs. The intercalation conditions such as GMP/LDH molar ratio and reaction temperature were systematically adjusted. When the GMP/LDH molar ratio was 1:2, which corresponds to the charge balance between positive LDH sheets and GMP anions, GMP molecules were well-intercalated to LDH. At high temperature (100 and 80 °C), a single GMP molecule existed separately in the LDH interlayer. On the other hand, at lower temperature (20, 40 and 60 °C), GMPs tended to form ribbon-type supramolecular assemblies. Differential scanning calorimetry showed that the ribbon-type GMP assembly had an intermolecular interaction energy of ≈101 kJ/mol, which corresponds to a double hydrogen bond between guanosine molecules. Once stabilized, the interlayer GMP orientations, single molecular and ribbon phase, were successfully converted to the other phase by adjusting the external environment by stoichiometry or temperature control.

Introduction

Since Bernal [1] and Cairns-Smith [2] suggested that layered clays contributed to the origin of life by affecting the conformation of prebiotic molecules in ancient environment, many scientists have begun to focus their research on the molecular arrangement of biological substances in the interlayer space of layered inorganics [3,4]. In those investigations, monomeric

prebiotic molecules such as amino acid, nucleoside or nucleotide were intercalated and it was suggested that the geometrical restriction of molecules under the confined interlayer space of inorganics would aid the polymerization of biological molecules.

Mann et al. intercalated two kinds of amino acids, aspartate and glutamate, into layered double hydroxide (LDH) to synthesize bioinorganic nanocomposites [5]. Post-synthetic thermal treatment resulted in polymerization of amino acids in LDH. It was also reported that amino acids such as arginine and glutamate were polymerized via peptidic condensation both on the surface and in the interlayer space of clay [6]. In that literature, peptidic condensation of amino acids was determined to favor heteropeptide rather than homopeptide. Besides polymerization of amino acids, it was reported that abiotic oligomerization of RNA nucleotides was catalyzed by montmorillonite clay [7]. In the presence of clay, the length of polymerized RNA oligonucleotides was three times longer than without clay.

Among biological molecules, guanosine derivatives are known to have various supramolecular assembly routes through intermolecular interactions. For instance, telomere in chromosome consists of stacks of guanosine quartets (G4), in which four guanosines are linked through hydrogen bonds in the presence of K^+ ions. There have been many attempts to synthesize guanosine-based supramolecular assemblies such as ribbon or quadruplex. Spada et al. verified that two kinds of ribbon structures could be obtained by self-assembly of lipophilic deoxyguanosine derivatives through hydrogen bonding [8]. They suggested those supramolecular nucleoside structures could be utilized for molecular nanowire fabrication or molecular electronics. Davis et al. prepared stable G4 hydrogels utilizing guanosine, potassium and borate [9]. Those hydrogels exhibited specific binding ability towards cationic dyes or nucleoside through noncovalent interactions. Due to its characteristic structure having K^+ in the center, G4 quartets can be considered as scaffolds for artificial ion channels. We have reported a stable G4 membrane film utilizing guanosine and bis(3-aminopropyl)polytetrahydrofuran [10]. These G4 membranes showed potential in Na^+/K^+ artificial ion channels.

Inspired by the above reports claiming that i) intermolecular interactions of biomolecules are strongly affected by the confined geometry of layered clays and that ii) guanosine derivatives form various supramolecular assemblies, depending on the chemical environment, we hypothesized that the orientation of guanosine derivatives can be controlled in the restricted nanospace of layered inorganics. In this study, we utilized layered double hydroxides (LDH), which are composed of positively charged layers ($Mg_2Al(OH)_6^+$) with equivalent area per charge ≈25 $Å^2$/(+) and charge compensating interlayer anions [11,12]. As it is known that interlayer anions in LDH can be easily exchanged by external anions, and that once introduced, anions are stabilized via electrostatic interaction [13,14], we utilized guanosine monophosphate (GMP) as a model molecule. First, we prepared LDHs with exchangeable anions and intercalated GMP through an ion exchange reaction. We evaluated the molecular conformation of GMP in the interlayer space of LDH by varying the GMP/Al^{3+} (in LDH) molar ratio and the reaction temperature. This was revealed that GMP molecules are separated or assembled into ribbons depending on the synthetic conditions. Furthermore, we confirmed that once stabilized GMP orientation in LDH could be converted to the other state by adjusting the physicochemical environment.

Results and Discussion

In order to promote intercalation of GMP into the interlayer space of LDH, we set the reaction temperature at 80 °C, and varied the GMP/Al^{3+} (in LDH) ratio to 1:0.25, 1:0.5, 1:1, 1:2, 1:4 and 1:10. According to the adsorption isotherm, we found that GMP adsorption (or intercalation) to LDH follows Langmuir adsorption (Supporting Information File 1, Figure S1). The theoretical anionic exchange capacity (AEC) was satisfied at GMP/LDH ratio of 1.5:1, while the ideal stoichiometry GMP/LDH is 1:2 (note that GMP is a dianion and that the chemical formula of LDH is $[Mg_2Al(OH)_6]^+(NO_3)^-$). Figure 1 shows X-ray diffraction (XRD) patterns of GMP/LDH (GL) hybrids prepared under various GMP/LDH molar ratios. At high GMP ratio (Figure 1c–e), the XRD patterns revealed amor-

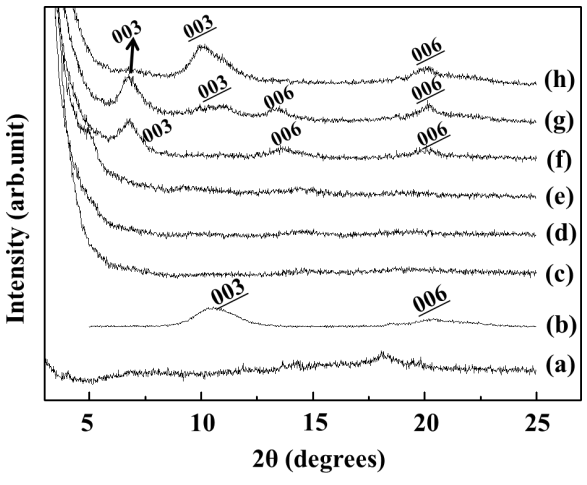

Figure 1: X-ray diffraction (XRD) patterns of products prepared by ion exchange between MgAl-LDH and GMP under controlled GMP/LDH molar ratios at 80 °C for 1 day. (a) GMP only, (b) MgAl-NO_3-LDH, (c) 1:0.25, (d) 1:0.5, (e) 1:1, (f) 1:2, (g) 1:4, (h) 1:10 (GMP/LDH). Underlined Miller indexes are (00*l*) of NO_3^- interlayer anion (MgAl-NO_3-LDH). Miller indexes without underline are (00*l*) of GMP intercalated LDH.

phous structures, which was attributed to the disordered layer stacking of LDH due to the large quantity of organic moieties (GMP) as shown previously [15]. At GMP/LDH molar ratio of 1:2 and 1:4 (Figure 1f and Figure 1g, respectively), (00*l*) peaks shifted to lower angles as compared to pristine LDH, indicating ordered layer stacking with interlayer GMP moiety. However, excessive loading of LDH resulted in the decrease of intercalated peaks and increase of pristine peaks (Figure 1g,h). The optimum GMP/LDH ratio, yielding single-phased GMP intercalated LDH, was determined to be 1:2, which was expected from the stoichiometry according to charge neutralization. From the adsorption isotherm, the GMP/LDH ratio of 1:2 resulted in 90% of GMP uptake compared to theoretical AEC. The diameter of one GMP molecule is ≈1,000 $Å^3$ and it is larger than the interlayer volume provided by the LDH (area per 2 charges (50 $Å^2$) × gallery height (8–13 Å) ≈ 400–650 $Å^3$). Thus, a GMP/LDH ratio of 1:2 would be sufficient to accommodate as many GMP molecules as possible in the LDH interlayer space. The d-spacing of GMP intercalated LDH was calculated to be 12.6 Å, which was the summation of the LDH layer thickness (≈4.8 Å) and the perpendicular arrangement of U-shaped GMP (≈7.8 Å).

In order to control the interlayer GMP arrangement, we fixed GMP/LDH to 1:2 and varied the reaction temperature. As shown in Figure 2, the GL hybrid obtained at 100 °C showed a similar XRD pattern (Figure 2b) compared with that obtained at 80 °C. On the other hand, those prepared at lower temperature (20, 40 and 60 °C) showed (00*l*) peaks shifted to lower angles (Figure 2c–e). The d-spacing values of the GL hybrid obtained at lower temperature was approximately 17.7 Å, which was 5.1 Å larger than for the single molecular orientation. Similar to the GMP adsorption at 80 °C, GMP uptake at 20 °C followed a Langmuir model. Although the Langmuir adsorption rate at 20 °C was slightly smaller than 80 °C, the overall adsorption patterns at the two temperatures were similar. Thus, the different interlayer space of GL hybrids at two different temperatures is thought to originate from interlayer molecular orientation of GMP. It is well known that guanosine moieties including GMP form various supramolecular structures result from its self-assembly. GMP makes quadruplex structures in the presence of specific metal as found in the telomere of chromosome [16]. Without metal cations, GMPs make ribbon-type structures through hydrogen bonding between H and electronegative sites (N or O). Two kinds of ribbon phases, I and II, have been reported [8].

Considering the molecular dimensions, the GMP intercalated to LDH layers at low temperature were thought to form in ribbon II supramolecular orientation (Figure 3b). At relatively high synthetic temperature, the formation of hydrogen bonds was

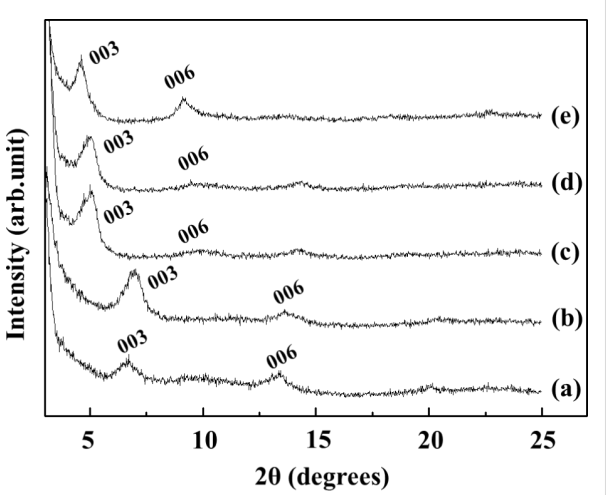

Figure 2: X-ray diffraction (XRD) patterns of GMP/LDH (GL) hybrid under controlled reaction temperature with GMP/LDH 1:2 for 1 day. (a) 100 °C, (b) 80 °C, (c) 60 °C, (d) 40 °C, (e) 20 °C.

disfavored and GMP existed as a single molecular arrangement (Figure 3a). Considering that double-helix DNA denatures to single-stranded DNA above 70 °C through hydrogen bonding breakage [17], the reaction temperature above 60 °C in this study might be sufficient to disrupt hydrogen bonding between GMPs. It was interesting to observe that the single molecular arrangement of GMP obtained at relatively high temperature was preserved between LDH layers after the material was cooled down to room temperature. Two kinds of GL hybrids with different GMP arranagements, single and ribbon, were named GL-S and GL-R, respectively.

Figure 4 shows powder XRD patterns of pristine LDH, GL-S and GL-R at the 2θ region 3–80°, showing clear lattice peaks at (012) and (110) for hybrids. This result showed that the lattice of LDH along *a*–*b*-plane direction was well preserved while there was lattice expansion along the *c*-axis resulting from molecular orientation of GMPs.

According to thermogravimetric analysis (TGA) and X-ray fluorescence (XRF) spectroscopy, the chemical formula of GL-S and GL-R were determined to be $Mg_{2.00}Al(OH)_6(GMP)_{0.37}(NO_3)_{0.26}\cdot(H_2O_{interlayer})(0.63H_2O_{surface})$ and $Mg_{2.00}Al(OH)_6(GMP)_{0.42}(NO_3)_{0.16}\cdot(H_2O_{interlayer})(0.82H_2O_{surface})$, respectively. Slightly larger GMP content in GL-R as compared to GL-S could explain the formation of the ribbon arrangement of GMP in the GL-R hybrid. The area of the LDH layer, $Mg_2Al(OH)_6^+$, is approximately 25 $Å^2$. Considering that the cross-sectional area of one GMP molecule is ≈60 $Å^2$, GMP occupies 22 $Å^2$ (60 $Å^2$ × 0.37) and 25 $Å^2$ (60 $Å^2$ × 0.42), respectively for GL-S and GL-R. Thus, the GMP moiety in GL-S could exist separately without effective intermolecular interac-

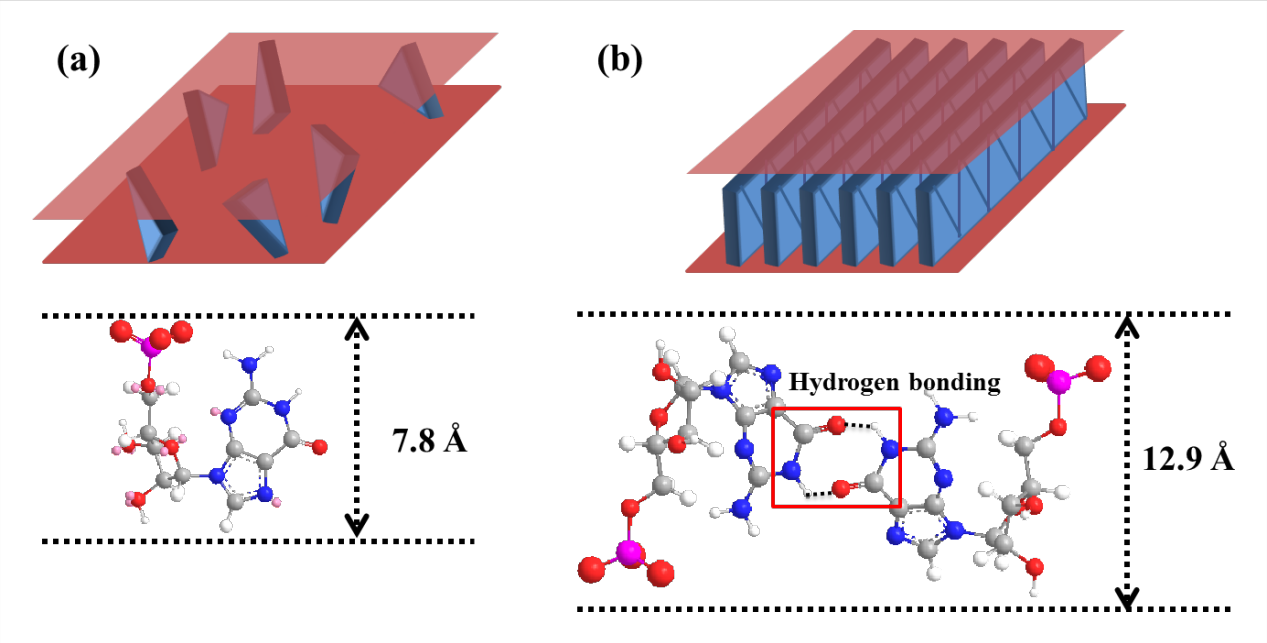

Figure 3: Schematic illustrations for interlayer structure of GMP/LDH hybrids according to molecular arrangement of GMPs: (a) single molecule arrangement (GL-S) and (b) ribbon II arrangement (GL-R).

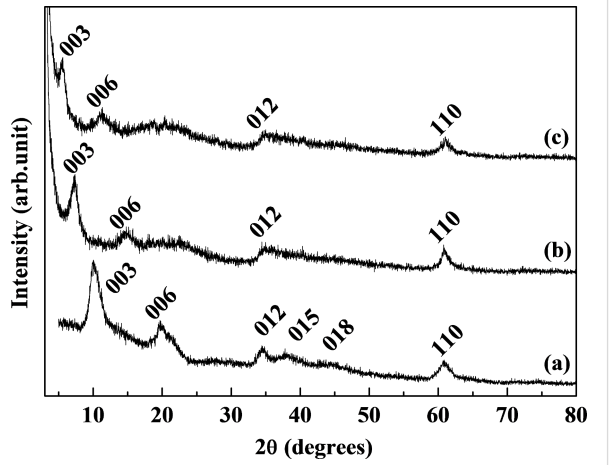

Figure 4: XRD patterns of (a) pristine MgAl-NO_3-LDH, (b) GL-S and (c) GL-R.

tion by GMP, while GMPs in GL-R packs to form a ribbon-type supramolecular arrangement.

Differential scanning calorimetry (DSC) diagrams for both GL hybrids suggested the hydrogen bonding among GMP moiety in GL-R hybrid (Figure 5). For comparison, we carried out DSC measurements of GMP only, which showed 177.33 kJ/mol of endothermic enthalpy change at 191.28 °C, indicating strong hydrogen bonding among GMP molecules. Also, we verified that the DSC diagram of pristine LDH showed an endothermic peak at 216.23 °C with an enthalpy change of 39.9 kJ/mol, which exactly matches the calculated water evaporation energy (≈40 kJ/mol) of $Mg_2Al(OH)_6(NO_3)\cdot H_2O$. Both hybrids showed a strong endothermic peak at around 200 °C, which was attributed to breaking intermolecular interaction of interlayer GMP as well as evaporating interlayer water molecules. Interlayer water was evaporated from the DSC of pristine LDH at around 210 °C with an enthalpy change of ≈40 kJ/mol, which was subtracted from the endothermic enthalpy of GL hybrids. The resulting intermolecular interaction between GMP was found to be 11.2 kJ/mol GMP and 101.6 kJ/mol GMP for GL-S and GL-R, respectively. The much higher energy for GL-R implied that there might be strong intermolecular interaction such as hydrogen bonding. According to the literature where hydrogen bonding energy between base pairs was simulated, double hydrogen bonded guanine–cytosine pair had 74–96 kJ/mol depending on bonding orientation [18]. Thus, the intermolecular energy of 101.6 kJ/mol (Figure 5d) might be attributed to the double hydrogen bonding between the GMP moiety as shown in Figure 3b. The DSC for GMP only (powder state) showed endothermic enthalpy of 177 kJ/mol GMP at 190 °C, implying that there was strong intermolecular interaction and possible formation of supramolecular structure in powder GMP.

To identify the supramolecular assembly of GMPs in GL-R, we carried out ^{13}C solid state nuclear magnetic resonance (NMR) utilizing a G4 quartet supramolecular assembly as the reference (Supporting Information File 1, Figure S2). The G4 quartet showed a single set of signals due to their symmetric structure. In GL-R, the signals for the quartet slightly shifted as well as the evolution of new signals. The result suggested that the

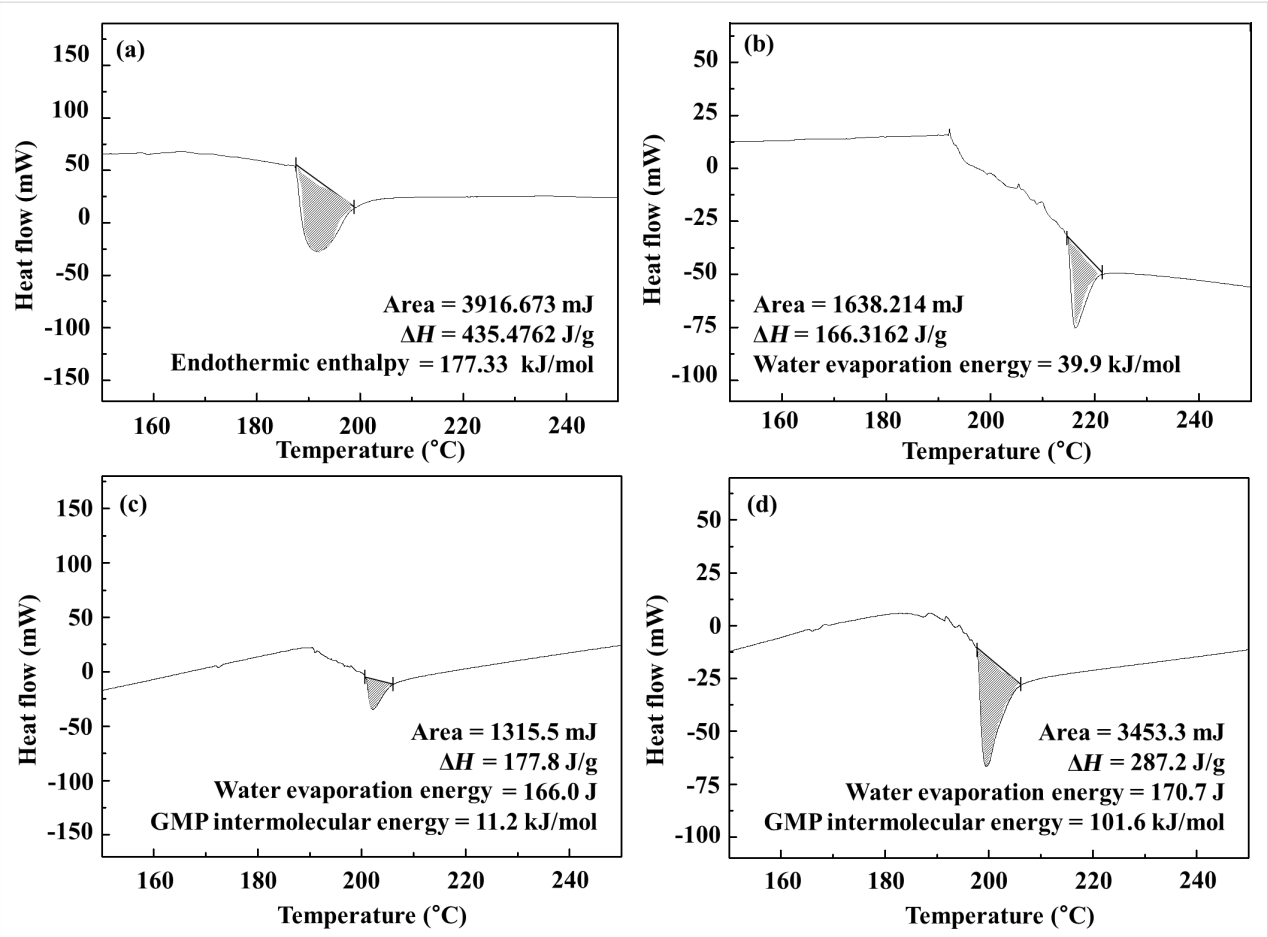

Figure 5: Differential scanning calorimetry (DSC) diagrams of (a) GMP powder, (b) pristine MgAl-NO_3-LDH, (c) GL-S and (d) GL-R.

supramolecular structure in GL-R was asymmetric and possibly ribbon-like. In order to verify that the intact structure of GMP is preserved after intercalation into LDH, we carried out Fourier transform infrared (FTIR) spectroscopy. As shown in Figure 6a, GMP (a) shows typical vibrational modes at 1695, 1605, 1535, and 1365 cm^{-1}, which were attributed to C=O, C=N, pyrimidine/imidazole and imidazole vibration, respectively. Two bands at 1080 and 980 cm^{-1} resulted from PO_3^{2-} antisymmetric stretching and PO_3^{2-} symmetric stretching [19]. Both GL-S (Figure 6a, line c) and GL-R (Figure 6a, line d) showed similar IR bands compared with GMP only, although the bands in the range 1550–1800 cm^{-1} could not be separated in detail due to the merging with the δ-mode of interlayer water (1640 cm^{-1}). Particle morphologies of GL hybrids are displayed in Figure 6b. Both images showed LDH particles with homogeneous size distribution. The average particle size was determined to be ≈90 nm and ≈50 nm for GL-S and GL-R, respectively. The slightly larger size of GL-S was attributed to the aging effect in inorganic particles [20], as GL-S was heated to 80 °C. Compared to the SEM image of the GMP reagent and pristine LDH (Supporting Information File 1, Figure S3), we verified that the particle morphology of both GL hybrids exhibited a typical pattern of organic moiety intercalated LDHs. Disk-shaped particles were agglomerated due to the particle-edge interaction between LDH particles [21].

We confirmed that interlayer arrangements of GMP molecules, such as single molecular or ribbon orientation, could be obtained according to specific synthetic conditions. As a further step, we tried to verify whether the interlayer arrangement could be converted to the other phase by adjusting the external conditions. The addition of LDH while heating was thought to convert GL-R to GL-S as the condition disrupts hydrogen bonding and provides more interlayer space, allowing molecules to be isolated. As shown in Figure 7a, one day of stirring at 80 °C with the addition of 1 equivalent LDH showed the evolution of the (003) peak at 7° (Figure 7a, line b), which corresponded to the interlayer space of single molecule arrangement. After two days, the (003) peak corresponding to the ribbon orientation almost disappeared and the peak at 7° became dominant, implying that the GL-R was converted into GL-S. In order to convert GL-S to GL-R, we applied a similar strategy. One

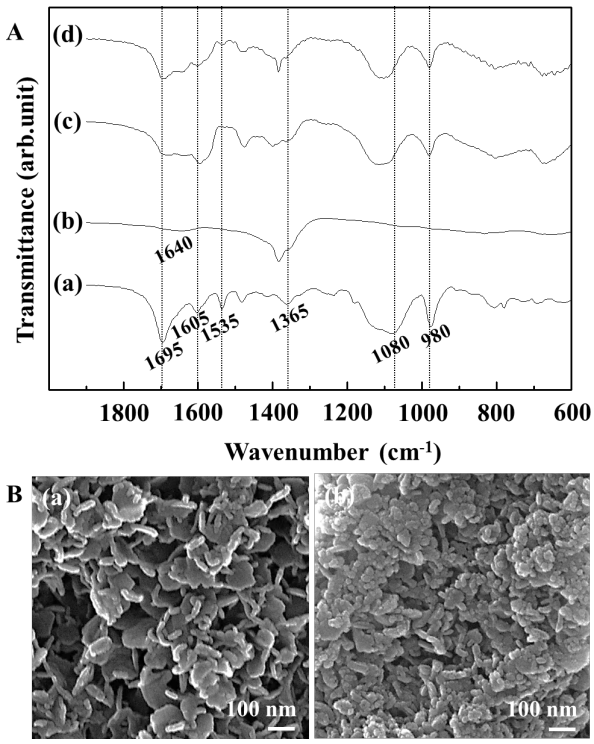

Figure 6: (a) Fourier transformed infrared (FTIR) spectra of GMP powder (line a), pristine MgAl-NO_3-LDH (line b), GL-S (line c) and GL-R hybrid (line d). (b) Scanning electron microscopic (SEM) images of GL-S (image a) and GL-R hybrid (image b).

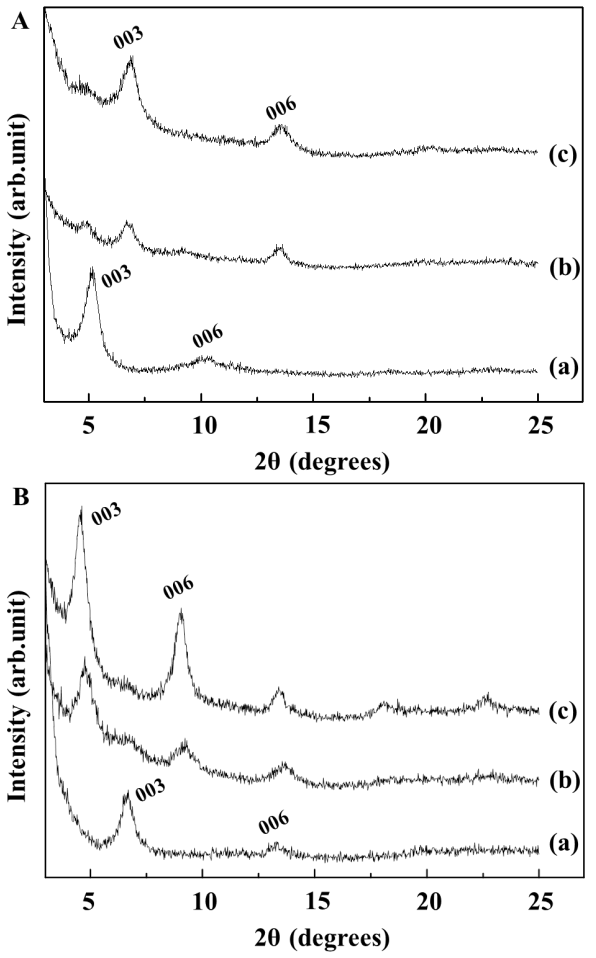

Figure 7: X-ray diffraction (XRD) patterns of GL hybrids obtained by interconverting interlayer GMP arrangement. (a): GL-R to GL-S and (b): GL-S to GL-R, for starting (line a), intermediate (line b) and final (line c) products.

equivalent of GMP was added in solution phase to the GL-S suspension, while the temperature was set to 20 °C. According to Figure 7b (line b), the intensity of (003) for GL-S decreases after one day of stirring and a new peak at 4.8°, which matched with that for GL-R, began to appear. After two days, we could obtain XRD patterns corresponding to GL-R. These results suggested that the surrounding conditions switch the stable interlayer molecular orientation of GMP.

Conclusion

GMP was intercalated into the interlayer space of LDH (GL hybrids) and its molecular arrangement was controlled to form in either single molecular orientation or ribbon-type supramolecular assembly according to synthetic conditions. At high temperature (80 and 100 °C), GMPs were separated in single molecules and at low temperature (20, 40, and 60 °C), GMPs assembled in a ribbon structure. The intermolecular energy for GMP, ≈101 kJ/mol, suggested the possibility of double hydrogen bond between GMPs in GL-R. We also verified that, once stabilized, GL-S or GL-R could be converted to the other phases by adjusting synthetic conditions like stoichiometry and temperature. The stoichiometry between the LDH and GMP determined interlayer molecular packing patterns, which in turn influenced intermolecular interaction among GMP molecules. Furthermore, even in confined space, the temperature affected the formation and breakage of hydrogen bonds.

Experimental

Materials

Magnesium nitrate hexahydrate ($Mg(NO_3)_2{\cdot}6H_2O$) and aluminum nitrate nonahydrate ($Al(NO_3)_3{\cdot}9H_2O$) were purchased from Sigma-Aldrich (St. Louis, USA). Guanosine 5'-monophosphate disodium salt hydrate ($C_{10}H_{12}N_5Na_2O_8P{\cdot}xH_2O$) was purchased from Tokyo Chemical Industry Co., Ltd. (Tokyo, Japan). Sodium hydroxide (NaOH) in pellet form was purchased from Daejung Chemicals & Metals Co., Ltd. (Siheung-si, Gyonggi-do, Korea).

Preparation of pristine MgAl-NO_3-LDH

An aqueous solution in which $Mg(NO_3)_2{\cdot}6H_2O$ (0.45 M, 45 mmol) and $Al(NO_3)_3{\cdot}9H_2O$ (0.225 M, 22.5 mmol) were dis-

solved in decarbonated water was titrated with NaOH (0.75 M) solution up to pH ≈9.5. After a white-colored suspension was formed, the reaction was kept stirring for 24 h. The obtained MgAl-NO_3-LDH sample was centrifuged and thoroughly washed with decarbonated water.

Preparation of GL hybrids

MgAl-NO_3-LDH was dispersed in decarbonated water to achieve a ≈0.06 g/mL concentration. In order to intercalate GMP into LDH (GL hybrid), two parameters, the GMP/Al^{3+} (in LDH) molar ratio and reaction temperature, were controlled individually. For the molar ratio control experiment, 0.186 mmol of GMP (0.07582 g) was dissolved in 10 mL of decarbonated water at 80 °C. Then LDH suspensions of 0.25, 0.5, 1, 2, 4, and 10 equiv Al^{3+} were added to the GMP solution and stirred for one day at 80 °C under N_2 atmosphere. For the temperature control measurement, a GMP/Al^{3+} (in LDH) molar ratio 1:2 was chosen and mixtures were reacted at 20, 40, 60, 80, and 100 °C, respectively, for one day. We found optimized preparation conditions for GL-S (GL hybrid with single molecular GMP orientation) and GL-R (GL hybrid with ribbon phase GMP structure) hybrid as follows. GMP/LDH molar ratio 1:2, reaction temperature 80 °C and two days reaction time for GL-S; GMP/LDH molar ratio 1:1, reaction temperature 20 °C and one day reaction for GL-R hybrid.

Conversion of interlayer GMP arrangement

In order to convert GL-R to GL-S, 1 equiv of LDH suspension was added to the GL-R suspension at 80 °C and was stirred for one day. For the reverse reaction (GL-S to GL-R), 1 equiv of GMP was added to the GL-S suspension at room temperature under stirring for two days.

Characterization

All the samples were thoroughly washed with decarbonated water and lyophilized before characterization. The adsorption isotherm experiment was carried out with a UV–vis spectrophotometer (UV–vis; Shimadzu UV-1800, Shimadzu Corporation, Kyoto, Japan) at λ_{max} = 253 nm. In order to identify the crystal structure of pristine LDH and to evaluate the lattice expansion of LDH along the *c*-axis upon GMP intercalation, X-ray diffraction patterns (XRD) were obtained with a Bruker D2 instrument with Ni-filtered Cu Kα radiation (λ = 1.5406 Å). The hydrogen bonding of the GL-R hybrid was verified by differential scanning calorimetry diagrams (DSC, PerkinElmer DSC 8000) with 5 °/min heating rate. To investigate the intact structure and intermolecular interaction of GMP in GL hybrids, Fourier transform-infrared spectra (FTIR, PerkinElmer, Spectrum One) with conventional KBr pellet method was carried out. The morphology of GL hybrids was observed by scanning electron microscopic (SEM) images obtained with an FEI QUANTA 250 FEG. For quantitative analysis, a thermogravimetric analyzer (TGA, SINCO STA S-1000) and X-ray fluorescence spectrometer (XRF, Thermo Scientific ARL QUANT'X) were used.

Supporting Information

Supporting Information File 1

Adsorption isotherm, theoretical Langmuir plots, solid-state NMR spectra, and additional SEM images.
[http://www.beilstein-journals.org/bjnano/content/supplementary/2190-4286-7-184-S1.pdf]

Acknowledgements

This work was supported by a grant from International Research & Development Program (NRF-2014K1A3A1A21001297) through the National Research Foundation of Korea (NRF) funded by the Ministry of Science, ICT, and Future Planning, Republic of Korea. This work was conducted within the framework of ANR DYNAMULTIREC and PHC STAR Program no. 32153VJ, France.

References

1. Bernal, J. D. *Proc. Phys. Soc., London, Sect. A* **1949,** *62,* 537. doi:10.1088/0370-1298/62/11/512
2. Cairns-Smith, A. G. *FEBS Lett.* **1983,** *154,* 219–220. doi:10.1016/0014-5793(83)80911-9
3. Choy, J.-H.; Kwak, S.-Y.; Park, J.-S.; Jeong, Y.-J.; Portier, J. *J. Am. Chem. Soc.* **1999,** *121,* 1399–1400. doi:10.1021/ja981823f
4. Nakayama, H.; Wada, N.; Tsuhako, M. *Int. J. Pharm.* **2004,** *269,* 469–478. doi:10.1016/j.ijpharm.2003.09.043
5. Whilton, N. T.; Vickers, P. J.; Mann, S. *J. Mater. Chem.* **1997,** *7,* 1623–1629. doi:10.1039/a701237c
6. Jaber, M.; Georgelin, T.; Bazzi, H.; Costa-Torro, F.; Lambert, J.-F.; Bolbach, G. R.; Clodic, G. *J. Phys. Chem. C* **2014,** *118,* 25447–25455. doi:10.1021/jp507335e
7. Burcar, B. T.; Jawed, M.; Shah, H.; McGown, L. B. *Origins Life Evol. Biospheres* **2015,** *45,* 31–40. doi:10.1007/s11084-015-9412-y
8. Gottarelli, G.; Masiero, S.; Mezzina, E.; Pieraccini, S.; Rabe, J. P.; Samorí, P.; Spada, G. P. *Chem. – Eur. J.* **2000,** *6,* 3242–3248. doi:10.1002/1521-3765(20000901)6:17<3242::AID-CHEM3242>3.0.CO;2-K
9. Peters, G. M.; Skala, L. P.; Plank, T. N.; Hyman, B. J.; Manjunatha Reddy, G.; Marsh, A.; Brown, S. P.; Davis, J. T. *J. Am. Chem. Soc.* **2014,** *136,* 12596–12599. doi:10.1021/ja507506c
10. Arnal-Hérault, C.; Pasc, A.; Michau, M.; Cot, D.; Petit, E.; Barboiu, M. *Angew. Chem., Int. Ed.* **2007,** *46,* 8409–8413. doi:10.1002/anie.200702605
11. Leroux, F.; Besse, J.-P. *Chem. Mater.* **2001,** *13,* 3507–3515. doi:10.1021/cm0110268
12. Lee, J.-Y.; Gwak, G.-H.; Kim, H.-M.; Kim, T.-i.; Lee, G. J.; Oh, J.-M. *Appl. Clay Sci.* **2016,** *134,* 44–49. doi:10.1016/j.clay.2016.03.029

13. Cavani, F.; Trifirò, F.; Vaccari, A. *Catal. Today* **1991,** *11,* 173–301. doi:10.1016/0920-5861(91)80068-K
14. Choy, J.-H.; Jung, J.-S.; Oh, J.-M.; Park, M.; Jeong, J.; Kang, Y.-K.; Han, O.-J. *Biomaterials* **2004,** *25,* 3059–3064. doi:10.1016/j.biomaterials.2003.09.083
15. Tammaro, L.; Vittoria, V.; Bugatti, V. *Eur. Polym. J.* **2014,** *52,* 172–180. doi:10.1016/j.eurpolymj.2014.01.001
16. Williamson, J. R.; Raghuraman, M.; Cech, T. R. *Cell* **1989,** *59,* 871–880. doi:10.1016/0092-8674(89)90610-7
17. Berg, J. M.; Tymoczko, J. L.; Stryer, L. *Biochemistry;* W.H. Freeman & Co. Ltd., 2006.
18. Madariaga, S. T.; Contreras, J. G. *J. Chil. Chem. Soc.* **2010,** *55,* 50–52. doi:10.4067/S0717-97072010000100012
19. Kumar, A.; Gupta, S. K. *J. Mater. Chem. B* **2013,** *1,* 5818–5830. doi:10.1039/c3tb20877j
20. Nývlt, J.; Söhnel, M.; Matachová, M.; Broul, M. *The kinetics of industrial crystallization;* Elsevier Science Ltd, 1985; pp 334 ff.
21. Kim, T.-H.; Lee, G. J.; Kang, J.-H.; Kim, H.-J.; Kim, T.-i.; Oh, J.-M. *BioMed Res. Int.* **2014,** *2014,* 193401. doi:10.1155/2014/193401

License and Terms

BEILSTEIN JOURNAL OF NANOTECHNOLOGY

Organoclay hybrid materials as precursors of porous ZnO/silica-clay heterostructures for photocatalytic applications

Marwa Akkari[1,2], Pilar Aranda[1], Abdessalem Ben Haj Amara[2] and Eduardo Ruiz-Hitzky[*1]

Full Research Paper

Open Access

Address:
[1]Instituto de Ciencia de Materiales de Madrid, CSIC, c/ Sor Juana Inés de la Cruz 3, Cantoblanco, 28049 Madrid, Spain and [2]Laboratory of Physics of Lamellar Materials and Hybrid Nano-Materials (LPLMHNM), Faculty of Sciences of Bizerte, University of Carthage, 7021 Zarzouna, Tunisia

Email:
Eduardo Ruiz-Hitzky[*] - eduardo@icmm.csic.es

* Corresponding author

Keywords:
delamination; montmorillonite; organoclays; photocatalysis; porous clay heterostructures; sepiolite; ZnO nanoparticles

Beilstein J. Nanotechnol. **2016,** *7,* 1971–1982.
doi:10.3762/bjnano.7.188

Received: 26 July 2016
Accepted: 11 November 2016
Published: 12 December 2016

This article is part of the Thematic Series "Hybrid nanomaterials: from the laboratory to the market".

Guest Editor: A. Taubert

Abstract

In this study, ZnO/SiO_2-clay heterostructures were successfully synthesized by a facile two-step process applied to two types of clays: montmorillonite layered silicate and sepiolite microfibrous clay mineral. In the first step, intermediate silica–organoclay hybrid heterostructures were prepared following a colloidal route based on the controlled hydrolysis of tetramethoxysilane in the presence of the starting organoclay. Later on, pre-formed ZnO nanoparticles (NP) dispersed in 2-propanol were incorporated under ultrasound irradiation to the silica–organoclay hybrid heterostructures dispersed in 2-propanol, and finally, the resulting solids were calcinated to eliminate the organic matter and to produce ZnO nanoparticles (NP) homogeneously assembled to the clay–SiO_2 framework. In the case of montmorillonite the resulting materials were identified as delaminated clays of ZnO/SiO_2-clay composition, whereas for sepiolite, the resulting heterostructure is constituted by the assembling of ZnO NP to the sepiolite–silica substrate only affecting the external surface of the clay. The structural and morphological features of the prepared heterostructures were characterized by diverse physico-chemical techniques (such as XRD, FTIR, TEM, FE-SEM). The efficiency of these new porous ZnO/SiO_2-clay heterostructures as potential photocatalysts in the degradation of organic dyes and the removal of pharmaceutical drugs in water solution was tested using methylene blue and ibuprofen compounds, respectively, as model of pollutants.

Introduction

In the last decades, great effort has been devoted to study ZnO as a very promising catalyst in the photocatalytic degradation of water pollutants. This is because of its elevated activity, its low cost and, in particular, its environmentally friendly behavior [1,2]. It has been confirmed that ZnO compared to TiO_2 exhibits better efficiency in the photocatalytic degradation of organic pollutants [3-6]. It should be remembered that nanoparticulated zinc oxide is a wide-band gap II–VI semiconductor with a band-

gap energy of around 3.4 eV, which is of great interest for photocatalytic applications [7]. ZnO nanoparticles (NP) have been assembled to microparticulated layered silicates of the smectite family, giving rise to materials exhibiting interesting properties [8,9]. The immobilization of those NP on clay surfaces represents an advantage for the easier recovering of the photocatalyst from the reaction medium compared to ZnO NP alone.

In recent years, the development of porous heterostructures based on clays attracts many researchers aiming to prepare adsorbents and catalysts for different applications [10]. Amongst the diverse strategies that have been applied in the preparation of these porous materials Letaïef and co-workers [11,12] proposed a methodology in which it was possible to reach the delamination of layered silicates previously exchanged with long-chain alkylammonium cations (organoclays) [13]. In this way, organo-smectites and organo-vermiculites have been used to prepare a new type of nanocomposites consisting of delaminated layered silicates assembled to diverse inorganic NP [10,14]. Moreover, those containing silica-clay entities appear as very attractive materials in view of their elevated specific surface area and the possibility of further functionalization. The more common silica sources used to prepare them are tetraethoxysilane (TEOS) and tetramethoxysilane (TMOS) although this methodology may involve the use of other alkoxysilanes as well as diverse metal alkoxides [14]. The influence of the surfactant incorporated into the organoclay on the characteristics of the obtained materials has been pointed out recently [15,16]. The methodology has been also applied to organoclays derived from fibrous clays (e.g., sepiolite) in which the presence of the surfactant at the external surface results in the formation of silica NP of diverse characteristics depending on the nature of both, silane precursor and surfactant present at the organic–inorganic interface [17]. In general, this sol–gel procedure leads to heterostructured clay-based materials with enhanced textural properties compared to the ones of pristine silicates [14]. The simultaneous use of silicon and metal-alkoxide precursors gives rise, for instance, to the formation of silica/alumina-clay heterostructures providing acid-catalyst behavior [18,19]. Similarly, silica–titania delaminated clays have been also prepared via the generation of TiO_2/SiO_2 NP in the interlayer space of smectites and vermiculites modified with long-chain alkylammonium species, promoting a clay delamination that leads to new porous TiO_2/SiO_2-layered clay heterostructures [20]. The procedure has been also applied to fibrous clays with the aim to form TiO_2/SiO_2 NP anchored on the external surface of sepiolite, leading to porous heterostructures exhibiting photocatalytical properties [21]. In this context, the presence of SiO_2 NP may play an additional role regarding the improvement of adsorption properties, although this effect has not been clarified neither its possible influence in photocatalytic behavior of resulting materials. Moreover, the simultaneous generation of TiO_2 and SiO_2 NP from the two alkoxide precursors may result in the formation of mixed oxides showing poorer photoactivity than the clay heterostructure containing only TiO_2 NP.

In the present work, we have explored a different approach to prepare ZnO/SiO_2-clay heterostructures derived from layered silicates and sepiolite fibrous clay, in which SiO_2-clay organoheterostructures are used for further assembling ZnO NP. In this way, heterostructures in which the surfactant is still present are formed from TMOS and organoclays derived from two types of silicates (smectites and sepiolite) and then the formed hybrid phases are treated with a colloidal suspension of ZnO NP in 2-propanol, following a methodology recently used for the preparation of ZnO/clay nanoarchitectures [22]. The final goal is to reach, in a simple way, ZnO-clay based heterostructures with improved textural properties where ZnO NP remain immobilized and photoactive. To confirm this, the resulting ZnO/silica-clay heterostructured porous solids have been tested in photocatalytic experiments using water solutions of methylene blue (MB) dye or ibupofren drug, as models of organic pollutants, to prove their efficiency as photocatalysts for environmental applications.

Results and Discussion

ZnO/silica-montmorillonite heterostructures

The synthesis of ZnO/silica-clay heterostructures was developed following in part the procedure already reported for the preparation of silica-clay nanocomposites [11,12]. The aim is to produce first silica-clay heterostructures in which the growth of SiO_2 NP from the controlled hydrolysis and polycondensation of TMOS provokes at least a partial delamination of the smectite and so the resulting system will offer a high specific surface area where ZnO NP will be assembled in a second step of the process. As described in the Experimental section, the intermediate/silica-organoclay samples were firstly prepared and, in a second step, were treated with freshly synthesized ZnO NP dispersed in 2-propanol (Figure 1A).

The XRD diagrams (Figure 2) of the two layered silicates treated with CTAB, Cloisite® (CLO-CTA) and smectite from the Gafsa region (TSM-CTA), indicate an increase of the interlayer spacing (d_{001}) from ca. 1.2 nm in the pristine Na^+-exchanged clays to ca. 1.85 nm (Figure 2Ab) and 3.34 nm (Figure 2Bb), respectively. This feature is due to the different degree of ion exchange and the different conformation in which the CTA^+ surfactant ions are intercalated in each type of layered silicate. After the generation of the SiO_2 network the XRD diagrams change drastically and the most intense (001) reflection is practically undetectable suggesting a loss of the stacking

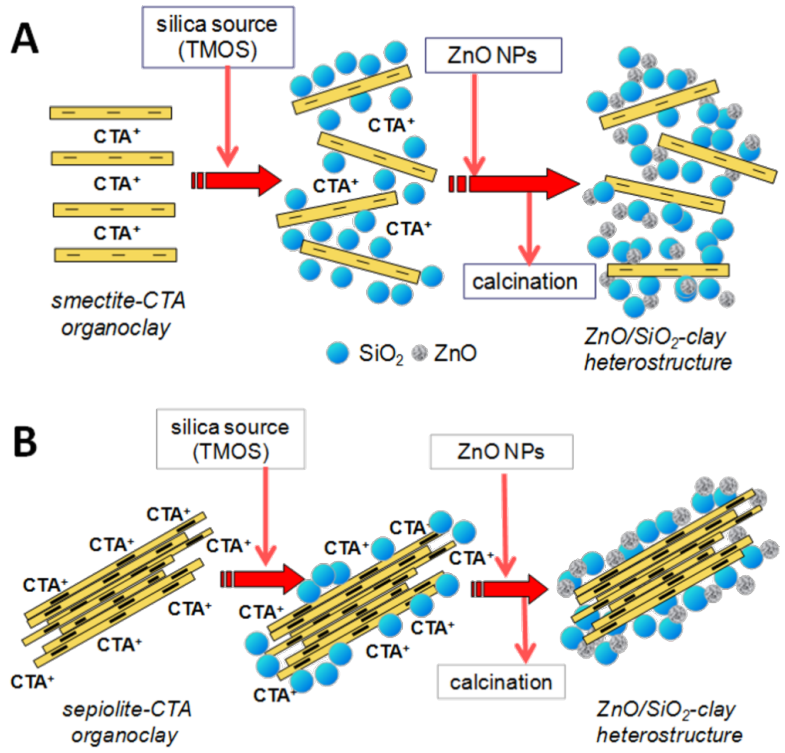

Figure 1: Scheme of the synthetic approach employed in the preparation of the ZnO/SiO_2-clay heterostructures derived from smectite (A) and sepiolite (B) clay minerals.

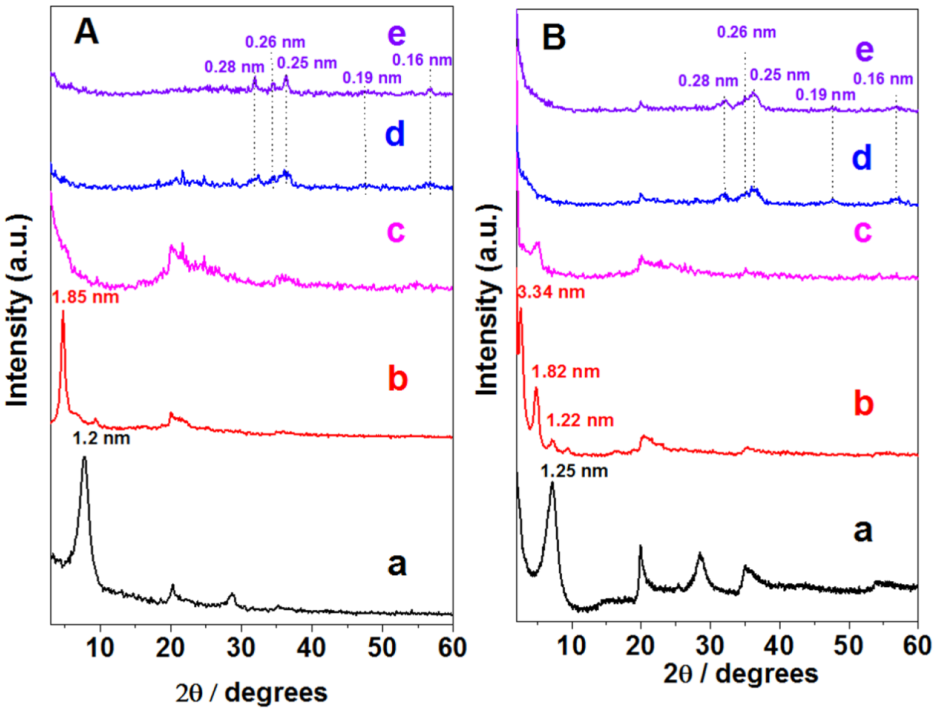

Figure 2: XRD patterns for Cloisite® (A) and TSM (B) corresponding to: (a) the starting clay, (b) CTA^+-exchanged clays (organoclays), (c) intermediate SiO_2-organoclay samples, (d) ZnO/SiO_2-clay heterostructures before calcination, and (e) ZnO/SiO_2-clay after calcination at 500 °C. Starting clays and organoclays are the same than in the previous study [22].

of the silicate layers through delamination (Figure 2Ac and Figure 2Bc). This feature is maintained in both smectite samples after assembling of the ZnO NP before and after the thermal treatment (i.e., diffractograms d and e in Figure 2A) and it is ascribed to the silicate delamination, which has also been reported in other layered systems [11,19,20]. The only difference between the XRD diagrams of the samples before and after thermal treatment refers to the presence of more intense diffraction peaks at 0.28, 0.26, 0.25, 0.19 and 0.16 nm in the final ZnO/SiO_2-clay heterostructures, which correspond to the (100), (002), (101), (102) and (110) reflections assigned to ZnO hexagonal wurtzite lattice (JCPDS 36-1451), respectively. The particle size calculated from these peaks using the Debye–Scherrer equation (vide infra) are 20 and 9 nm for ZnO/SiO_2-CLO and ZnO/SiO_2-TSM samples, respectively, which is close to the dimensions observed by TEM.

The characteristics of the heterostructures at the different stages of preparation were also evaluated by FTIR (data not shown). In both ZnO/SiO_2-organoclay heterostructures, the presence of bands at around 2920 and 2850 cm^{-1} as well as in the 1470 cm^{-1} region is clearly observed. These bands are typical for the ν_{C-H} stretching and δ_{CH2} deformation vibration modes of $-CH_2-$ and CH_3- groups belonging to the CTA^+ ions, respectively. After the thermal treatment, these bands completely disappear from the infrared spectrum corroborating the whole removal of the organic species by calcination in accordance also with results from thermogravimetric curves (data not shown). The bands in the 950–1200 cm^{-1} region correspond to the ν_{Si-O} stretching vibration modes of the clay, typically appearing as an intense band centered in the range of 1020–1050 cm^{-1} with a shoulder around 1100 cm^{-1}. In the samples containing SiO_2 the shoulder shifts to higher wavenumbers and even a second shoulder is observable in the 1180–1200 cm^{-1} range, as the bands ascribed to vibration modes of the silica network overlap those of the clay substrate, as it was also observed in other SiO_2-clay nanocomposites [11].

FE-SEM images (Figure 3) show the typical spongy morphology of SiO_2-organosmectite materials which is also preserved in

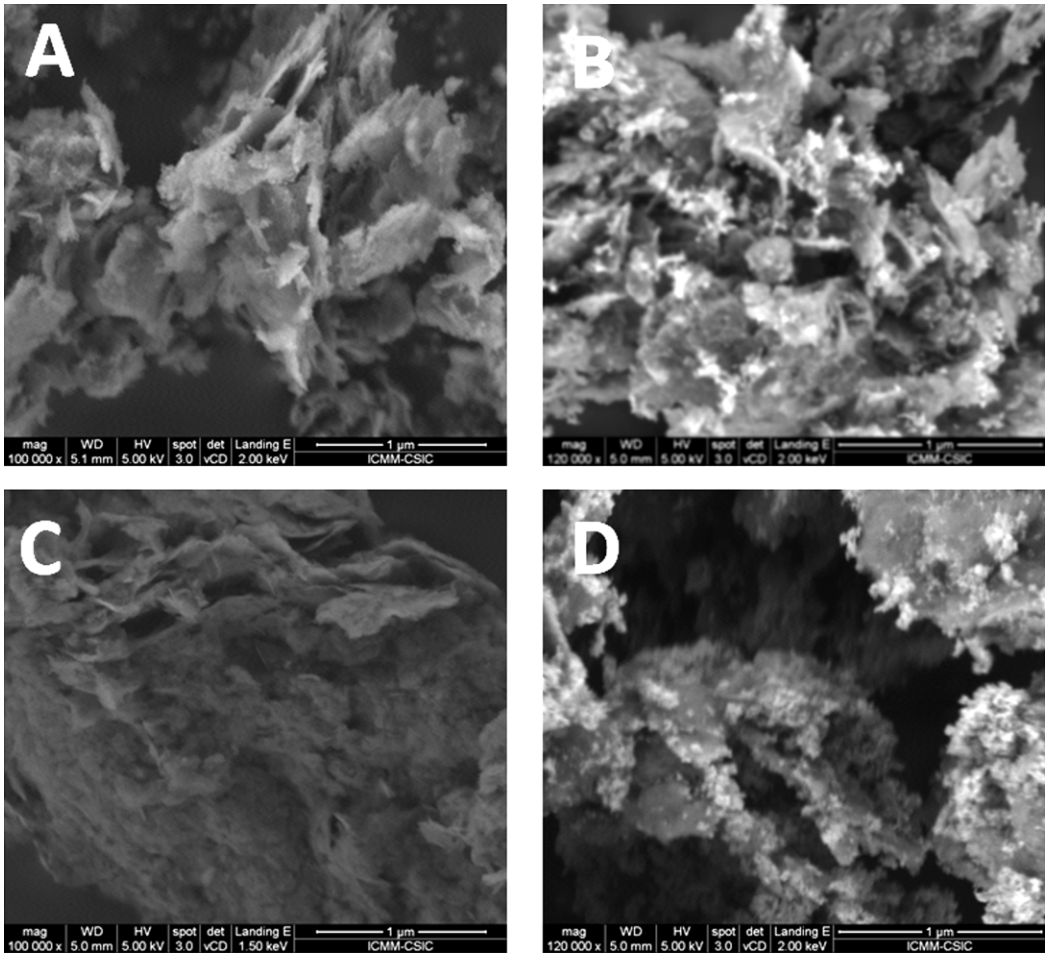

Figure 3: FE-SEM images of the heterostructures: (A) SiO_2-CLO-CTA, (B) ZnO/SiO_2-CLO, (C) SiO_2-TSM-CTA and (D) ZnO/SiO_2-TSM.

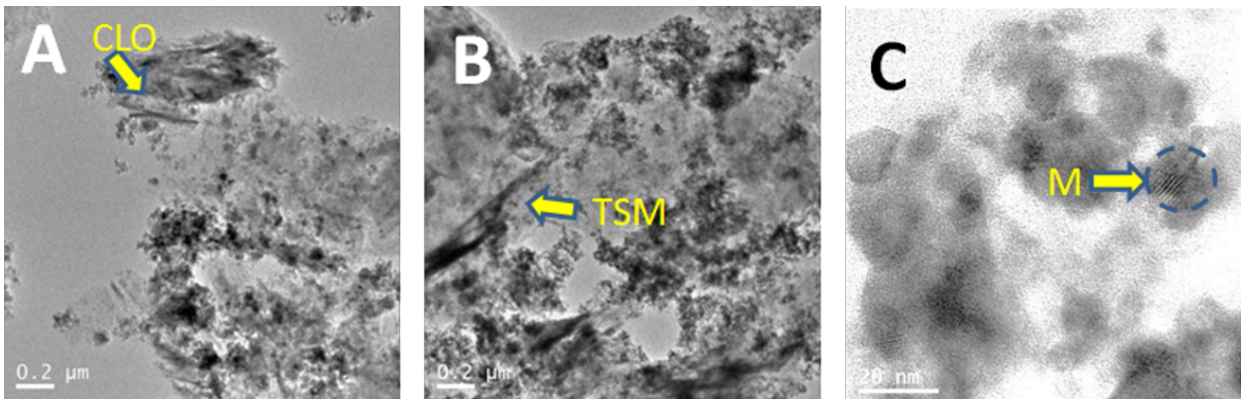

Figure 4: TEM images of the heterostructures: (A) ZnO/SiO_2-CLO and (B) ZnO/SiO_2-TSM, in both images the arrows show regions with the presence of delaminated clay particles (CLO and TSM, respectively). Image (C) represents a detail of A at higher magnification showing a ZnO nanoparticle within the silica matrix (M arrow: Moiré fringe).

the ZnO/SiO_2-clay heterostructures formed after thermal treatment at 500 °C, detecting in the latest the presence also of ZnO NP (Figure 3B and Figure 3D). From the TEM images corresponding to the final heterostructures (Figure 4) one can observe: i) the presence of delaminated clay platelets (the region indicated by the arrow in Figure 4A and 4B); ii) the presence of ZnO NP (showing in some cases Moiré fringes, Figure 4C); and iii) the presence of aggregates of SiO_2 NP which in some cases may remain assembled to ZnO particles, perhaps organized even as core–shell structures (Figure 4C). EDX analysis of ZnO/silica-clay heterostructures shows the presence of Zn in a significant amount with respect to the Si content in all the samples. However, it is complicated to estimate the precise ZnO/clay/SiO_2 ratio because of the difficulty to ascertain how much of the Si contribution is coming from the clay silicate and how much from the generated silica.

The porous nature of ZnO/SiO_2-montmorillonite materials was characterized by nitrogen adsorption–desorption isotherms at 77 K (Figure 5), obtained as described in the Experimental section [12]. The ZnO/SiO_2-montmorillonite heterostructure derived from Closite® shows an type-I/II isotherm with a H3-type hysteresis loop, according to the IUPAC classification [23]. This isotherm is compared in Figure 5A with the one of the SiO_2-organoclay without assembly of ZnO NP but submitted to a similar thermal treatment. The silica-clay (SiO_2-CLO) heterostructure is a porous material the isotherm of which exhibits a comparable trend with a greater adsorption capacity but also shows the presence of microporosity. This microporosity in the ZnO/SiO_2-CLO heterostructure is probably blocked by the ZnO NP. In the case of the ZnO/SiO_2-clay heterostructure derived from TSM smectite, the isotherm type is also quite similar to that of the ZnO/SiO_2-CLO heterostructure with scarce microporosity. Clearly, the related SiO_2-TSM heterostructure exhibits a slightly different type of isotherm (type I with H4 hysteresis loop) (Figure 5B). The textural parameters calculated from these isotherms are summarized in Table 1, where they are compared to related porous materials including the

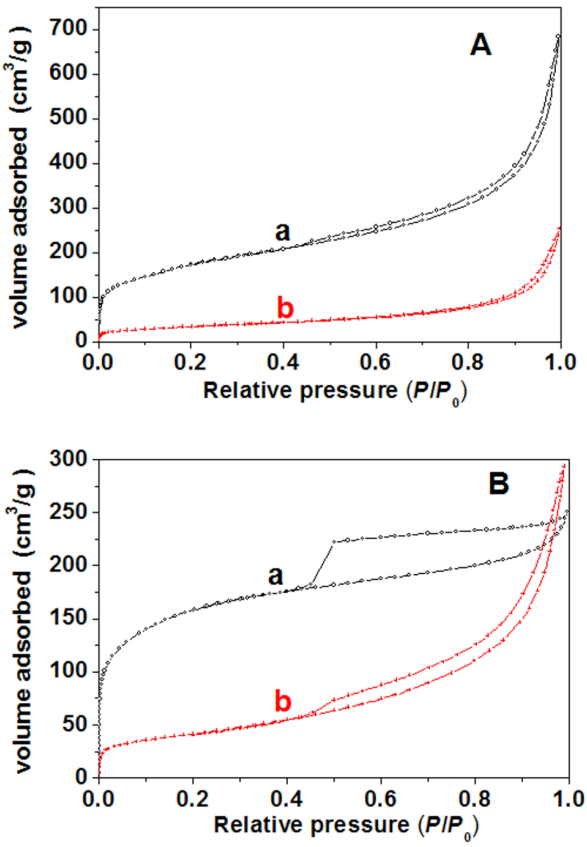

Figure 5: N_2 adsorption–desorption isotherms (77 K) of SiO_2-clay (a) and ZnO/SiO_2-clay (b) heterostructures based on Cloisite® (A) and TSM (B) clays, respectively.

Table 1: Textural characteristics of diverse smectite- and sepiolite-based heterostructures calculated from their N_2 adsorption–desorption isotherms (77 K).

sample	S_{BET}[a] (m^2/g)	S_{ext}[b] (m^2/g)	V_{MP}[c] (cm^3/g)	V_T[d] (cm^3/g)
ZnO/SiO_2-CLO	126	135	—	0.367
SiO_2-CLO	604	574	0.0155	0.987
ZnO/CLO[e]	95	94	—	0.252
ZnO/SiO_2-TSM	148	137	0.0459	0.433
SiO_2-TSM	518	360	0.0857	0.377
ZnO/TSM[e]	51	48	0.0007	0.200
ZnO/SiO_2-SEP	111	94	0.0089	0.354
SiO_2-SEP	332	176	0.0822	0.455
ZnO/SEP[e]	104	83	0.0104	0.366

[a]Specific surface area from BET method, [b]specific external surface area, [c]micropore volume calculated by the t-method and, [d]total pore volume at P/P_0 = 0.99; [e]values from reference [22].

SiO_2-clay hetererostructures without ZnO NP and previously reported ZnO-clay heterostructures prepared by direct assembly of ZnO NP to the organoclays (without silica incorporation) [22]. The ZnO/SiO_2-clay samples show specific surface areas of around 126 and 148 m^2/g for Cloisite® and TSM smectites, respectively. By comparing these values to those of the related ZnO-clay materials [22] a significant increase in the specific surface area values in the heterostructures prepared incorporating previously silica is clearly evident. However, it should be noted that these materials exhibit reduced specific surface area values compared to that developed by silica-clay heterostructures obtained by calcination under the same conditions but without assembling of ZnO NP (Table 1). Anyway, as it occurs with other related materials affected by delamination processes, the solids prepared here exhibit higher values of total porosity and specific surface area than ZnO-clay heterostructures, which is of paramount importance for catalytic purposes.

ZnO/SiO_2-sepiolite heterostructures

The preparation of ZnO/sepiolite heterostructures in which sepiolite was previously modified by assembling of SiO_2 NP has been also explored with the aim to increase the accessible surface area to ZnO NP. As indicated in the Experimental section, the resulting SiO_2-organosepiolite material was used in a second step for the assembly of freshly synthetized ZnO NP following a protocol similar than the one applied for the preparation of the smectite-based heterostructures (Figure 1B).

XRD patterns of pristine sepiolite fibrous clay and the organoclay obtained by treatment with CTAB revealed not changes, confirming that the surfactant is just assembled to the external surface of the clay (Figure 6). This technique also reveals that the hydrolysis and polycondensation of TMOS to produce silica NP on the organo-sepiolite surface did not cause any relevant structural change, as it was already reported for related titania-clay heterostructures [21]. The further assembly of ZnO NP to produce the final ZnO/SiO_2-SEP heterostructure is confirmed by the presence of new peaks in the corresponding XRD patterns of the heterostructure before and after the calcination step (Figure 6d and Figure 6e). As occurs in the heterostructures derived from layered clays, here the presence of ZnO NP stabilized in the wurtzite phase (JCPDS 36-1451) is also observed. Interestingly, the calcination procedure here applied did not cause the complete structural collapse of the sepiolite, as revealed by the presence of the (110) reflection in all the patterns, being still quite intense and centered at around 1.17 nm in the XRD diagrams of the final heterostructure (Figure 6e). Comparable behavior has been also reported for diverse heterostructured materials based on sepiolite, where organic or inorganic components can partially penetrate the sepiolite structural tunnels impeding the silicate folding [18,24].

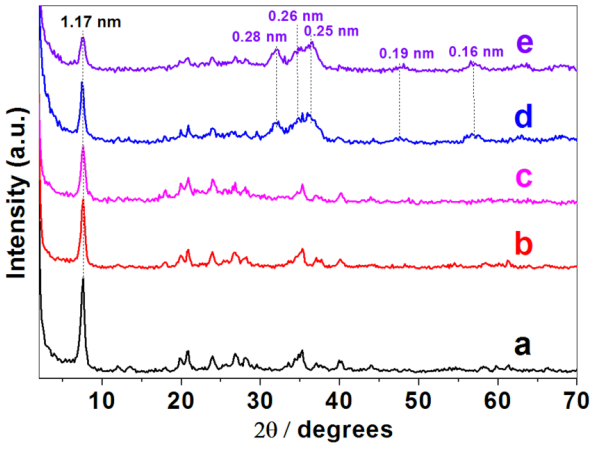

Figure 6: XRD patterns of (a) starting sepiolite (SEP), (b) SEP-CTA organoclay, and (c) SiO_2/SEP-CTA, (d) ZnO/SiO_2-SEP-CTA and (e) ZnO/SiO_2-SEP heterostructures. Samples SEP and SEP-CTA are the same than in the previous study [22].

From the FE-SEM images of the SiO_2-SEP-CTA sample before (Figure 7A) and after the assembly of ZnO NP to form the heterostructure ZnO/SiO_2-SEP (Figure 7B) it is clearly observed the presence of the metal oxide NP associated with the clay. In the SiO_2-SEP-CTA heterostructure (Figure 7A) the fibers covered by a coating, which after calcination is transformed in more discrete nanoparticles of both SiO_2 and the assembled ZnO NP, can be seen clearly (Figure 7B). TEM images of the ZnO/SiO_2-SEP heterostructure (Figure 7C) show more clearly the presence of sepiolite fibers surrounded by the generated SiO_2 nanoparticles and by ZnO NP showing pseudo-spherical morphology. A good homogeneity in the ZnO NP distribution on the sepiolite surface is corroborated from these images. Furthermore, both types of NP remain attached to the silicate covering almost completely the fibers anchored to the silanol (Si-OH) groups located at the external surface of sepiolite, which can be confirmed by FTIR spectroscopy (Figure 8). Thus, the ν_{O-H} stretching vibration mode of the Si–OH groups appearing around 3720 cm^{-1} in the spectrum of pristine sepiolite is neither detectable in the spectrum of the organo-sepiolite nor in that of the sepiolite heterostructures. The disappearance of this band is attributed to the direct interaction of silanol groups with the diverse species located at the sepiolite surface in each case. Proof of this is the fact that the ν_{O-H} stretching vibration band ascribed to Mg-OH groups appearing at 3680 cm^{-1} remains unaltered in all the spectra, which was expected as they are located at the interior of the structural blocks of sepiolite without access to the adsorbed species on the silicate [18,24].

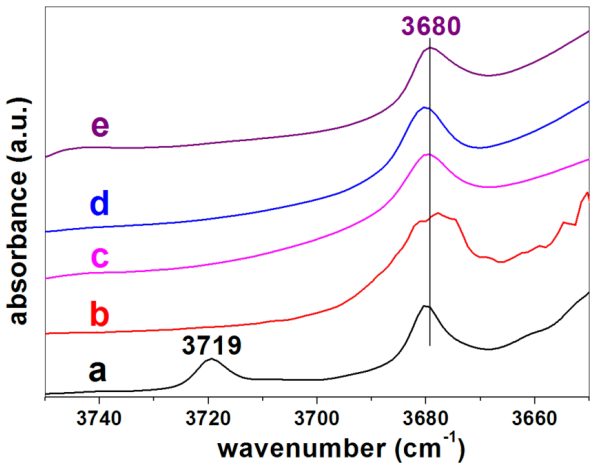

Figure 8: FTIR spectra (3750–3650 cm^{-1} region) of (a) pristine sepiolite (SEP), (b) SEP-CTA, and the (c) SiO_2/SEP-CTA, (d) ZnO/SiO_2-SEP-CTA and (e) ZnO/SiO_2-SEP heterostructures. Samples SEP and SEP-CTA are the same than those in the previous study [22].

Concerning the ^{29}Si NMR spectra (Figure 9), the one of the ZnO/SiO_2-SEP heterostructure is complex as it is composed of ^{29}Si signals coming from silicon nuclei of sepiolite structure, from generated silica with different condensation degrees as well as from some other components involving more complex interactions, e.g., silica in interaction with ZnO and sepiolite. ^{29}Si NMR spectra of pure sepiolite shows three characteristic signals at approximately −92.4, −95.0, and −98.6 ppm (Figure 9a) typical of Q^3 signals attributed to Si atoms in different structural environments [25]. There is also a small Q^2 signal at −85.7 ppm, which is related to the silanol groups located at the surface of the silicate [25]. The ^{29}Si NMR spectrum of the ZnO/SiO_2-SEP heterostructure is clearly different showing a strong decrease in the intensity of the Q^2 signal, which is attributed to the reaction of sepiolite silanol groups with TMOS. This is similar to reports of other authors related to sepiolite-based heterostructures [17,19,26]. Simultaneously the Q^3 signals are highly perturbed and the ones of sepiolite are overlapped with those signals from the formed silica, with only two well-defined peaks appearing at −93.2 and −96.7 ppm with two shoulders at −94.7 and −98.7 ppm. In addition, a signal at −104.0 ppm and a large band centered at about −110 ppm are observed. These are related to Q^4 signals of silica involving Si in different environments and probably also those related to silica–ZnO interactions.

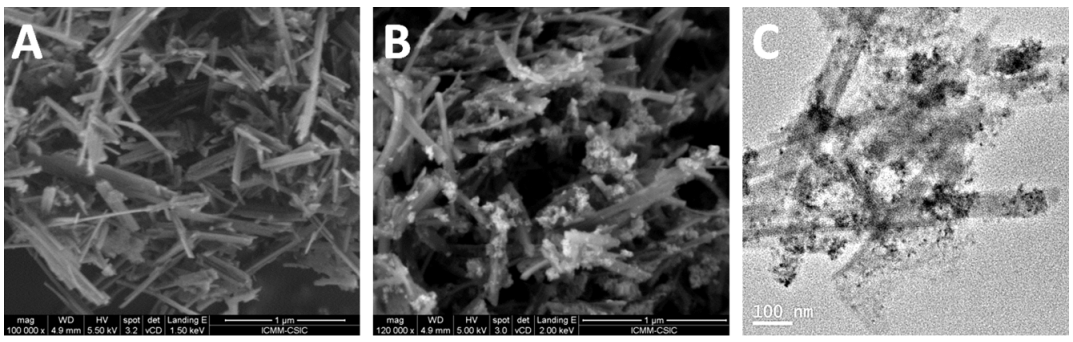

Figure 7: FE-SEM images of SiO_2-SEP-CTA (A) and ZnO/SiO_2-SEP (B) heterostructures, and TEM image of ZnO/SiO_2-SEP heterostructure (C).

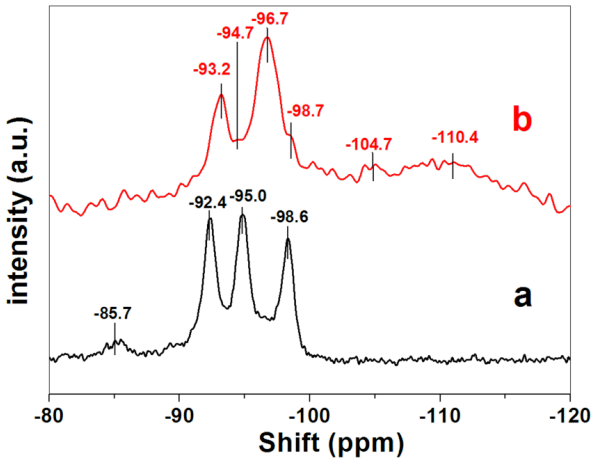

Figure 9: ^{29}Si solid-state NMR spectra of (a) sepiolite and (b) ZnO/SiO_2-SEP heterostructure.

The N_2 adsorption isotherm for the ZnO/SiO_2-sepiolite heterostructure (Figure 10) is assigned to the type I/II with hysteresis loops of type H3 according to the IUPAC classification. For comparison, a similar isotherm corresponding to the SiO_2-sepiolite heterostructure prepared from SiO_2-SEP-CTA by calcination under the same conditions applied to prepare the ZnO/SiO_2-sepiolite heterostructure is also shown. From Table 1, the significant decrease of the specific surface area from ca. 331 m^2/g to ca. 111 m^2/g calculated for silica-sepiolite and ZnO/silica-sepiolite heterostructures, respectively, can be seen. This decrease in surface area can be attributed to the presence of ZnO NP, which partially blocks the tunnels of the sepiolite as well as the porosity created by the SiO_2 NP attached to sepiolite. A collapse of sepiolite after the thermal treatment at 500 °C (folding of the sepiolite structure) [27] can be ruled out, because XRD revealed not significant structural changes in sepiolite (Figure 6e).

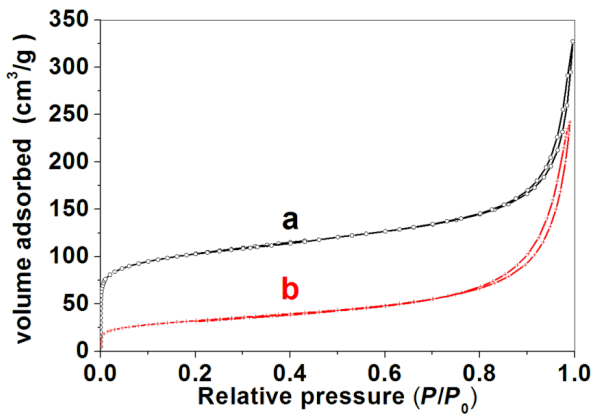

Figure 10: N_2 adsorption–desorption isotherms at 77 K for SiO_2-SEP (a) and ZnO/SiO_2-SEP (b) heterostructures.

Catalytic properties of ZnO/SiO_2-clay heterostructures

The ZnO/SiO_2-clay heterostructures presented here can be of interest for different applications as a photocatalyst. Hence, their activity has been tested using methylene blue (MB) model dye molecule. Figure 11 shows the concentration of methylene blue solutions (C/C_0) as a function of the UV irradiation time in

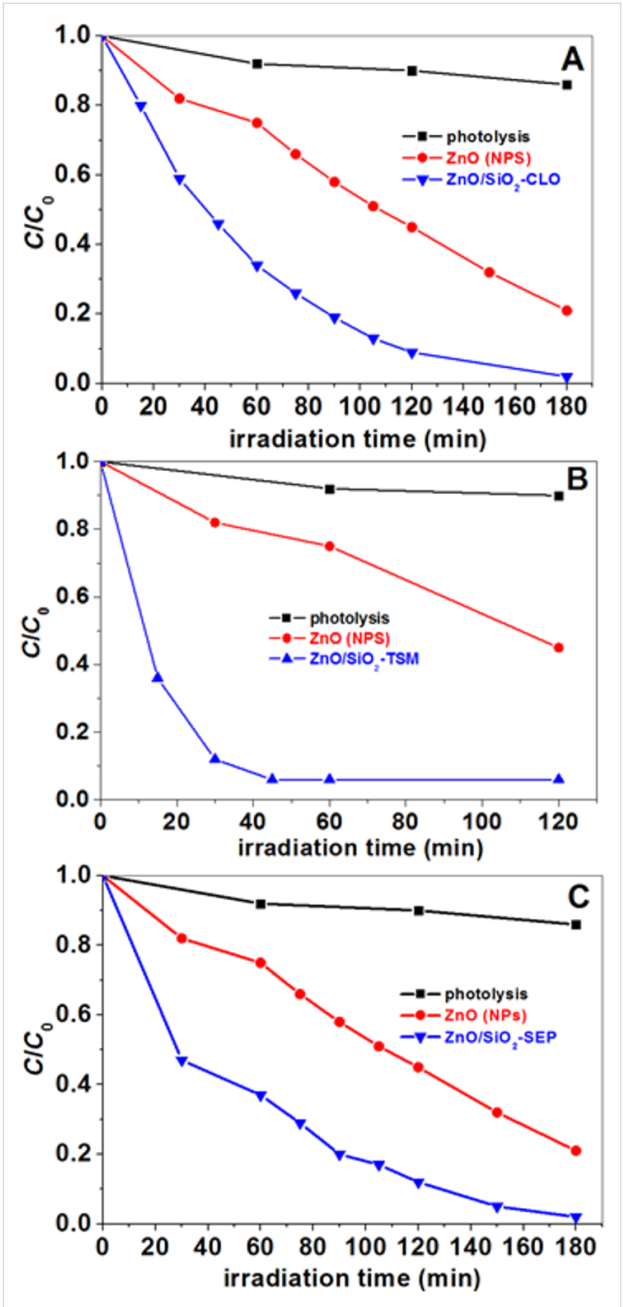

Figure 11: C/C_0 ($C_0 = 3 \cdot 10^{-5}$ M) of MB as a function of the UV irradiation time in presence of the heterostructures (experiments carried out at 17 °C): (A) ZnO/SiO_2-CLO, (B) ZnO/SiO_2-TSM and (C) ZnO/SiO_2-SEP. "Photolysis" corresponds to photodegradation of MB in the absence of catalyst. "Photolysis" and ZnO(NP) data are the same than in the previous study [22].

presence of SiO_2/ZnO montmorillonite and ZnO/SiO_2-sepiolite heterostructures acting as photocatalysts. Apparently, ZnO/SiO_2-clay materials act as efficient photocatalysts as MB is completely degraded after 180 min of irradiation in presence of ZnO/SiO_2-SEP or ZnO/SiO_2-CLO heterostructures, and after only 120 min in presence of the ZnO/SiO_2-TSM clay heterostructure. It should be noted that the ZnO-heterostructures based on clays are photocatalytically more active when they were modified by introducing silica to improve the textural characteristics. Table 2 shows a comparison of the photoactivity of diverse clay-ZnO systems in the degradation of MB. Probably, the higher activity of ZnO/SiO_2-clay heterostructures compared to the ZnO-clay materials maybe related to the much higher specific surface area and the larger pore volume of the former. This could also lead to a removal of the pollutant by adsorption instead of just photocatalytic degradation. The current results suggest that an appropriate pore volume with an optimized pore size distribution besides a large specific surface area of these materials, can promote a more efficient photocatalytic activity but also a higher adsorption capacity of MB molecules, which also contributes to the removal of these molecules from solution. This is especially relevant in the present case as MB is a cationic molecule that may be adsorbed by the clay component due to electrostatic interactions in an ion-exchange mechanism. The initial amount of MB adsorbed by the different substrates is in the range of 8–12 mmol/100g. The photoactivity efficiency is determined considering the initial concentration of MB after the adsorption process and measuring its evolution with irradiation time from that point. Moreover, the possibility that MB was only partially degraded reaching structural changes in the molecule that affect the solution color and hence the UV–vis results should be considered. In this sense, work is undergoing to clarify the degradation mechanism when using these porous solids as well as their efficiency of the removal of various pollutants in water.

To explore the potential application of these ZnO-based materials as photocatalyst for the degradation of drug pollutants in water, ibuprofen was selected as a model pharmaceutical. Ibuprofen shows a low adsorption affinity towards silica/silicate substrates and the observed degradation could be directly related to the photocatalytic activity of the tested materials. Figure 12 displays the evolution of the ibuprofen concentration after 6 h of UV irradiation. In absence of catalysts, i.e., the photolysis experiment, there is only 5% of degradation after 360 min, indicating that ibuprofen shows good photostability under UV–vis irradiation. The ZnO/SiO_2-clay heterostructures clearly show photoactivivity in the degradation of ibuprofen under UV irradiation. The highest activity was observed for the ZnO/SiO_2-TSM sample (65% degradation after 6 h irradiation), followed by ZnO/SiO_2-SEP and ZnO/SiO_2-CLO samples that show 60% and 45% degradation, respectively. Contrarily to that observed in the MB photodegradation study, ZnO nanoparticles alone exhibit a higher activity compared to the activity of the heterostructures, reaching 84% of ibuprofen decomposition after 6 h of irradiation. This feature could be tentatively explained by admitting a more effective UV shielding in the reaction medium under the conditions of ibuprofen study, where the concentration of solids was slightly higher than the one used in

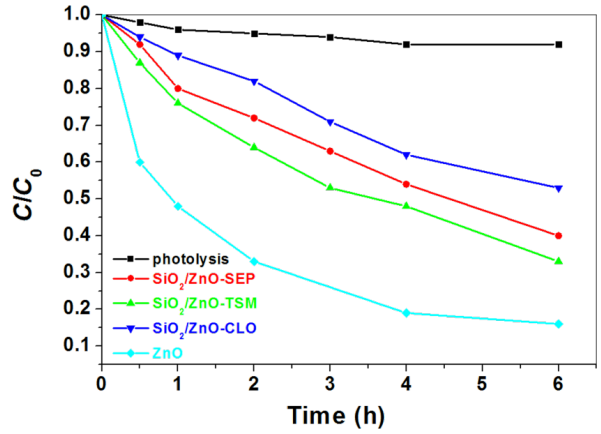

Figure 12: Photoactivity of ZnO NP and ZnO-SiO_2-clay heterostructures showing degradation of ibuprofen in aqueous solution (C_0 = 15 mg/L) under UV irradiation (experiments carried out at 17 °C).

Table 2: The degradation percent of MB aqueous solution over different samples under UV irradiation in comparison with literature.

sample	photodegradation efficiency (%) (after 120 min)	reference
ZnO/SiO_2-SEP	87	this work
ZnO/SiO_2-CLO	90	this work
ZnO/SiO_2-TSM	96	this work
ZnO/SEP	84	[22]
ZnO/CLO	96	[22]
ZnO/TSM	62	[22]
ZnO/montmorillonite	40% (150 min)	[28]
ZnO/montmorillonite	15.7 (50 min)	[29]

the case of MB degradation (see above). It should be also noted that the ibuprofen degradation by the ZnO NP synthesized in this work is lower than that already reported for other ZnO NP, which could be attributed to differences in the NP size [30].

Conclusion

We introduced a new family of ZnO/SiO_2 porous clay heterostructures synthesized from organoclay hybrid materials the interfaces of which turned out to be especially useful for the growing and assembling of silica and ZnO NP. The involved clays were layered silicates of the smectite type (a Wyoming montmorillonite commercialized under the name Cloisite® and a Tunisian smectite from the Gafsa region) as well as the sepiolite fibrous clay from Vallecas-Vicálvaro (Spain). Both smectites can be exfoliated during the incorporation of SiO_2 NP giving rise to delaminated heterostructures, whereas sepiolite is modified exclusively on its external surface. The SiO_2 NP are generated by controlled hydrolysis and polycondensation of TMOS on the organophilic surface of both types of silicates previously treated with CTAB surfactant to form the corresponding organoclays. The second step in this synthetic strategy consists in the incorporation of ZnO nanoparticles to the SiO_2-organoclay heterostructures before calcination. As it has been previously observed [22], the presence of the surfactant offers a more convenient interface for the further assembly of ZnO NP. Thermal treatment of these resulting intermediate materials eliminates the organic matter, generating ZnO/SiO_2-sepiolite and ZnO/SiO_2-montmorillonite heterostructured materials. In the case of montmorillonite the process is accompanied by the delamination of the involved clay [12,19,20]. Interestingly, the heterostructures described here exhibit advantages, such as a larger specific surface area, over related materials prepared by the direct attachment of metal oxide NP to the clay without incorporation of silica NP [22]. Moreover, the investigation on the photocatalytic ability of the present materials indicates that ZnO/SiO_2-clay heterostructures derived from smectites showed an enhanced photocatalytic activity for the degradation of methylene blue, probably due to the most suitable textural features among these ZnO-silica clay heterostructures. The observed activity in the degradation of ibuprofen points out to the potential applicability of these catalysts for the removal of pharmaceuticals present in domestic water. The encouraging preliminary results for the obtained catalytic tests should be confirmed in further studies involving various experimental conditions as well as the analysis of the nature of the degraded organic molecules and studies extended to other pollutants.

Experimental

Materials

The starting clays used in this work were i) the commercial sodium montmorillonite named as Cloisite®-Na (abbreviated as CLO), supplied by Southern Clay Products; ii) the iron-rich smectite from Gafsa (Tunisia) described elsewhere [31], here noted as TSM; and iii) the sepiolite fibrous clay mineral (SEP) from the Vallecas-Vicálvaro clay deposits (Madrid, Spain) provided by TOLSA S.A. with the commercial trade name of Pangel® S9 (rheological grade), which contains more than 95% of pure sepiolite [32]. Methylene blue dye (MB, $C_{16}H_{18}N_3SCl$, RPE) and the ibuprofen sodium salt ($C_{13}H_{17}NaO_2$) were supplied by (Analyticals Carlo Erba) and Sigma-Aldrich, respectively. Hexadecyltrimethylammonium bromide (cetyltrimethylammonium bromide, CTAB, purum, Aldrich) was used in the preparation of the CTA-clay derivatives. Ultra-pure deionized water (18.2 MΩ·cm) was produced in an Elga Maxima Ultra-Pure Water system). Methanol and 2-propanol (Fluka, p.a.) were used as solvents or reactants. Zinc(II) acetate dihydrate $(CH_3COO)_2Zn{\cdot}2H_2O$ and KOH were purchased from Merck. Tetramethoxyorthosilicate (TMOS) from Fluka (>98 %) was used here as silica precursor.

Sample preparations

ZnO (NP) synthesis was achieved as reported by Akkari et al. [22]. In a first step, SiO_2-clay organo-heterostructures (Figure 1) were synthesized by a heterocoagulation reaction involving a sol–gel process with the controlled hydrolysis and polycondensation of silica from silicon-alkoxides in the presence of swollen organosmectites, using the method reported by Letaiëf and co-workers [11,12]. In the present case, the organosmectites were dispersed in 2-propanol and then TMOS was added as silica source to produce materials with a final ratio of 1:1 (SiO_2/clay). Upon addition of the stoichiometric amounts of water and alcohol (4:2:1 H_2O/alcohol/TMOS and 1 drop of 1 M HCl) the controlled hydrolysis and polycondensation of the alkoxide took place. The preparation of the SiO_2-organosepiolite derivative was based on a methodology adapted from a previous one reported by Aranda and co-workers [21]. Shortly, SiO_2-organosepiolite heterostructure was prepared from a homogenous suspension (5% w/w) of the SEP-CTA organo-sepiolite in 2-propanol to which TMOS was added to produce materials with a final ratio of 1:1 (SiO_2/clay). This suspension was stirred at 50 °C to homogenize the system and then stoichiometric amounts of water and isopropanol (H_2O/isopropanol/TMOS 4:2:1 molar ratio) is added to start the hydrolysis of TMOS. After the sol–gel transition the system was dried overnight at 50 °C. The final ZnO/SiO_2-clay heterostructures were then prepared from this SiO_2-organoclay dispersed in 2-propanol (5% w/w), to which are slowly added ZnO NP also dispersed in 2-propanol to reach a molar ratio of 0.5:1 ZnO/SiO_2-organoclay. This suspension is homogenized by ultrasound irradiation (SONICS Vibracell 750 W, 20 kHz) for 20 min in sequential pulses of 10 s of active vibration and 10 s of time-out, using a 13 mm tip operated at 50% amplitude.

The resulting solids were dried overnight at 60 °C generating the ZnO/SiO_2-organoclay samples, which were finally heated to 500 °C for 2 h in N_2 and 4 h in air, in order to get the desired ZnO/SiO_2-clay heterostructures. The resulting samples were denoted as ZnO/SiO_2-CLO, ZnO/SiO_2-TSM and ZnO/SiO_2–SEP for the Cloisite®, Tunisian clay and sepiolite based materials respectively.

Characterization of the solids

Powder X-ray diffraction (XRD) diagrams were obtained on a Bruker D8 ADVANCE diffractometer using monochromatic Cu Kα radiation, scanning from 2 to 70° in 2θ degrees with steps of 0.02 degrees. The average size of the crystallites was calculated by using the Debye–Scherrer formula [33]. Fourier transform infrared spectroscopy (FTIR) was performed in a Bruker IFS 260 66v/S spectrophotometer. The samples were prepared as pellets in KBr, in the case of smectite-based materials, or as pure products, in the case of sepiolite-based materials, and the spectra were recorded in the 4000–250 cm^{-1} wavenumber range with 2 cm^{-1} resolution. Transmission electron microscopy (TEM) images were taken using a JEOL 2100F STEM microscopy, operating at 200 kV equipped with an EDX (INCA x-sight of Oxford Instruments) detector for semiquantitative analysis. The specimens for TEM were prepared by putting the as-grown products in ethanol and immersing them in an ultrasonic bath for 15 min, then dropping a few drops of the resulting suspension containing the synthesized materials onto the TEM grid. The morphology of the samples was examined by field-emission scanning electron microscopy (FE-SEM), using a FEI microscope NOVA NanoSEM 230 model coupled to an EDAX Apollo SDD microanalysis system. For visualization, the particle samples were adhered on a carbon tap for direct observation without applying any conductive coating on their surface. Solid-state ^{29}Si MAS-NMR spectra were collected on a Bruker Avance 400 spectrometer operating at 79.49 MHz in samples spun at 10 kHz, using a single-pulse sequence of 4.5 and 6 μs recycle delay between accumulations and nearly 3000 accumulations. The ^{29}Si chemical shifts were evaluated in relation to tetramethylsilane.

Nitrogen adsorption/desorption isotherms at −196 °C were obtained in a Micromeritics ASAP 2010 analyzer. Before measurement, the samples (150–200 mg) were outgassed under dynamic vacuum for 12 h at 120 °C. The BET specific surface area was calculated from the nitrogen adsorption data in the relative pressure range of 0.05 to 0.2. The external surface area and micropore volume values were achieved by means of the t-plot method according to De Boer's procedure [34], and the pore volume (V_p) was evaluated from the volume adsorbed at $P/P_0 = 0.99$ in the desorption branch of the corresponding isotherm.

Photocatalytic activity

Photocatalytic activity of the prepared ZnO/SiO_2-clay heterostructures was evaluated from degradation of MB and ibuprofen in water, using custom-made equipment. A 300 W UV lamp (Osram Ultra Vitalux E27, 240 V, 300 W, UVA/UVB) with the strongest emission at 354 nm was used as light source and placed above a glass reactor at a distance of 10 cm. Water was circulated through the reactor jacket to ensure a constant temperature of 17 ± 0.5 °C inside the reactor controlled by a thermostatic bath. This temperature below room temperature was chosen to minimize water evaporation.

Batch tests were performed using aqueous solutions of MB and ibuprofen. To a volume of 100 mL containing a $3{\cdot}10^{-5}$ $mol{\cdot}L^{-1}$ MB water solution, were added 20 mg of the ZnO/SiO_2-clay heterostructures photocatalyst, the mixture being stirred in dark for 30 min to allow for the physical absorption of dye molecules on the catalyst particles to reach equilibrium. In the case of ibuprofen, 25 mg photocatalyst were added to 100 mL of a water solution containing 15 $mg{\cdot}L^{-1}$ of ibuprofen, the mixture being stirred in dark overnight. Subsequently, the mixture was poured into the glass reactor to start the photocatalytic degradation tests. In these experiments, the reaction solution under magnetic stirring was placed under the UV lamp. The photocatalytic activity of the prepared photocatalyst was compared to that of synthetic ZnO NP under the same conditions. The concentration of MB was determined by measuring the absorption intensity at the maximum absorbance wavelength of MB (663 nm) and ibuprofen (222 nm) by using a UV–vis 2401 PC Shimadzu spectrophotometer. The percentage of the dye degradation was defined as: degradation (%) = $(C_0 - C)/C_0 \times 100$, where C_0 is the initial concentration of MB and C is the residual concentration of MB at varying intervals of UV irradiation [35].

Acknowledgements

The authors thank the CSIC (i-COOP+ project COOPA20077) and the MINECO (project MAT2012-31759 and MAT2015-71117-R), Spain, and the EU (COST Action MP1202). We also thank Dr. C. Belver for valuable discussions of the results as well as Mr. A. Valera (ICMM-CSIC) and Dr. L. Pascual (ICP-CSIC) for technical assistance with the FE-SEM and TEM studies, respectively, and Mr. R. Barrios (ICMM-CSIC) for technical support in the gas adsorption measurements.

References

1. Hariharan, C. *Appl. Catal., A* **2006,** *304,* 55–61. doi:10.1016/j.apcata.2006.02.020
2. Pauporté, T.; Rathouský, J. *J. Phys. Chem. C* **2007,** *111,* 7639–7644. doi:10.1021/jp071465f
3. Daneshvar, N.; Rasoulifard, M. H.; Khataee, A. R.; Hosseinzadeh, F. *J. Hazard. Mater.* **2007,** *143,* 95–101. doi:10.1016/j.jhazmat.2006.08.072

4. Daneshvar, N.; Salari, D.; Khataee, A. R. *J. Photochem. Photobiol., A* **2004,** *162,* 317–322. doi:10.1016/S1010-6030(03)00378-2
5. Dindar, B.; Içli, S. *J. Photochem. Photobiol., A: Chem.* **2001,** *140,* 263–268. doi:10.1016/S1010-6030(01)00414-2
6. Lizama, C.; Freer, J.; Baeza, J.; Mansilla, H. D. *Catal. Today* **2002,** *76,* 235–246. doi:10.1016/S0920-5861(02)00222-5
7. Wang, Z. L. *J. Phys.: Condens. Matter* **2004,** *16,* 829–858. doi:10.1088/0953-8984/16/25/R01
8. Khaorapapong, N.; Khumchoo, N.; Ogawa, M. *Mater. Lett.* **2011,** *65,* 657–660. doi:10.1016/j.matlet.2010.11.052
9. Khumchoo, N.; Khaorapapong, N.; Ogawa, M. *Appl. Clay Sci.* **2015,** *105–106,* 236–242. doi:10.1016/j.clay.2015.01.001
10. Aranda, P.; Belver, C.; Ruiz-Hitzky, E. Clays and Materials. In *CMS Workshop Lectures Series;* Drummy, L. F., Ed.; Clay Minerals Society: Chantilly, VA, USA, 2014; Vol. 18, pp 21–40.
11. Letaief, S.; Ruiz-Hitzky, E. *Chem. Commun.* **2003,** 2996–2997. doi:10.1039/B310854F
12. Letaïef, S.; Martín-Luengo, M. A.; Aranda, P.; Ruiz-Hitzky, E. *Adv. Funct. Mater.* **2006,** *16,* 401–409. doi:10.1002/adfm.200500190
13. Lagaly, G.; Ogawa, M.; Dékány, I. *Dev. Clay Sci.* **2013,** *5,* 435–505.
14. Ruiz-Hitzky, E.; Aranda, P. *J. Sol-Gel Sci. Technol.* **2014,** *70,* 307–316. doi:10.1007/s10971-013-3237-9
15. Rhouta, B.; Bouna, L.; Maury, F.; Senocq, F.; Lafont, M. C.; Jada, A.; Amjoud, M.; Daoudi, L. *Appl. Clay Sci.* **2015,** *115,* 260–265. doi:10.1016/j.clay.2015.04.024
16. Rhouta, B.; Bouna, L.; Maury, F.; Senocq, F.; Lafont, M. C.; Jada, A.; Amjoud, M.; Daoudi, L. *Appl. Clay Sci.* **2015,** *115,* 266–274. doi:10.1016/j.clay.2015.04.025
17. Gómez-Avilés, A.; Aranda, P.; Fernandes, F. M.; Belver, C.; Ruiz-Hitzky, E. *J. Nanosci. Nanotechnol.* **2013,** *13,* 2897–2907. doi:10.1166/jnn.2013.7429
18. Belver, C.; Aranda, P.; Ruiz-Hitzky, E. *J. Mater. Chem. A* **2013,** *1,* 7477–7487. doi:10.1039/c3ta01686b
19. Belver, C.; Aranda, P.; Martín-Luengo, M. A.; Ruiz-Hitzky, E. *Microporous Mesoporous Mater.* **2012,** *147,* 157–166. doi:10.1016/j.micromeso.2011.05.037
20. Manova, E.; Aranda, P.; Martín-Luengo, M. A.; Letaïef, S.; Ruiz-Hitzky, E. *Microporous Mesoporous Mater.* **2010,** *131,* 252–260. doi:10.1016/j.micromeso.2009.12.031
21. Aranda, P.; Kun, R.; Martin-Luengo, M. A.; Letaïef, S.; Dékány, I.; Ruiz-Hitzky, E. *Chem. Mater.* **2008,** *20,* 84–91. doi:10.1021/cm702251f
22. Akkari, M.; Aranda, P.; Ben Rhaiem, H.; Ben Haj Amara, A.; Ruiz-Hitzky, E. *Appl. Clay Sci.* **2016,** *131,* 131–139. doi:10.1016/j.clay.2015.12.013
23. Rouquerol, F.; Rouquerol, J.; Sing, K. *Adsorption by Powders and Porous Solids: Principles, Methodology and Applications;* Academic Press: London, UK, 1999.
24. Fernandes, F. M.; Manjubala, I.; Ruiz-Hitzky, E. *Phys. Chem. Chem. Phys.* **2011,** *13,* 4901–4910. doi:10.1039/C0CP00882F
25. Sanz, J. *Dev. Clay Sci.* **2006,** *1,* 919–938. doi:10.1016/S1572-4352(05)01033-0
26. Letaief, S.; Liu, Y.; Detellier, C. *Can. J. Chem.* **2011,** *89,* 280–288. doi:10.1139/V10-142
27. Ahlrichs, J. L.; Serna, J. C.; Serratosa, J. M. *Clays Clay Miner.* **1975,** *23,* 119–124. doi:10.1346/CCMN.1975.0230207
28. Fatimah, I.; Wang, S.; Wulandari, D. *Appl. Clay Sci.* **2011,** *53,* 553–560. doi:10.1016/j.clay.2011.05.001
29. Sohrabnezhad, S.; Seifi, A. *Appl. Surf. Sci.* **2016,** *386,* 33–40. doi:10.1016/j.apsusc.2016.05.102
30. Choina, J.; Bagabas, A.; Fischer, C.; Flechsig, G.-U.; Kosslick, H.; Alshammari, A.; Schulz, A. *Catal. Today* **2015,** *241,* 47–54. doi:10.1016/j.cattod.2014.05.014
31. Letaïef, S.; Casal, B.; Kbir-Ariquib, N.; Trabelsi-Ayadi, M.; Ruiz-Hitzky, E. *Clay Miner.* **2002,** *37,* 517–529. doi:10.1180/0009855023730050
32. Ruiz-Hitzky, E. *J. Mater. Chem.* **2001,** *11,* 86–91. doi:10.1039/b003197f
33. Cullity, B. D. *Elements of X-Ray Diffraction;* Addison-Wesley: Reading, MA, USA, 1978; p 102.
34. Lippens, B. C.; de Boer, J. H. *J. Catal.* **1965,** *4,* 319–323. doi:10.1016/0021-9517(65)90307-6
35. Dai, X.-J.; Luo, Y.-S.; Zhang, W.-D.; Fu, S.-Y. *Dalton Trans.* **2010,** *39,* 3426–3432. doi:10.1039/b923443h

License and Terms

BEILSTEIN JOURNAL OF NANOTECHNOLOGY

Intercalation and structural aspects of macroRAFT agents into MgAl layered double hydroxides

Dessislava Kostadinova[1,2], Ana Cenacchi Pereira[3], Muriel Lansalot[3], Franck D'Agosto[3], Elodie Bourgeat-Lami[3], Fabrice Leroux[1,2], Christine Taviot-Guého[1,2], Sylvian Cadars[4] and Vanessa Prevot[*1,2]

Full Research Paper

Open Access

Address:
[1]Université Clermont Auvergne, Université Blaise Pascal, Institut de Chimie de Clermont-Ferrand, BP 10448, F-63000 Clermont-Ferrand, France, [2]CNRS, UMR 6296, ICCF, F-63171 Aubière, France, [3]Univ Lyon, Université Claude Bernard Lyon 1, CPE Lyon, CNRS 5265, Chemistry, Catalysis, Polymers and Processes (C2P2), 43 Bvd du 11 Novembre 1918, 69616 Villeurbanne, France and [4]Institut des Matériaux Jean Rouxel (IMN) - UMR6502, 2 rue de la Houssinière, BP32229 44322 Nantes cedex 3, France

Email:
Vanessa Prevot* - vanessa.prevot@univ-bpclermont.fr

* Corresponding author

Keywords:
hybrid materials; hydrophilic copolymers; intercalation; layered double hydroxides; RAFT; solid-state NMR

Beilstein J. Nanotechnol. **2016,** *7,* 2000–2012.
doi:10.3762/bjnano.7.191

Received: 14 September 2016
Accepted: 06 December 2016
Published: 15 December 2016

This article is part of the Thematic Series "Hybrid nanomaterials: from the laboratory to the market".

Guest Editor: A. Taubert

Abstract

Increasing attention has been devoted to the design of layered double hydroxide (LDH)-based hybrid materials. In this work, we demonstrate the intercalation by anion exchange process of poly(acrylic acid) (PAA) and three different hydrophilic random copolymers of acrylic acid (AA) and *n*-butyl acrylate (BA) with molar masses ranging from 2000 to 4200 g mol^{-1} synthesized by reversible addition-fragmentation chain transfer (RAFT) polymerization, into LDH containing magnesium(II) and aluminium(III) intralayer cations and nitrates as counterions (MgAl-NO_3 LDH). At basic pH, the copolymer chains (macroRAFT agents) carry negative charges which allowed the establishment of electrostatic interactions with the LDH interlayer and their intercalation. The resulting hybrid macroRAFT/LDH materials displayed an expanded interlamellar domain compared to pristine MgAl-NO_3 LDH from 1.36 nm to 2.33 nm. Depending on the nature of the units involved into the macroRAFT copolymer (only AA or AA and BA), the intercalation led to monolayer or bilayer arrangements within the interlayer space. The macroRAFT intercalation and the molecular structure of the hybrid phases were further characterized by Fourier transform infrared (FTIR) and solid-state ^{13}C, ^{1}H and ^{27}Al nuclear magnetic resonance (NMR) spectroscopies to get a better description of the local structure.

Introduction

Within the emergence of a wide range of organic–inorganic hybrid materials with interesting physical and chemical properties [1], hybrid layered double hydroxides (LDH) have attracted considerable attention in the scientific community [2,3]. LDH matrices are layered materials which can be described by the general formula $[M(II)_{1-x}M(III)_x(OH)_2]$ $[A^{n-}_{x/n}mH_2O]$ that clearly evidences the highly tunable LDH chemical composition depending on the layer cations and the interlayer anions [4]. Owing to their anion exchange capacity, LDH can accommodate in their interlamellar domain a large variety of negatively charged molecular organic species with different functional properties. This opens the way to a wide range of applications such as anion scavengers, adsorbents, heterogeneous catalysts, supports for species of interest in nanomedicine and fillers in polymer matrices [5-7]. For instance, hybrid LDH involving amino acids, peptides, nucleosides, nucleic acids [8-10], biopolymers [11,12] and various drugs [13-15] were investigated to develop efficient systems for therapeutic applications [16,17]. Various dyes (sulfonated spyrospiran, methyl orange, fluorescein pigment red, …) [18,19] were confined by intercalation within LDH for applications as pigments or studies in photophysics or photochromism. Due to their high aspect ratio, their layered feature extended to the nanoscale and their hydroxylated surface, LDH are also particularly interesting for fabricating polymer nanocomposites [20-23]. To favor the dispersion of LDH platelets into polymers, hybrid surfactant (usually dodecyl sulphate)-intercalated LDH were prepared and incorporated into polymer matrices such as polyethylene [24], polypropylene [25], poly(methyl methacrylate) [26], elastomers [27], epoxy polymers [28], poly(ε-caprolactone) [29], polyesters [30], polyurethane [31] and polyimide [21]. Alternatively, Leroux et al. described the preparation of a hybrid LDH phase intercalated by an anionic polymerizable surfactant acting further as an anchor that compatibilizes the inorganic LDH with the polymer matrix during the polymerization [32]. Water soluble macromolecules such as poly(vinyl alcohol), poly(acrylic acid) (PAA), poly(styrene sulfonate) were also intercalated into the layered structure to avoid the use of surfactant molecules which can alter nanocomposite properties [33,34]. To design polymer-intercalated LDH hybrid materials, an elegant alternative consists in performing in situ polymerization of monomer-intercalated LDH. Such approach was applied for instance to make LDH intercalated with vinyl benzene sulfonate [33,35], acrylate anion [10,36,37], sulfopropyl methacrylate [38], or aniline derivative monomers [39]; the polymerization being subsequently induced either by moderate thermal treatment, by initiator addition or thanks to the oxidative LDH layer properties. Localizing the polymerization into the layers of LDH can also be performed by attaching an initiator or a controlling agent and further conduct a free radical polymerization [40,41]. Qu et al. [42] applied the latter strategy by adsorbing 4-(benzodithioyl)-4-cyanopentanoate controlling agent and successfully conducting styrene reversible addition-fragmentation chain transfer (RAFT) polymerization [43] in the LDH matrix. This resulted in an exfoliated LDH/polystyrene nanocomposite with a good control of the molar mass of the polystyrene chains.

Recently, we reported that highly stable dispersions at elevated macroRAFT copolymer concentrations [44] could be obtained by adsorbing statistical copolymers of acrylic acid (AA) and *n*-butyl acrylate (BA) (P(AA-*stat*-BA)) of low molar mass (1800 g mol^{-1}) synthesized by RAFT polymerization onto MgAl LDH. In this work, we focus on the possibility to design functional hybrid LDH phases by direct intercalation of similar pre-synthesized macroRAFT agents displaying molar masses in the range of 2000–4200 g mol^{-1}. PAA and three copolymers composed of AA and BA units obtained by RAFT were designed to interact with the LDH layers after deprotonation of the AA units at neutral pH. The assembly between these macroRAFT polymers and the LDH layers was investigated using an anionic exchange process and the resulting hybrid materials were thoroughly characterized by a set of solid-state characterization techniques including powder X-ray diffraction (PXRD), transmission and scanning electron microscopy (TEM and SEM, respectively), Fourier transform infrared (FTIR) spectroscopy and solid-state ^{13}C, ^{1}H and ^{27}Al nuclear magnetic resonance (NMR) measurements. A particular attention was paid to the macromolecular anion arrangement into the LDH interlayer domain.

Results and Discussion

MacroRAFT (co)polymers denoted PAA_n-CTPPA and P(AA_n-*stat*-BA_n)-CTPPA (see Table 1) were synthesized by RAFT (co)polymerization of AA and BA in 1,4-dioxane at 80 °C using 4-cyano-4-thiothiopropylsulfanyl pentanoic acid (CTPPA) as RAFT agent and 4,4'-azobis(4-cyanopentanoic acid) (ACPA) as an initiator.

These macroRAFT agent compositions were selected with AA units promoting electrostatic interaction with the LDH and BA units to investigate the effect of the insertion of butyl hydrophobic units on the hybrid LDH material structure (Figure 1).

In using AA as hydrophilic monomer, a macroRAFT polymer containing 49 AA units was obtained (M_n = 3800 g mol^{-1}; $Đ$ = 1.18). During the copolymerization of AA and BA, both monomers were converted at the same rate and were therefore incorporated statistically with negligible composition drift. Well-defined copolymers were obtained with on average 8.5,

Table 1: Characteristics of the macroRAFT agents synthesized in this work.

macroRAFT	DP_n[a]	M_n (g·mol^{-1})	Charge$^-$/mol	Abbreviation
PAA-CTPPA	49	3800	50	PAA_{49}-CTPPA
P(AA-*stat*-BA)-CTPPA	8.5/8.5	2000	9.5	P($AA_{8.5}$-*stat*-$BA_{8.5}$)-CTPPA
P(AA-*stat*-BA)-CTPPA	14.5/14.5	3200	15.5	P($AA_{14.5}$-*stat*-$BA_{14.5}$)-CTPPA
P(AA-*stat*-BA)-CTPPA	19.5/19.5	4200	20.5	P($AA_{19.5}$-*stat*-$BA_{19.5}$)-CTPPA

[a]Number-average degree of polymerization.

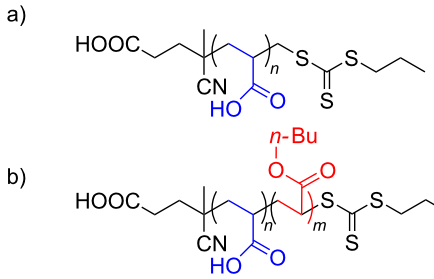

Figure 1: Chemical structures of the macroRAFT agents synthesized in this work: a) PAA_n-CTPPA and b) P(AA_n-*stat*-BA_n)-CTPPA.

14.5 and 20.5 units of each monomer per chain (M_n = 2000; 3200 and 4200 g mol^{-1}) and a narrow molar mass distribution ($Đ$ = 1.1 ± 0.1). The macroRAFT (co)polymers were neutralized at pH 8 before use, which induced the presence of negative charges on the chains due to the deprotonation of the AA units and of the carboxylic acid end group of CTPPA, leading to 50, 9.5, 15.5 and 19.5 negative charges per mole for PAA_{49}-CTPPA, P($AA_{8.5}$-*stat*-$BA_{8.5}$)-CTPPA, P($AA_{14.5}$-*stat*-$BA_{14.5}$)-CTPPA and P($AA_{19.5}$-*stat*-$BA_{19.5}$)-CTPPA, respectively.

The hybrid LDH materials were prepared through anion exchange at room temperature from MgAl-NO_3 LDH precursor obtained by fast precipitation followed by moderate hydrothermal treatment. Chemical analysis performed on the different samples (Table 2) showed similar Mg/Al ratios, confirming that the layer structure was hardly affected by the anion exchange process.

Compared to the XRD pattern of the LDH precursor (Figure 2) displaying characteristic diffraction lines of a MgAl-NO_3 phase with a basal spacing of 0.85 nm, a net shift of the 00*l* harmonic

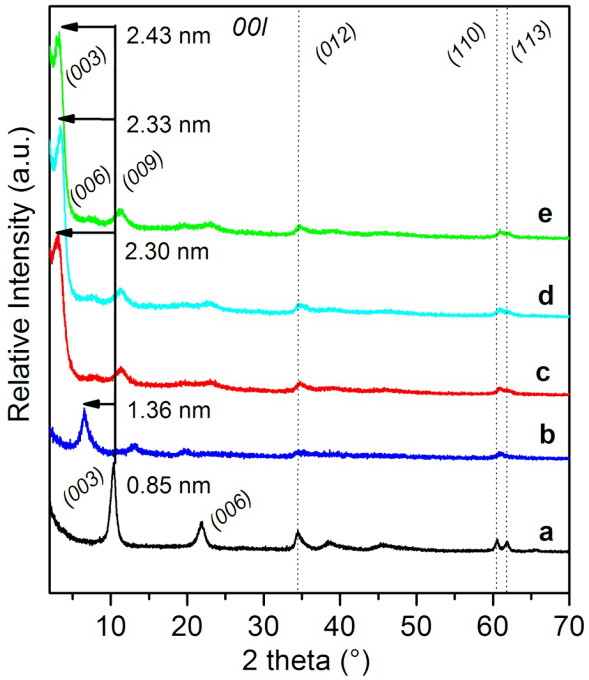

Figure 2: PXRD patterns of: (a) MgAl-NO_3 LDH and (b–e) macroRAFT agent-intercalated LDH obtained by anion exchange in presence of (b) PAA_{49}-CTPPA, (c) P($AA_{8.5}$-*stat*-$BA_{8.5}$)-CTPPA, (d) P($AA_{14.5}$-*stat*-$BA_{14.5}$)-CTPPA and (e) P($AA_{19.5}$-*stat*-$BA_{19.5}$)-CTPPA. The solid line indicates the position of the first 003 reflection in the pristine MgAl-NO_3 LDH, and the arrows indicate the shift of this reflection due to polymer intercalation.

Table 2: Characteristics of the MgAl-NO_3 LDH precursor and of the hybrid macroRAFT agent-intercalated LDH.

Interlayer anion	d_{003} nm	d_{110} nm	a[a] nm	c[a] nm	Mg/Al EDX	ζ mV
NO_3	0.85	0.152	0.304	2.40	2.8	43
PAA_{49}-CTPPA	1.36	0.152	0.304	4.08	2.7	−49
P($AA_{8.5}$-*stat*-$BA_{8.5}$)-CTPPA	2.326	0.152	0.304	6.90	2.8	−51
P($AA_{14.5}$-*stat*-$BA_{14.5}$)-CTPPA	2.331	0.152	0.304	6.99	2.8	−53
P($AA_{19.5}$-*stat*-$BA_{19.5}$)-CTPPA	2.328	0.152	0.304	7.29	2.8	−51

[a]Considering a R-3m space group.

reflections to lower values of 2θ below 20° was observed for the LDH-macroRAFT compounds, which is consistent with the replacement of nitrate ions by larger anionic species ensuring the layer surface charge neutralization. For PAA_{49}-CTPPA, this modification corresponds to an increase of the interlamellar distance from 0.85 nm to 1.36 nm. This interlamellar distance is similar to that reported in the literature for acrylate anion intercalated LDH and slightly higher than the value obtained for hybrid PAA-intercalated phases formed by in situ free radical polymerization of intercalated AA [37], which can be tentatively attributed to the presence of the CTPPA RAFT end group on the PAA macromolecule. If we consider a layer thickness of 0.21 nm and two hydrogen bond distances between the macromolecule and two adjacent LDH layers (2 × 0.27 nm), the interslab available for the PAA_{49}-CTPPA corresponds to 0.6 nm, and indicates an orientation of the macromolecules as a monolayer with the carboxylate groups interacting with the positive adjacent inorganic layers (Figure 3a).

The intercalation of P(AA-*stat*-BA)-CTPPA copolymers led to a larger basal spacing ranging from 2.32 to 2.33 nm, regardless of their molar mass (Table 2). This indicates that the copolymer molar mass did not strongly affect the intercalation and the interlayer arrangement of the macromolecules in between the LDH layers. The crystallinity of the samples was quite low leading to poorly defined X-ray diffraction lines. However, using the Le Bail method (see Supporting Information File 1), we were able to properly reproduce the profile shapes and widths of the reflections and therefore to extract the intensity of the 00*l* diffraction lines reflection, allowing then the calculation of the one-dimensional electron density distribution along the *c*-stacking axis $\rho_{(z)}$. As demonstrated elsewhere, this approach can provide valuable information on the structure of the interlayer space [45]. In the present case, up to 8 isolated 00*l* reflections are expected at low 2θ (<32°) related to the large value of the interlayer distance $d_{003} \approx 2.33$ nm and assuming a 3R polytype. Due to the close resemblance of the XRD patterns of P(AA-*stat*-BA)-CTPPA intercalates, the Le Bail analysis led to similar values of the unit cell parameters whatever the molar mass of the copolymer (Table 2), and the extracted intensities of the 00*l* diffraction lines were also found very similar. We therefore assume identical interlayer arrangements such as the one that can be deduced from the 1D plot of MgAl-P($AA_{8.5}$-*stat*-$BA_{8.5}$)-CTPPA and presented in Figure 3b. The peaks observed match perfectly with a bilayer arrangement of the copolymers. The two most intense peaks are due to the hydroxide layers containing Mg/Al cations. The carboxylate groups from the AA units and the end group of CTPPA would cause maxima at the outer parts of the interlayer space at a distance of ≈0.39 nm from the center of the hydroxide layers which is consistent with hydrogen bond interactions between carboxylate and OH groups: C–O· · ·HO–Mg/Al. The second maximum at a distance of ≈0.44 nm from the latter is attributed to both the carboxylate groups in BA units and the thiopropylsulfanyl groups that would be arranged in an aligned configuration. Finally, the small maximum in the center is attributed to the dangling butyl chains of BA units. This peak assignment is supported by the interatomic distances within the molecules and was determined using the ChemBio 3D Ultra chemical structure drawing program. It is noteworthy that the host LDH layers offer a sufficient surface area per unit charge (0.312 nm^2/charge) to accommodate the AA subunit

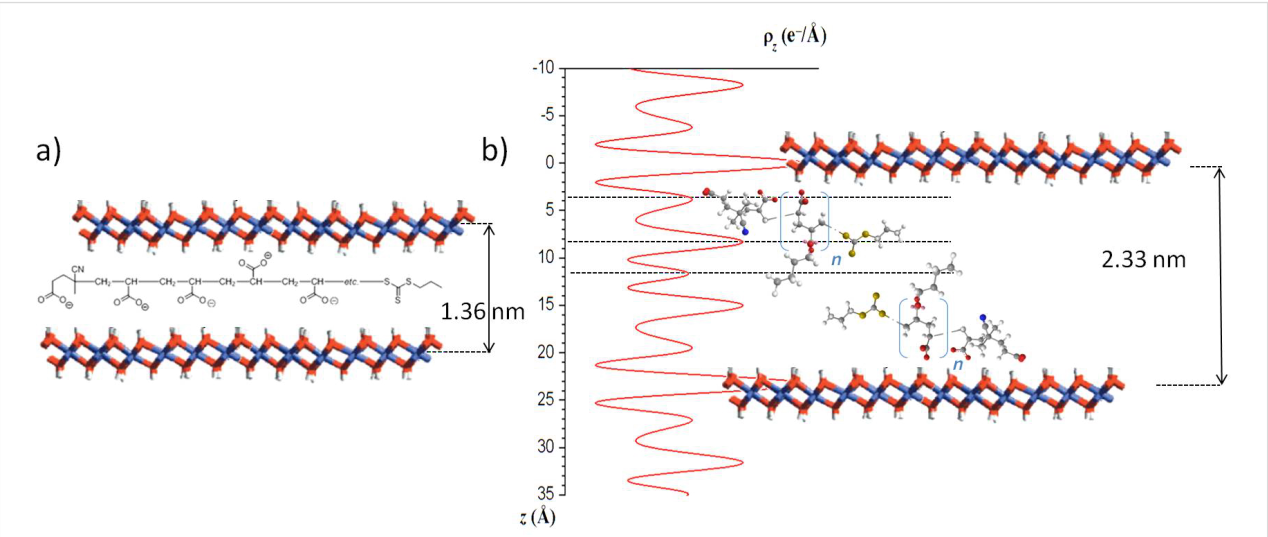

Figure 3: a) Schematic representation of the arrangement of MgAl-PAA_{49}-CTPPA, and b) One-dimensional electron density projection along the *c*-stacking axis $\rho_{(z)}$ determined from the analysis of the intensity of 00l X-ray diffraction lines for MgAl-P($AA_{8.5}$-*stat*-$BA_{8.5}$)-CTPPA and schematic representation of the macromolecule into the LDH interlayer domain.

(0.06 nm^2/e) and AA-BA subunit (0.34 nm^2/e) in the idealistic model proposed in Figure 3.

FTIR spectroscopy further confirmed the presence of the macromolecules within the hybrid compounds. The main band assignations are gathered in Table 3.

As expected, all the FTIR spectra of the prepared compounds (Figure 4) exhibit the LDH characteristic bands [46] in particular those at 3700–3200 and 1647 cm^{-1} attributed to the stretching vibration of OH groups in the LDH layers and the stretching and bending mode of the water molecules, respectively.

In the low wavenumber region, the bands at 783, 651, 558 and 453 cm^{-1} can be attributed to the O–M–O and M–O vibration bands in the brucite-like layers. MacroRAFT (co)polymer intercalation was further confirmed by FTIR due to the intensity decrease of the nitrate vibration band at 1350 cm^{-1} (Figure 4), and the increasing intensities of new vibrations in both the 2961–2877 cm^{-1} region (νCH_3, νCH_2, νCH) and the 1750–1150 cm^{-1} region ($\nu C{-}O$, $\nu C{=}O$). For the PAA_{49}-CTPPA-intercalated LDH, the shift of the OH vibration band at 3346 cm^{-1} in comparison with the precursor phase could traduce a modification of the hydrogen bond network in the interlayer domain due to macroRAFT polymer intercalation evidenced by the presence of the typical vibration of the carboxylate (ν_{as} and ν_s). In the case of P(AA-*stat*-BA)-CTPPA copolymers, the nitrate vibration band is also replaced by the C–H, C=S, C=O, COO– stretching and bending modes of the macromolecules (Table 3).

As previously reported for macroRAFT copolymers adsorption onto LDHs [44], polymer intercalation systematically led to an inversion of the surface charges with ζ potential values close to

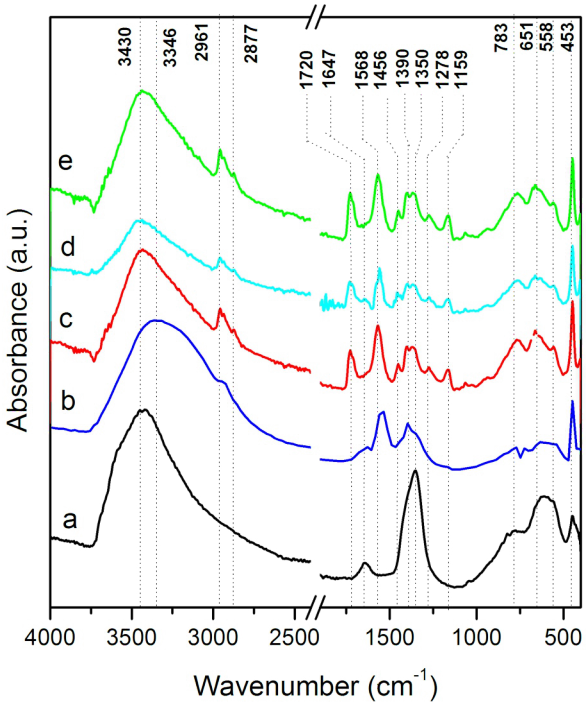

Figure 4: FTIR spectra of: a) pristine MgAl-NO_3 and macroRAFT agent-intercalated LDHobtained by anion exchange in presence of b) PAA_{49}-CTPPA, c) P($AA_{8.5}$-*stat*-$BA_{8.5}$)-CTPPA, d) P($AA_{14.5}$-*stat*-$BA_{14.5}$)-CTPPA and e) P($AA_{19.5}$-*stat*-$BA_{19.5}$)-CTPPA.

−51 mV compared to the positive value of +43 mV measured for the MgAl-NO_3 LDH precursor. This clearly evidences a modification of the particle surface through intercalation/adsorption phenomena. Interestingly, such a chemical and surface modification of LDH through anion exchange did not modify the particle shape and aggregation as evidenced by FESEM analysis (Figure 5). The different hybrid LDH compounds display similar platelet-like particle shapes aggregated in a house of cards morphology by edge-to-face associations.

Table 3: Attribution of the main vibration bands of pristine and hybrid LDH phases.

MgAl-NO_3	MgAl-PAA_{49}-CTPPA	MgAl-P(AA_n-*stat*-BA_n)-CTPPA	Attribution
3430	3346	3430	ν OH
	2936	2961, 2932, 2877	νCH_3, νCH_2, νCH
		1720	νC=O (ester)
1647	1647	1647	δH_2O
	1547, 1390	1568, 1390	ν_{as}, ν_s –COO–
		1456	δCH_2, δCH_3
1350	1350	1350	νNO_3
		1278, 1159	νC–O (ester)
		1068	νC=S
783, 651, 558	783, 651, 558	783, 651, 558	ν_{M-O}
453	453	453	δ_{O-M-O}

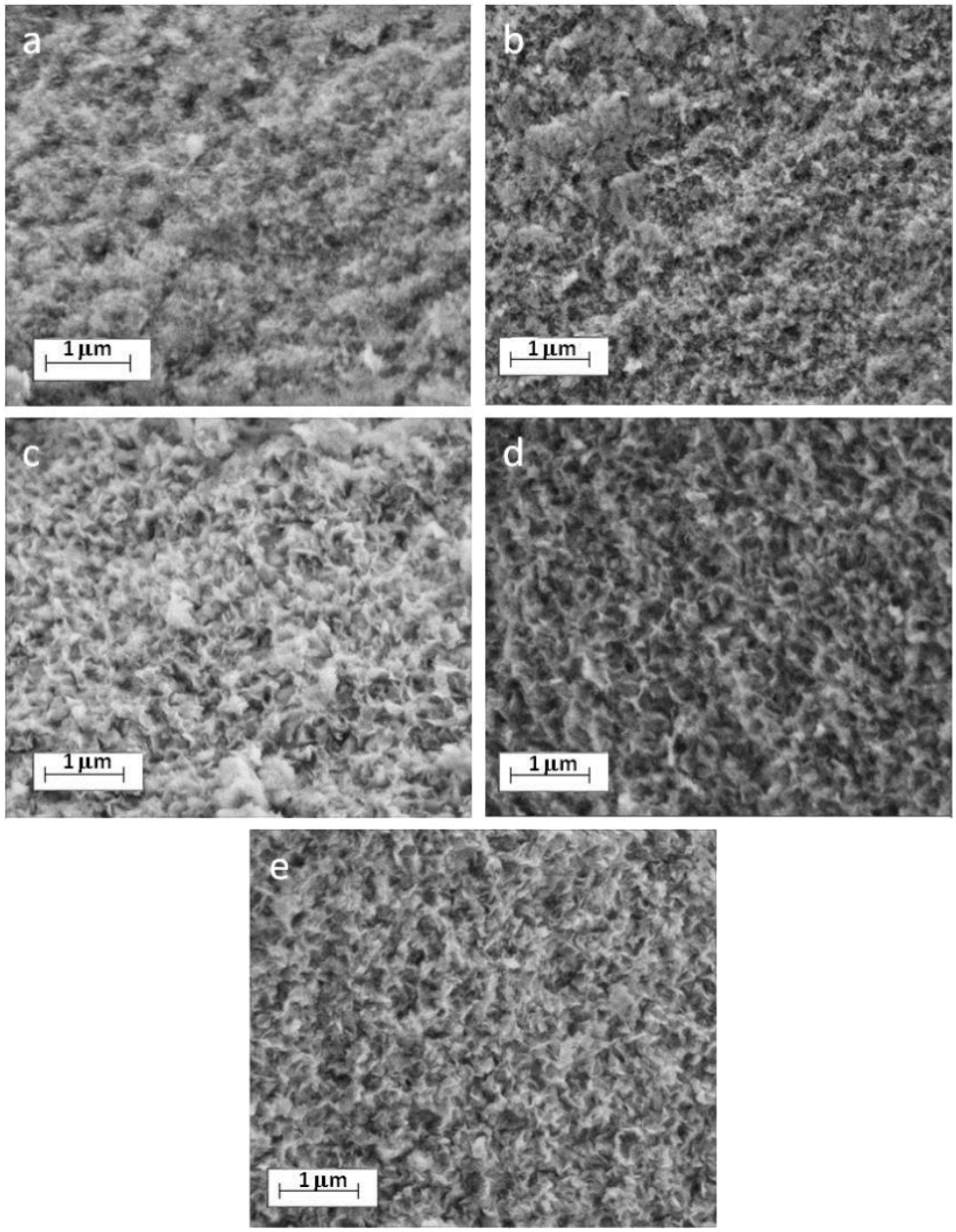

Figure 5: FESEM images of: a) pristine MgAl-NO_3 LDH and macroRAFT agent-intercalated LDH obtained by anion exchange in presence of: b) PAA_{49}-CTPPA, c) P($AA_{8.5}$-*stat*-$BA_{8.5}$)-CTPPA, d) P($AA_{14.5}$-*stat*-$BA_{14.5}$)-CTPPA and e) P($AA_{19.5}$-*stat*-$BA_{19.5}$)-CTPPA.

To get further insight into the interaction between the macroRAFT (co)polymer and the LDH layer within the hybrid phases, solid state NMR experiments were also performed. One-dimensional (1D) ^{13}C quantitative and $^{13}C\{^1H\}$ CP-MAS NMR spectra of the P(AA_n-*stat*-BA_n)-CTPPA materials are presented in Figure 6c–f along with similar spectra collected for PAA_{49}-CTPPA (Figure 6a,b).

Comparisons of the spectra obtained for these two types of materials make it possible to distinguish and identify carbonyl signals from the AA and the BA units at 182 and 176 ppm, respectively. Higher shift of the AA carbonyl as compared to the BA carbonyl signal is consistent with stronger deshielding of the ^{13}C nuclei due to the hydrogen bonding between C–O- and the LDH OH groups, which pulls electrons further away from the carbon, as compared to the butyl chain. In contrast with the PAA_{49}-CTPPA system, where spectral contributions from backbone CH and CH_2 carbon atoms are well distinguished (albeit overlapping), this backbone region is more severely crowded in the P(AA_n-*stat*-BA_n)-CTPPA spectra.

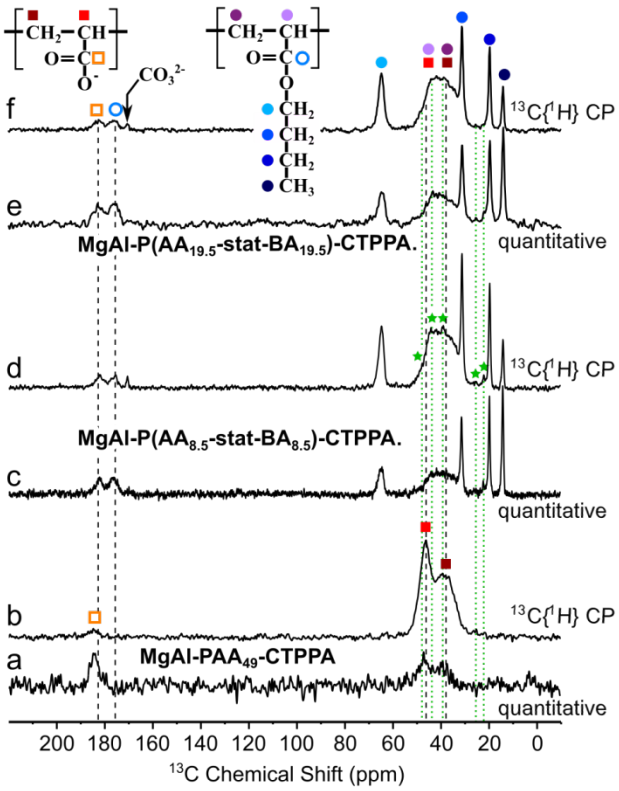

Figure 6: Solid-state ^{13}C NMR spectra of (a,b) MgAl-PAA_{49}-CTPPA; (c,d) MgAl-P($AA_{8.5}$-*stat*-$BA_{8.5}$)-CTPPA and (e,f) MgAl-P($AA_{19.5}$-*stat*-$BA_{19.5}$)-CTPPA. Spectra (a,c,e) are quantitative spin-echo experiments recorded in non-saturating quantitative conditions, whereas (b,d,f) correspond to $^{13}C\{^1H\}$ CP-MAS experiments recorded at short contact time (0.2 ms). Peak assignments are indicated by colored circles and squares for signals attributed to the AA and BA units, respectively. The green stars and dotted lines presumably correspond to C atoms within the terminal fragments of the copolymer.

Attempts to model this spectral region with 4 distinct (Gausso/Lorentzian) contributions, with or without constraints from the PAA_{49}-CTPPA peak positions and/or widths, did not lead to sensible solutions. Best models were obtained with 3 lines, one at ca. 44 ppm attributed to CH groups (both from AA and BA units) and two additional contributions at ca. 39 and ca. 35 ppm representing CH_2 groups, possibly one from AA and the other from BA units. Regardless of the model selected, the full width at half maximum (FWHM) of individual contributions was 5 ppm or more, which seems to indicate a large degree of chain conformational disorder. The comparison of echo-MAS quantitative (Figure 6a,c,e) and $^{13}C\{^1H\}$ CP spectra at short contact time (Figure 6b,d,f) did not show strong contrasts in the relative peak intensities, except for quaternary carbon atom (which were located further away from protons), which indicates homogeneous chain rigidity (or dynamics). There is no evidence, for example, of (co-)polymer domains being less immobilized by weaker interactions with the LDH surface or inter-chain interactions. Importantly, no significant difference can be observed between the AA and BA chain dynamics, except for the butyl group (full blue circles) whose faster re-orientational dynamics are illustrated by the very narrow peak widths of butyl CH_3 (at 14 ppm) and middle-chain CH_2 groups (at 22 and 20 ppm) in comparison with backbone CH_2 groups (ca. 35–40 ppm). The butyl O-CH_2 (at 65 ppm) shows only partial dynamic averaging due to its closer proximity to the more rigid backbone, indicating dynamics of the order of the peak width (ca. 10^3 s^{-1}). In addition, small signals detected at identical positions for different samples and marked with green stars and dotted lines in Figure 6 most likely correspond to some of the C atoms within end-chain fragments of the macro-RAFT agents (see Figure 1). Two-dimensional (2D) ^{13}C–^1H correlation spectra exploiting ^{13}C–^1H proximities were collected to shed light on the ^1H NMR peak assignments and provide further insights into the interactions between the (co)polymer guest and the LDH host. Figure 7 shows two $^{13}C\{^1H\}$ heteronuclear correlation (HETCOR) spectra based on the CP magnetization transfer between ^1H and ^{13}C nuclei, in which cross peaks indicate a spatial proximity between the ^1H and ^{13}C signals at the corresponding frequencies.

The two experiments probe different ranges of ^1H–^{13}C distances by means of different CP contact times: the short contact time (0.25 ms) used in Figure 7a reveals short ^1H–^{13}C dis-

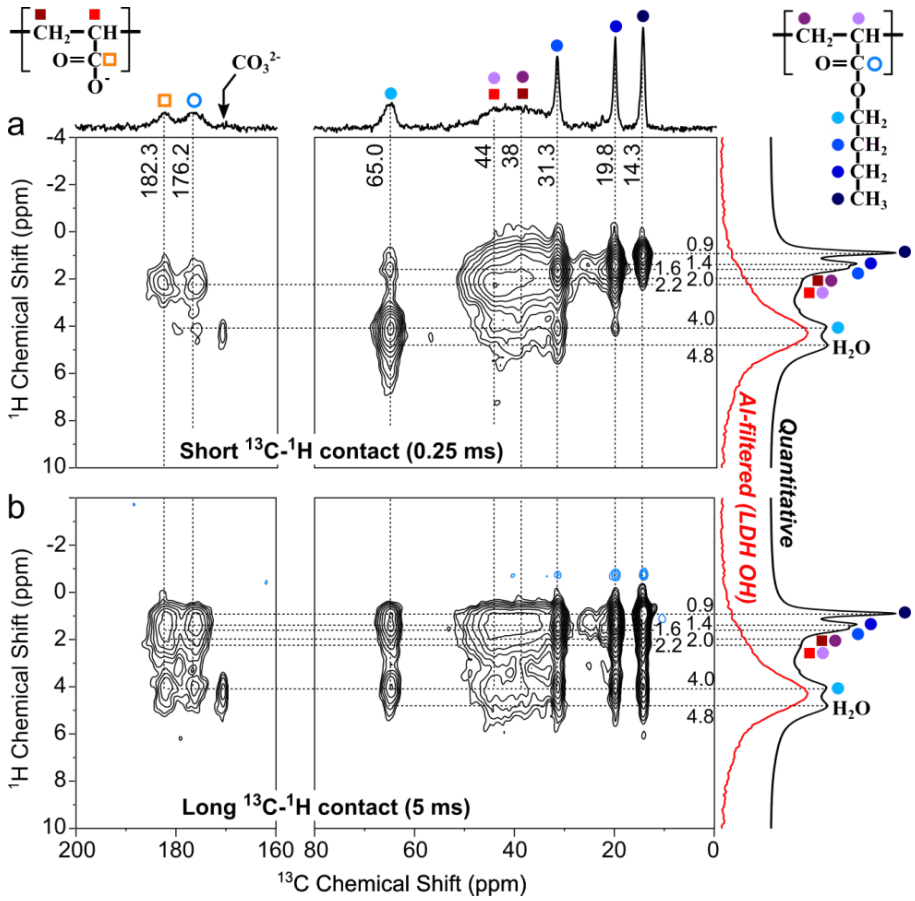

Figure 7: Solid-state ^{13}C{^{1}H} HETCOR NMR spectra of MgAl-P(AA$_{8.5}$-*stat*-BA$_{8.5}$)-CTPPA, and collected at: a) short CP contact time (0.25 ms) to emphasize short ^{1}H–^{13}C proximities (primarily C–H bonds) and b) at long CP contact time (5 ms) to allow magnetization transfer across longer ^{1}H–^{13}C distances. The 1D spectrum on the top is the quantitative ^{13}C echo-MAS spectrum. 1D ^{1}H spectra on the right were collected at fast (60 kHz) MAS to reduce broadening due to ^{1}H–^{1}H interactions: the black spectrum is a quantitative ^{1}H echo-MAS and the red corresponds to a ^{1}H{^{27}Al} CP-MAS experiment selectively probing the LDH OH protons in close proximity to the framework Al sites.

tances: primarily (but not exclusively) C–H bonds, whereas the longer mixing time (5 ms) in Figure 7b is used to establish proximities between more distant ^{1}H and ^{13}C pairs (several Å to ca. 1 nm). The moderate spinning frequency (12 kHz) at which these spectra were collected should in principle yield very low resolution in the ^{1}H dimension due to line broadening caused by dipole–dipole interactions that are too strong to be properly averaged by MAS. However, this is circumvented in the 2D HETCOR spectra by the application of homonuclear ^{1}H decoupling during the ^{1}H evolution period (see details in Experimental). For the same reason, the 2D peak positions in the ^{1}H (vertical) dimension of the 2D spectra are compared to 1D ^{1}H NMR spectra recorded at a faster spinning frequency (60 kHz) and shown on the right side. In both Figure 7a and 7b, the black spectrum corresponds to a quantitative ^{1}H spin-echo experiment, whereas the red spectrum corresponds to a selective detection of ^{1}H nuclei located in close proximity to the ^{27}Al nuclei of the framework LDH host, i.e., primarily from the LDH OH groups, showing a broad peak at ca. 4.3

It was obtained by means of a ^{1}H{^{27}Al} CP-MAS experiment consisting in an excitation of ^{27}Al nuclei followed by a CP transfer allowing through-space magnetization transfer from ^{27}Al to ^{1}H nuclei (via dipole–dipole couplings), for a time sufficiently short (0.5 ms) to selectively probe Al–O–H proximities within the LDH layers. 2D cross-peak positions along the ^{13}C (horizontal) dimension are compared to the quantitative ^{13}C NMR spectrum (same as in Figure 6c).

The cross peaks observed in the ^{13}C{^{1}H} HETCOR spectrum at short contact time (Figure 7a) and the associated increase in resolution facilitate the assignment of the otherwise poorly-resolved ^{1}H (compared to ^{13}C) NMR spectra. Assignment of ^{1}H signals to the different protonated carbons within the copolymer are displayed in Figure 7. Even with this 2D spectrum, the ^{1}H spectra are challenging to analyze due the overlap of the LDH OH signal at ca. 4.3 ppm with the butyl O–CH_2 ^{1}H signal at 4.0 ppm and the water signal at 4.8 ppm. There is also (as in ^{13}C NMR) poor resolution within the backbone AA and BA

CH_2 and CH ^1H signals (at ca. 2 ppm), which furthermore partially overlap with the butyl CH_2 signals at 1.4 and 1.6 ppm. Nevertheless, the slightly tilted shape of the broad backbone correlation peak confirms that the ^{13}C and ^1H regions centered at ca. 44 and 2.2 ppm, respectively, are primarily due to the backbone CH of both AA and BA units. This ^1H frequency indeed also correlates with the attached ^{13}C carbonyl signals, consistent with this assignment. On the other hand, the contribution of ^{13}C signals centered at ca. 38 ppm tends to correlate with a slightly shifted ^1H signal at 2.0 ppm, which can thus be attributed to backbone CH_2 groups of (undifferentiated) AA and BA units.

Despite these difficulties, the spectra can be analyzed in an attempt to gain insights into the (co)polymer interactions with the LDH surface. What we are seeking in particular are correlations between guest ^{13}C nuclei and host hydroxyl protons. Carbonyl groups are expected to be most directly involved in such host–guest interactions. At short contact time (Figure 7a), the corresponding carbons (182 and 176 ppm for AA and BA units, respectively) are primarily found to be in close proximity to the backbone ^1H protons (at 2.2 ppm), with also a small correlation between the BA carbonyl and the butyl O–CH_2-protons. Only the carbonate signal at 171 ppm of the hydrotalcite(-like) impurity shows a clear correlation with the LDH OH groups at 4.2 ppm, in strong contrast with the very small amount of this impurity (less than 0.2% of the total C content). This indicates that host–guest interactions are considerably weaker in the (co)polymer-intercalated LDH material than in hydrotalcite. At longer contact times, correlations appear between the butyl ^1H signals and both the AA and BA carbonyl ^{13}C signals, which confirms the homogeneous (as opposed to segregated) repartition of AA and BA units along the polymer chains, such that most (if not all) AA units are located nearby BA units, permitting magnetization transfer from AA carbonyl ^{13}C to nearby BA butyl protons. Among those, the butyl O–CH_2 (4.0 ppm) ^1H signal unfortunately overlaps with the LDH hydroxyl (4.3 ppm) and consequently prevents unambiguous observation of the spatial proximity between the guest carbonyl and the host hydroxyl groups. The same observations apply to the backbone ^{13}CH and $^{13}CH_2$ signals, which at long contact time also correlate with the butyl signal, similarly preventing the direct observation of a correlation with the LDH OH protons.

An alternative way to more directly probe the interactions between the host LDH and the guest (co)polymer is to selectively create magnetization on the LDH Al site to first transfer it to nearby hydroxyl protons and then let it propagate to more remote protons (including those of the (co)polymer) using the strong ^1H–^1H dipolar couplings. This is done by means of a radio-frequency (rf)-pulse experiment shown in Figure 8a, which contains three main steps labeled 1, 2 and 3 therein. The ^{27}Al magnetization is first created by exciting the LDH framework Al sites (by a pulse on the ^{27}Al channel on Figure 8a). A short (0.5 ms) cross polarization (using rf irradiation on both ^1H and ^{27}Al channels simultaneously) then transfers this magnetization from ^{27}Al to nearby protons, i.e., almost exclusively those of the LDH hydroxyl groups. In a last step, the obtained ^1H magnetization is stored parallel to the external magnetic field axis for a time τ_M to allow this magnetization to diffuse among abundant ^1H nuclei within both the LDH host and the (co)polymer guest. This process occurs through a magnetization exchange mechanism called spin-diffusion that results from ^1H–^1H dipolar interactions (hence the designation of τ_M as "spin-diffusion mixing time"). A final excitation pulse enables the detection of all the ^1H nuclei to which magnetization has

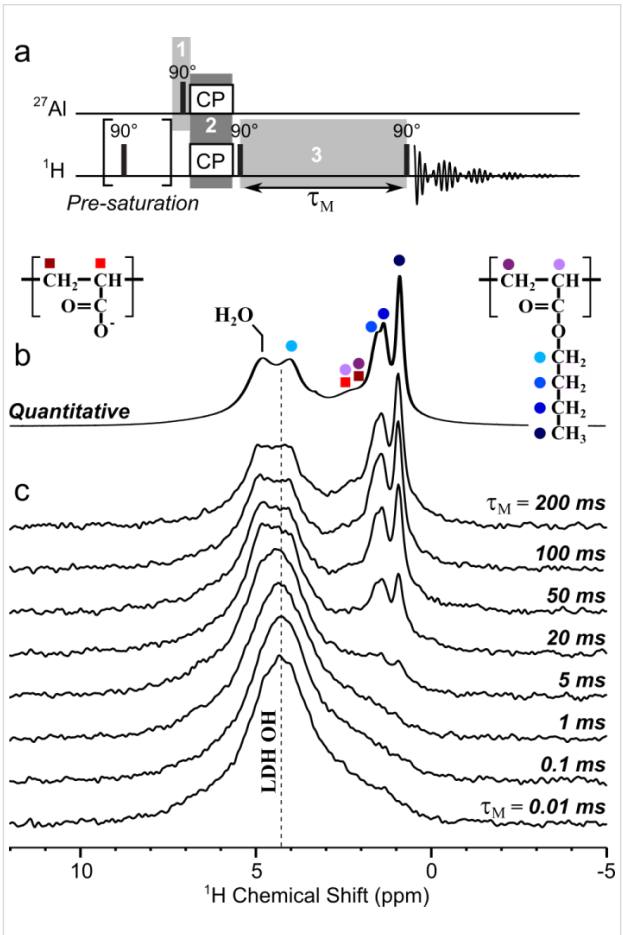

Figure 8: a) Radio-frequency-pulse NMR sequence used to probe LDH/copolymer interactions. Shaded regions labeled 1 to 3 correspond to the main three steps of the experiment, as described in the text. b) Quantitative solid-state ^1H echo-MAS NMR spectrum of MgAl-P($AA_{8.5}$-stat-$BA_{8.5}$)-CTPPA collected at 60 kHz MAS and 17.6 T. c) Series of ^1H MAS NMR spectra collected (in the same conditions as in b)) with the NMR rf-pulse sequence shown in a) using spin-diffusion mixing times τ_M of 0.01 to 200 ms to allow progressive propagation of the magnetization from the selectively-excited LDH OH protons to other nearby protons.

been transferred, depending on their proximity to the initial Al sites (and their connected OH) and the time during which the spin-diffusion processes. Similar approaches have been used to characterize, e.g., surfactants interacting with silica surfaces [47,48].

Figure 8c shows the results of a series of such an experiment conducted using different spin-diffusion mixing times for the P($AA_{8.5}$-*stat*-$BA_{8.5}$)-CTPPA system, at fast MAS and high magnetic field to maximize spectral resolution. These can be compared with the quantitative ^{1}H echo-MAS spectrum collected under the same conditions, shown in Figure 8b (same as shown in black on the right side of Figure 7). At shortest τ_M values (bottom), no significant diffusion of the ^{1}H magnetization occurs, such that the spectrum selectively displays the LDH OH sites, which are located closest to the framework Al atoms (as in the ^{27}Al{^{1}H} CP-MAS spectrum shown in red on the right side of Figure 7).

As the mixing time increases, this initial magnetization propagates to increasingly long distances, which results in the progressive growth of all ^{1}H NMR peaks associated with protons located close enough to the LDH layers, which includes the water signal at 4.8 ppm, the backbone CH and CH_2 protons at 2.2 and 2.0 ppm (respectively), and the butyl CH_2 (4.0, 1.6 and 1.4 ppm) and CH_3 signals (0.9 ppm). Due to the low spectral resolution, it is difficult to tell whether some contributions are appearing before others. In fact the contributions to which slowest diffusion is expected are the mobile butyl protons (since mobility averages down the dipolar interactions), and yet these are the most clearly visible on the spectra because they are (for the same reason) the narrowest. Despite these limitations, it is clear that all ^{1}H signals observed in the quantitative spectrum are indeed located nearby the LDH surface. The fact that we do not observe a particularly faster diffusion to the backbone CH signals (closest to the carbonyl groups) than to the other protons suggests that the interaction of the (co)polymer with the LDH surface is not particularly strong, consistent with the less-efficient CP transfer observed for the (co)polymer than for the residual carbonate (Figure 6 and Figure 7). Again, no clear distinction can be made between the AA and BA units, which is an important common feature of all NMR data reported here for the (co)polymer-intercalated LDHs (Figure 6, Figure 7 and Figure 8).

Conclusion

In this study, hybrid materials were prepared by associating macromolecular macroRAFT anions with LDH inorganic layers through an anion exchange process from a nitrate LDH precursor phase. The full characterization of the hybrid materials evidenced a successful intercalation for both AA- and AA/BA-based macroRAFT polymers. Larger interlamellar distances were obtained in presence of BA units underlying the influence of the nature of the macroRAFT chain on the interlayer arrangement. Such difference indicates that the macroRAFT polymer involving only AA units was arranged as a monolayer in the interlamellar domain whereas the presence of BA units into the chain induced a bilayer arrangement whatever the chain length. Contrarily to what may be expected, based on NMR experiments, the negatively-charged AA units did not appear to interact sizeably more strongly with the LDH host than the BA units.

Our results demonstrate that hydrophilic macroRAFT polymers can be efficiently intercalated into MgAl-NO_3 LDH forming a functional hybrid material which can be further involved in RAFT polymerization to promote grafting from polymerization or the formation of nanocomposite particles using an emulsion polymerization process [49].

Experimental

Magnesium and aluminium nitrate salts, $Mg(NO_3)_2{\cdot}6H_2O$ and $Al(NO_3)_3{\cdot}9H_2O$ were of analytical grade (Acros Organics, Merck). Acrylic acid (AA, Aldrich, 99%), *n*-butyl acrylate (BA, 99%, stabilized, Acros Organics), 1,4-dioxane (Sigma-Aldrich, puriss. p.a., >99.5%), 1,3,5-trioxane (Sigma-Aldrich, >99%), the initiator 4,4-azobis(4-cyanopentanoic acid) (ACPA, Fluka, >98%), diethyl ether (Sigma-Aldrich, >99.5%) and NaOH (Acros Organics, Merck) were used without further purification. The RAFT agent: 4-cyano-4-thiothiopropylsulfanyl pentanoic acid (CTPPA) was synthesized following a protocol reported in the literature [50].

Preparation of MgAl-NO_3-LDH precursor. LDH containing magnesium(II) and aluminium(III) metal cations and nitrate interlayer anions were prepared by flash coprecipitation followed by hydrothermal treatment [44,51,52]. Typically, a metallic nitrate solution (Mg/Al = 3; 0.3 M) was rapidly added to a NaOH (0.185 M) solution at 0 °C. The pH of the resulting suspension was adjusted to 9.5 and the solution was transferred to an autoclave and heated to 150 °C for 4 h. The resulting particles were collected by centrifugation and the resulting gel washed twice with deionized water. The nanoparticles were finally redispersed in deionized water and stored as a colloidal suspension (≈10 wt %) at room temperature.

Synthesis of macroRAFT (co)polymers. Four different hydrophilic polymers were synthesized by CTPPA-mediated RAFT polymerization of AA or statistical copolymerization of AA and BA (hereafter noted PAA_n-CTPPA and P(AA_n-*stat*-BA_n)-CTPPA, respectively). Typically, AA, BA, CTPPA, ACPA and 1,3,5-trioxane, used as internal standard for NMR

analysis, were dissolved in a round bottom flask, in 1,4-dioxane with a ratio of [monomer]/[RAFT]/[initiator] of 45:1:0.1 (mol/mol/mol) and a total monomer concentration of 3 and 6 M for AA homopolymerization and copolymerization with BA (AA/BA = 50:50 mol/mol), respectively. The solution was degassed with nitrogen for 30 minutes and placed in an oil bath at 80 °C. The reaction was conducted for 5 h and the obtained polymers were purified by precipitation in diethyl ether. Samples were taken during polymerization to determine conversion by ^{1}H NMR spectroscopy as a function of time, and molar mass evolution with conversion by size exclusion chromatography (SEC). SEC measurements were carried out at 40 °C with a flow rate of 1 mL min^{-1} using toluene as a flow rate marker. Before analyses, carboxylic acid groups of the polymers were methylated in a THF/H_2O (90:10 v/v%) mixture using tri(methylsilyl)diazomethane methylation agent to prevent interactions between acid groups and the stationary phase. Samples were filtered on a 0.45 μm pore size membrane and analyzed at 3 mg mL^{-1}. Separation was carried out on three columns from Malvern Instruments (T6000 M General Mixed Org (300 × 8 mm)). The device (Viscotek TDA305) was equipped with a refractive index (RI) detector (λ = 670 nm). The number-average molar mass (M_n) and dispersity ($Đ = M_w/M_n$), with M_w: weight-average molar mass) were derived from the RI signal using a calibration curve based on polystyrene standards (from Polymer Laboratories) [53]. Table 1 presents the main characteristics of the well-defined polymers obtained with a narrow molar mass distributions ($Đ$ = 1.15 ± 0.05) and further used in the intercalation process.

MacroRAFT agent intercalation. Standard anionic exchange was carried out at room temperature under nitrogen for 18 h. Typically, a gel mass corresponding to 0.1 g of dried MgAl-NO_3 LDH was dispersed in 50 mL of water containing a twofold charge excess of macroRAFT agents per Al^{3+}. Prior to be used, the aqueous macroRAFT agent solutions were neutralized by NaOH (0.5 M) addition at pH 8.0. The suspensions were stirred at a constant speed (800 rpm) and the products were recovered by centrifugation at 4500 rpm for 10 min followed by three washing cycles with deionized water and further dried at room temperature.

Characterisations. Powder X-ray diffraction patterns were recorded on a X'Pert Pro Philips diffractometer with a diffracted beam graphite monochromator and a Cu Kα radiation source in the 2θ range of 2–70°. The one-dimensional (1D) electron density distribution along the *c*-stacking axis $\rho_{(z)}$ for MgAl-P($AA_{8.5}$-*stat*-$BA_{8.5}$)-CTPPA was calculated from the intensity of the 00*l* diffraction lines according to the following equation:

$$\rho_{(z)} = \sum_{l=0}^{\infty} F_{00l} \cos\left(\frac{2\pi l z}{c}\right)$$

where c is the unit cell parameter, z is the fractional coordinate along the *c*-stacking axis, and F_{00l} are the structure factors of the 00*l* diffractions [54]. Seven isolated 00*l* diffraction lines were used for calculating the 1D plot for X with a basal spacing of $d_{003} \approx 2.33$ Å; the first peak corresponding to the 00*3* diffraction line was not considered being in the direct beam. First, the Le Bail-method consisting in the refinement of the total envelope of the XRD patterns was used to determine cell parameters assuming the *R*3*m* space group, typical for LDH materials, and to extract the intensities of diffraction peaks. The Thompson, Cox and Hastings (TCH) pseudo-Voigt function was chosen as profile function [55]. The background was refined by adjusting the height of preselected points for linear interpolation modeled and the spherical harmonics correction for an anisotropic peak broadening was applied. Afterwards, the hydroxide part of the structure was entered [56] and the F_{00l} structure factors calculated; the signs of the structure factors were directly obtained from the scattering contributions of the $Mg_3Al(OH)_6$ hydroxide layers assuming a relatively small contribution of the intercalated molecules. The treatment of the XRD data was carried out using the Fullprof suite program [57]. ChemBio 3D Ultra suite program was used to draw the molecular structure of macroRAFT copolymers, running MM2 energy-minimization.

Attenuated total reflectance Fourier transform infrared (ATR-FTIR) spectra were measured in the range 400–4000 cm^{-1} on a FTIR Nicolet 5700 (Thermo Electron Corporation) spectrometer equipped with a Smart Orbit accessory. Field Emission SEM characteristics of the samples were imaged by a Zeiss supra 55 FEG-VP operating at 3 keV. Specimens were mounted on conductive carbon adhesive tabs and imaged after gold sputter coating to make them conductive. Zeta potentials of pristine LDH and macroRAFT-intercalated LDH were measured with a ZetaNano ZS (Malvern instruments) apparatus, using a laser Doppler electrophoresis. The measurements were performed in specific cells provided by Malvern Instruments Company.

Solid-state NMR spectra were collected on a Bruker 17.6 Tesla superconducting magnet operating at ^{1}H, ^{13}C, and ^{27}Al Larmor frequencies of 750.10, 188.6, and 195.6 MHz. ^{13}C experiments were performed at a magic-angle spinning (MAS) frequency of 12 kHz with a Bruker double-resonance 4 mm probehead. Cross-polarization (CP) contact times were set to 0.25 ms to favor short C–H distances, with 1024 scans for signal accumulation. Quantitative ^{13}C experiments were collected with Hahn echo experiments at a total echo length of two rotor periods

(167 μs), with a 50 s recycling delay to ensure non-saturating conditions. Signal accumulation was performed with 128 scans for the copolymer-intercalated LDH, and 32 scans for the PAA-intercalated material. Two-dimensional (2D) $^{13}C\{^1H\}$ heteronuclear correlation experiments used frequency-switched Lee–Goldburg (FSLG) homonuclear decoupling [58] at a nutation frequency of 75 kHz during the (indirect) ^1H evolution period to reduce ^1H–^1H dipolar couplings and increase resolution. The associated frequency scaling factor (0.535) was measured and corrected for, based on a ^1H–^1H correlation experiment (spin-diffusion with null mixing time) conducted under identical homonuclear decoupling conditions. Contact times of 0.2 and 5 ms were used to observe contrast between short and long C–H distances, with (respectively) 512 and 480 scans for signal accumulation, 160 increments for the indirect dimension, and 1.2 s recycling delay (total acquisition time: 30 and 26 h, respectively).

Solid-state ^1H NMR experiments were recorded with a Bruker 1.3 mm double-resonance probehead at the MAS frequency of 60 kHz. Quantitative echo experiments used a recycling delay of 5 s, ensuring non-saturating conditions, and a total echo length of two rotor periods (33 μs). $^1H\{^{27}Al\}$ CP-MAS experiments were performed with a short contact time of 0.5 ms (at constant amplitude on both channels) to ensure selective observation of the LDH hydroxyl protons (see [59] for further details on the application of this technique to MgAl LDHs). The signal was accumulated over 4096 transients with a recycle delay of 0.5 s. A 10-pulse pre-saturation on the ^1H channel is used just before the initial ^{27}Al excitation (90° pulse of 1.75 μs) to eliminate residual ^1H signal, the absence of which was checked in an identical experiment in which the ^{27}Al rf excitation pulse power was turned off. The same CP conditions were used for the $^1H\{^{27}Al\}$ CP-^1H–^1H spin-diffusion experiments, with the addition of two 90° pulses to first bring back the magnetization along the *z*-axis to allow spin-diffusion during mixing times τ_M of 0.01 to 200 ms, and to then send the resulting magnetization back to the transverse plane for detection. All experiments in the series used 4096 scans for signal accumulation with a recycle delay of 0.5 s. All ^{13}C and ^1H chemical shifts are referenced to (pure) tetramethylsilane.

Supporting Information

Full PXRD patterns fitting using Le Bail method.

Supporting Information File 1

Additional PXRD analysis.
[http://www.beilstein-journals.org/bjnano/content/supplementary/2190-4286-7-191-S1.pdf]

Acknowledgements

The authors acknowledge financial support from ANR -11-JS08-0013 and the IR-RMN-THC Fr3050 CNRS for NMR facility access.

References

1. Judeinstein, P.; Sanchez, C. *J. Mater. Chem.* **1996,** *6,* 511. doi:10.1039/jm9960600511
2. Leroux, F.; Taviot-Guého, C. *J. Mater. Chem.* **2005,** *15,* 3628. doi:10.1039/b505014f
3. Prevot, V.; Forano, C.; Besse, J. P. *Appl. Clay Sci.* **2001,** *18,* 3. doi:10.1016/S0169-1317(00)00025-9
4. Forano, C.; Constantino, U.; Prevot, V.; Taviot Gueho, C. Layered Double Hydroxides. In *Handbook of Clay Science;* Faiza Bergaya, G. L., Ed.; Elsevier: Amsterdam, Netherlands, 2013; Vol. 5, Part A, pp 745 ff.
5. Constantino, U.; Leroux, F.; Nocchetti, M.; Mousty, C. LDH in physical, chemical, bio-chemical and life science. In *Handbook of Clay Science;* Faıza Bergaya, G. L., Ed.; Elsevier: Amsterdam, Netherlands, 2013; Vol. 5, Part A, pp 765 ff.
6. Wang, Q.; O'Hare, D. *Chem. Rev.* **2012,** *112,* 4124. doi:10.1021/cr200434v
7. Tian, R.; Liang, R.; Wei, M.; Evans, D. G.; Duan, X. *Applications of Layered Double Hydroxide Materials: Recent Advances and Perspective;* Springer: Berlin, Germany, 2016.
8. Choy, J.-H.; Choi, S.-J.; Oh, J.-M.; Park, T. *Appl. Clay Sci.* **2007,** *36,* 122. doi:10.1016/j.clay.2006.07.007
9. Desigaux, L.; Belkacem, M. B.; Richard, P.; Cellier, J.; Léone, P.; Cario, L.; Leroux, F.; Taviot-Guého, C.; Pitard, B. *Nano Lett.* **2006,** *6,* 199. doi:10.1021/nl052020a
10. Thyveetil, M.-A.; Coveney, P. V.; Greenwell, H. C.; Suter, J. L. *J. Am. Chem. Soc.* **2008,** *130,* 12485. doi:10.1021/ja8037068
11. Darder, M.; López-Blanco, M.; Aranda, P.; Leroux, F.; Ruiz-Hitzky, E. *Chem. Mater.* **2005,** *17,* 1969. doi:10.1021/cm0483240
12. Leroux, F.; Gachon, J.; Besse, J.-P. *J. Solid State Chem.* **2004,** *177,* 245. doi:10.1016/j.jssc.2003.08.013
13. Ambrogi, V.; Perioli, L.; Ciarnelli, V.; Nocchetti, M.; Rossi, C. *Eur. J. Pharm. Biopharm.* **2009,** *73,* 285. doi:10.1016/j.ejpb.2009.06.007
14. Cunha, V. R. R.; Petersen, P. A. D.; Gonçalves, M. B.; Petrilli, H. M.; Taviot-Gueho, C.; Leroux, F.; Temperini, M. L. A.; Constantino, V. R. L. *Chem. Mater.* **2012,** *24,* 1415. doi:10.1021/cm202953y
15. Li, B.; He, J.; Evans, D. G.; Duan, X. *Appl. Clay Sci.* **2004,** *27,* 199. doi:10.1016/j.clay.2004.07.002
16. Ladewig, K.; Niebert, M.; Xu, Z. P.; Gray, P. P.; Lu, G. Q. *Appl. Clay Sci.* **2010,** *48,* 280. doi:10.1016/j.clay.2009.11.032
17. Prevot, V.; Mousty, C.; Forano, C. State of the art in LDH -Biomolecules association. *Advances in Chemistry Research;* Nova Science Publishers, Inc.: New York, NY, U.S.A., 2013; pp 35 ff.
18. Latterini, L.; Nocchetti, M.; Aloisi, G. G.; Costantino, U.; Elisei, F. *Inorg. Chim. Acta* **2007,** *360,* 728. doi:10.1016/j.ica.2006.07.048
19. Yan, D.; Lu, J.; Wei, M.; Qin, S.; Chen, L.; Zhang, S.; Evans, D. G.; Duan, X. *Adv. Funct. Mater.* **2011,** *21,* 2497. doi:10.1002/adfm.201002446
20. Costa, F. R.; Saphiannikova, M.; Wagenknecht, U.; Heinrich, G. Layered Double Hydroxide Based Polymer Nanocomposites. *Wax Crystal Control · Nanocomposites · Stimuli-Responsive Polymers;* Advances in Polymer Science, Vol. 210; Springer: Berlin, Germany, 2008; pp 101–168. doi:10.1007/12_2007_123

21. Hsueh, H.-B.; Chen, C.-Y. *Polymer* **2003,** *44,* 1151. doi:10.1016/S0032-3861(02)00887-X
22. Leroux, F.; Prévot, V. Nano/Microporous Materials: Nanostructured Layered Double Hydroxides. *Encyclopedia of Inorganic Chemistry;* John Wiley & Sons: Hoboken, NJ, U.S.A., 2006.
23. Basu, D.; Das, A.; Stöckelhuber, K. W.; Wagenknecht, U.; Heinrich, G. *Prog. Polym. Sci.* **2014,** *39,* 594. doi:10.1016/j.progpolymsci.2013.07.011
24. Costa, F. R.; Satapathy, B. K.; Wagenknecht, U.; Weidisch, R.; Heinrich, G. *Eur. Polym. J.* **2006,** *42,* 2140. doi:10.1016/j.eurpolymj.2006.04.005
25. Nagendra, B.; Mohan, K.; Gowd, E. B. *ACS Appl. Mater. Interfaces* **2015,** *7,* 12399. doi:10.1021/am5075826
26. Matusinović, Z.; Rogošić, M.; Šipušić, J. *Polym. Degrad. Stab.* **2009,** *94,* 95. doi:10.1016/j.polymdegradstab.2008.10.001
27. Costa, F. R.; Pradhan, S.; Wagenknecht, U.; Bhowmick, A. K.; Heinrich, G. *J. Polym. Sci., Part B: Polym. Phys.* **2010,** *48,* 2302. doi:10.1002/polb.22116
28. Becker, C. M.; Gabbardo, A. D.; Wypych, F.; Amico, S. C. *Composites, Part A* **2011,** *42,* 196. doi:10.1016/j.compositesa.2010.11.005
29. Tammaro, L.; Tortora, M.; Vittoria, V.; Costantino, U.; Marmottini, F. *J. Polym. Sci., Part A: Polym. Chem.* **2005,** *43,* 2281. doi:10.1002/pola.20701
30. Martínez-Gallegos, S.; Herrero, M.; Barriga, C.; Labajos, F. M.; Rives, V. *Appl. Clay Sci.* **2009,** *45,* 44. doi:10.1016/j.clay.2009.04.007
31. Hintze-Bruening, H.; Troutier, A.-L.; Leroux, F. *Prog. Org. Coat.* **2011,** *70,* 240. doi:10.1016/j.porgcoat.2010.08.016
32. Illaik, A.; Taviot-Gueho, C.; Lavis, J.; Cornmereuc, S.; Verney, V.; Leroux, F. *Chem. Mater.* **2008,** *20,* 4854. doi:10.1021/cm800212g
33. Moujahid, E. M.; Besse, J.-P.; Leroux, F. *J. Mater. Chem.* **2002,** *12,* 3324. doi:10.1039/B205837P
34. Oriakhi, C. O.; Farr, I. V.; Lerner, M. M. *J. Mater. Chem.* **1996,** *6,* 103. doi:10.1039/JM9960600103
35. Vieille, L.; Moujahid, E. M.; Taviot-Gueho, C.; Cellier, J.; Besse, J.-P.; Leroux, F. *J. Phys. Chem. Solids* **2004,** *65,* 385. doi:10.1016/j.jpcs.2003.08.029
36. Vaysse, C.; Guerlou-Demourgues, L.; Delmas, C.; Duguet, E. *Macromolecules* **2004,** *37,* 45. doi:10.1021/ma025882w
37. Vaysse, C.; Guerlou-Demourgues, L.; Duguet, E.; Delmas, C. *Inorg. Chem.* **2003,** *42,* 4559. doi:10.1021/ic026229s
38. Roland-Swanson, C.; Besse, J.-P.; Leroux, F. *Chem. Mater.* **2004,** *16,* 5512. doi:10.1021/cm040165x
39. Moujahid, E. M.; Dubois, M.; Besse, J.-P.; Leroux, F. *Chem. Mater.* **2005,** *17,* 373. doi:10.1021/cm0401701
40. Manzi-Nshuti, C.; Chen, D.; Su, S.; Wilkie, C. A. *Polym. Degrad. Stab.* **2009,** *94,* 1290. doi:10.1016/j.polymdegradstab.2009.03.021
41. Qiu, L.; Chen, W.; Qu, B. *Colloid Polym. Sci.* **2005,** *283,* 1241. doi:10.1007/s00396-005-1305-6
42. Ding, P.; Zhang, M.; Gai, J.; Qu, B. *J. Mater. Chem.* **2007,** *17,* 1117. doi:10.1039/b615334h
43. Moad, G.; Rizzardo, E.; Thang, S. H. *Polymer* **2008,** *49,* 1079. doi:10.1016/j.polymer.2007.11.020
44. Pavlovic, M.; Sipiczki-Adok, M.; Vebert, C.; Pearson, S.; Bourgeat-Lami, E.; Prevot, V.; Szilagyi, I. *Langmuir* **2015,** *31,* 12609–12617. doi:10.1021/acs.langmuir.5b03372
45. Rocha, M. A.; Petersen, P. A. D.; Teixeira-Neto, E.; Petrilli, H. M.; Leroux, F.; Taviot-Gueho, C.; Constantino, V. R. L. *RSC Adv.* **2016,** *6,* 16419. doi:10.1039/C5RA25814F
46. Rives, V. *Layered Double Hydroxides: Present and Future;* Nova Science Publishers, Inc.: New York, NY, U.S.A., 2001; pp 439 ff.
47. Alonso, B.; Fayon, F.; Massiot, D.; Amenitsch, H.; Malfatti, L.; Kidchob, T.; Costacurta, S.; Innocenzi, P. *J. Phys. Chem. C* **2010,** *114,* 11730. doi:10.1021/jp101652a
48. Baccile, N.; Laurent, G.; Bonhomme, C.; Innocenzi, P.; Babonneau, F. *Chem. Mater.* **2007,** *19,* 1343. doi:10.1021/cm062545j
49. Ali, S. I.; Heuts, J. P. A.; Hawkett, B. S.; van Herk, A. M. *Langmuir* **2009,** *25,* 10523. doi:10.1021/la9012697
50. Boursier, T.; Chaduc, I.; Rieger, J.; D'Agosto, F.; Lansalot, M.; Charleux, B. *Polym. Chem.* **2011,** *2,* 355. doi:10.1039/C0PY00237B
51. Xu, Z. P.; Stevenson, G.; Lu, C.-Q.; Lu, G. Q. *J. Phys. Chem. B* **2006,** *110,* 16923. doi:10.1021/jp062281o
52. Xu, Z. P.; Stevenson, G. S.; Lu, C.-Q.; Lu, G. Q.; Bartlett, P. F.; Gray, P. P. *J. Am. Chem. Soc.* **2006,** *128,* 36. doi:10.1021/ja056652a
53. Hashimoto, N.; Aoyama, T.; Shioiri, T. *Chem. Pharm. Bull.* **1981,** *29,* 1475. doi:10.1248/cpb.29.1475
54. Whittingham, M.; Jacobson, A. *Intercalation Chemistry;* Academic Press: New York, NY, U.S.A., 1982.
55. Thompson, P.; Cox, D. E.; Hastings, J. B. *J. Appl. Crystallogr.* **1987,** *20,* 79. doi:10.1107/S0021889887087090
56. Allmann, R.; Jepsen, H. P. *Neues Jahrb. Mineral., Monatsh.* **1969,** *1969,* 544.
57. Rodriguez-Carvajal, J. *Commission on powder diffraction (IUCr). Newsletter* **2001,** *26,* 12.
58. Bielecki, A.; Kolbert, A. C.; de Groot, H. J. M.; Griffin, R. G.; Levitt, M. H. *Adv. Magn. Opt. Reson.* **1990,** *14,* 111. doi:10.1016/B978-0-12-025514-6.50011-3
59. Cadars, S.; Layrac, G.; Gérardin, C.; Deschamps, M.; Yates, J. R.; Tichit, D.; Massiot, D. *Chem. Mater.* **2011,** *23,* 2821. doi:10.1021/cm200029q

License and Terms

BEILSTEIN JOURNAL OF NANOTECHNOLOGY

Functionalized TiO_2 nanoparticles by single-step hydrothermal synthesis: the role of the silane coupling agents

Antoine R. M. Dalod[1], Lars Henriksen[2], Tor Grande[1] and Mari-Ann Einarsrud[*1,§]

Full Research Paper

Open Access

Address:
[1]Department of Materials Science and Engineering, NTNU, Norwegian University of Science and Technology, NO-7491 Trondheim, Norway and [2]poLight AS, Kongeveien 77, NO-3188 Horten, Norway

Email:
Mari-Ann Einarsrud[*] - mari-ann.einarsrud@ntnu.no

* Corresponding author
§ Telephone: +47 73 59 40 02

Keywords:
core–shell nanoparticles; functionalized nanoparticles; hydrothermal synthesis; oriented attachment; silane coupling agent

Beilstein J. Nanotechnol. **2017,** *8,* 304–312.
doi:10.3762/bjnano.8.33

Received: 23 August 2016
Accepted: 16 December 2016
Published: 31 January 2017

This article is part of the Thematic Series "Hybrid nanomaterials: from the laboratory to the market".

Guest Editor: A. Taubert

Abstract

A simple, robust and versatile hydrothermal synthesis route to in situ functionalized TiO_2 nanoparticles was developed using titanium(IV) isopropoxide as Ti-precursor and selected silane coupling agents (3-aminopropyltriethoxysilane (APTES), 3-(2-aminoethylamino)propyldimethoxymethylsilane (AEAPS), and *n*-decyltriethoxysilane (DTES)). Spherical nanoparticles (ca. 9 nm) with narrow size distribution were obtained by using DTES or by synthesis performed without silane coupling agents. Rod-like nanoparticles along with 9 nm spherical nanoparticles were formed using aminosilane coupling agents because of a combination of oriented attachment of nanoparticles and specific adsorption of the aminosilane on crystallographic faces of anatase nanoparticles. The nanoparticles were functionalized in situ and became hydrophobic as silanes reacted to form covalent bonds on the surface of TiO_2. The versatility of the aqueous synthesis route was demonstrated, and by selecting the type of silane coupling agent the surface properties of the TiO_2 nanoparticles could be tailored. This synthesis route has been further developed into a two-step synthesis to TiO_2–SiO_2 core–shell nanoparticles. Combustion of the silane coupling agents up to 700 °C leads to the formation of a nanometric amorphous SiO_2 layer, preventing growth and phase transition of the in situ functionalized nanoparticles.

Introduction

Because of the high surface-to-volume ratio, the intrinsic properties of titanium dioxide (TiO_2) nanoparticles have led to exploitation in many fields such as in photocatalysis [1], solar cells [2], and in biomedical applications [3]. The naturally occurring phases of TiO_2 are rutile (thermodynamically stable polymorph), brookite, and anatase [4]. Due to the differences in surface energy, anatase and brookite are more stable than rutile at nanosize, and anatase is more stable than brookite at even smaller sizes (generally below 15–30 nm) [5-7]. Surface modification of TiO_2 nanoparticles, via core–shell structures or grafted nanoparticles [8], has resulted in new applications such as nanofiller for polymer nanocomposites [9,10], coatings [11],

and biosensors [3,12]. Classical synthesis routes for surface-functionalized particles are following two steps: particles synthesis followed by a post-functionalization process [9,10,13].

Post-functionalization of TiO_2 nanoparticles with silane coupling agents was obtained via reflux in aqueous solution [14,15]. Chen et al. investigated interactions of 3-aminopropyltrimethoxysilane (APTMS) and phenyltrimethoxysilane with commercially available TiO_2 nanoparticles (Degussa P-25) [14]. They concluded that the silane coupling agents covalently bond onto the surface of TiO_2 nanoparticles. Using a mixture of isomeric octyltriethoxysilanes (OTES), Milanesi et al. focused on the structure of the hydrophobic layer and proposed that cross-linking (via Si–O–Si bonds) and chemical bonding (via Ti–O–Si bonds) of silanes onto TiO_2 nanoparticles occurred [16]. Later, Zhao et al. detailed the cross-linking and chemical bonding mechanisms of APTMS and 3-isocyanatopropyltrimethoxysilane on TiO_2 nanoparticles [15]. A contact angle of about 150° for water was measured demonstrating hydrophobic nanoparticles. Wang et al. functionalized commercial TiO_2 nanoparticles in aqueous solution via ultrasonic treatment at room temperature with 3-(trimethoxysilyl)propyl methacrylate [17]. The resulting particles exhibited hydrophobic behavior. Another study reported room-temperature surface functionalization of commercial TiO_2 nanoparticles in ethanol using *n*-(6-aminohexyl)aminopropyltrimethoxysilane [18].

Nanoparticle synthesis with in situ surface functionalization has the advantage to reduce the number of reaction steps and is thus of greater interest for potential industrial applications. Teleki et al. developed a route for the continuous production of surface-functionalized TiO_2 via flame spray pyrolysis where the particles were directly functionalized after synthesis with OTES [19]. Depending on the conditions, they obtained surface-functionalized TiO_2 nanoparticles with an average size of 40 nm and they determined a maximum surface coverage of about 2.6 OTES molecules per square nanometer. Niederberger et al. developed a room-temperature non-aqueous in situ functionalization process of TiO_2 nanoparticles with 4-*tert*-butylcatechol and dopamine [20]. A brittle brown solid and a dark red powder was obtained for 4-*tert*-butylcatechol and dopamine surface functionalized samples, respectively. More recently, Gao and Cui reported a sol–gel method in which TiO_2 nanoparticles functionalized with chlorinated alcohols through hydrogen bonding were produced [21]. However, sol–gel synthesis often leads to poorly crystalline particles [22].

Hydrothermal synthesis [23] is simple and cost efficient [24] and allows for improved crystallinity compared to sol–gel methods [22] giving improved TiO_2 characteristics for applications such as photocatalysis and solar cell applications [2,25,26]. Typically used precursors are titanium alkoxides where the formation of anatase nanocrystals occurs through hydrolysis and condensation [22]. To our knowledge there is only one work where in situ functionalization of TiO_2 nanoparticles using solvothermal synthesis is reported. Koziej et al. used trimethoxy(7-octen-1-yl)silane (7-OTS) and 3-(trimethoxysilyl)propyl methacrylate coupling agents during TiO_2 nanoparticle synthesis from titanium isopropoxide in anhydrous benzyl alcohol [27]. The particles however needed further post functionalization with 7-OTS for better compatibility with organic solvent and PMMA.

Here, we report on a novel and versatile in situ aqueous hydrothermal synthesis route to surface-functionalized TiO_2 nanoparticles using selected silane coupling agents. The nanoparticles were characterized with respect to crystal structure, size, size distribution, specific surface area, surface coverage, and hydrophobicity. Tuning the surface properties of the nanoparticles for different applications by selecting the silane coupling agent is discussed. We further report the effect of heat treatment of the nanoparticles for the formation of core–shell TiO_2–SiO_2 nanoparticles.

Experimental

Synthesis

The synthesis of the non-functionalized TiO_2 nanoparticles was based on a hydrothermal route previously described by Hayashi and Torii, using titanium(IV) isopropoxide (TIP) as precursor [28]. The synthesis method was further developed for in situ surface functionalization using selected silane coupling agents: 3-aminopropyltriethoxysilane (Sigma-Aldrich, 99%), 3-(2-aminoethylamino)propyldimethoxymethylsilane (Fluka, ≥95%), and *n*-decyltriethoxysilane (ABCR, 97%); abbreviated APTES, AEAPS, and DTES, respectively.

TIP (28 mmol, Sigma-Aldrich, ≥97%) was mixed with distilled water, to which the silane coupling agent (TIP/silane molar ratio equal to 10:1) was initially added to give a filling factor of 70% in the autoclave. The solutions were vigorously stirred for 10 min prior to transfer into a PTFE-lined autoclave (Parr, 125 mL) and heated for 2 h at 200 °C. After cooling to room temperature, the products were centrifuged (10000 rpm, 10 min) and washed with distilled water. This process was repeated three times. The obtained slurries were dried for about 12 h at 100 °C for analysis.

TiO_2 samples in situ surface-functionalized with APTES, AEAPS, and DTES are labeled Ti-APTES, Ti-AEAPS, and Ti-DTES, respectively. Heat-treated samples at 700 °C in synthetic air during thermogravimetric analysis (see details below) were further investigated and are labeled adding the suffix

"-HT" to the original sample name, i.e., TiO_2-HT, Ti-APTES-HT, Ti-AEAPS-HT, and Ti-DTES-HT.

Characterization

Powder X-ray diffraction (XRD) was performed on a Bruker D8 Advance DAVINCI working in Bragg–Brentano (θ/2θ) geometry. Diffractograms were recorded under Cu Kα radiation, with a step size of 0.013°, an integration time of 0.4 s, and using variable divergent slits. Rietveld refinements and crystallite sizes were obtained using TOPAS (Bruker AXS version 4.2).

Scanning electron microscopy (SEM) images were recorded on an in-lens cold-field-emission S(T)EM Hitachi S-5500. The acceleration voltage was set at 7 kV and secondary electrons were detected. For the preparation of the samples, a drop of particles in water obtained after the centrifugation steps was placed on an aluminum sample holder which was set to dry overnight. The line-intercept method was used to calculate average particle sizes, using sample pictures containing more than 300 intercepts.

Transmission electron microscopy (TEM) images were recorded on a JEOL 2100 equipped with Oxford X-Max 80 SDD detector for energy-dispersive X-ray spectroscopy (EDS) analysis. The acceleration voltage was set at 200 kV. For the preparation of the samples, the nanoparticles were dispersed in anhydrous 2-propanol (Sigma-Aldrich, 99.5%) by sonication for 15 min. A droplet of the suspension was then placed on a carbon-coated copper TEM grid, which was set to rest until evaporation of the solvent. The d_{hkl} distances were measured by extracting an area of interest from the HR-TEM images with fast Fourier transform analysis, and calculating the average distance over more than ten consecutive *hkl* planes, using DigitalMicrograph (Gatan Inc. version 3.01).

Specific surface area (BET method [29]) and pore size distribution (BJH method [30]) were measured by nitrogen adsorption on a Micrometrics Tristar 3000. Samples were degassed for 12 h at 180 °C in vacuum prior to analysis. Particle sizes were estimated from the surface area assuming non-porous and spherical particles.

Fourier-transform infrared (FTIR) spectra were acquired on a Bruker Vertex 80v FTIR equipped with Bruker Platinum ATR diamond system from 400 to 4000 cm^{-1}, under medium vacuum (280 Pa). A background was collected under medium vacuum, without sample. Between each analysis, the ATR diamond was cleaned with isopropanol, for which vacuum provides fast evaporation and no specific adsorption bands of isopropanol were observed. A total of 128 scans were acquired for each sample at a resolution of 1 cm^{-1}.

Thermogravimetric analysis (TGA) was acquired on a Netzsch Jupiter STA 449 C using an alumina crucible. The nanoparticles were firstly heat-treated from 25 to 150 °C (10 °C·min^{-1}), maintained at 150 °C for 30 min, cooled down to room temperature, and heat-treated again from 25 to 200 °C (2 °C·min^{-1}) in order to remove adsorbed water. The samples were finally heat-treated from 100 to 700 °C (2 °C·min^{-1}). All treatments were performed under synthetic air.

Results and Discussion

Structure, particle size and morphology

XRD patterns of TiO_2 and in situ surface-functionalized TiO_2 nanoparticles, presented in Figure 1, show anatase as main phase with around 25 wt % of brookite in the case of pure TiO_2 and Ti-DTES samples (for Rietveld refinements see Figure S1 of Supporting Information File 1). The broad diffraction lines demonstrate small crystallite sizes, which were determined by refinement to be between 4.7 and 9.1 nm (Table 1). The HR-TEM image of the pure TiO_2 sample (Figure 2a) demonstrates that anatase and brookite nucleate as individual monocrystalline nanoparticles. The electron diffraction patterns also show anatase and brookite in the case of TiO_2 (Figure 2b) while Ti-APTES (Figure 2d) is purely anatase.

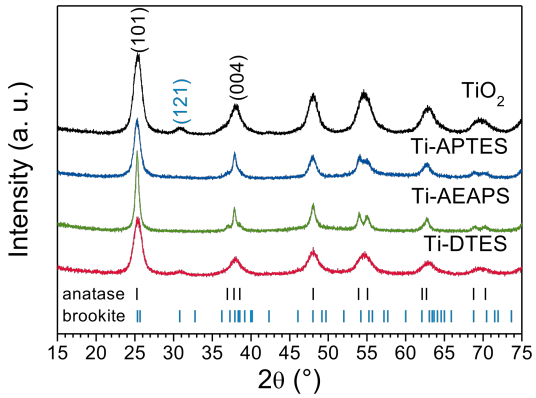

Figure 1: XRD patterns of TiO_2 and in situ surface-functionalized TiO_2 nanoparticles (the bars show diffraction lines of anatase from ICDD card #00-021-1272 and brookite from ICDD card #00-029-1360).

SEM images of TiO_2 and in situ surface-functionalized TiO_2 nanoparticle agglomerates are displayed Figure 3. The measured particle sizes are included in Table 1. TiO_2 (Figure 3a), and Ti-DTES (Figure 3b) samples consist of non-porous spherical nanoparticles with an average diameter of 9 nm and a narrow size distribution. Samples functionalized with aminosilane (Figure 3c,d) exhibit similar nanoparticles, but also larger rod-like nanoparticles. Similar crystallite size and roughness of the rod-like nanostructures suggest that they are formed by oriented attachment [31] of the nanoparticles. HR-TEM image of Ti-APTES (Figure 2c) shows {004} planes

Table 1: Properties of TiO_2 and in situ surface-functionalized TiO_2 nanoparticles from nitrogen adsorption, XRD, SEM, and TGA analysis.

sample	S_{BET}[a] ($m^2 \cdot g^{-1}$)	d_{BET}[b] (nm)	d_{BJH}[c] (nm)	d_{XRD}[d] (nm)	d_{SEM}[e] (nm)	organic mass loss (%)	surface coverage (nm^{-2})
TiO_2	195	7.9	7.9	5.7	9.0 ± 0.6	n/a	n/a
Ti-APTES	178	8.7	9.2	6.0	16.4 ± 1.4	5.8	3.4
Ti-AEAPS	149	10.3	11.8	9.1	20.9 ± 3.2	6.7	2.3
Ti-DTES	114	13.5	9.7	4.7	9.2 ± 0.9	10.8	4.0

[a]BET specific surface area from nitrogen adsorption measurements; [b]particle size estimated from BET specific surface area; [c]average pore diameter from BJH desorption calculations; [d]crystallite size from Rietveld refinement of XRD measurements; [e]particle size from SEM observations.

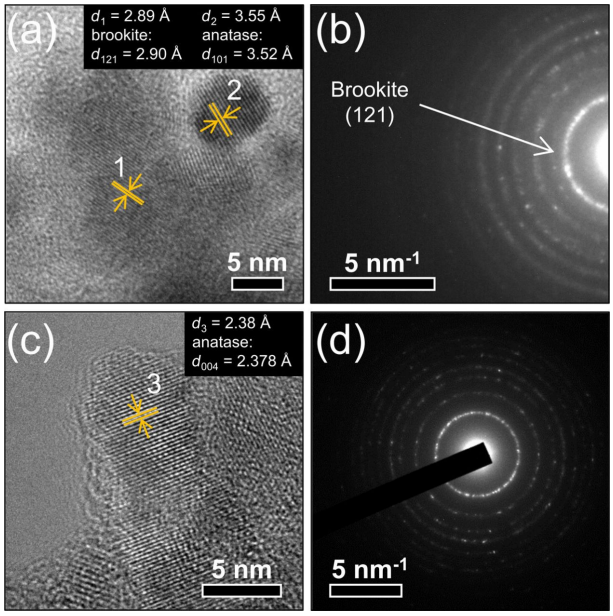

Figure 2: (a) HR-TEM image showing two individual nanoparticles of (1) brookite and (2) anatase and (b) electron diffraction pattern of pure TiO_2 (top); (c) HR-TEM image of a rod-like nanoparticle and (d) electron diffraction pattern of Ti-APTES (bottom).

oriented perpendicularly to the elongation direction of a rod-like nanoparticle indicating growth along the [001] crystallographic direction, as previously reported for hydrothermally formed anatase [32]. This is also confirmed by the narrower FWHM of the (004) diffraction line at 37.80° (Figure 1 and Figure S1 of Supporting Information File 1) compared to other reflections. The rod-like nanoparticles are longer in the Ti-AEAPS sample (50–200 nm) compared to the Ti-APTES sample (50–100 nm) and they are not observed with the alkylsilane functionalization agent (DTES). Ahmad et al. [33] reported that different crystallographic faces of anatase exhibit different polarity and Kassir et al. [18] demonstrated that aminosilanes do not react homogeneously on the different faces of TiO_2 nanoparticles. Thus, we propose that as the nanoparticles growth and functionalization occur simultaneously, rod-like nanoparticles originate from aminosilanes that guide the growth of the nanoparticles along the [001] crystallographic direction of anatase. The aminosilane-functionalized TiO_2 nanoparticles are also the only ones that are purely anatase (Figure 1 and Figure S1 of Supporting Information File 1). Particle size and surface energy are some of the main factors for phase stability crossovers in nanotitania [5-7] and specific adsorption of aminosilanes could reduce the surface energy of the forming nanoparticles, promoting anatase nucleation during the synthesis, even if the crystallite and particle sizes are in this case larger than those measured for pure TiO_2 (Table 1).

The measured BET specific surface area and the corresponding calculated size of the nanoparticles are included in Table 1. The particle sizes are consistent with the SEM and TEM observations and the crystallite sizes determined by XRD, which suggest only weakly agglomeration in the powders after drying.

The nitrogen adsorption and desorption isotherms of TiO_2 and in situ surface-functionalized TiO_2 nanoparticles demonstrate the hysteresis profile similar to mesoporous materials (Figure 4a). Since particle sizes from SEM and surface area are similar, porosity is associated with inter-particle volume of the agglomerates and can be directly correlated with the particle sizes [34]. Figure 4b displays the pore size distribution from desorption isotherms of TiO_2 and in situ surface-functionalized TiO_2 nanoparticles. The pore size distribution is centered between 4 and 7 nm for TiO_2 and Ti-DTES, while for the aminosilane-functionalized samples, the size distribution is broader and shifted towards larger pores and two features are observed. The first feature centered between 4 and 7 nm is assigned to interstitial volume of the spherical nanoparticles and the second broader feature is assigned to interstitial volume of the rod-like particles. Coherently with SEM observations, as less spherical nanoparticles are observed in Ti-AEAPS, the volume of the feature between 4 and 7 nm is decreasing (relative comparison to Ti-APTES), and as rod-like particles are larger, the feature at 10 nm is shifted towards larger pores. The average pore diameters from BJH desorption curves are included in Table 1.

Functionalization and hydrophobicity

Thermogravimetric analysis of TiO_2 and the in situ surface-functionalized TiO_2 nanoparticles are presented in Figure 5a. In

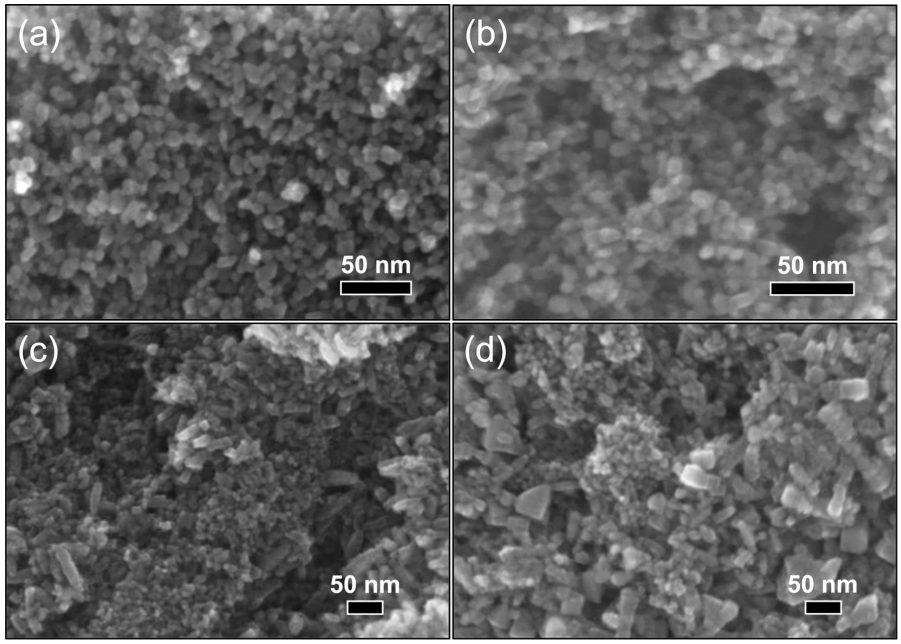

Figure 3: SEM images of (a) TiO_2 and in situ surface-functionalized TiO_2 nanoparticles, (b) Ti-DTES, (c) Ti-APTES, and (d) Ti-AEAPS.

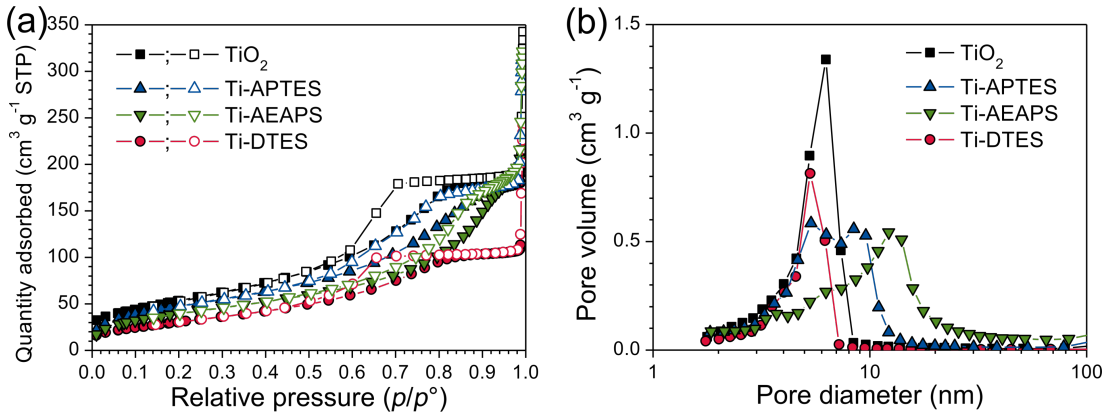

Figure 4: (a) Adsorption (solid symbols) and desorption (open symbols) isotherms and (b) BJH desorption d*V*/dlog(*D*) pore volume, from nitrogen adsorption measurements, of TiO_2 and in situ surface-functionalized TiO_2 nanoparticles.

case of pure TiO_2, a significant mass loss assigned to hydroxy groups was observed until 400 °C. For the in situ surface-functionalized samples, the mass loss (at 230–460 °C) was assigned to the combustion of the organic part of the silane. The average surface coverages (molecules per square nanometer) of the nanoparticles were calculated based on the specific surface area and the mass loss due to combustion of the organic part, considering loss of C, H, and N of the silanes [35] (Table 1).

The FTIR spectra of TiO_2 and in situ surface-functionalized TiO_2 nanoparticles are shown in Figure 5b (see Table S1 of Supporting Information File 1 for the assignments of the absorption bands). No specific bands from isopropanol were observed indicating full reaction of the TIP precursor and high purity of the nanoparticles. In the case of in situ surface-functionalized samples, Si–O–Si bands at 1020 and 1120 cm^{-1} and the Ti–O–Si shoulder at 910 cm^{-1} confirmed that the silanes react via a condensation mechanism, cross-link, and covalently bond on the surface of the TiO_2 nanoparticles [15,16,36]. The degree of order in the organic monolayer can be qualitatively estimated by comparing the CH_2 stretching modes in crystalline (highly ordered) and liquid (highly disordered) states [36,37]. For Ti-DTES sample, the CH_2 stretching modes at 2852 and 2921 cm^{-1} are close to those measured for crystalline polymethylene and for $CH_3(CH_2)_9SH$ adsorbed on gold [37] indicating well-ordered organic monolayers. In case of the aminosilane-

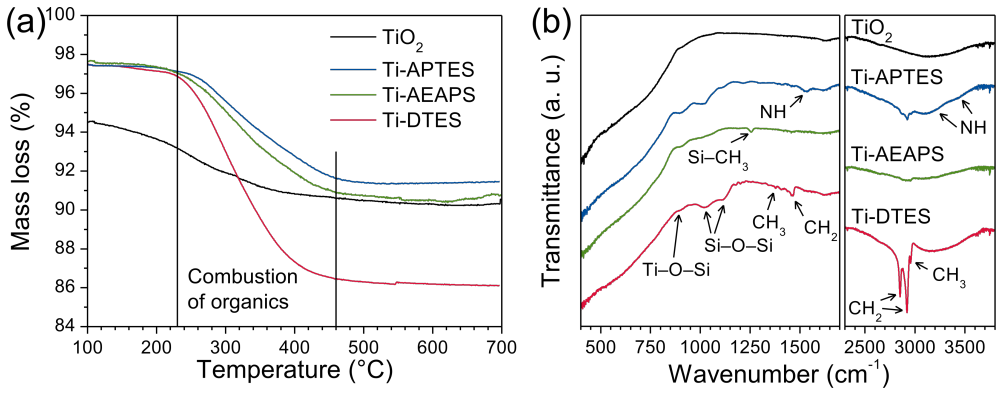

Figure 5: (a) TGA curves and (b) FTIR spectra of TiO_2 and in situ surface-functionalized TiO_2 nanoparticles.

functionalized samples, the low signal/noise ratios do not allow for an accurate measurement of the band positions. Additionally, because of possible surface contamination (from the carbon-coated grid) and/or optical aberration, the HR-TEM observation of Ti-APTES (Figure 2c) did not show clear evidence of the organic layer, confirming the nanometric nature of the organic coating.

A photo of TiO_2 and in situ surface-functionalized TiO_2 nanoparticles in a mixed solution of diethyl ether and water is displayed in Figure 6. Pure TiO_2 entirely dispersed in the water phase and formed a blurred suspension, showing hydrophilic behavior. The Ti-APTES sample dispersed in both phases, indicating partial hydrophobic behavior. The Ti-AEAPS and Ti-DTES samples completely dispersed in the diethyl ether phase, demonstrating the hydrophobic behavior of these materials. The resulting hydrophobic properties of the nanoparticles depend on organic chain length and surface coverage [17], and are comparable to results reported by Iijima and co-workers on TiO_2 nanoparticles post-modified with decyltrimethoxysilane and APTMS in mixed solutions of toluene and methanol [38].

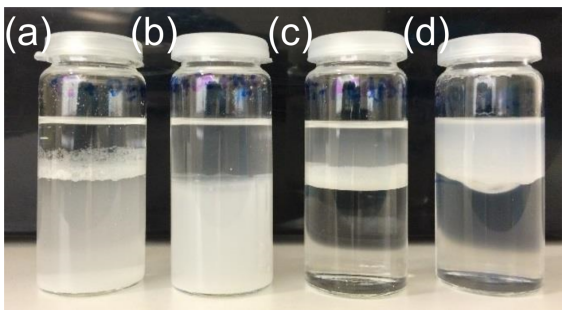

Figure 6: Photograph showing the behavior of (a) TiO_2 and in situ surface-functionalized TiO_2 nanoparticles, (b) Ti-APTES, (c) Ti-AEAPS, and (d) Ti-DTES in a mixed solutions of diethyl ether (top) and water (bottom).

Heat treatment

XRD patterns of heat-treated TiO_2 and the in situ surface-functionalized TiO_2 nanoparticles are shown Figure 7a, and these patterns were also refined (Figure S2 of Supporting Informa-

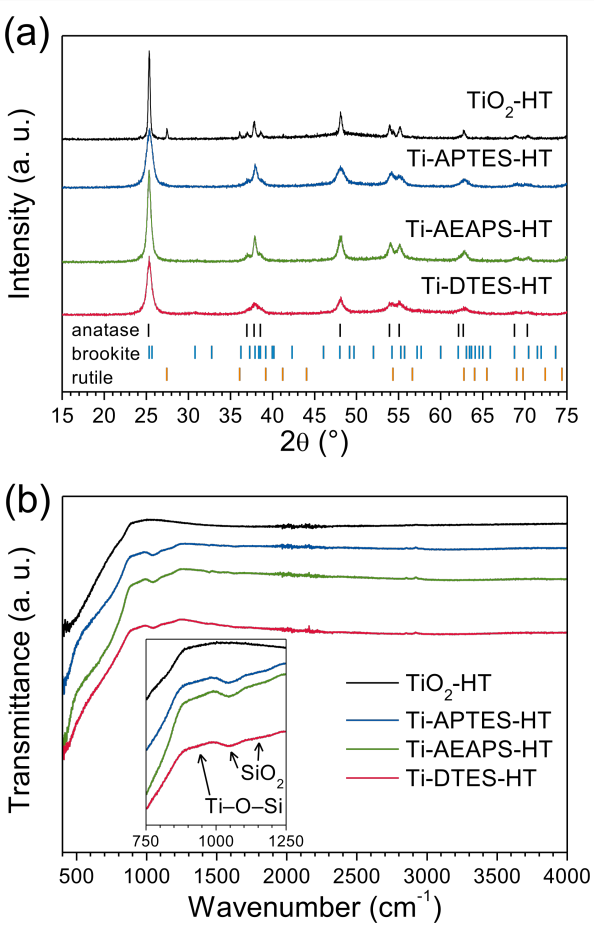

Figure 7: (a) XRD patterns (bars show diffraction lines of anatase from ICDD card #00-021-1272, brookite from ICDD card #00-029-1360, and rutile from ICDD card #00-021-1276) and (b) FTIR spectra of heat-treated TiO_2 and in situ surface-functionalized TiO_2 nanoparticles.

tion File 1). While the pure TiO_2 sample exhibits crystallites growth (from 5.7 to 28.8 nm), the functionalized nanoparticles with silane coupling agents showed only negligible growth of the crystallites after the heat treatment. Calculated crystallite sizes of the heat-treated samples are listed in Table 2. Additionally, in TiO_2-HT, the heat treatment induced a partial phase transition from brookite and anatase to rutile, the thermodynamically stable polymorph of TiO_2 [4]. In the case of in situ surface-functionalized TiO_2 nanoparticles, the heat treatment has negligible effects on the crystallographic structure of the samples.

Table 2: Properties of heat-treated TiO_2 and in situ surface-functionalized TiO_2 nanoparticles from XRD and SEM analysis.

sample	d_{XRD}[a] (nm)	d_{SEM}[b] (nm)
TiO_2-HT	28.8	30.0 ± 2.9
Ti-APTES-HT	7.8	15.5 ± 2.1
Ti-AEAPS-HT	10.4	23.7 ± 2.2
Ti-DTES-HT	8.9	12.0 ± 0.6

[a]crystallite size from Rietveld refinement of XRD measurements; [b]particle size from SEM observations.

The SEM images of heat-treated nanoparticles (Figure 8) confirmed the conclusions regarding both the morphology and the particles sizes (Table 2) showing the growth of the TiO_2-HT nanoparticles.

The FTIR investigations of the heat-treated nanoparticles (Figure 7b) show absorption bands at 1050 and 1150 cm^{-1}, which were assigned to Si–O–Si vibrations in silica [39] and a weak shoulder centered at 930 cm^{-1} was assigned to Ti–O–Si vibrations, in addition of the large absorption band below 900 cm^{-1} due to Ti–O–Ti vibrations.

The EDS maps of the Ti-APTES-HT nanoparticles (Figure 9) show that silicon is homogeneously distributed over the particles. EDS spectra over relatively large areas of the heat-treated in situ surface-functionalized nanoparticles and the pure TiO_2 samples (Figure S3 of Supporting Information File 1) confirm the presence and the absence of silicon, respectively.

Removal of the organic part of the silane coupling agent during the heat treatment induces the formation of a SiO_2 layer on the surface of the TiO_2 nanoparticles. The nature of the amorphous SiO_2 layer could not be fully determined by TEM observation (Figure S4 of Supporting Information File 1), but it indicated nanometric thickness of the layer. The amorphous SiO_2 layer inhibits surface diffusion of titanium, which prevents growth and phase transition of the nanoparticles, even at relatively high

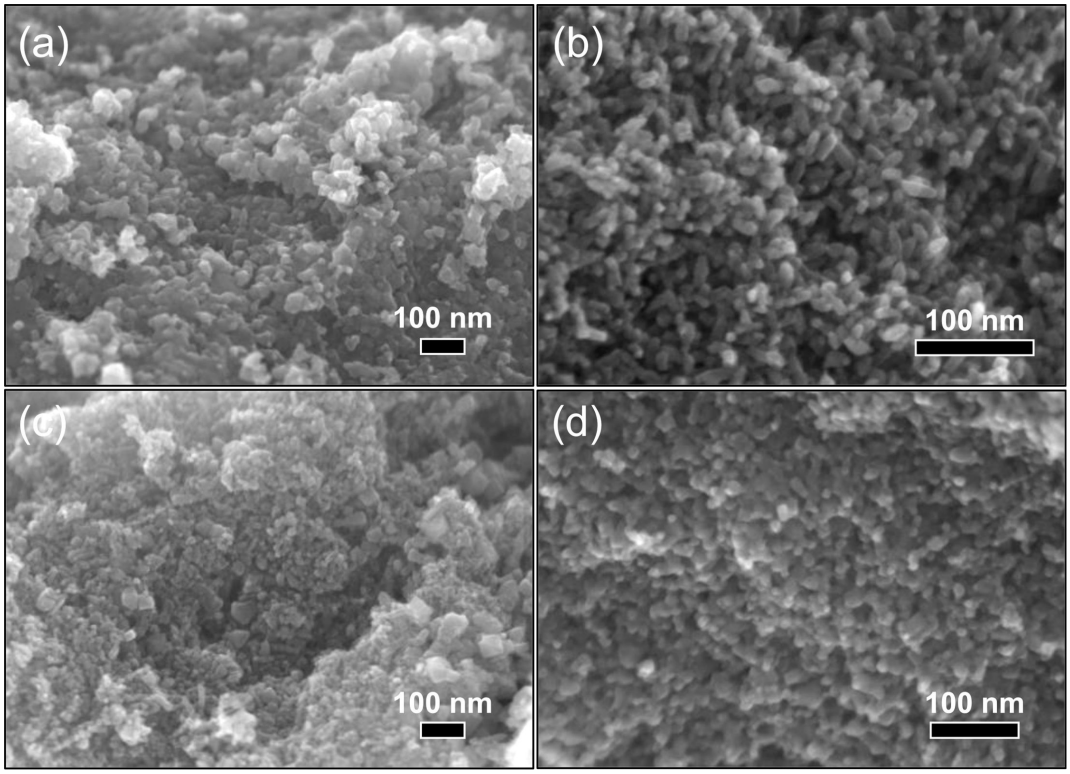

Figure 8: SEM images of (a) TiO_2-HT and heat-treated in situ surface-functionalized TiO_2 nanoparticles, (b) Ti-APTES-HT, (c) Ti-AEAPS-HT, and (d) Ti-DTES-HT.

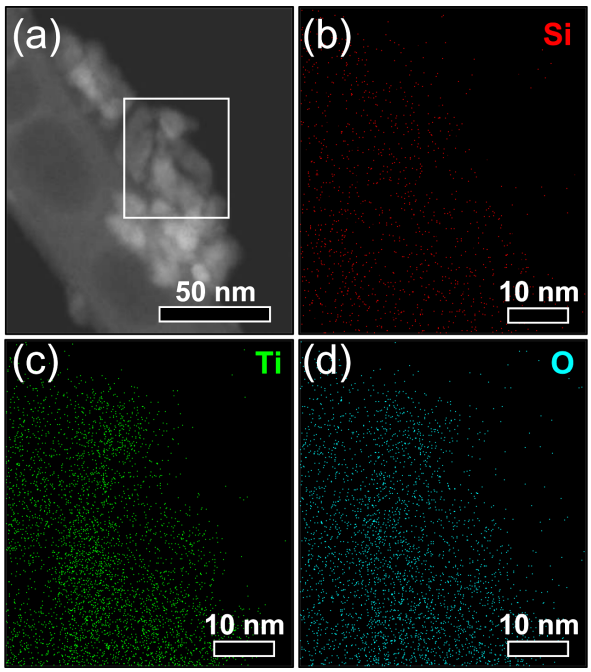

Figure 9: (a) Scanning electron image of Ti-APTES-HT with localization of the mapping (white rectangle) and EDS maps of (b) Si Kα$_1$, (c) Ti Kα$_1$, and (d) O Kα$_1$ signals.

temperatures. Reduced crystallite growth and retarded phase transition have also been observed when firing mixtures of TiO_2 and SiO_2 powders [40].

Conclusion

A new simple hydrothermal route to in situ surface-functionalized TiO_2 nanoparticles has successfully been developed. Spherical hydrophobic TiO_2 nanoparticles with a size of about 9 nm were prepared using silane coupling agents to functionalize the surface. Using aminosilane, the TiO_2 nanoparticles showed oriented attachment along the [001] crystallographic direction of anatase to form rod-like nanostructures with a diameter close to the one of the spherical particles and a length in the range 50–200 nm dependent on the type of silane coupling agent. Surface coverage of the nanoparticles was measured to be between 2.3 and 4.0 molecules per square nanometer. The one-step aqueous synthesis reported here reduces time, the number of steps needed, and the complexity of production of surface-functionalized TiO_2 nanoparticles. Despite the hydrothermal conditions, the synthesis is simple, robust, and reproducible. The numerous varieties of silane coupling agents offer versatility for tuning the surface properties of the TiO_2 nanoparticles that are required for selected applications. Further modifications of the synthesis route are also possible for tuning the properties towards various types of applications. For example, applying the nanoparticles as filler in polymer nanocomposites, hydrophobicity is a parameter of utmost importance [10,27].

Heat treatment of the in situ surface-functionalized nanoparticles at 700 °C revealed neither crystallite growth nor phase transition of TiO_2 because of the formation of an amorphous SiO_2 layer, originating from the silane coupling agents, and leading to TiO_2–SiO_2 core–shell nanoparticles.

Supporting Information

Supporting Information features Rietveld refinements of diffractograms of in situ functionalized and heat-treated nanoparticles, EDS spectra, additional TEM images, and assignments of the FTIR absorption bands.

Supporting Information File 1

Additional experimental data.
[http://www.beilstein-journals.org/bjnano/content/supplementary/2190-4286-8-33-S1.pdf]

Acknowledgements

Financial support from The Research Council of Norway to the project "Beat the Human Eye" (number 235210) and for the support to NTNU NanoLab through the Norwegian Micro- and Nano-Fabrication Facility, NorFab (197411/V30), is gratefully acknowledged. The TEM work was carried out on the NORTEM JEOL 2100 instrument, TEM Gemini Centre, NTNU, Norway, and we want to acknowledge Dr. Ragnhild Sæterli for help in operating the TEM.

References

1. Schneider, J.; Matsuoka, M.; Takeuchi, M.; Zhang, J.; Horiuchi, Y.; Anpo, M.; Bahnemann, D. W. *Chem. Rev.* **2014,** *114,* 9919–9986. doi:10.1021/cr5001892
2. Bai, Y.; Mora-Seró, I.; De Angelis, F.; Bisquert, J.; Wang, P. *Chem. Rev.* **2014,** *114,* 10095–10130. doi:10.1021/cr400606n
3. Rajh, T.; Dimitrijevic, N. M.; Bissonnette, M.; Koritarov, T.; Konda, V. *Chem. Rev.* **2014,** *114,* 10177–10216. doi:10.1021/cr500029g
4. Smith, S. J.; Stevens, R.; Liu, S.; Li, G.; Navrotsky, A.; Boerio-Goates, J.; Woodfield, B. F. *Am. Mineral.* **2009,** *94,* 236–243. doi:10.2138/am.2009.3050
5. Levchenko, A. A.; Li, G.; Boerio-Goates, J.; Woodfield, B. F.; Navrotsky, A. *Chem. Mater.* **2006,** *18,* 6324–6332. doi:10.1021/cm061183c
6. Zhang, H.; Banfield, J. F. *J. Phys. Chem. B* **2000,** *104,* 3481–3487. doi:10.1021/jp000499j
7. Zhang, H.; Banfield, J. F. *Chem. Rev.* **2014,** *114,* 9613–9644. doi:10.1021/cr500072j
8. Tao, P.; Viswanath, A.; Li, Y.; Siegel, R. W.; Benicewicz, B. C.; Schadler, L. S. *Polymer* **2013,** *54,* 1639–1646. doi:10.1016/j.polymer.2013.01.032
9. Lü, C.; Yang, B. *J. Mater. Chem.* **2009,** *19,* 2884–2901. doi:10.1039/B816254a

10. Kango, S.; Kalia, S.; Celli, A.; Njuguna, J.; Habibi, Y.; Kumar, R. *Prog. Polym. Sci.* **2013,** *38,* 1232–1261. doi:10.1016/j.progpolymsci.2013.02.003
11. Faure, B.; Salazar-Alvarez, G.; Ahniyaz, A.; Villaluenga, I.; Berriozabal, G.; De Miguel, Y. R.; Bergström, L. *Sci. Technol. Adv. Mater.* **2013,** *14,* 023001. doi:10.1088/1468-6996/14/2/023001
12. Vashist, S. K.; Lam, E.; Hrapovic, S.; Male, K. B.; Luong, J. H. T. *Chem. Rev.* **2014,** *114,* 11083–11130. doi:10.1021/cr5000943
13. Mallakpour, S.; Madani, M. *Prog. Org. Coat.* **2015,** *86,* 194–207. doi:10.1016/j.porgcoat.2015.05.023
14. Chen, Q.; Yakovlev, N. L. *Appl. Surf. Sci.* **2010,** *257,* 1395–1400. doi:10.1016/j.apsusc.2010.08.036
15. Zhao, J.; Milanova, M.; Warmoeskerken, M. M. C. G.; Dutschk, V. *Colloids Surf., A* **2012,** *413,* 273–279. doi:10.1016/j.colsurfa.2011.11.033
16. Milanesi, F.; Cappelletti, G.; Annunziata, R.; Bianchi, C. L.; Meroni, D.; Ardizzone, S. *J. Phys. Chem. C* **2010,** *114,* 8287–8293. doi:10.1021/jp1014669
17. Wang, C.; Mao, H.; Wang, C.; Fu, S. *Ind. Eng. Chem. Res.* **2011,** *50,* 11930–11934. doi:10.1021/ie200887x
18. Kassir, M.; Roques-Carmes, T.; Hamieh, T.; Razafitianamaharavo, A.; Barres, O.; Toufaily, J.; Villiéras, F. *Adsorption* **2013,** *19,* 1197–1209. doi:10.1007/s10450-013-9555-y
19. Teleki, A.; Bjelobrk, N.; Pratsinis, S. E. *Langmuir* **2010,** *26,* 5815–5822. doi:10.1021/la9037149
20. Niederberger, M.; Garnweitner, G.; Krumeich, F.; Nesper, R.; Cölfen, H.; Antonietti, M. *Chem. Mater.* **2004,** *16,* 1202–1208. doi:10.1021/cm031108r
21. Gao, X.; Cui, H. *J. Sol-Gel Sci. Technol.* **2014,** *70,* 355–360. doi:10.1007/s10971-014-3289-5
22. Cargnello, M.; Gordon, T. R.; Murray, C. B. *Chem. Rev.* **2014,** *114,* 9319–9345. doi:10.1021/cr500170p
23. Rabenau, A. *Angew. Chem., Int. Ed. Engl.* **1985,** *24,* 1026–1040. doi:10.1002/anie.198510261
24. Einarsrud, M.-A.; Grande, T. *Chem. Soc. Rev.* **2014,** *43,* 2187–2199. doi:10.1039/c3cs60219b
25. Kwon, S. J.; Im, H. B.; Nam, J. E.; Kang, J. K.; Hwang, T. S.; Yi, K. B. *Appl. Surf. Sci.* **2014,** *320,* 487–493. doi:10.1016/j.apsusc.2014.09.110
26. Anajafi, Z.; Marandi, M.; Taghavinia, N. *Physica E* **2015,** *70,* 113–120. doi:10.1016/j.physe.2015.02.023
27. Koziej, D.; Fischer, F.; Kränzlin, N.; Caseri, W. R.; Niederberger, M. *ACS Appl. Mater. Interfaces* **2009,** *1,* 1097–1104. doi:10.1021/am9000584
28. Hayashi, H.; Torii, K. *J. Mater. Chem.* **2002,** *12,* 3671–3676. doi:10.1039/B207052A
29. Brunauer, S.; Emmett, P. H.; Teller, E. *J. Am. Chem. Soc.* **1938,** *60,* 309–319. doi:10.1021/ja01269a023
30. Barrett, E. P.; Joyner, L. G.; Halenda, P. P. *J. Am. Chem. Soc.* **1951,** *73,* 373–380. doi:10.1021/ja01145a126
31. Niederberger, M.; Cölfen, H. *Phys. Chem. Chem. Phys.* **2006,** *8,* 3271–3287. doi:10.1039/b604589h
32. Penn, R. L.; Banfield, J. F. *Geochim. Cosmochim. Acta* **1999,** *63,* 1549–1557. doi:10.1016/s0016-7037(99)00037-x
33. Ahmad, M. A.; Prelot, B.; Razafitianamaharavo, A.; Douillard, J. M.; Zajac, J.; Dufour, F.; Durupthy, O.; Chaneac, C.; Villiéras, F. *J. Phys. Chem. C* **2012,** *116,* 24596–24606. doi:10.1021/jp307707h
34. Viana, M. M.; Soares, V. F.; Mohallem, N. D. S. *Ceram. Int.* **2010,** *36,* 2047–2053. doi:10.1016/j.ceramint.2010.04.006
35. García-González, C. A.; Fraile, J.; López-Periago, A.; Domingo, C. *J. Colloid Interface Sci.* **2009,** *338,* 491–499. doi:10.1016/j.jcis.2009.06.035
36. Helmy, R.; Fadeev, A. Y. *Langmuir* **2002,** *18,* 8924–8928. doi:10.1021/la0262506
37. Porter, M. D.; Bright, T. B.; Allara, D. L.; Chidsey, C. E. D. *J. Am. Chem. Soc.* **1987,** *109,* 3559–3568. doi:10.1021/ja00246a011
38. Iijima, M.; Kobayakawa, M.; Kamiya, H. *J. Colloid Interface Sci.* **2009,** *337,* 61–65. doi:10.1016/j.jcis.2009.05.007
39. Gärtner, M.; Dremov, V.; Müller, P.; Kisch, H. *ChemPhysChem* **2005,** *6,* 714–718. doi:10.1002/cphc.200400185
40. Tobaldi, D. M.; Tucci, A.; Škapin, A. S.; Esposito, L. *J. Eur. Ceram. Soc.* **2010,** *30,* 2481–2490. doi:10.1016/j.jeurceramsoc.2010.05.014

License and Terms

BEILSTEIN JOURNAL OF NANOTECHNOLOGY

Tailoring bifunctional hybrid organic–inorganic nanoadsorbents by the choice of functional layer composition probed by adsorption of Cu^{2+} ions

Veronika V. Tomina[1], Inna V. Melnyk[1,2], Yuriy L. Zub[1], Aivaras Kareiva[3], Miroslava Vaclavikova[2], Gulaim A. Seisenbaeva[*4] and Vadim G. Kessler[4]

Full Research Paper

Open Access

Address:
[1]Chuiko Institute of Surface Chemistry of NASU, 17, Generala Naumova Str., Kyiv 03164, Ukraine, [2]Institute of Geotechnics SAS, 45, Watsonova, Kosice 04001, Slovak Republic, [3]Department of Inorganic Chemistry, Vilnius University, 24, Naugarduko Str., Vilnius LT-03225, Lithuania, and [4]Department of Chemistry and Biotechnology, Swedish University of Agricultural Sciences, 8, Almas allé, Uppsala 75007, Sweden

Email:
Gulaim A. Seisenbaeva* - gulaim.seisenbaeva@slu.se

* Corresponding author

Keywords:
copper(II) ions; methyl groups; N- and F-containing functional groups; silica nanospheres; sol–gel processes; sorption; surface chemistry

Beilstein J. Nanotechnol. **2017,** *8,* 334–347.
doi:10.3762/bjnano.8.36

Received: 30 September 2016
Accepted: 18 January 2017
Published: 02 February 2017

This article is part of the Thematic Series "Hybrid nanomaterials: from the laboratory to the market".

Guest Editor: A. Taubert

Abstract

Spherical silica particles with bifunctional (≡Si$(CH_2)_3NH_2$/≡$SiCH_3$, ≡Si$(CH_2)_3NH_2$/≡Si$(CH_2)_2(CF_2)_5CF_3$) surface layers were produced by a one-step approach using a modified Stöber method in three-component alkoxysilane systems, resulting in greatly increased contents of functional components. The content of functional groups and thermal stability of the surface layers were analyzed by diffuse reflectance infrared Fourier transform (DRIFT) spectroscopy, and ^{13}C and ^{29}Si solid-state NMR spectroscopy revealing their composition and organization. The fine chemical structure of the surface in the produced hybrid adsorbent particles and the ligand distribution were further investigated by electron paramagnetic resonance (EPR) and electron spectroscopy of diffuse reflectance (ESDR) spectroscopy using Cu^{2+} ion coordination as a probe. The composition and structure of the emerging surface complexes were determined and used to provide an insight into the molecular structure of the surfaces. It was demonstrated that the introduction of short hydrophobic (methyl) groups improves the kinetic characteristics of the samples during the sorption of copper(II) ions and promotes fixation of aminopropyl groups on the surface of silica microspheres. The introduction of long hydrophobic (perfluoroctyl) groups changes the nature of the surface, where they are arranged in alternately hydrophobic/hydrophilic patches. This makes the aminopropyl groups huddled and less active in the sorption of metal cations. The size and aggregation/morphology of obtained particles was optimized controlling the synthesis conditions, such as concentrations of reactants, basicity of the medium, and the process temperature.

Introduction

Materials with bi- or multifunctional surface layers have been of considerable interest in the recent years [1-11]. Such materials possess, undoubtedly, certain advantages over the materials with monofunctional coatings. For example, multifunctional drug-delivery agents may have functionalities ensuring their transportation to the desired target after introduction in the human body, whereas the functionalities of a different nature exert their, e.g., therapeutic effect [12]. Moreover, the creation of a multifunctional surface layer is an instrument for the subtle tuning of the sorption properties of materials by varying the nature, as well as the ratio of functional groups in the surface layer. Furthermore, combining hydrophobic and hydrophilic groups, reveals opportunities for creating, for example, the "pockets" with hydrophobic walls and a hydrophilic center (sorption or catalytic) [13], as well as the possibility of influencing the hydrophobicity of the surface layer.

The most suitable objects for such application are apparently hybrid organic–inorganic materials bearing surface-anchored functional groups. The methodology for their synthesis has reached a high-level, opening for broad practical application [14]. It is noteworthy that, as early as in the later part of the 20th century, Slinyakova et al. [15] drew attention to the extended possibilities of constructing new hybrid adsorbents systematizing data on polysiloxane xerogels containing hydrophobic surface layers, $(O_{3/2}SiR')_x$ and $[(SiO_2)_y(O_{3/2}SiR')_z]$, R' = $–CH_3$, $–C_2H_5$, $–CH=CH_2$, $–C_6H_5$. The papers describing the production of polysiloxane xerogels with complexing groups using one- [16] and two-component [17-19] (considering alkoxysilanes) systems brought about the understanding of such opportunities, and in [20] the results dealing with the synthesis, structure, and properties of polysiloxane xerogels with bifunctional surface layers were summarized. In the beginning of the 21st century, the studies of synthesis of mesoporous silicas functionalized with various groups emerged, [21,22] applying the well-known template method. Mann et al. were first to report it for the synthesis of hybrid organic–inorganic materials bearing functional groups of different nature [23-26]. Finally, there have been published papers describing the synthesis of non-porous silica nano- and sub-microspheres with functional groups in the surface layer [27,28]. The suggested technique was based on the Stöber method [29]. These silica spheres, because of their excellent properties, such as adjustable size and surface layer composition, along with their chemical stability and biocompatibility, are promising materials for the application in a wide range of areas (chromatography, controlled drug delivery, bioseparation, chemo- and biosensors, biocatalysis). Naturally, there arose a question about the possibility of synthesis for such particles with bi- and multi-functional surface layers.

The synthesis of functionalized silica nano- and sub-microspheres is achieved usually via two commonly used techniques. The first is based on the surface modification of Stöber silica spheres using trialkoxy silanes, $(RO)_3SiR'$. The second technique applies a one-step synthesis, where the network-forming agent (usually tetraethoxysilane, TEOS) and the functionalizing agent, $(RO)_3SiR'$ are introduced simultaneously or sequentially (in a given order) in the reaction medium. However, already the very first reports showed that, despite their simplicity, both approaches were dependent on a multitude of not fully understood factors affecting the shape and size of the particles, the content of functional groups, hydrolytic stability of the surface layer, and even the final product yield.

The amino group is one of the most desired functions on surfaces. It is capable both to bind directly to metal cations and is also useful in further grafting of new functions via organic condensation reactions [30]. In the studies examining one-step preparations of nanoparticles bearing 3-aminopropyl groups it was shown that heating a suspension in DMF at 100 °C for 24 h did not increase the content of surface amino groups, but improved the stability of the surface layer [28]. It was shown [27] that the introduction of 3-aminopropyltriethoxysilane (APTES) to TEOS sol in ethanol in a molar ratio of 1:1 yielded nanoparticles with an average diameter around 66 nm, but their surface layer contained almost no amino groups. At a TEOS/APTES molar ratio of 3:1, the surface layer did contain amino groups (1.56 mmol/g), but the particle size decreases to about 9 nm. When the order of components introduction was changed, the content of functional groups increased to 3.2 mmol/g. However, according to ^{29}Si NMR spectroscopy, the content of Q^4 structural units decreased. This might indicate lower degree of cross-linking in the polysiloxane networks in the particles.

The most broadly used technique for the preparation of aminoalkyl functionalized silica has been, however, the surface modification of pre-produced nanoparticles with trialkoxy silanes. For example, in [31] APTES or phenyltriethoxysilane were used as modifiers. However, the amount of modifiers was negligible (4.79×10^{-4} mol), and the process time was as long as 19 h. The size of the particles bearing APTES was 150 nm (while the size of the initial TEOS particles was 149 nm). The moment when the second silane is added plays an important role. It was demonstrated that the availability of ligands on the surface could be affected by the time of addition for such functions as amino, monocarboxylate, ethylenediaminetriacetic acid, and dihydroimidazole-terminated ones [32]. The best surface availability of organofunctional groups was achieved for the amino-terminated ligands when the organosilane was added 30 min after start of the particle growth, and for the carboxylate-termi-

nated ones the optimal addition time was 5.5 h after particle growth initialization. No efficient one-step approaches to dual functional particles bearing an aminopropyl group have been reported so far to the best of our knowledge.

The major interest in the studies of bifunctional particles bearing an amino function lies in achieving control over its stability to hydrolysis and especially over its availability and chemical reactivity. In monofunctional layers it is often involved in direct hydrogen bonding to the Si–OH groups on the surface, which decreases its chemical availability and can cause hydrolytic elimination of the siloxane fragment bearing this group [33-35]. The mechanisms of stabilization and the relation to the activity in adsorption of copper(II) cations has been more recently discussed in the works of Soler-Illia and co-workers [36,37]. Using DFT calculations it was demonstrated that the protonated amino groups are irreversibly transmitting a proton to the $Si–O^-$ groups on the surface with subsequent breaking of the Si–O–Si bridges and potential release of silane species [36]. Apparently, the complexation with Cu(II) ions is additionally catalyzing this process, resulting in the loss of amino functions [37]. It was demonstrated that stability of the surface layer could be improved by gentle thermal treatment, leading to additional condensation of the –OH groups and elimination of the surface $Si–O^-$ groups [37]. This transformation is, however, difficult to control. In the present work we propose to use a principally different strategy for stabilization of the surface layer inserting instead different hydrolytically stable hydrophobic functions, hindering the formation of H-bonds. We have applied two types of such groups, namely small ones with considerably reduced capacity to van der Waals bonding such as methyl groups, and rather large and long ones with potentially strong van der Waals bonding such as fluorinated groups.

We also aimed to test the availability and reactivity of the amino function via Cu^{2+}-cation adsorption as a probe, using electron paramagnetic resonance (EPR) and electron spectroscopy of diffuse reflectance (ESDR) spectroscopy. This approach permits also to identify the nature of the surface complexes and thus probe the arrangement of the amino groups.

An effort has also been made to summarize the effects of factors influencing the size and aggregation of the produced particles.

Results

We synthesized samples with aminopropyl groups, aminopropyl and methyl groups, aminopropyl and fluorine-containing groups. The samples, bearing only the aminopropyl groups were denoted as **N**, those bearing both aminopropyl and methyl groups as **NM** and those, bearing the fluorinated along with aminopropyl groups as **NF**. A detailed description is provided below in the Experimental section.

It is known that the temperature influences the process of hydrolysis and condensation of silanes, resulting in the formation of oligomers of different length. Therefore, the size of the silica particles depends on the synthesis temperature [38]. The particles with bifunctional surface layers at a TEOS/APTES/MTES (methyl triethoxysilane) ratio of 3:0.5:0.5 were synthesized at different temperatures (samples **NM**, **NMh** and **NMi**). Also bifunctional samples with amino and perfluorooctyl groups in the surface layer at various TEOS/APTES/PFES ratios (**NF1**–**NF4**) were synthesized. During synthesis APTES was first added to the ethanol–water–ammonium solution, and then the mixture of alkoxysilanes with different TEOS/PFES ratios was introduced.

Morphology and particle size distribution of bifunctional silica samples were examined using SEM (Figure 1 and Figure 2). It is important to note that for the amino/methyl samples no direct link between the temperature and the particle size could be observed (contrary to aminosilica samples (Table S1, Supporting Information File 1). Lowering the temperature did not lead to a particle size change but the morphology of the particles was improved. At all temperatures, the sizes of the bifunctional amino/methyl particles that formed were smaller compared to monofunctional amino samples (Figure 1, Table S1, Supporting Information File 1). The nanoparticles with bifunctional amino-/fluorine-containing surface layer are not uniform in size (Figure 2), but their shape is close to spherical.

The particle size and morphological features were also reflected in the measured active surface area (see Table S1, Figure S1, Supporting Information File 1). The values were the highest for the bifunctional particles bearing methyl groups. The dominating feature of the monofunctional fluoroalkyl-substituted particles was that with increasing surface coverage they became more smooth and uniform in size (see Figure S3, Supporting Information File 1), which led to a loss of surface area.

The presence of target functional groups in the surface layers of the particles was confirmed by IR spectroscopy (diffuse reflectance infrared Fourier transform, DRIFT, for details see Figure S6, Supporting Information File 1) and their structure was analyzed by solid-state NMR.

All the ^{13}C CP/MAS NMR spectra (Figure 3, Figure S2 and assignment in Tables S2 and S3, Supporting Information File 1) contained signals from three carbon atoms of the aminopropyl chain of APTES [27]. In addition, the spectra of some samples obtained at lower temperatures showed signals from carbon

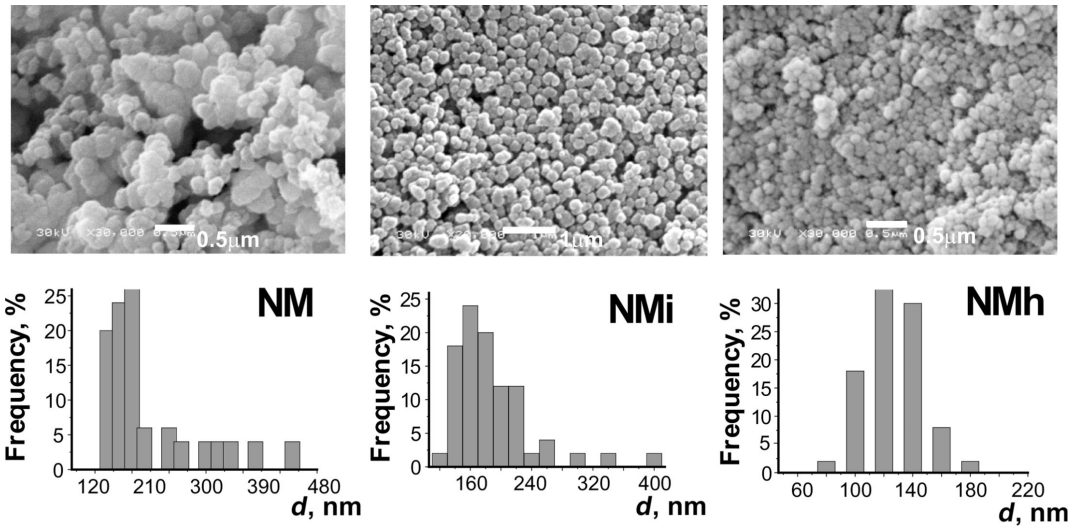

Figure 1: SEM images and particle size distribution curves for amino/methyl-containing samples **NM**, **NMi**, **NMh**.

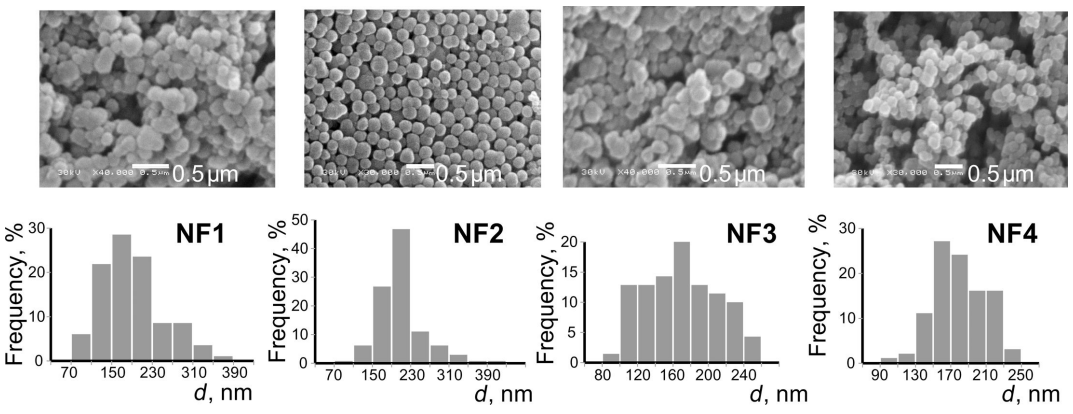

Figure 2: SEM images of amino-/fluorine-containing samples.

atoms of residual ethoxysilyl groups absent in the spectra of samples obtained at 50 °C.

In the case of the bifunctional samples (Figure 3), the ^{13}C CP/MAS NMR spectrum of **NMh** also exhibits the signal of the carbon atom from methylsilyl group and the spectrum of **NF3** contains a group of signals in the region of 108–120 ppm characteristic of carbon atoms from the perfluoric chain ($-(CF_2)_5CF_3$) [39]. The signal with the highest frequency (δ = 119.5 ppm) apparently corresponds to the carbon atom from CF_3, and a shoulder at 108 ppm corresponds to the carbon atom from the CF_2 group adjacent to CF_3. The overlapping peaks at 110–113 ppm apparently belong to other CF_2 carbon atoms. Two more signals in ^{13}C CP/MAS NMR spectrum of **NF3** are due to the presence of perfluorooctyl groups of PFES. The peak at δ = 65.2 ppm originates from CH_2 carbon adjacent to CF_2 and the peak at δ = 3.8 ppm from the first carbon atom of the perfluorooctyl group bound to the silicon atom. Thus, the synthesized particles contain functional groups introduced with trialkoxy silanes during their syntheses.

The ^{29}Si CP/MAS NMR spectra of the samples shown in Figure 3 are similar and contain two groups of signals. The first one (in the region from −110 to −90 ppm) indicates the presence of structural units Q^4, Q^3, and Q^2. The signal with a chemical shift of −109 to −110 ppm is typical for silicon atom in a polysiloxane network $Si(O_{0.5})_4$ (structural units of Q^4 type). The signal at δ = −101 ppm refers to Q^3 units, namely, the silicon atoms bound to terminal silanol groups $Si(O_{0.5})_3OH$ or to unhydrolyzed ethoxy groups $Si(O_{0.5})_3OC_2H_5$. The weak signal at about −91 ppm, which is distinct for the sample **NF3** (for other samples it features a weak shoulder, see Figure 3), indicates the presence of Q^2 structural units $(Si(O_{0.5})_2(OR)_2$, where R = H or C_2H_5). The second group of signals (at about

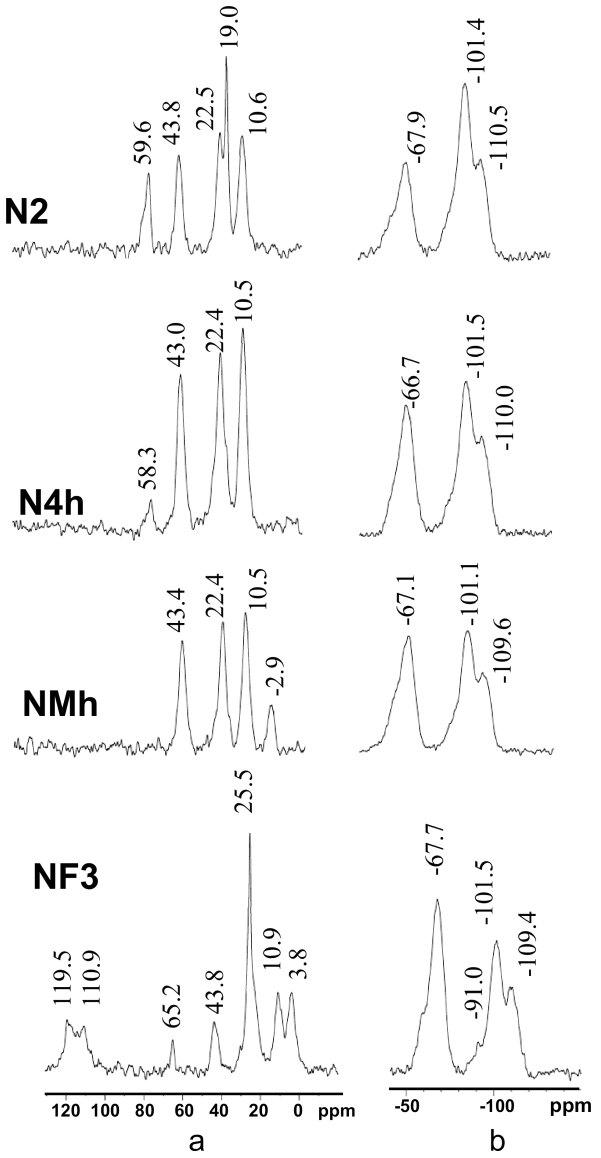

Figure 3: ^{13}C (a) and ^{29}Si (b) CP/MAS NMR spectra of the synthesized samples.

−68 ppm with a pronounced shoulder at −59 ppm, see Figure 3) belongs to T^3 and T^2 structural units, respectively (≡SiR' and ≡Si(OR)R', where R' is a functional group $–(CH_2)_2(CF_2)_5CF_3$ or $–(CH_2)_3NH_2$) [40,41].

The contents of the functional groups present in mono- and bifunctional samples were quantified using thermal analysis (Figure S7 and Table S1, Supporting Information File 1), acid–base titration, elemental analysis and EDXS analysis (Table S4, Figure S4, Supporting Information File 1). According to these data, the content of amino groups in monofunctional silica particles is in the range of 0.5–2.0 mmol/g (at a ratio of TEOS/APTES = 3:1), which is about half of what is expected from the ratio of reacting alkoxysilanes. For the bifunctional samples with methyl groups we observed an amount of amino functional groups of 1.8–2.0 mmol/g at the ratio of TEOS/APTES/MTES = 3:0.5:0.5 (i.e. at half the applied amount of APTES). The content of methyl groups is about a third of what is expected from the ratio of silanes.

The content of amino and perfluorooctyl groups in bifunctional fluorinated samples (according to elemental analysis) generally agree with the theoretically calculated values. However, according to acid–base titration data not all amino groups are available for H^+ sorption.

The intrinsic structure and reactivity of the aminopropyl groups were investigated using Cu^{2+} adsorption. In the view that EPR spectra of the copper(II) complexes provide direct insight into the coordination of these cations, they were thus revealing the spatial arrangement of the ligands. The kinetic studies were performed first to estimate the equilibrium time (see kinetic sorption parameters obtained using pseudo-first and pseudo-second-order models for metal ions sorption in Table S5, Supporting Information File 1). According to the presented data, the kinetic curves for the samples fit the pseudo-second-order model (Figure 4). The fastest is the reaction on amino/methyl bifunc-

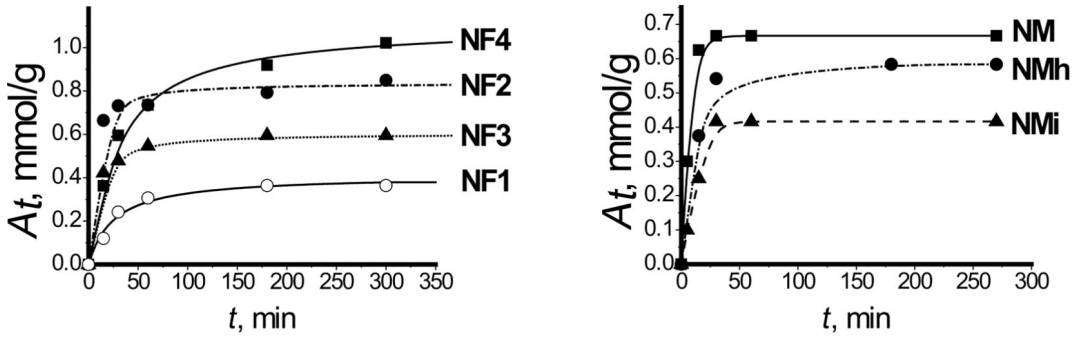

Figure 4: Pseudo-second-order kinetic curves for the sorption of copper(II) ions by the synthesized samples (the continuous lines are showing the fit of the model for each case with experimental points indicated by geometrical symbols).

tional samples, where the equilibrium is reached within 30 min. Thus, based on the kinetic curves, specific times for the adsorption of copper(II) ions were chosen for each sample. The adsorption isotherms are presented in Figure 5.

To determine the formal coordination surrounding of Cu(II) ions in the adsorption layer, the isotherms were plotted in the form of C^s_{Cu}:C^s_R as a function of C^0_{Cu}:C^0_R (Figure 6, Figure S8, Supporting Information File 1).

These data were complemented by EPR and diffuse reflectance spectra (Figure 7 and Figure 8). Generally, the composition of the complexes of copper(II) ions with amine groups of monofunctional samples has a Cu^{2+}/Lig ratio in the range of 1:1–1:4

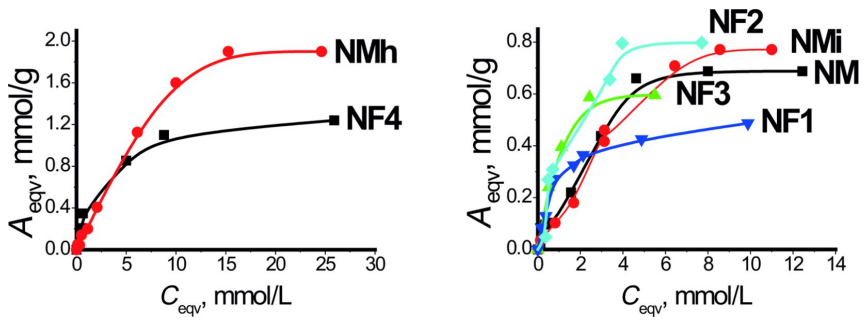

Figure 5: Copper(II) ion adsorption isotherms at 28 °C.

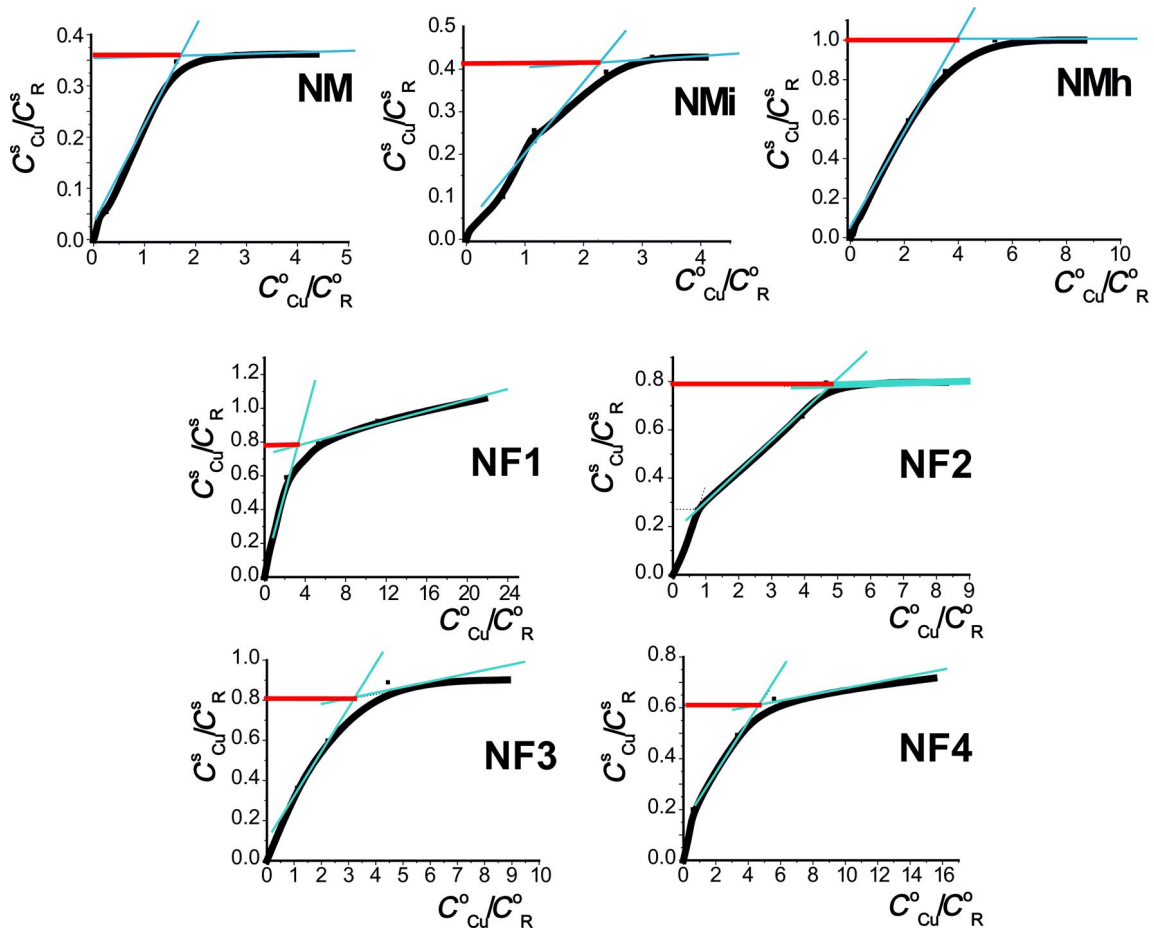

Figure 6: The molar ratio of copper(II)/aminopropyl groups in the surface of the microspheres as a function of that ratio in the initial solution.

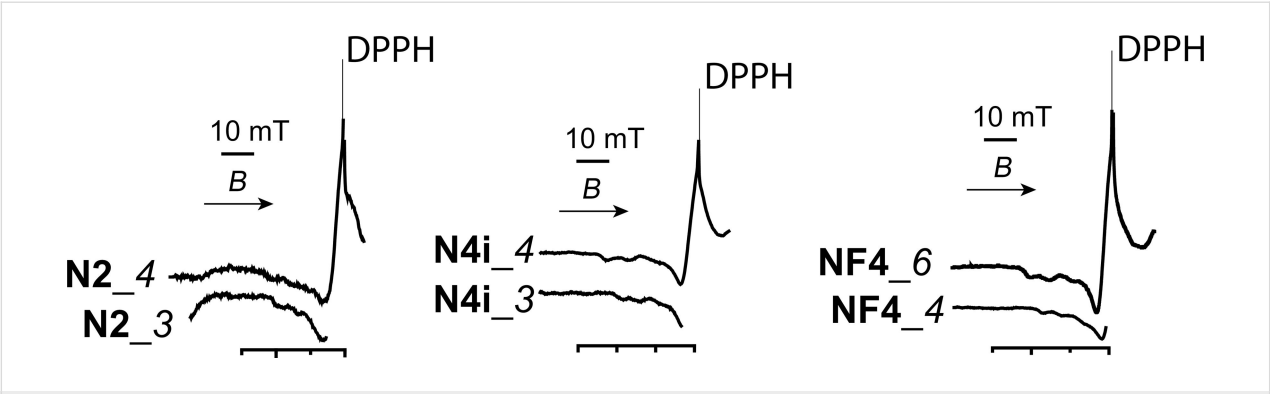

Figure 7: EPR spectra of some samples after adsorption of copper(II) ions (see Table S7, Supporting Information File 1 for details).

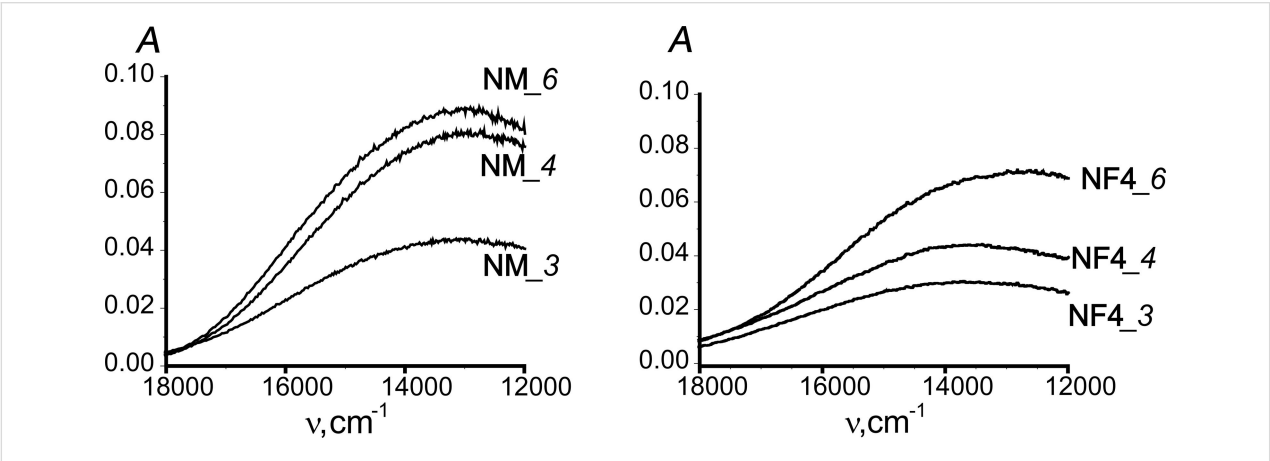

Figure 8: ESDR spectra for samples with different contents of Cu^{2+} in the surface layer.

(Table S6, Supporting Information File 1). For bifunctional samples, especially those containing fluoroalkyl radicals, the gross compositions of Cu^{2+}/Lig complexes are close to 1:1.

Table S7 (Supporting Information File 1) provides parameters of the EPR spectra of copper(II) complexes formed on the surface of some carriers discussed in this paper, and Figure 7 represents the EPR spectra of some of these systems.

Unfortunately, in some cases, we could not obtain satisfactory EPR spectra, especially when the sorption was carried out from an excess concentration of copper(II) in the solution. But for all the samples, at a molar metal/ligand ratio of 1:2, satisfactory EPR spectra were recorded, the parameters of which (Table S6, Supporting Information File 1) are very close to the values characteristic of the Cu/Lig = 1:2 complex composition. Complexes of such composition also formed at an excess concentration of metal ions (see Table S7, **NF4**_*6*, Supporting Information File 1). Similar copper(II) complexes were found on the surfaces of various xerogels containing 3-aminopropyl groups [42].

Figure 8 and Figure S9 (Supporting Information File 1) present ESDR spectra for some samples with different contents of Cu^{2+} ions in their surface layers. All spectra feature a broad band in the region of 13000–20000 cm^{-1}, which is characteristic of copper(II) complexes with amino ligands and refers to d→d transitions [43]. The position of the maximum of this band depends on the nature of the functional group and on the C^S_{Cu}/C^S_R ratio (the degree of surface filling with metal). However, in almost all cases, the maximum of this band is at about 13000–14000 cm^{-1}.

We measured adsorption isotherms of *n*-hexane, acetonitrile and water (Figure S10, Supporting Information File 1) to compare the properties of silica nanoparticles with fluorine (see Supporting Information File 1) and amino/perfluoroalkyl-containing bifunctional surface layers. In the case of bifunctional sample **NF2**, at low fillings, the three vapor adsorption isotherms of *n*-hexane, acetonitrile, and water coincide. However, with increasing P/P_s values, motre acetonitrile is adsorbed compared to water and *n*-hexane. During the synthesis, the ratio of amino/fluorine-containing groups was 1:1. Acetonitrile is electrostati-

cally repelled from amino groups of the surface [44]. However, in spite of this, its sorption volume is similar to that of water and *n*-hexane.

Discussion

Our interest was to identify the molecular mechanisms of how the hydrophobic groups influence stability and reactivity of the aminopropyl groups. We decided to apply additional groups with rather different characteristics to be able to distinguish the principles of their action, namely small alkyl (methyl) groups and rather long perfluoroalkyl ones.

Factors controlling size and morphology of the particles

Previously it was shown that the introduction of alkyl groups along with 3-aminopropyl groups in the surface layer improves its hydrolytic stability [45] and enhances the adsorption of biomolecules [46,47].

In developing the synthesis in the present work we took into account the already developed principles of the production of APTES-derived materials [48,49]. The particles are generally smaller when higher TEOS/APTES ratios are applied [31]. They are less coalesced in the presence of higher ammonia content because of a stronger negative charging of the growing entities, which is especially important for highly hydrophobic materials that can otherwise form gels separating from solutions [50-52]. The most efficient way to keep the aminopropyl groups on the surface is to add TEOS after the APTES and, especially, to slightly increase the ammonia content [28] (see also Figure S1, Table S1, Supporting Information File 1).

Carrying out the process at higher temperatures resulted in smaller particles that, however, aggregated. MTES is characterized by a more facile hydrolysis and condensation compared to TEOS. This results, in combination with the fact that methyl groups are not charged and in their turn "dilute" the charged groups on the surface, in the observed difference between **N4** and **NM** samples produced under similar conditions. The particle growth facilitated by quick condensation with MTES leads to better shaped particles at lower temperatures, while the increased temperature favors nucleation with less charged and easier coalescing nuclei that aggregate easier (sample **NMh**). The behavior of the three-component system APTES/TEOS/MTES is thus more complex and is not dominated by the reactivity of any single component.

The decrease in TEOS concentration in the reaction solution (at the same PFES/APTES ratio) causes a decrease in particle size (see average diameters of samples **NF3** and **NF1** in Table S1, Supporting Information File 1). Finally, reducing the amount of fluorinated groups compared to **NF3** (Figure 2) leads to the formation of substantially spherical **NF2** (Figure 2). The particles turn more uniform in size with slightly bigger average diameters (Table S1, Supporting Information File 1). The reverse trend is observed in the case of increasing the APTES concentration at a constant TEOS/PFES ratio (see Table S1, samples **NF2** and **NF4**, Supporting Information File 1).

It is important to mention that particles in both **NF4** (Figure 2) and **NM** (Figure 1) samples are considerably smaller in size with of d_{av} = 190 nm and 180 nm, respectively, compared to their monofunctional analogues, **N2** (d_{av} = 360 nm) and **N4** (d_{av} = 280 nm) (Figure S1, Supporting Information File 1). It can be deduced that the introduction of a silane bearing a hydrophobic group possibly favors nucleation over growth and results in relatively smaller particles.

Molecular structure of the functional layers from IR and NMR data

IR spectroscopy was used to identify the presence of functional groups in the surface layers of nanoparticles. Consequently, IR spectroscopy confirmed the presence of a polysiloxane network containing 3-aminopropyl and methyl or fluorinated functional groups, as well as silanol groups, and alkyl radicals in the synthesized particles. Furthermore, all samples contained water (DRIFT analysis in Supporting Information File 1).

Solid-state CP/MAS NMR spectroscopy, especially ^{13}C and ^{29}Si NMR spectroscopy, has been widely used to study silica materials, it can provide information about hydrolysis and condensation processes. Clearly, hydrolysis and polycondensation of ethoxysilyl groups significantly accelerated with increasing synthesis temperature [38]. With the introduction of hydrophobic groups, the intensity of the signals from ethoxy groups (at 58–60 ppm and a shoulder at 18–19 ppm) in the ^{13}C CP/MAS NMR spectra (Figure 3a, Table S2, Supporting Information File 1) is significantly reduced. As for the characteristic signals from ethoxysilyl groups in the spectrum of fluorinated sample, they are faint, indicating completeness of their hydrolysis during the synthesis. Apparently, the ethoxy groups constitute a part of the interface between the particles and the solution. Their weak hydrophobic interactions with the ethanol-based solvent are apparently outcompeted by either stronger hydrogen bonding to the amino/ammonium functions or the strong hydrophobic interactions involving the fluoroalkyl groups.

Thus, taking into account the ^{13}C CP/MAS NMR data, it may be concluded that R = H for the fluorinated samples, while for other samples R = ethyl radical in structural units $(Si(O_{0.5})_2(OR)_2$ or $(Si(O_{0.5})_3(OR)$. According to ^{29}Si CP/MAS

NMR data the cores of the synthesized particles are likely to consist of condensed tetrahedral SiO_4, and their surface layer contains functional and silanol groups belonging to structural units of different composition.

Probing the ligand layer structure by Cu(II) adsorption

There are several key factors affecting the adsorption of ions on the surface, namely the content, availability, and arrangement of functional complexing groups. The content of functional groups was determined by various physical methods (Table S4, Supporting Information File 1). For all the samples, the content of amino groups calculated from elemental analysis is higher than determined by titration, which means that not all amino groups are available for the sorption of ions. It may be connected with the partial aggregation of particles. The arrangement of amino groups in the surface layer of bifunctional silica particles depends on the length and nature of the second functional group.

The topography of the functional groups attached to the surface of the amorphous carriers, and their conformational behavior are the least extensively studied matters so far. This prevents the fully reliable interpretation of the experimental results and hinders the prediction of the behavior of such functionalized carriers in various chemical processes. Such limited knowledge results from the intricacy of the problem, which requires the application of different physical methods for its solution. We used the highly reliable metal-probing method. Copper(II) ions were chosen as metal ions for probing, since the composition and structure of copper–ammonia complexes are well known. They also correlate well with the data obtained by some other physical methods (e.g., electron spectroscopy and EPR) as is traced in detail in [53].

Comparing the values of the sorption rate constants for monofunctional and amino/methyl samples, we can conclude, that the rate of sorption for the latter is almost twice as high (Figure 4, Table S5, Supporting Information File 1). This may be due to the fact that amino groups located on the surface of monofunctional amino silica particles can form hydrogen bonds with silanol groups. In contrast, the amino groups on the surface of amino/methyl silica particles are surrounded by methyl groups, which prevent the formation of hydrogen bonds with silanol groups (Figure 9a,b), increasing the speed of interaction with copper(II) ions. As for amino/fluorine-containing particles, their smaller rate constant values (Table S5, Supporting Information File 1) indirectly indicate the "island-like" structure of the surface layer, where the "islands" of amino groups are surrounded with long hydrophobic radicals (Figure 9c,d) preventing the diffusion of ions to the centers of adsorption. Consequently, the introduction of methyl groups thus either stabilizes the surface layer or leads to enhanced accessibility of amino groups. The latter correlates well with the data from the adsorption of Cu^{2+} cations (see below).

The composition of complexes depends on several factors. For example, the composition of complexes for the samples with amino/methyl groups obtained at different temperatures appeared to be different. Thus, for the sample **NMi**, the Cu^{2+}/Lig ratio is close to 1:2, which is similar to xerogels synthesized on an ice bath [54], where amino groups are located on the surface in pairs. When the synthesis temperature is higher (sample **NMh**), the rate of condensation is also higher, and more methyl groups get fixed on the surface according to TGA and elemental analysis data (Table S1 and Table S4, Supporting Information File 1). Therefore, some of the amino groups are located at a distance that does not favor the formation of stable 1:2 complexes, and the form dominating at higher Cu^{2+}/Lig ratios can be assumed to have the 1:1 composition. As for the sample **NM**, synthesized at room temperature, it appears that the ratio of copper(II) ions to aminopropyl groups in the upper layer is 1:3. It may be explained by the presence of the combination of Cu^{2+}/Lig complexes 1:2 and 1:4 (Figure 6).

This is consistent with the 1:2 composition of Cu^{2+}/Lig complexes suggested by the EPR spectra. According to literature [43,55], the tetragonally distorted octahedral copper(II) complexes, which contain four amine ligands in the equatorial plane are characterized by a band of d→d transitions around 17000–19000 cm^{-1}, whereas ESDR spectra of the complexes with two amine ligands in the equatorial plane exhibit a band in the region of 14500–15000 cm^{-1}. This suggests that the coordination sphere of copper(II) ions in the surface layers of the discussed samples contains two amino groups. The shift of the maximum to lower frequencies may result from the distortion of the octahedral coordination of the central atom. Obviously, with increasing C^S_{Cu}/C^S_R ratio the sorption will also take place in the surface regions less favorable for the formation of ideal coordination polyhedra. The calculations of the Langmuir and Freundlich isotherm sorption parameters are presented in Table S6 (Supporting Information File 1). According to Table S6, the adsorption isotherms for amino and amino/methyl samples fit well the Freundlich isotherm model, whereas the fluorine-containing samples fit the Langmuir isotherm model.

Correlation between the structure of the surface layers and adsorption of small molecule substrates

As it can be deduced from the results of EPR and ESDR studies, the surface of the particles is energetically and chemically heterogeneous due to the presence of different functional

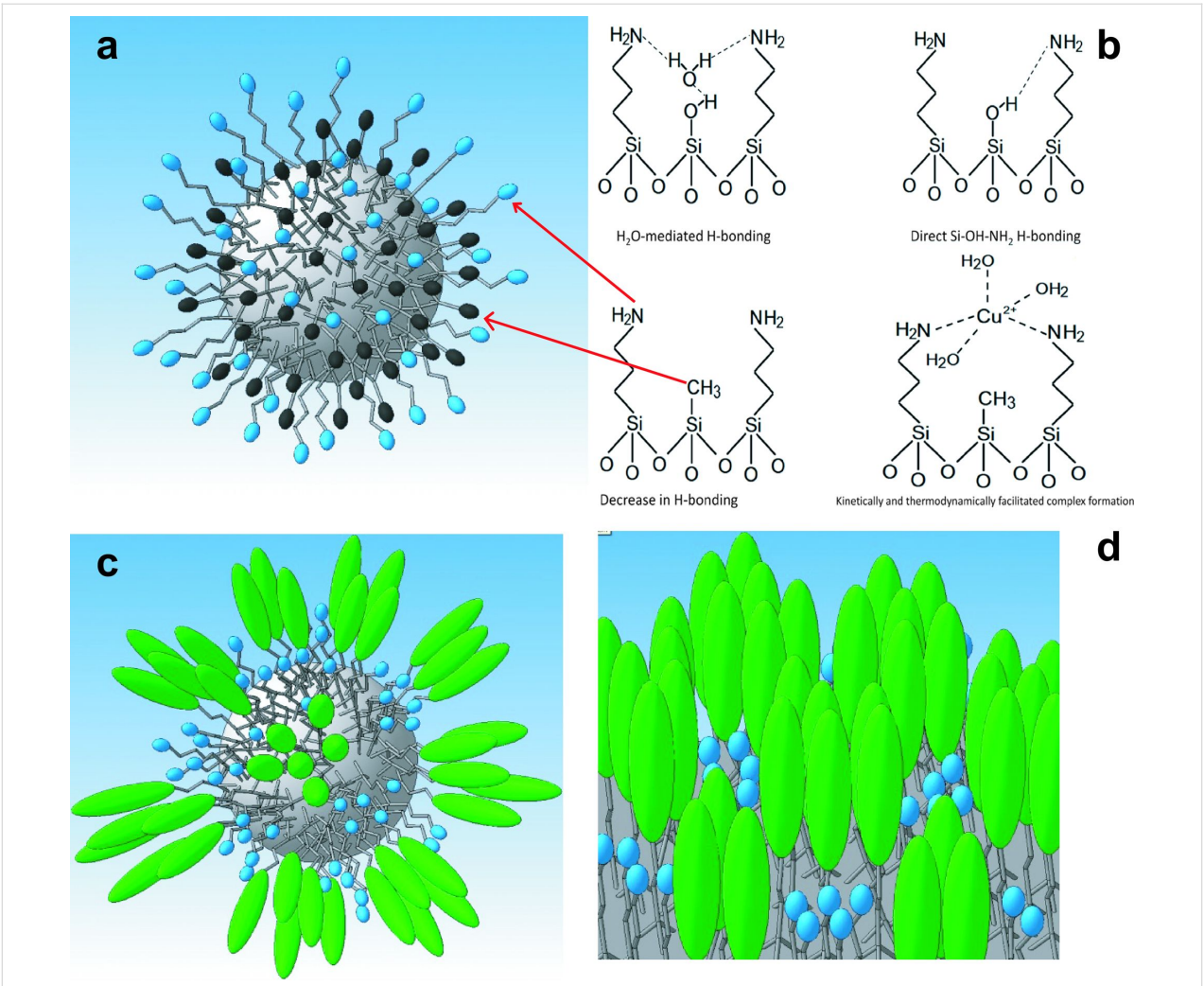

Figure 9: a) Proposed structure of the surface layer on the of bifunctional silica particles bearing methyl and aminopropyl groups (in the image chains with black and blue headgroups, respectively); b) scheme of molecular interactions in the monofunctional layer bearing aminopropyl groups and the bifunctional layer with aminopropyl and methyl groups; c,d) proposed surface structure of the bifunctional layer for particles bearing perfluoroctyl and aminopropyl (in the image chains with green and blue head groups, respectively) groups on the surface.

groups, arranged either as a "random forest" in the samples bearing methyl group, or as islands with distinctly different properties and structures. Therefore, such a surface is predisposed for specific adsorption interactions with molecules of different electronic structure and especially different polarity. The molecules of *n*-hexane are capable of adsorption interactions due to dispersion forces, whereas interaction of acetonitrile with the surface is dominated by the basic properties of the nitrogen atom.

Obviously, acetonitrile (as well as *n*-hexane) interacts with hydrophobic sites formed by fluorine-containing groups, while the water molecules interact with hydrophilic sections created by amino groups. Thus the introduction of aminopropyl groups in the fluorine-containing surface layer changes the nature of the surface, which is confirmed by the order of the adsorption isotherms in Figure S10 (Supporting Information File 1). But because of the long length of the fluorinated "tails", 3-aminopropyl groups do not overhang on the surface, which promotes the adsorption of acetonitrile by such bifunctional samples.

Thus, we can assume that the affinity to acetonitrile is probably related to its sorption on hydrophobic "islands" formed by fluorine-containing "tails". Furthermore, the values of sorption volume of the vapors of *n*-hexane, acetonitrile, and water for sample **NF2** are similar, which indirectly confirms the "island" structure of the surface layer (Figure 9c,d).

Conclusion

Silica particles with bifunctional surface layers and high content of available aminopropyl groups were successfully produced by a modified one-step Stöber approach. Combining hydrophobic

ligands with the aminopropyl grous in the surface layers of hybrid silica particles appears to offer generally smaller particles. Their surface is apparently porous when methyl groups are introduced as co-ligand and becomes smoother when perfluoroalkyl groups are applied, especially when their coverage fraction is increased. The molecular structure of the bifunctional layers depends strongly on the nature and fraction of the co-ligand. The methyl groups dilute the aminopropyl groups uniformly, opening for uptake of higher amounts of Cu^{2+} ions used as probes in relation to the amount of grafted amino functions. This should even improve potentially the reactivity used for further functionalization of amino modified silica. The introduction of perfluoroalkyl co-functions even at low fraction leads to the formation of "island" structures. Increase in the content of the perfluoroalkyl co-ligands leads to huddling and inactivation of amino functions. As a consequence the amino functions become apparently partly inaccessible for the complexation with Cu^{2+} as testified by low Cu^{2+}/Lig ratios (0.35 and lower), while the simultaneous EPR and ESDR measurements reveal the formation of the trans $Cu(Lig)_2^{2+}$ complexes. Changes in the surface geometry in the bifunctional layers even result in unusual patterns of adsorption of small organic molecules, making the particles capable to use both hydrophobic and hydrophilic functions simultaneously.

Experimental

Materials

The applied precursors were: tetraethoxysilane, $Si(OC_2H_5)_4$ (TEOS, 98%, Aldrich); 3-aminopropyltriethoxysilane, $(C_2H_5O)_3Si(CH_2)_3NH_2$ (APTES, 98%, Fluka); methyltriethoxysilane, $(C_2H_5O)_3SiCH_3$ (MTES, 99%, Aldrich); 1*H*,1*H*,2*H*,2*H*-perfluorooctyltriethoxysilane, $(C_2H_5O)_3Si(CH_2)_2(CF_2)_5CF_3$ (PFES, 98%, ABCR); ethanol (96%); aqueous ammonia (25% aq) (reagent grade, Macrochem, Ukraine). Reagents for acid–base titration and sorption: $Cu(NO_3)_2{\cdot}3H_2O$ (reagent grade, Macrochem, Ukraine), NH_4Cl, $NaNO_3$, NaCl (chemically pure, Macrochem, Ukraine); HNO_3, HCl, NaOH, EDTA - fixanal concentrates (Reahim, Ukraine); murexide (analytical grade, Reahim, Ukraine).

Synthesis of nanoparticles

The particles were produced by a single-step Stöber approach (for details see Supporting Information File 1) using TEOS, APTES and an additional hydrophobic reagent and differed either in the ratio of the reactants or in the temperature conditions.

Methyl-substituted samples were synthesized using a ratio of TEOS/APTES/MTES = 3:0.5:0.5 at different temperatures and are denoted as **NM** (RT.), **NMi** (0 °C, ice bath), and **NMh** (50 °C). Perfluorooctyl-substituted samples were produced at room temperature at different reactant ratios and are denoted as **NF1**, **NF2**, **NF3**, and **NF4** (TEOS/APTES/PFES = 3:0.25:0.25, 3:0.5:0.1; 3:0.5:0.5, and 3:1:0.1, respectively).

For the sake of comparison monofunctional samples were produced, denoted as **N1** (TEOS/APTES = 1:1, RT), **N2**, **N3** and **N4** (TEOS/APTES = 3:1, RT; the first with addition of first APTES, the second with first addition of TEOS, and the third with later addition of the NH_3 catalyst). The labels **N4i** and **N4h** stand for carrying out the **N4** procedure at 0 °C and 50 °C, respectively. The labels **F1** and **F2** stand for the RT procedures with TEOS/PFES = 3:1 and 3:0.5, respectively.

Characterization techniques

Thermal analysis was performed on the MOM Q-1500 D (Paulik–Paulik–Erdey) derivatograph operating in the range of 20–1000 °C, with a heating rate of 10 °C·min^{-1}.

DRIFT spectra were recorded on a Thermo Nicolet Nexus Fourier-transform infrared spectrometer in the range of 400–4000 cm^{-1}, working in "Nexus Smart Collector" mode and averaging 50 scans with a resolution of 8 cm^{-1}. The samples were previously ground with solid KBr (Spectral, Aldrich).

^{13}C and ^{29}Si MAS NMR experiments were carried out on a Bruker Avance II 400 spectrometer using 4 mm rotors (ZrO_2) spun at 10 kHz. ^{13}C NMR spectra were recorded using $^{1}H \rightarrow {}^{13}C$ CP/MAS, ^{1}H decoupling during acquisition, 3 ms contact time, and 5 s recycling delay. The number of scans was between 768 and 2300. ^{29}Si NMR spectra were recorded with 3 µs excitation pulses, a contact time of 2 ms, and 5 s recycling delay. The number of scans was between 640 and 1024. ^{13}C and ^{29}Si chemical shifts are referenced towards 4,4-dimethyl-4-silapentane-1-sulfonic acid (DSS).

CHNS elemental analysis was performed by elementary analyzer Vario MACRO cube (Elementar Analysensysteme GmbH, Germany) using a thermal conductivity detector. Helium and oxygen (both purity 99.995%) were used as the carrier and combusting gases, respectively, with 2 bar intake pressure. The combustion tube was set at 1150 °C and the reduction tube at 850 °C. Sulfanilamide $C_6H_8N_2O_2S$ was used as CHNS standard.

For SEM studies with a JSM-6060LA analytical scanning electron microscope (Jeol, Tokyo, Japan) using secondary electrons at an accelerating voltage of 30 kV, the samples were fixed on the objective tables. To prevent the accumulation of the positive charges and to receive contrasting images, the surface of the samples was covered with a thin continuous layer of gold or platinum by cathodic sputtering in vacuum. The morphology of

the obtained samples was also studied by Hitachi TM-1000 tabletop microscope capable of energy-dispersive X-ray spectroscopy (EDXS) analysis.

The measurement of nitrogen adsorption isotherms was carried out on a Kelvin-1042 (Costech Microanalytical) analyzer. The time for preliminary degassing was 1 h at 110 °C. The BET surface area [55] was evaluated at relative pressures of 0.05–0.35.

Adsorption isotherms of *n*-hexane, water and acetonitrile were obtained at 20 °C using a vacuum microbalance (balance sensitiveness: 1.9–2.8 mg/mm). The samples were first evacuated at 105 °C to a constant weight. Air was removed from the adsorbate by cycles of freezing/defreezing during vacuum pumping.

Acid–base titration was used to determine the content of amino groups [56]. This method is based on the determination of the number of protons captured by amine groups after submerging the sample batch (0.1 g) in excess of 0.01–0.05 M HCl till equilibrium was established (which was 24 h). The excess of HCl was determined by back titration with 0.01–0.05 M NaOH solution (using methyl orange as indicator).

The study of the equilibrium time for copper(II) sorption was performed using 0.02 g of sorbent at 28 °C. 20 cm^3 of solution containing double excess of copper(II) in relation to stoichiometry was added, varying only the contact time from 5 min to 24 h. The linear pseudo-first-order and pseudo-second-order equations [57] were used for the description of the kinetic model:

$$\ln\left(a_{\mathrm{eqv}} - A_t\right) = \ln a_{\mathrm{eqv}} - k_1 t,$$

$$\frac{t}{A_t} = \frac{1}{k_2 a_{\mathrm{eqv}}^2} + \frac{t}{a_{\mathrm{eqv}}},$$

where A_t and a_{eqv}, are the adsorbed amounts at time t and at equilibrium (mmol/g), respectively; k_1 and k_2 are the rate constants of pseudo-first-order (min^{-1}) and pseudo-second-order adsorption process ($g{\cdot}mmol^{-1}{\cdot}min^{-1}$).

The sorption of copper(II) ions from water solution was studied under static conditions at 28 °C. The sorbent batch of 0.03 g was placed in a 50 cm^3 weighing bottle, and 20 cm^3 of $Cu(NO_3)_2$ solution was added to it. The ionic strength was maintained by 1 M $NaNO_3$ solution. The concentration of metal ions in aqueous medium was determined by direct titration of metal ions with 0.0125–0.025 M EDTA (indicator: murexide, buffer: ammonia).

Isotherm model evaluation: the Langmuir isotherm is a broadly used model, assuming adsorption to occur on specific sites uniformly spread on the surface of the adsorbent. It is commonly used for description of processes, where adsorbed species form a monolayer, and is described by the following equation:

$$\frac{C_{\mathrm{eqv}}}{a_{\mathrm{eqv}}} = \frac{1}{K_{\mathrm{L}} \cdot a_{\max}} + \frac{1}{a_{\max}} \cdot C_{\mathrm{eqv}},$$

where C_{eqv} is the concentration of solute remaining in solution after equilibrium to be reached (mmol/L); a_{eqv} is the amount of solute adsorbed under the same conditions (mmol/g); $a_{\max}$ is the maximum adsorption capacity in the monolayer and K_{L} is the equilibrium constant of the adsorption process.

The Freundlich isotherm describes multilayer adsorption and has been used to establish a mathematical relationship between the amounts of solute adsorbed and its concentrations in solution at equilibrium:

$$\ln q = \ln K_{\mathrm{F}} + \frac{1}{n} \cdot \ln C_{\mathrm{eqv}},$$

where q is the amount of solute adsorbed (mmol/g); C_{eqv} is the concentration of solute remaining in solution after equilibrium (mmol/L); K_{F} and $1/n$ are parameters related to maximum adsorption capacity in the multilayer of the adsorbent [58,59].

X-band EPR spectra of the samples were recorded at room temperature using a radio spectrometer PE-1306 equipped with a frequency meter ChZ-54 and frequency converter YaZCh-87. The magnetic field was calibrated using 2,2-diphenyl-1-picrylhydrazyl (DPPH) (g = 2.0036) and ions of Mn^{2+} in MgO matrix (g = 2.0015). The sorption of copper(II) ions on the samples analyzed with EPR was conducted from acetonitrile solutions.

Electron spectra of diffuse reflectance (ESDR) of the amino-functionalized particles containing copper(II) ions were recorded on a spectrophotometer Specord UV–vis (model M-40).

Supporting Information

Supporting Information File 1

Additional experimental data.
[http://www.beilstein-journals.org/bjnano/content/supplementary/2190-4286-8-36-S1.pdf]

Acknowledgements

We express gratitude to the Swedish Research Council (grant 2012-9772-98229-17) and the programme SASPRO 3rd call

(grant agreement n°1298/03/01) for financial support of the present work. B. Alonso from ICG Montpellier and O. Matkovskiy from CISC Kyiv are acknowledged for their help in NMR experiments and adsorption from the gas phase experiments, respectively.

References

1. Argyo, C.; Weiss, V.; Bräuchle, C.; Bein, T. *Chem. Mater.* **2014,** *26,* 435–451. doi:10.1021/cm402592t
2. Cheng, L.; Wang, C.; Li, Z. *Nanoscale* **2013,** *5,* 23–37. doi:10.1039/C2NR32311G
3. Valtchev, V.; Tosheva, L. *Chem. Rev.* **2013,** *113,* 6734–6760. doi:10.1021/cr300439k
4. Chaudhuri, R. G.; Paria, S. *Chem. Rev.* **2012,** *112,* 2373–2433. doi:10.1021/cr100449n
5. Pansare, V. J.; Hejazi, S.; Faenza, W. J.; Prud'homme, R. K. *Chem. Mater.* **2012,** *24,* 812–827. doi:10.1021/cm2028367
6. Dong, F.; Ha, C.-S. *Macromol. Res.* **2012,** *20,* 335–343. doi:10.1007/s13233-012-0151-x
7. Lee, J. E.; Lee, N.; Kim, T.; Kim, J.; Hyeon, T. *Acc. Chem. Res.* **2011,** *44,* 893–902. doi:10.1021/ar2000259
8. Suh, W. H.; Suh, Y.-H.; Stucky, G. D. *Nano Today* **2009,** *4,* 27–36. doi:10.1016/j.nantod.2008.10.013
9. Cauda, V.; Schlossbauer, A.; Kecht, J.; Zürner, A.; Bein, T. *J. Am. Chem. Soc.* **2009,** *131,* 11361–11370. doi:10.1021/ja809346n
10. Sanvicens, N.; Marco, M. P. *Trends Biotechnol.* **2008,** *26,* 425–433. doi:10.1016/j.tibtech.2008.04.005
11. Huh, S. Morphological control of multifunctionalized mesoporous silica nanomaterials for catalysis applications. Ph.D. Thesis, Iowa State University, Ames, IA, USA, 2004.
12. Rosenholm, J. M.; Sahlgren, C.; Linden, M. *Curr. Drug Targets* **2011,** *12,* 1166–1186. doi:10.2174/138945011795906624
13. Yatsimirskii, K. B.; Shevchenko, Y. N.; Yashina, N. I.; Samodumova, I. M.; Nazarenko, V. A.; Kiseleva, L. I. *Russ. J. Gen. Chem.* **1985,** *55,* 405–412.
14. Sanchez, C.; Shea, K. J.; Kitagawa, S. *Chem. Soc. Rev.* **2011,** *40,* 471–472. doi:10.1039/c1cs90001c
15. Slinyakova, I. B.; Denisova, T. I. *Organo-silicon Adsorbents: Production, Properties, and Application;* Naukova Dumka: Kyiv, Ukraine, 1988.
16. Voronkov, M. G.; Vlasova, N. N.; Pozhidaev, Yu. N. *Appl. Organomet. Chem.* **2000,** *14,* 287–303. doi:10.1002/(SICI)1099-0739(200006)14:6<287::AID-AOC989>3.0.CO;2-Y
17. Zub, Y.; Parish, R. *Stud. Surf. Sci. Catal.* **1996,** *99,* 285–299. doi:10.1016/s0167-2991(06)81024-4
18. Zub, Yu.; Chuiko, A. Salient Features of Synthesis and Structure of Surface of Functionalized Polysiloxane Xerogels. In *Colloidal Silica: Fundamentals and Applications;* Bergna, H.; Roberts, W., Eds.; Surfactant science series, Vol. 131; CRC Press: Boca Raton, 2006; pp 397–424.
19. Zub, Yu. Design of functionalized polysiloxane adsorbents and their environmental applications. In *Sol-Gel Methods for Materials Processing;* Innocenzi, P.; Zub, Yu.; Kessler, V., Eds.; Springer: Dordrecht, 2008; pp 1–29. doi:10.1007/978-1-4020-8514-7_1
20. Melnyk, I. V.; Dudarko, O. A.; Stolyarchuk, N. V.; Goncharyk, V. P.; Zub, Yu. L. Polysiloxane xerogels with a bifunctional surface layer. In *Physico-chemistry of materials and supramoleculat structures;* Shpak, A. P.; Gorbyk, P. P., Eds.; Naukova Dumka: Kyiv, 2007; Vol. 2, pp 392–430.
21. Mehdi, A.; Reye, C.; Corriu, R. *Chem. Soc. Rev.* **2011,** *40,* 563–574. doi:10.1039/B920516K
22. Sanchez, C.; Belleville, P.; Popall, M.; Nicole, L. *Chem. Soc. Rev.* **2011,** *40,* 696–753. doi:10.1039/c0cs00136h
23. Burkett, S. L.; Sims, S. D.; Mann, S. *Chem. Commun.* **1996,** 1367–1368. doi:10.1039/CC9960001367
24. Sims, S. D.; Burkett, S. L.; Mann, S. *Mater. Res. Soc. Symp. Proc.* **1996,** *431,* 77–82. doi:10.1557/PROC-431-77
25. Fowler, C. E.; Burkett, S. L.; Mann, S. *Chem. Commun.* **1997,** 1769–1770. doi:10.1039/A704644H
26. Mel'nyk Seredyuk, I. V.; Zub, Yu. L.; Chuiko, A. A.; Jaroniec, M.; Mann, S. *Stud. Surf. Sci. Catal.* **2002,** *141,* 205–212. doi:10.1016/S0167-2991(02)80543-2
27. Badley, R. D.; Ford, W. T.; McEnroe, F. J.; Assink, R. A. *Langmuir* **1990,** *6,* 792–801. doi:10.1021/la00094a013
28. van Blaaderen, A.; Vrij, A. J. *J. Colloid Interface Sci.* **1993,** *156,* 1–18. doi:10.1006/jcis.1993.1073
29. Stöber, W.; Fink, A.; Bohn, E. *J. Colloid Interface Sci.* **1968,** *26,* 62–69. doi:10.1016/0021-9797(68)90272-5
30. Doro, F. G.; Rodrigues-Filho, U. P.; Tfouni, E. *J. Colloid Interface Sci.* **2007,** *307,* 405–417. doi:10.1016/j.jcis.2006.11.013
31. Wu, Z.; Xiang, H.; Kim, T.; Chun, M.-S.; Lee, K. *J. Colloid Interface Sci.* **2006,** *304,* 119–124. doi:10.1016/j.jcis.2006.08.055
32. Deng, G.; Markowitz, M. A.; Kust, P. R.; Gaber, B. P. *Mater. Sci. Eng., C* **2000,** *11,* 165–172. doi:10.1016/S0928-4931(00)00203-4
33. White, L. D.; Tripp, C. P. *J. Colloid Interface Sci.* **2000,** *232,* 400–407. doi:10.1006/jcis.2000.7224
34. Jal, P. K.; Patel, S.; Mishra, B. K. *Talanta* **2004,** *62,* 1005–1028. doi:10.1016/j.talanta.2003.10.028
35. Dąbrowski, A.; Barczak, M.; Stolyarchuk, N. V.; Melnyk, I. V.; Zub, Yu. L. *Adsorption* **2005,** *11,* 501–517. doi:10.1007/s10450-005-5609-0
36. Calvo, A.; Angelomé, P. C.; Sánchez, V. M.; Scherlis, D. A.; Williams, F. J.; Soler-Illia, G. J. A. A. *Chem. Mater.* **2008,** *20,* 4661–4668. doi:10.1021/cm800597k
37. Lombardo, M. V.; Videla, M.; Calvo, A.; Requejo, F. G.; Soler-Illia, G. J. A. A. *J. Hazard. Mater.* **2012,** *223–224,* 53–62. doi:10.1016/j.jhazmat.2012.04.049
38. Tan, C. G.; Bowen, B. D.; Epstein, N. *J. Colloid Interface Sci.* **1987,** *118,* 290–293. doi:10.1016/0021-9797(87)90458-9
39. Ribeiro, A. A. *J. Fluorine Chem.* **1997,** *83,* 61–66. doi:10.1016/s0022-1139(96)03572-5
40. Massiot, D.; Fayon, F.; Capron, M.; King, I.; Le Calvé, S.; Alonso, B.; Durand, J.-O.; Bujoli, B.; Gan, Z.; Hoatson, G. *Magn. Reson. Chem.* **2002,** *40,* 70–76. doi:10.1002/mrc.984
41. Engelhardt, C.; Michel, D. *High-resolution solid-state NMR of Silicates and Zeolites;* Wiley: Chichester, 1987.
42. Stechenko, O. V.; Yakubovych, T. M.; Teslenko, V. V.; Veysov, B. K.; Zub, Y. L.; Chuiko, A. A. *Khim., Fiz. Tekhnol. Poverkhni* **1999,** *3,* 46–50.
43. Volchenskova, I. I. *Theor. Exp. Chem.* **1973,** *9,* 627–634.
44. Stechenko, O. V.; Yurchenko, G. R.; Matkovskiy, O. K.; Zub, Y. L. *Sci. Bull. Uzhgorod Univ., Ser. Chem.* **2000,** *5,* 107–112.

45. Luechinger, M.; Prins, R.; Pirngruber, G. D. *Microporous Mesoporous Mater.* **2005,** *85,* 111–118. doi:10.1016/j.micromeso.2005.05.031
46. Melnyk, I. V.; Zub, Yu. L. *Microporous Mesoporous Mater.* **2012,** *154,* 196–199. doi:10.1016/j.micromeso.2011.11.012
47. Pogorilyi, R. P.; Melnyk, I. V.; Zub, Yu. L.; Seisenbaeva, G. A.; Kessler, V. G.; Shcherbatyik, M. M.; Košak, A.; Lobnik, A. *J. Sol-Gel Sci. Technol.* **2013,** *68,* 447–454. doi:10.1007/s10971-013-2991-z
48. Melnyk, I. V.; Tomina, V. V.; Zub, Yu. L. Synthesis Submicro- and Nanoscale Spherical Silica Particles with 3-aminopropyl Groups in the Surface Layer. In *Proceedings of the international conference nanomaterials: applications and properties,* Alushta, Crimea, Ukraine, Sept 16–21, 2013; 02PCN40-1-3.
49. Melnyk, I. V. *Chem. J. Mold.* **2014,** *9* (1), 123–127.
50. Tomina, V. V.; Yurchenko, G. R.; Matkovsky, A. K.; Zub, Yu. L.; Kosak, A.; Lobnik, A. *J. Fluorine Chem.* **2011,** *132,* 1146–1151. doi:10.1016/j.jfluchem.2011.07.010
51. Bagwe, R. P.; Hilliard, L. R.; Tan, W. H. *Langmuir* **2006,** *22,* 4357–4362. doi:10.1021/la052797j
52. Markowitz, M. A.; Schoen, P. E.; Kust, P.; Gaber, B. P. *Colloids Surf., A* **1999,** *150,* 85–94. doi:10.1016/S0927-7757(98)00715-8
53. Hathaway, B. J.; Tomlinson, A. A. G. *Coord. Chem. Rev.* **1970,** *5,* 1–43. doi:10.1016/S0010-8545(00)80073-9
54. Stechenko, O. V.; Yakubovych, T. M.; Teslenko, V. V.; Zub, Y. L. *Ukr. Khim. Zh.* **2003,** *69,* 19–24.
55. Brunauer, S.; Emmet, P. H.; Teller, E. *J. Am. Chem. Soc.* **1938,** *60,* 309–319. doi:10.1021/ja01269a023
56. Khatib, I. S.; Parish, R. V. *J. Organomet. Chem.* **1989,** *369,* 9–16. doi:10.1016/0022-328X(81)80002-2
57. Azizian, S. *J. Colloid Interface Sci.* **2004,** *276,* 47–52. doi:10.1016/j.jcis.2004.03.048
58. Langmuir, I. *J. Am. Chem. Soc.* **1918,** *40,* 1361–1403. doi:10.1021/ja02242a004
59. Freundlich, H.; Heller, W. *J. Am. Chem. Soc.* **1939,** *61,* 2228–2230. doi:10.1021/ja01877a071

License and Terms

BEILSTEIN JOURNAL OF NANOTECHNOLOGY

Association of aescin with β- and γ-cyclodextrins studied by DFT calculations and spectroscopic methods

Ana I. Ramos[*1,2], Pedro D. Vaz[3,4], Susana S. Braga[5] and Artur M. S. Silva[5]

Full Research Paper

Open Access

Address:
[1]CICECO, Complexo de Laboratórios Tecnológicos, Campus Universitário de Santiago, 3810-193 Aveiro, Portugal, [2]Current affiliation: INEGI-FEUP Faculty of Engineering of the University of Porto, Rua Dr. Roberto Frias, 4200-465, Porto, Portugal, [3]CQB, Departamento de Química e Bioquímica, Faculdade de Ciências da Universidade de Lisboa, 1749-016 Lisboa, Portugal, [4]ISIS Neutron & Muon Source, Rutherford Appleton Laboratory, Chilton, Didcot, Oxfordshire OX11 0QX, United Kingdom and [5]QOPNA, Departamento de Química, Universidade de Aveiro, Campus de Santiago, 3810-193 Aveiro, Portugal

Email:
Ana I. Ramos[*] - shortinha.sa@gmail.com

* Corresponding author

Keywords:
aescin; cyclodextrin inclusion; DFT; ^{1}H NMR; ROESY

Beilstein J. Nanotechnol. **2017,** *8,* 348–357.
doi:10.3762/bjnano.8.37

Received: 15 September 2016
Accepted: 06 January 2017
Published: 03 February 2017

This article is part of the Thematic Series "Hybrid nanomaterials: from the laboratory to the market".

Guest Editor: A. Taubert

Abstract

Background: Aescin, a natural mixture of saponins occurring in *Aesculus hippocastanum*, exhibits important flebotonic properties, being used in the treatment of chronic venous insufficiency in legs. The inclusion of aescin into cyclodextrins (CDs) is a technical solution for its incorporation into the textile of stockings, but details of the physicochemistry of these host–guest systems are lacking. This work investigates the inclusion of aescin into the cavities of two native cyclodextrins, β-CD and γ-CD.

Results: The continuous variation method applied to aqueous-phase ^{1}H nuclear magnetic resonance (^{1}H NMR) has demonstrated that the preferred CD/aescin inclusion stoichiometries are 2:1 with β-CD and 1:1 with γ-CD. The affinity constant calculated for γ-CD·aescin was 894 M^{-1}, while for 2β-CD·aescin it was estimated to be 715 M^{-1}. Density functional theory (DFT) calculations on the interaction of aescin Ib with CDs show that an inclusion can indeed occur and it is further demonstrated that the wider cavity of γ-CD is more adequate to accommodate this large guest. ROESY spectroscopy is consistent with the formation of a complex in which the triterpenic moiety of aescin is included into the cavity of γ-CD. The higher stability of this geometry was confirmed by DFT. Furthermore, DFT calculations were applied to determine the chemical shifts of the protons H3 and H5 of the CDs in the optimised structures of the inclusion complexes. The calculated values are very similar to the experimental data, validating the approach made in this study by NMR.

Conclusion: The combination of experimental data from aqueous-state NMR measurements and theoretical calculations has demonstrated that γ-CD is the most suitable host for aescin, although the inclusion also occurs with β-CD. The geometry of the γ-CD·aescin complex is characterised by the inclusion of the triterpene segment of aescin into the host cavity.

Introduction

Aescin is the main component of the crystalline saponins obtained from the seeds of the horse chestnut tree, *Aesculus hippocastanum* (Hippocastanaceae). It is a natural mixture of acylated triterpene glycosides. In early studies, the saponins present in aescin were divided into two forms, α-aescin and β-aescin, with distinct melting point, hemolytic index, specific rotation and aqueous solubility [1]. β-Aescin was identified as the main active component and it is presently known to be not a pure compound, but rather a mixture of aescin Ia and aescin Ib (Figure 1). In turn, α-aescin was demonstrated to comprise the isomers isoaescin Ia and isoaescin Ib.

Aescin has a broad range of biological activities, the best-known being anti-oedematous, anti-inflammatory and veno-tonic actions [1]. In China, injectable forms of aescin are widely used in the clinic to prevent inflammatory oedema after trauma from fracture or surgery, in spite of the known side effects (phlebitis and allergic reactions) [2,3]. Anti-inflammatory and anti-oedematous activities following oral administration have also been reported, both in rodents [4] and in human patients with proven chronic venous insufficiency [5]. The anti-inflammatory properties are associated with down-regulation of pro-inflammatory mediators in vivo. Aescin helps decreasing the mortality resulting from the pathophysiology of sepsis in mice [6]. Moreover, it was proved to possess remarkable efficiency in both prevention and treatment of vascular disorders. Aescin increases the vascular tone by enhancing the formation of prostaglandin F2α in a variety of human tissues, including veins, and by allowing improved response to Ca^{2+} ions [1]. Aescin was also tested as a cytotoxic agent. It demonstrated trypanocidal activity in vitro and increased the longevity of *Trypanosome evansi* infected mice, however without curative

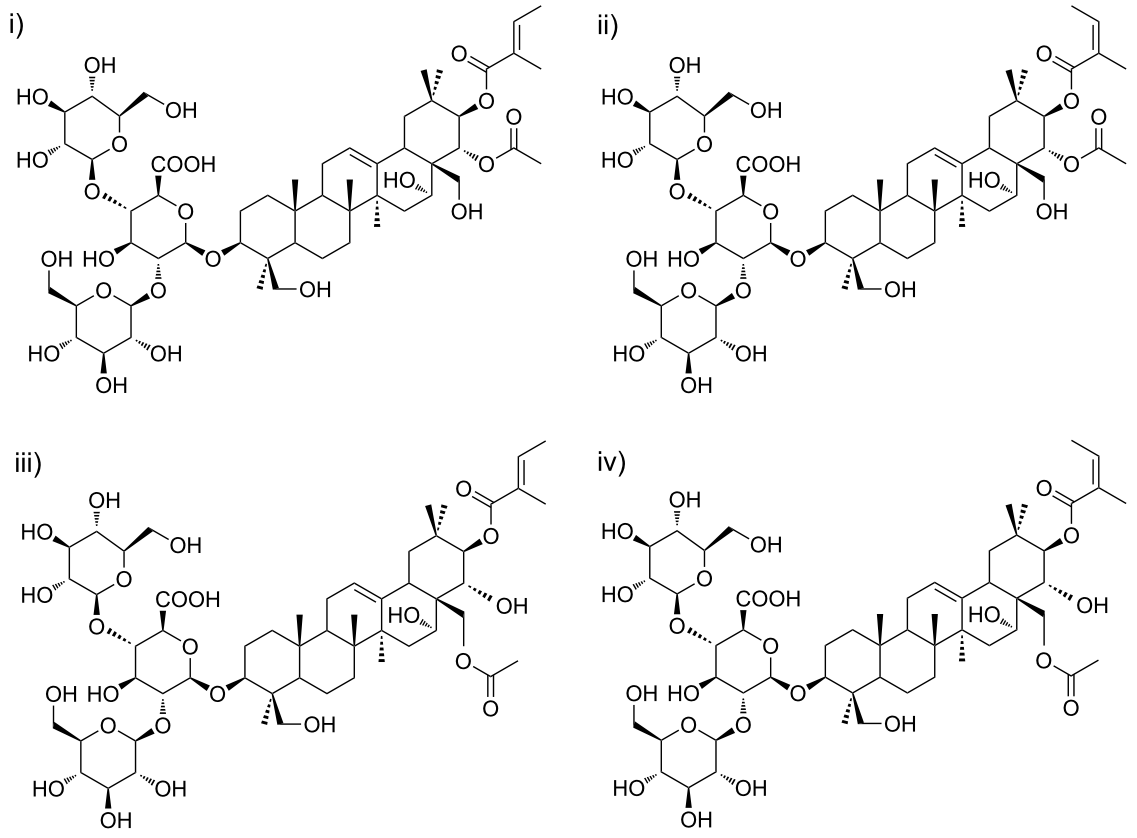

Figure 1: Isomeric structures for (top line) aescin Ia (i) and aescin Ib (ii) and for (bottom line) isoaescin Ia (iii) and isoaescin Ib (iv).

effect [7]. In vitro incubation with cells of the C6 (glioma) and A549 (lung adenocarcinoma) tumoural lines showed that aescin has potent dose- and time-dependent antiproliferative effects [8]. Studies with human castration-resistant prostate cancer, both in vitro, using the cell lines PC-3 and DU-145, and in vivo using xenograft mice, showed cytotoxic effects for aescin, through the induction of apoptosis and G2/M cell cycle arrest [9].

Currently, aescin is mostly employed for venotonic action, being available in the form of topical formulations such as lotions, gels and creams. Many of these products resource to controlled release strategies, which can be achieved by encapsulating aescin into liposomes [2,3], phytosomes (phospholipidic self-emulsifying particles) [10], zeolites [11], poly(lactic co-glycolic acid) nanoparticles [12] or cyclodextrins. Cyclodextrins are cyclic oligosaccharides, typically with six (α-CD), seven (β-CD) and eight (γ-CD) units of α-D-glucose, which occur in nature from bacterial degradation of starch [13]. Their particular shape – a truncated cone with a hydrophobic cavity and a large number of hydroxy groups at the rims – enables them to include a variety of hydrophobic molecules and to enhance their stability in solution and their aqueous solubility. The only requisite of the encapsulated molecule, named guest, is that it possesses an adequate size and geometry to fit inside the cavity of the CD [14]. The ability of γ-CD to interact with triterpenic glycosides is known for over two decades, being first reported as a sequestering agent and sweetness inhibitor for strognin, a natural sweetener found in the Malaysian plant *Staurogyne merguensi* [15]. With glycemnic acid, a sweetness suppressing agent, γ-CD also acts as inhibitor, thus restoring one's ability to taste sweets [16]. Inclusion of triterpenic compounds of medicinal interest is a topic of growing interest due to the ability of cyclodextrins to increase the solubility of these molecules. Currently, CDs are being used to afford non-toxic aqueous formulations with antitumoural single triterpenoids such as oleanoic [17-19], ursolic [18,19] and betulinic [18,20-22] acids. Ammonium glycyrrhizinate or glyciram (from licorice roots), sold in Russia and Japan as a natural anti-inflammatory, antiallergic and anti-spasmodic medicine, was also reported to become more stable against epoxidation upon inclusion into β-CD, thus gaining increased shelf-life [23,24].

Interaction of aescin with β-CD was studied only from an application viewpoint. A viscose textile grafted with β-CD allows loading a good amount of aescin for a sustained topical delivery [25]. The cosmeto-textile can be used to produce stocking with both compression and venotonic actions, with strong advantages for the symptomatic treatment of leg chronic venous insufficiency.

The aim of the present study is to evaluate the physicochemical aspects of the interaction of aescin with β-CD and γ-CD. The affinity and geometry of inclusion of aescin in the cavity of β-CD, having an inner diameter of 0.78 nm, is not known. Furthermore, and in spite of the many reports pointing to the preference of triterpenic guests for the larger host γ-CD [15,16,18,20], with cavity diameter of 0.95 nm, the γ-CD·aescin inclusion complex, herein reported, had not been studied to date. The present work demonstrates the stronger affinity of aescin to γ-CD and the formation of a 1:1 inclusion complex, presenting its most plausible geometry.

Results and Discussion

NMR studies in aqueous solution

Evaluation of the inclusion stoichiometries by the continuous variation method

In the evaluation of the interaction of cyclodextrin with a guest molecule in aqueous solution, one first needs to investigate the stoichiometry [26]. For this, the continuous variation method (Job plot) [27] was employed. This assay consists in mixing aqueous solutions of host and guest in varying molar fractions while keeping constant the sum of their concentrations (see details in the dedicated Experimental section) and registering the variations in the chemical shifts of their protons (Δδ) relative to those of the individual components. The plot maximum corresponds to the preferred stoichiometric proportion of CD to aescin for each inclusion compound under study [27]. The H3 and H5 of the CDs are located inside their cavity and thus they are excellent probes for inclusion. Typically, these protons are the ones that exhibit the highest chemical shifts upon changes in the cavity's environment. The variation in the chemical shift of H3 and H5 of the two CDs under study as a function of the molar fraction of the CD/aescin mixtures is represented in the Figure 2.

A closer look at Figure 2 allows observing that the variations in the H3 proton of γ-CD are not changing monotonically. For this reason, we have chosen to exclude the H3 shifts from the Job plot (an example for one of these data sets is shown in Supporting Information File 1, Figure S1.1). The shifts of protons H5 of both CDs were selected for the Job plot, depicted in Figure 3.

In the β-CD/aescin mixtures, the points associated with solutions having molar fractions of β-CD of 0.6 and 0.7 show approximately the same *y*-value. This indicates that the plot maximum is located between them, most likely at a molar fraction of 0.66 corresponding to a preferred stoichiometry of 2:1 (β-CD/aescin). In the γ-CD/aescin mixtures, the plot maximum was achieved at a molar fraction of γ-CD of 0.5, indicating that the preferred stoichiometry for the inclusion complex is 1:1; nonetheless, it should be noted that this plot is quite asym-

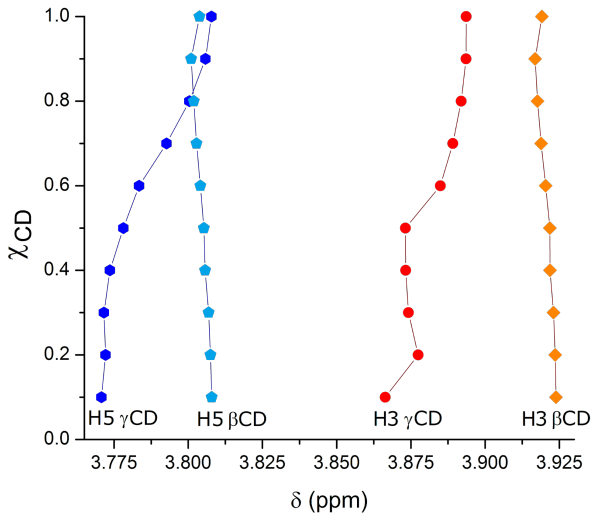

Figure 2: Chemical shift variation for the H3 and H5 protons of β-CD and γ-CD while performing the continuous variation method: [CD] + [aescin] = 10 mM. See Figure 9 for ^{1}H labelling. Full lines connecting the experimental points are for indicative purposes only.

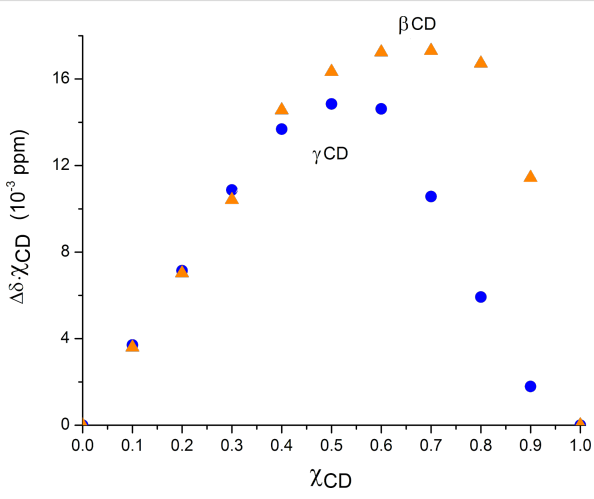

Figure 3: Job plot for the aescin complexes with β-CD (orange triangles) and γ-CD (blue dots) in D_2O.

metric and the shift observed at 0.6 (χ of γ-CD) denotes the presence of at least another specimen in solution, most likely the 2:1 γ-CD/aescin species.

Apparent association constant

The samples used for the calculation of the apparent association constant (K_{app}) comprised aqueous solutions with a fixed concentration of cyclodextrin and variable concentrations of aescin (in excess from five to ten folds regarding the concentration of the host, see the Experimental section for further details). The inclusion constants of the complexes were estimated according to a graphical method developed by Seal et al. [28] by rearrangement of the Benesi–Hildebrand equation [29]. This method afforded values of 894 M^{-1} (±13.5%) for γ-CD·aescin and 715 M^{-1} (±10.6%) for 2β-CD·aescin, where values between parenthesis indicate the relative standard deviation. This may indicate a preference of aescin towards the larger cavity of γ-CD. It must be noted, though, that the possible occurrence of more than one species in solution, as denoted by the Job plot, implies that the K_{app} values herein presented are only a rough estimate of affinity. Furthermore, the values are within the same order of magnitude, meaning that the affinity of aescin towards these two hosts is not markedly different.

ROESY spectrum of γ-CD·aescin

The 2D ROESY spectrum of a D_2O/CD_3OD solution of an aescin and γ-CD mixture is consistent with inclusion. An expansion showing the region of interest to the observation of host–guest interactions is depicted in the Figure 4 (refer to the Supporting Information File 2 for the full spectrum). The resonance of the H5 protons, which are directed towards the inner cavity of γ-CD, appears centred at 3.15 ppm, slightly shifted regarding the values reported for pure γ-CD [30]. This feature is associated with the formation of inclusion complexes in solution. Furthermore, correlations were found between the host's H5 and several protons ascribed to the triterpenic moiety of aescin and some of its methyl groups, namely H1, H19, H27 and methylene protons H23, H29 and H30 (see Figure 5 for labelling) [31]. In the region associated with protons H2 and H4 of γ-CD, some correlations with aescin triterpenic protons were also found, namely with H5, H7 and H15. This suggests that aescin is included into γ-CD by its triterpenic moiety, in a good

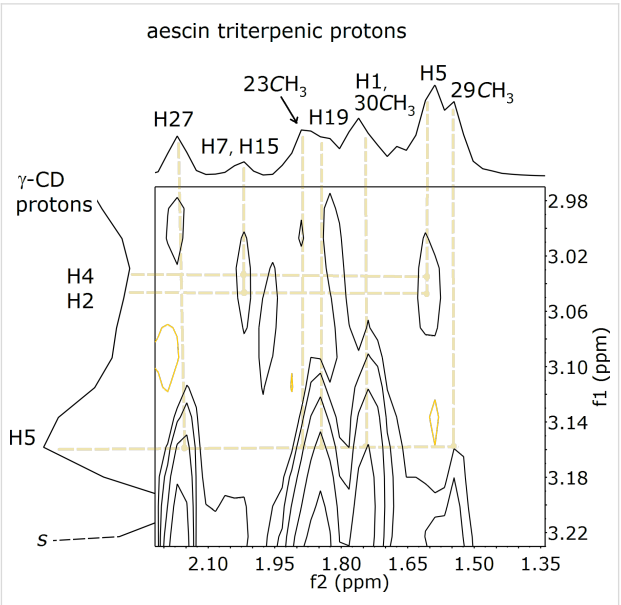

Figure 4: Partial 2D ROESY spectrum of a water/methanol solution containing equimolar amounts of γ-CD and aescin.

match with the geometry calculated for the complex γ1 in the following section.

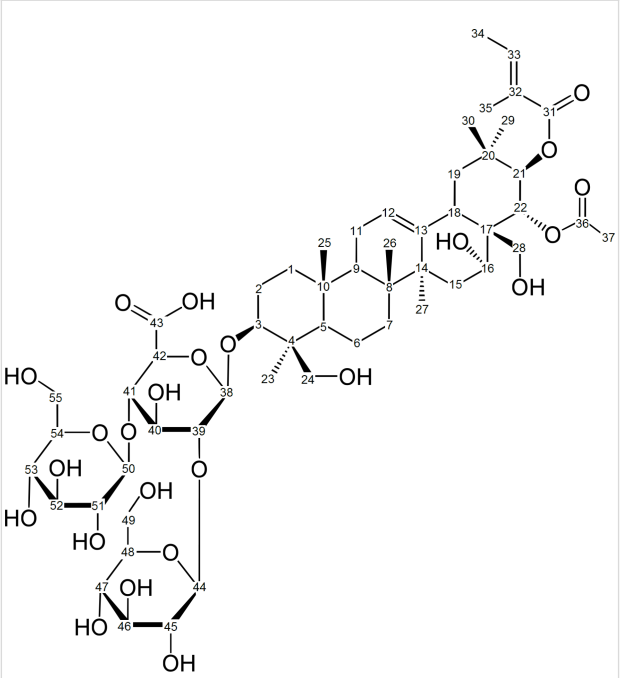

Figure 5: Carbon (and corresponding proton) numbering of aescin.

Investigation of the CD·aescin inclusion modes by DFT calculations

The geometry of interaction of aescin with β-CD and γ-CD was further studied by means of theoretical calculations. For this, and given that aescin is a mixture of components, the main active ingredient, aescin Ib, was chosen as representative guest molecule. Its interaction with the CDs was evaluated by means of DFT calculations by creating different complex geometries that could represent the real complex. The geometries were optimised at the M06-2X/6-31g(d) level with tight convergence criteria, including dispersion energy corrections (D3) and in the presence of a solvation model to simulate the presence of water. It should be mentioned that all atoms were optimised at the same level of theory, i.e., the ONIOM approach was not considered. Afterwards NMR chemical shifts were estimated at the more accurate M06-2X/6-311g(d,p) level with D3 correction and the solvation model, while using the GIAO algorithm. Furthermore, for each optimised inclusion complex geometry, the ^{1}H NMR chemical shifts of signals of the protons H3 and H5 of the host were calculated and compared with those calculated for the neat cyclodextrins.

For the 2β-CD·aescin complex two possible geometries were optimised. These structures are represented in the Figure 6 and will be hereafter named complex β1 and complex β2.

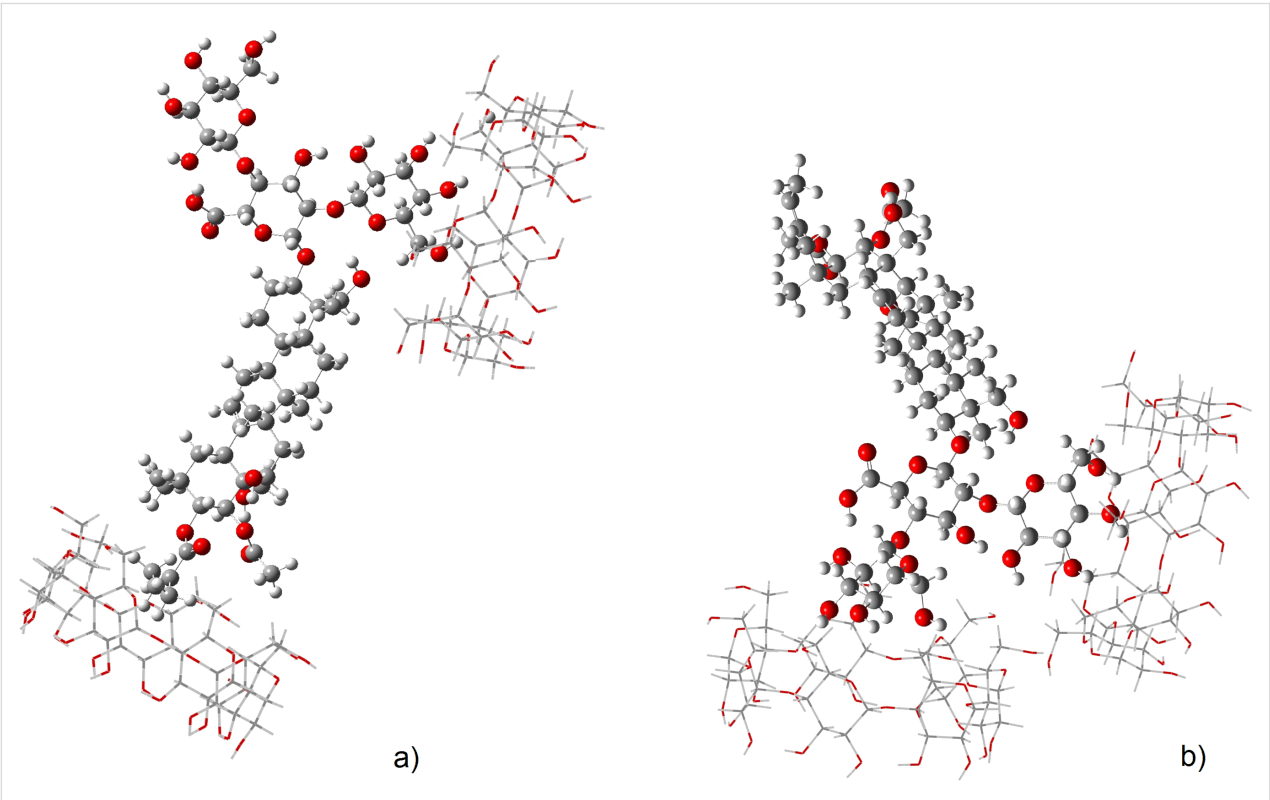

Figure 6: Optimised structures of the theoretical 2β-CD·aescin complex β1 (a) and complex β2 (b).

The first observation that strikes to the sight is that the cavity of β-CD is not large enough to allow a deep encapsulation of the guest molecule. This was reflected by the calculated NMR chemical shifts, which yielded negligible changes matching the experimental observation for H3 and H5 (Figure 2). In terms of formation energies of the theoretical 2β-CD·aescin structures, the complex β2 is the most stable, while the complex β1 is less stable by 135 kJ/mol. From Figure 6, it can be seen that the structure of complex β2 shows vicinal β-CD units resulting in an extended network of H-bonds which does not occur in the complex β1, being that a reason for the lower energy of the former structure.

For the γ-CD·aescin complex, three possible geometries were computed. The resulting optimised structures, shown in Figure 7, allow observing that the main interactions in the γ-CD·aescin complexes γ1 and γ2 occur for an almost complete encapsulation while for complex γ3 the interaction occurs at the upper rim of γ-CD.

The formation energies of the structures represented in the Figure 7 follow the order complex γ1 ≤ complex γ2 << complex γ3. The most stable geometry is found with complex γ1 and it involves inclusion of the triterpenic moiety of aescin into γ-CD. Nonetheless, the difference in energy to that of complex γ2 is only +27.1 kJ/mol. This means that this second geometry, in which γ-CD docks at one of the glucose residues, is also quite plausible. Finally, complex γ3 has the less stable geometry, with an energy difference of +82.7 kJ/mol. These findings are confirmed by the calculated NMR chemical shifts (Figure 8), which show changes in the two most stable structures, while the third displays little changes as will be discussed next.

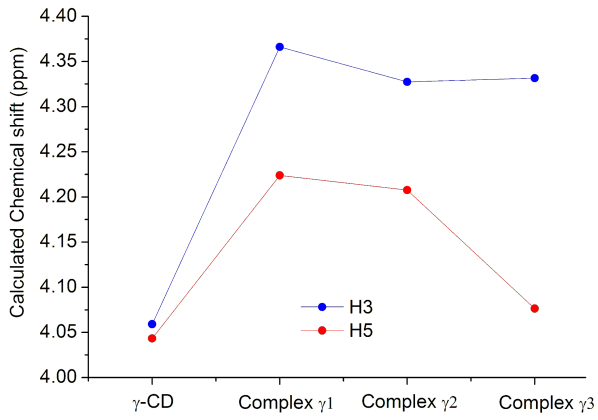

Figure 8: DFT [M06-2X/6-311G(d,p) with D3 dispersion and IEFPCM polarizable continuum solvent corrections] calculated NMR chemical shifts for protons H3 and H5 for neat γ-CD and the γ-CD·aescin theoretical complexes γ1, γ2 and γ3.

As can be seen from Figure 8, the calculated values match the same trend as the experimental ones for neat γ-CD. The same

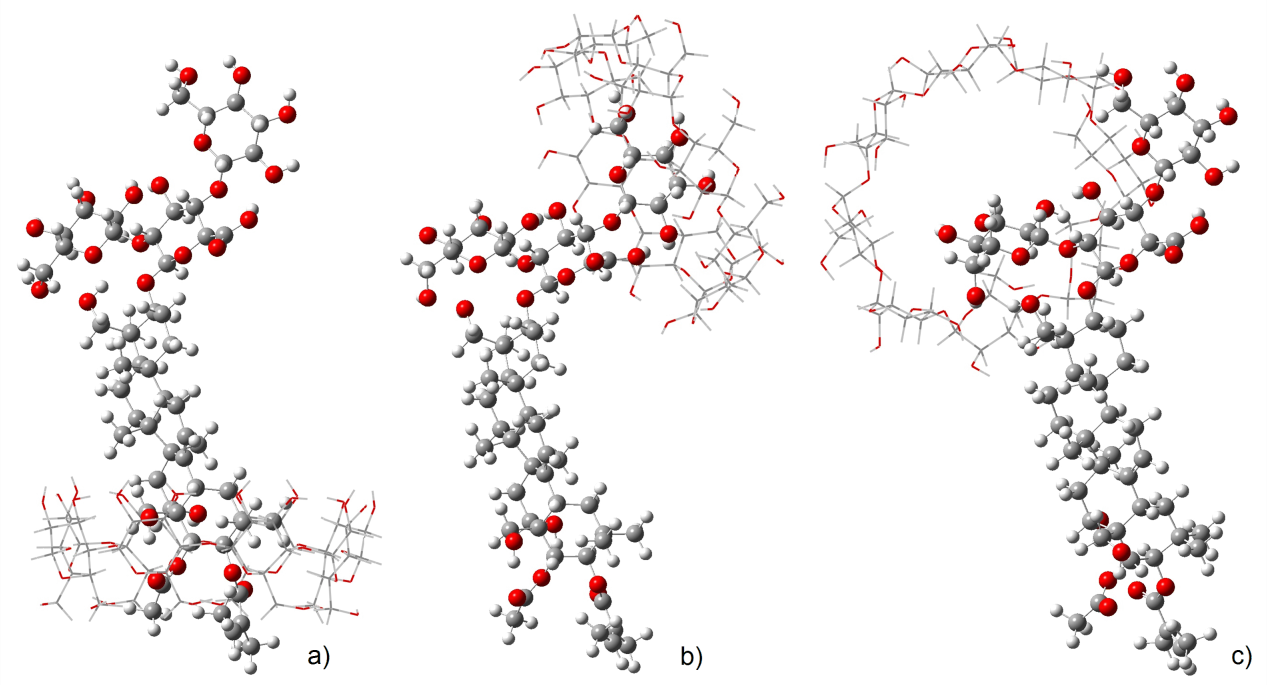

Figure 7: Optimised geometries for three different hypothetical structures of γ-CD·aescin, deemed complex γ1 (a) complex γ2 (b) and complex γ3 (c). The structures have the same orientation to facilitate viewing.

applies to the observed changes in the chemical shifts after formation of the complexes. Comparing the calculated and experimental data (for the Job plot) complex γ3 can be discarded, since it does not allow for a change in the chemical shift of H5. This result further confirms that the most plausible geometries are those of complexes γ1 and γ2. It should be mentioned as well that the predicted shifts from neat to complexed in γ-CD for H3 and H5 are in excellent agreement with the experimentally measured NMR chemical shifts for those nuclei where the shift experienced for H5 is larger than that for H3.

Conclusion

In the present work, the interaction of aescin with the oligosaccharide hosts β-CD and γ-CD is investigated, combining NMR characterisation in aqueous solution with DFT theoretical calculations to determine the stoichiometry, the host–guest affinity, and the geometry of inclusion. The results show that aescin forms preferentially 2:1 complexes with β-CD, having a moderate affinity (K_{app} = 715 M^{-1}) for this host. DFT calculations allowed postulating that the two β-CD molecules interact with aescin at one of the glucose fragments to form a complex stabilised by an extensive network of hydrogen bonds. Inclusion of aescin into γ-CD is favoured by the larger diameter of its cavity, where aescin fits more adequately. This results in the occurrence of complexes with 1:1 stoichiometry and a slightly higher host−guest affinity (K_{app} = 894 M^{-1}). Regarding the geometry of inclusion of the γ-CD·aescin complex, ROESY indicates inclusion of the triterpenic moiety, with correlations between the host cavity protons (H5) and several triterpenic protons of aescin. DFT calculations further confirmed that this geometry is the most stable. The γ-CD·aescin inclusion complex may find applications in liquid formulations. Aescin solutions produce foam when shaken, which causes an undesirable visual effect (refer to the Supplementary Information File 4 for details). γ-CD stabilises aescin and allows to shorten the time of permanence of the foam bubbles in solution.

Experimental

Materials

Aescin (purum, mixture of saponins, ≥96.0%) was obtained from Fluka and used as received. Pharmaceutical grade β-CD and γ-CD (manufactured by Wacker, tradenames Cavamax W7 and W8, water content of ca. 14% for β-CD and 9% for γ-CD) were kindly donated by Ashland Specialty Ingredients (Düsseldorf, Germany). All other materials and solvents were of analytical reagent grade.

NMR spectroscopy

One- and two-dimensional NMR spectra were recorded on a Bruker Avance 500 spectrometer at 500.13 MHz at room temperature. ^{1}H NMR spectra recorded in D_2O were referenced to HOD at δ = 4.79. For the Rotating-frame Overhauser Spectroscopy (ROESY, spin lock 200 ms) experiments, solutions with equimolar quantities of aescin and γ-CD were used (concentration 15 μM, solvent D_2O/CD_3OD in an 80:20 proportion).

Job plot

The stoichiometry of CD·aescin complexes in deuterium oxide solution was determined using the continuous variation method or Job's method [27]. It involves running a series of experiments varying the host and guest concentrations while keeping their sum constant ([CD] + [aescin]) at well-defined *r*-values (r = [CD]/{[CD] + [aescin]}). In particular, 10 mM fresh D_2O solutions of aescin and each CD were mixed (i) to constant volume, i.e., the sum of the initial concentrations of β-CD and aescin remained equal to 10 mM, and (ii) to defined values of *r*, where *r* took values from 1/10 to 9/10, in steps of 1/10. The stoichiometry was finally determined by plotting Δδ·[CD] against *r*, where Δδ is the NMR shift of the selected proton, H5 (see Figure 9 for atom numbering), and finding the *r* value corresponding to the maximum of this distribution.

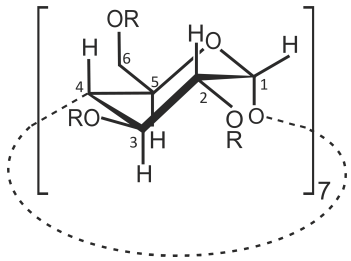

Figure 9: Carbon (and corresponding proton) numbering of cyclodextrins, herein demonstrated for β-CD.

Determination of the apparent formation constant (K_{app})

The equilibrium for the inclusion process in aqueous solution is ruled by a constant deemed apparent association constant or K_{app}. The inclusion constant was estimated by an adaptation of the Benesi–Hildebrand method [29], derived by Seal et al. [28], as shown in Equation 1:

$$[CD_0]+[G_0]=\frac{[CD_0]^n\times[G_0]}{\Delta\delta_{H5}}-\frac{1}{k} \quad (1)$$

In complexes having 1:1 stoichiometry, n = 1 and in complexes with 2:1 stoichiometry, as is the case of β-CD with aescin, n = 2. For each host–guest system, five NMR samples were prepared, each containing [CD] = 0.25 mM and [aescin] = 2.5 to 4.5 mM. Plotting ($[CD_0]$ + $[G_0]$) vs ($[CD_0]^n$ + $[G_0]$)/$\Delta\delta_{H5}$

allows obtaining $1/K_{app}$ as the yy-intercept (see Supporting Information File 1 for the plot graphics).

Computational details

DFT calculations [32] were performed using the Gaussian09 program, revision D01 [33], with the M06-2X hybrid functional, which includes a mixture of 54% Hartree–Fock exchange with DFT exchange correlation as developed by Truhlar and Zhao [34]. Pople's 6-31G(d) basis set was used on all atoms. All geometries were optimised without any geometry constraints at the M06-2X/6-31G(d) level of theory as mentioned above. The optimisation approach also included the use of tight convergence criteria. To evaluate the effects of solvation, to account for the effects of water the IEFPCM model was used for the description of the solvent continuum. Furthermore, the ONIOM approach was not used with all atoms being optimised at the same level of theory.

The initial geometries of the hosts and the guest were taken from structures available in the Cambridge Structural Database (CSD) [35]. For β-CD, the coordinates were procured from the structure of inclusion complex β-cyclodextrin·*S*-(+)-ibuprofen chlathrate hydrate (refcode TUXKUS) [36]; for γ-CD data was taken from the inclusion complex γ-cyclodextrin·methanol·*n*·H_2O (refcode NUNRIX [37]), in which the glucopyranose units already feature a high symmetry due to the presence of the methanol guest. The geometry of γ-CD after further optimisation is depicted in Figure 10. The initial geometry of aescin Ib was taken from its single-crystal diffraction data (refcode GACZIT [38]). A similar simulation strategy has been adopted by some of us previously to address accurate geometries and energies of organic molecules [39].

NMR shielding tensors were calculated using the gauge-independent atomic orbital method (GIAO) [40-44] with the same functional, dispersion correction and solvent continuum model, an improved basis set – 6-311G(d,p) – on the geometries optimised previously at the M06-2X/6-31g(d) level.

For comparison purposes the same calculations were accomplished with both the M06-2X and the B3LYP hybrid functional, but without the D3 or solvation corrections. In all cases

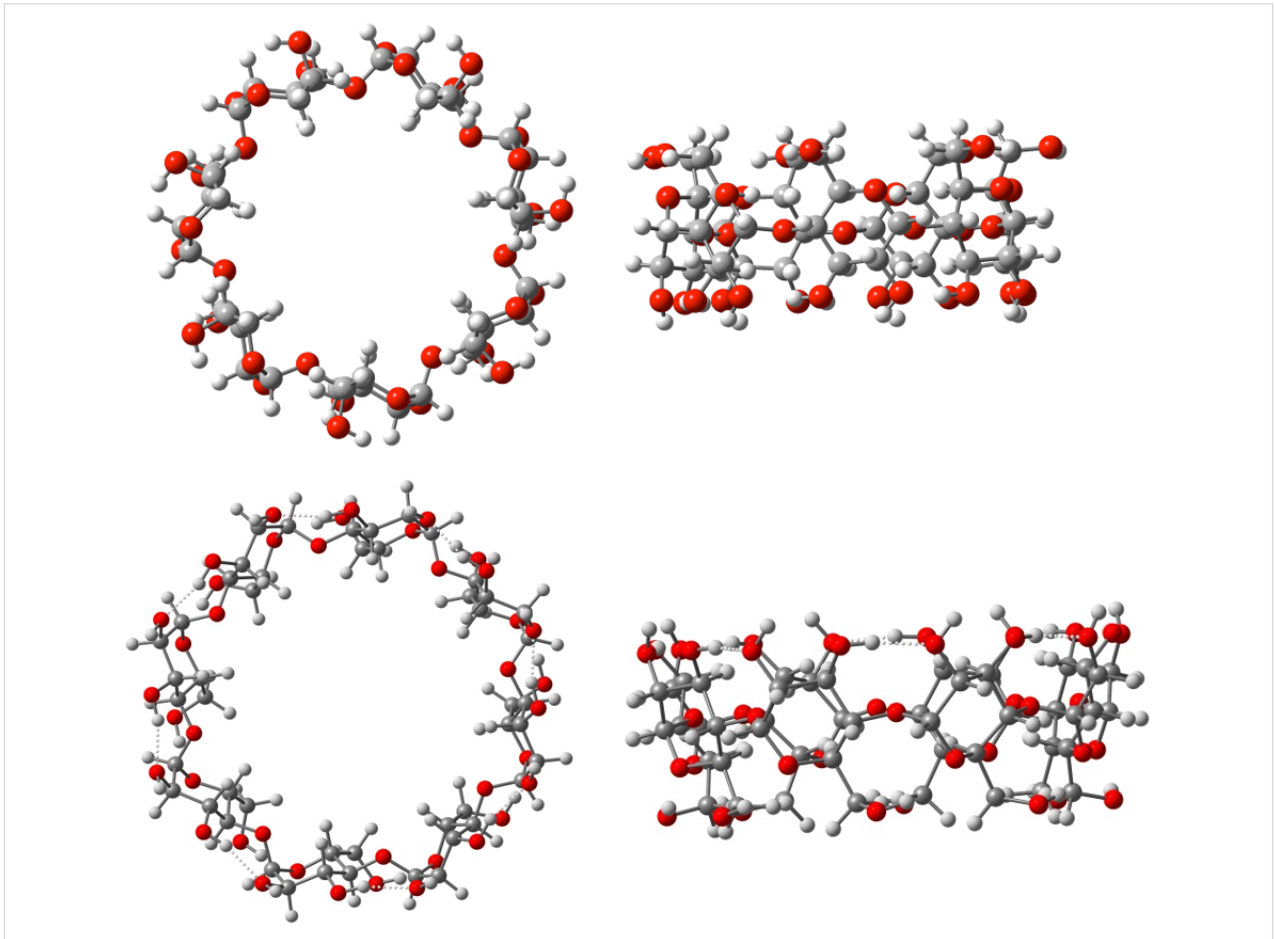

Figure 10: Optimised geometry for β-CD (top) and γ-CD (bottom), viewed from above (left) and from the side (right).

the obtained results were consistent (including with the M06-2X with D3 and solvation corrections).

Supporting Information

The details on the host–guest association constant (K_{app}) estimation by the graphical method of Seal et al. [28] are demonstrated, with one example for each cyclodextrin, in Supporting Information File 1, as well as the plot of the H3 shifts of γ-CD according to the Job method.

The selected region of the ROESY spectrum of γ-CD·aescin is shown in Supporting Information File 2.

The γ-CD·aescin complex formation in the solid state was also investigated and characterised by FTIR spectroscopy. Results are presented in Supporting Information File 3.

The foam disrupting capacity of the encapsulated aescin is presented in Supporting Information File 4.

Supporting Information File 1

Supplement to ^{1}H NMR studies in solution.
[http://www.beilstein-journals.org/bjnano/content/supplementary/2190-4286-8-37-S1.pdf]

Supporting Information File 2

ROESY spectrum of γ-CD·aescin.
[http://www.beilstein-journals.org/bjnano/content/supplementary/2190-4286-8-37-S2.pdf]

Supporting Information File 3

FTIR studies of the solid γ-CD·aescin inclusion compound.
[http://www.beilstein-journals.org/bjnano/content/supplementary/2190-4286-8-37-S3.pdf]

Supporting Information File 4

Studies on the influence of encapsulation on the foam-forming properties of aescin.
[http://www.beilstein-journals.org/bjnano/content/supplementary/2190-4286-8-37-S4.pdf]

Acknowledgements

The authors acknowledge the University of Aveiro and FCT/MEC (Fundação para a Ciência e a Tecnologia, Ministério da Educação e da Ciência), through national funds and, where applicable, co-financed by the FEDER (European Fund for Regional Development) within the PT2020 Partnership Agreement, for the financial support to the QOPNA research project (FCT UID/QUI/00062/2013) and the Portuguese NMR Network. DFT calculations were made possible due to the computing resources provided by STFC Scientific Computing Department's SCARF cluster.

Thanks are also due to the COST Action MP1202: Rational design of hybrid organic-inorganic interfaces) and to the COST Action MP 1302 Nanospectroscopy, where parts of the findings presented in this manuscript have been previously presented, as shown:

– MP1202:

- HINT Training School “Bottom-up Approaches of Hybrid Materials: Preparation and Design” (26–28 May 2015, Ljubljana, Slovenia) - poster communication “Inclusion of aescin into beta and gamma cyclodextrins”;
- HINT General Scientific Workshop and Review Meeting (12–14 October 2015, Milan, Italy) – oral communication “Nano-encapsulation of triclosan and aescin with cyclodextrins”;
- HINT - General Scientific Workshop and Final Review Meeting 2016 (10–12 October 2016, Aveiro, Portugal) – oral communication “Aescin inclusion into native β- and γ-cyclodextrins: characterization and application”.

– COST Action MP 1302:

- Nanospectroscopy for Two-dimensional Materials (8–10 September 2015, Chemnitz, Germany) – poster communication “NMR studies on the nanoencapsulation of aescin by the native β- and γ-cyclodextrins” and oral communication “Aescin”.

References

1. Sirtori, C. R. *Pharmacol. Res.* **2001,** *44,* 183–193. doi:10.1006/phrs.2001.0847
2. Liu, Z. P.; Hu, P.; Li, C. H.; Wang, X. L.; Xiao, X. *J. Trauma. Surg.* **2013,** *15,* 497–499. http://en.cnki.com.cn/Article_en/CJFDTOTAL-CXWK201306007.htm
3. Wang, Y.; Zhang, W. G.; Jiang, L.; Wang, Q. B. *Chinese J. Biochem. Pharm.* **2014,** *34,* 102–104. http://en.cnki.com.cn/Article_en/CJFDTotal-SHYW201402035.htm
4. Li, M.; Lu, C.; Zhang, L.; Zhang, J.; Du, Y.; Duan, S.; Wang, T.; Fu, F. *J. Evidence-Based Complementary Altern. Med.* **2015,** *2015,* No. 503617. doi:10.1155/2015/503617
5. Bisler, H.; Pfeifer, R.; Klüken, N.; Pauschinger, P. *Dtsch. Med. Wochenschr.* **1986,** *111,* 1321–1329. doi:10.1055/s-2008-1068628
6. Cheng, Y.; Wang, H.; Mao, M.; Liang, C.; Zhang, Y.; Yang, D.; Wei, Z.; Gao, S.; Hu, B.; Wang, L.; Cai, Q. *Cell. Physiol. Biochem.* **2015,** *36,* 1577–1586. doi:10.1159/000430320

7. Baldissera, M. D.; Bottari, N. B.; Grando, T. H.; Santos, R. C. V.; Dalcin, A. J. F.; Gomes, P.; Raffin, R. P.; Zimmerman, C. E. P.; Santurio, J. M.; Monteiro, S. G.; Da Silva, A. S. *Asian Pac. J. Trop. Biomed.* **2014,** *4,* 947–951. doi:10.12980/APJTB.4.2014APJTB-2014-0435
8. Çiftçi, G. A.; Işcan, A.; Kutlu, M. *Cytotechnology* **2015,** *67,* 893–904. doi:10.1007/s10616-015-9877-6
9. Piao, S.; Kang, M.; Lee, Y. J.; Choi, W. S.; Chun, Y.-S.; Kwak, C.; Kim, H. H. *Urol.* **2014,** *84,* 982.e1–982.e7. doi:10.1016/j.urology.2014.06.019
10. Indena (Industria Derivati Naturali), “Escin β-Sitosterol Phytosome". http://www.indena.com/products/escin-%CE%B2-sitosterol-phytosome/ (accessed Aug 16, 2016).
11. Tomečková, V.; Reháková, M.; Mojžišová, G.; Wadsten, T.; Zelenáková, K.; Komanický, V. *Spectrosc. Lett.* **2015,** *49,* 63–72. doi:10.1080/00387010.2015.1072095
12. Van de Ven, H.; Vandervoort, J.; Weyenberg, W.; Apers, S.; Ludwig, A. *J. Microencapsulation* **2012,** *29,* 115–125. doi:10.3109/02652048.2011.630108
13. Szejtli, J. *Chem. Rev.* **1998,** *98,* 1743–1753. doi:10.1021/cr970022c
14. Pereira, A. B.; Braga, S. S. Cyclodextrin Inclusion of Nutraceuticals, from the Bench to your Table. In *Cyclodextrins: Synthesis, Chemical Applications and Role in Drug Delivery;* Ramirez, F. G., Ed.; Novascience publishers: Hauppauge, NY, 2015; pp 195–224.
15. Sugita, D.; Inoue, R.; Kurihara, Y. *Chem. Senses* **1998,** *23,* 93–97. doi:10.1093/chemse/23.1.93
16. Sanematsu, K.; Kusakabe, Y.; Shigemura, N.; Hirokawa, T.; Nakamura, S.; Imoto, T.; Ninomiya, Y. *J. Biol. Chem.* **2014,** *289,* 25711–25720. doi:10.1074/jbc.M114.560409
17. Jäger, S.; Strüh, C. M.; Schempp, C. M.; Scheffler, A.; Martin, S. F. *Phytomedicine* **2011,** *18,* S20. doi:10.1016/j.phymed.2011.09.048
18. Fontanay, S.; Kedzierewicz, F.; Duval, R. E.; Clarot, I. *J. Inclusion Phenom. Macrocyclic Chem.* **2012,** *73,* 341–347. doi:10.1007/s10847-011-0063-y
19. Quan, P.; Liu, D.; Li, R.; Zhang, Q.; Qian, Y.; Xu, Q. *J. Inclusion Phenom. Macrocyclic Chem.* **2009,** *63,* 181–188. doi:10.1007/s10847-008-9505-6
20. Dehelean, C. A.; Soica, C.; Peev, C.; Ciurlea, S.; Feflea, S.; Kasa, P., Jr. *Farmacia (Bucharest, Rom.)* **2011,** *59,* 51–59.
21. Claude, B.; Morin, P.; Lafosse, M.; Andre, P. *J. Chromatogr. A* **2004,** *1049,* 37–42. doi:10.1016/j.chroma.2004.06.133
22. Soica, C.; Danciu, C.; Savoiu-Balint, G.; Borcan, F.; Ambrus, R.; Zupko, I.; Bojin, F.; Coriocovac, D.; Ciurlea, S.; Avram, S.; Dehelean, C. A.; Olariu, T.; Matusz, P. *Int. J. Mol. Sci.* **2014,** *15,* 8235–8255. doi:10.3390/ijms15058235
23. Yakovishin, L. A.; Grishkovets, V. I.; Korzh, E. N.; Vetrova, E. V.; Borisenko, N. I. *Macroheterocycles* **2015,** *8,* 94–98. doi:10.6060/mhc141139y
24. Oda, M.; Kuroda, M. *J. Inclusion Phenom. Macrocyclic Chem.* **2016,** *85,* 271–279. doi:10.1007/s10847-016-0626-z
25. Cravotto, G.; Beltramo, L.; Sapino, S.; Binello, A.; Carlotti, M. E. *J. Mater. Sci.: Mater. Med.* **2011,** *22,* 2387–2395. doi:10.1007/s10856-011-4399-z
26. Fernandes, J. A.; Ramos, A. I.; Ribeiro-Claro, P.; Paz, F. A. A.; Braga, S. S. *CrystEngComm* **2015,** *17,* 937–946. doi:10.1039/C4CE02041C
27. Job, P. *Ann. Chim. Appl.* **1928,** *9,* 113–203.
28. Seal, B. K.; Sil, H.; Mukherjee, D. C. *Spectrochim. Acta, Part A: Mol. Spectrosc.* **1982,** *38,* 289–292. doi:10.1016/0584-8539(82)80210-9
29. Benesi, H. A.; Hildebrand, J. H. *J. Am. Chem. Soc.* **1949,** *71,* 2703–2707. doi:10.1021/ja01176a030
30. Schneider, H.-J.; Hacket, F.; Rüdigger, V.; Ikeda, H. *Chem. Rev.* **1998,** *98,* 1755–1786. doi:10.1021/cr970019t
31. Oledzka, E.; Pachowska, D.; Sobczak, M.; Lis-Cieplak, A.; Nalecz-Jawecki, G.; Zgadzaj, A.; Kolodziejski, W. *Polymers (Basel, Switz.)* **2015,** *7,* 1820–1836. doi:10.3390/polym7091484
32. Parr, R. G.; Yang, W. *Density-Functional Theory of Atoms and Molecules;* Oxford University Press: Oxford, 1989.
33. *Gaussian 09,* Revision E.01; Gaussian, Inc.: Wallingford CT, 2009.
34. Zhao, Y.; Truhlar, D. G. *Theor. Chem. Acc.* **2008,** *120,* 215–241. doi:10.1007/s00214-007-0310-x
35. Allen, F. H. *Acta Crystallogr., Sect. B: Struct. Sci.* **2002,** *B58,* 380–388. doi:10.1107/s0108768102003890
36. Braga, S. S.; Gonçalves, I. S.; Herdtweck, E.; Teixeira-Dias, J. J. C. *New J. Chem.* **2003,** *27,* 597–601. doi:10.1039/B207272F
37. Steiner, T.; Saenger, W. *Acta Crystallogr., Sect. B: Struct. Sci.* **1998,** *B54,* 450–455. doi:10.1107/S0108768197014547
38. Yang, X.-W.; Zhao, J.; Cui, Y.-X.; Liu, X.-H.; Ma, C.-M.; Hattori, M.; Zhang, L.-H. *J. Nat. Prod.* **1999,** *62,* 1510–1513. doi:10.1021/np990180u
39. Amorim Madeira, P. J.; Faddoul, M.; Afonso, M. B.; Vaz, P. D.; Fernandez, M. T.; Leal, J. P. *J. Mass Spectrom.* **2011,** *46,* 640–648. doi:10.1002/jms.1933
40. Wolinski, K.; Hilton, J. F.; Pulay, P. *J. Am. Chem. Soc.* **1990,** *112,* 8251–8260. doi:10.1021/ja00179a005
41. Woliński, K.; Sadlej, A. J. *Mol. Phys.* **1980,** *41,* 1419–1430. doi:10.1080/00268978000103631
42. Ditchfield, R. *Mol. Phys.* **1974,** *27,* 789–807. doi:10.1080/00268977400100711
43. McWeeny, R. *Phys. Rev.* **1962,** *126,* 1028–1034. doi:10.1103/PhysRev.126.1028
44. London, F. *J. Phys. Radium* **1937,** *8,* 397–409. doi:10.1051/jphysrad:01937008010039700

License and Terms

BEILSTEIN JOURNAL OF NANOTECHNOLOGY

Methods for preparing polymer-decorated single exchange-biased magnetic nanoparticles for application in flexible polymer-based films

Laurence Ourry‡, Delphine Toulemon‡, Souad Ammar*,‡ and Fayna Mammeri*,‡

Full Research Paper

Open Access

Address:
Université Paris Diderot, Sorbonne Paris Cité, CNRS UMR 7086 ITODYS, Case 7090, 5 rue Thomas Mann, Paris, France

Email:
Souad Ammar* - ammarmer@univ-paris-diderot.fr; Fayna Mammeri* - fayna.mammeri@univ-paris-diderot.fr

* Corresponding author ‡ Equal contributors

Keywords:
assembly; ATRP; magnetic nanoparticle; exchange-bias; films; functionalization; polymerization; poly(methyl methacrylate); polystyrene; seed-mediated growth; surface

Beilstein J. Nanotechnol. **2017,** *8,* 408–417.
doi:10.3762/bjnano.8.43

Received: 12 October 2016
Accepted: 19 January 2017
Published: 09 February 2017

This article is part of the Thematic Series "Hybrid nanomaterials: from the laboratory to the market".

Guest Editor: A. Taubert

Abstract

Background: Magnetic nanoparticles (NPs) must not only be well-defined in composition, shape and size to exhibit the desired properties (e.g., exchange-bias for thermal stability of the magnetization) but also judiciously functionalized to ensure their stability in air and their compatibility with a polymer matrix, in order to avoid aggregation which may seriously affect their physical properties. Dipolar interactions between NPs too close to each other favour a collective magnetic glass state with lower magnetization and coercivity because of inhomogeneous and frustrated macrospin cluster freezing. Consequently, tailoring chemically (through surface functionalization) and magnetically stable NPs for technological applications is of primary importance.

Results: In this work, well-characterized exchange-biased perfectly epitaxial $Co_xFe_{3-x}O_4$@CoO core@shell NPs, which were isotropic in shape and of about 10 nm in diameter, were decorated by two different polymers, poly(methyl methacrylate) (PMMA) or polystyrene (PS), using radical-controlled polymerization under various processing conditions. We compared the influence of the synthesis parameters on the structural and microstructural properties of the resulting hybrid systems, with special emphasis on significantly reducing their mutual magnetic attraction. For this, we followed two routes: the first one consists of the direct grafting of bromopropionyl ester groups at the surface of the NPs, which were previously recovered and redispersed in a suitable solvent. The second route deals with an "all in solution" process, based on the decoration of NPs by oleic acid followed by ligand exchange with the desired bromopropionyl ester groups. We then built various assemblies of NPs directly on a substrate or suspended in PMMA.

Conclusion: The alternative two-step strategy leads to better dispersed polymer-decorated magnetic particles, and the resulting nanohybrids can be considered as valuable building blocks for flexible, magnetic polymer-based devices.

Introduction

Polymer-based hybrid materials are opening the way for engineering new, multifunctional, flexible materials exhibiting novel properties (e.g., mechanical, magnetic, electrical, optical) due to the synergy between the two components, polymer and inorganic nanoparticles (NPs) [1]. In the case of magnetic hybrids, one of the main challenges is to avoid NP aggregation. The magnetic response of NPs to external magnetic stimulus depends strongly on their intrinsic properties (composition, size, and shape) but also on their spatial arrangement (self-assembly, dispersion in organic media, compatibility with polymers) [2,3]. If the interparticle distances are decreased too much, a collective magnetic glass state is set up, reducing magnetization and coercivity because of inhomogeneous and frustrated macrospin cluster freezing [4-6]. Ideally, flexible magnetic devices require dense but well-separated magnetic NPs to decrease interparticle interactions, particularly dipolar ones [7,8].

The general strategy for such a purpose consists of forming core–shell hybrid structures in which the shell consists of a corona of polymer chains grafted onto the inorganic NP surface. Among the available polymer grafting processes, living-radical polymerization (e.g., atom-transfer radical polymerization (ATRP), reversible addition–fragmentation chain transfer (RAFT) or nitroxide-mediated polymerization (NMP)) makes it possible to establish robust polymer–particle bonds and then grow polymer brushes of controlled molecular weight and polydispersity with a satisfactory grafting density. The polymer chains also stabilize the inorganic NPs with respect to the ambient atmosphere and provide compatibility with the resulting polymer matrix.

This strategy has been widely investigated with magnetic NPs. To date, most NPs studied were of iron oxide [9-14]. Exchange-biased NPs (ENPs) have been scarcely considered [15] despite their improved magnetic properties. These particles consist of ferro- or ferrimagnetic (F) cores coated with nanocrystalline antiferromagnetic (AF) layers, and exhibit exchange coupling at the F–AF interface (see for instance [16-18]), leading to an enhanced effective magnetic anisotropy constant (K_{eff}) and a higher temperature of transition from a magnetically blocked state to a superparamagnetic one (T_B) [19,20]. Focusing on such particles, in this work, we propose various material processing routes to prepare weakly interacting and densely arranged hybrid ENPs. The ENPs used were prepared by seed-mediated growth in a polyol medium; they consist of ferrimagnetic $Co_xFe_{3-x}O_4$ single crystals, almost isotropic in shape and of about 10 nm in diameter, coated in a perfectly epitaxial fashion with an antiferromagnetic CoO polycrystalline shell about 1 nm thick, as described in previous work [16]. We then controlled their surface functionality to tentatively design well-tailored nano-building-blocks for the aforementioned devices. To reduce mutual magnetic attraction and aggregation as far as possible in the first stage of polymer grafting, mechanical stirring and dilute suspensions of reactants were used, even if the functionalization of large amounts of particles becomes difficult. We specifically graft poly(methyl methacrylate) (PMMA) and polystyrene (PS) chains around $Co_xFe_{3-x}O_4$@CoO. Several key parameters have to be taken into account to realize a controlled polymerization reaction and especially when one aims to graft an ATRP initiator at the surface of particles: the nature of the surface (e.g., oxide or metal) and the interface between the components of the resulting hybrid, namely polymer chains and inorganic NPs (e.g., covalent, ionic, van der Waals). Several halogenated coupling agents can be used to covalently graft an organic group onto the surface of oxide NPs, e.g., organosilanes [21-23], carboxylate [24,25] or phosphonate/phosphate molecules [26,27].

Organosilanes present the disadvantage of condensing after hydrolysis and leading to a thin shell of polysiloxane whose structure and thickness cannot be well controlled. Carboxylates can be degrafted in solution [28], and are, consequently, not the best candidates for the desired applications. Phosphates and phosphonates are suitable for functionalizing iron and silicon oxide surfaces [29,30] through covalent bonds, in mono-, bi- or tridentate modes; but to date, they have not been used for cobalt oxide and ferrite surfaces.

In the case of PMMA, we followed two routes: the first one consists of a direct grafting of bromopropionyl ester molecules ob the surface of ENPs that were previously recovered and redispersed in a suitable solvent. The second uses an “all in solution” process, based on a prior decoration of ENPs by oleic acid ligands, which were subsequently exchanged by the desired bromopropionyl ester species. In the case of PS, we followed exclusively the first route, but in all the cases, the polymer chains were grown by ATRP (see the general synthesis scheme summarized in Figure 1), acting on the NP/monomer weight ratio and on the polymerization time parameters. The resulting nanohybrids were then characterized with special emphasis on the effect of the reaction parameters on their main microstructural properties and taking into account the fact that PS polymerizes more slowly than PMMA.

Results and Discussion

We chose to work on two very common thermoplastic polymers: PMMA and PS, which have very similar properties (e.g., specific temperatures, mechanical properties, density) but rather different side chains; PMMA has an aliphatic ester group while PS has a more rigid aromatic ring. However, despite their struc-

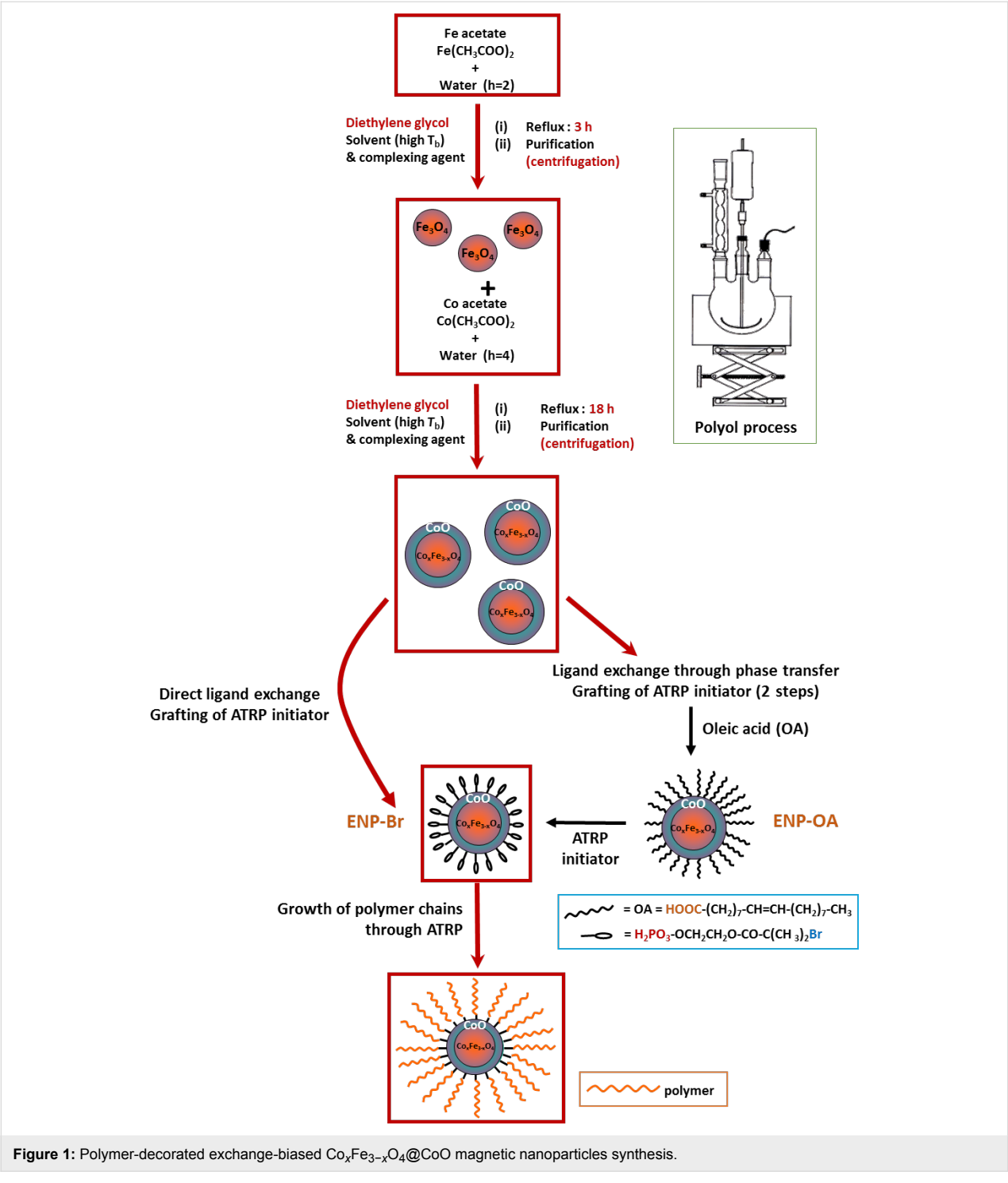

Figure 1: Polymer-decorated exchange-biased $Co_xFe_{3-x}O_4$@CoO magnetic nanoparticles synthesis.

tural and reactivity differences, we followed the same reaction pathway to elaborate ENPs decorated by the two polymers (Figure 1).

Growth of PMMA chains

We previously developed a two-step pathway to produce the hybrid polymer-decorated ENPs [15]. First, an ATRP initiator, 2-phosphonooxy-2-bromo-2-methylpropanoate, was grafted onto the ENP surface. Under the conditions used (see Experimental), the grafting density of the initiator molecules is 2.8 molecules nm^{-2}, in good agreement with previous studies [27]. Then, the PMMA chains were grown by ATRP at 30 °C in the presence of cuprous bromide and *N*,*N*,*N*′,*N*′,*N*″-pentamethyldiethylenetriamine (PMDTA) to form the

catalytic Cu-PMDETA complex, with polymerization times of 1 to 3 h. The polymer coating was characterized by X-ray photoelectron spectroscopy (XPS) and thermogravimetric analysis (TGA) [15]. For all samples the grafted chain density was 1.4 chain nm^{-2}, i.e., significantly higher than the results previously reported [15]. A chain density ranging between 0.1 and 1 chain nm^{-2} is commonly reported [13,26,31,32]. In the present case, a higher grafting density means better protection of the magnetic particles against oxidation and more stable magnetic properties over time [33]. Indeed, the aim here is not necessarily to grow very long polymer chains which are diamagnetic, but to functionalize ENPs efficiently in order to increase their compatibility with polymer matrices. Comparison of the grafting densities obtained here with those reported elsewhere suggests that, for ENPs of similar size, phosphates and phosphonates are better grafted and in greater quantity to the surface of ENPs than carboxylates and organosilanes.

Growth of PS chains

Styrene polymerizes more slowly than methyl methacrylate. Yousi et al. [34] demonstrated that the propagation rate, for similar conversion yields, can be increased by catalysts. Masson et al. [35] reported an increase in the styrene polymerization rate, using malonitrile as a catalyst and from initiator molecules anchored on iron oxide NPs. However, it appears that bonding the initiator to the surface through a phosphonate group limits the rate, reducing the effect of the catalyst. The length of the carbon backbone of the initiator (between phosphate and α-bromo-ester functions) is very important to the ATRP polymerization rate when initiators are directly anchored to the particle surface. Sunday et al. [36] reported that long alkyl chains (16 carbon atoms) or short ones (3 carbon atoms) lead to higher polymerization rates and grafting densities than intermediate chains (e.g., 11 carbon atoms). Masson et al. used an 11-carbon-long initiator. That which we used, the same as for PMMA (2-phosphonooxy-2-bromo-2-methylpropanoate), has only two carbon atoms, and might be expected to give good polymerization rates.

Working under the same conditions previously used for PMMA growth on ENPs, we prepared a series of samples by varying the polymerization time from 18 to 24 h; the resulting hybrids will be referred to as ENP-PS-h (where h corresponds to the polymerization time in hours). The survey XPS spectra of the resulting hybrids evidence all the characteristic signals of ENPs and initiator species (Figure 2). Hence, the O 1s (531.0 eV), Fe $2p_{3/2}$ (711.5 eV), Co $2p_{3/2}$ (781.7 eV), P 2p (133.5eV), and Br $3p_{3/2}$ (190.7 eV) peaks can be assigned to $Co_xFe_{3-x}O_4$@CoO and $PO(OH)_2O(CH_2)_2OCOC(CH_3)_2Br$ phases, respectively. The absence of Cu signals in the ENP-PS spectra suggests that all metallic Cu complexes were eliminated during the washing and purification steps. Chemical compositions (provided by XPS data) of as-produced NPs and ENP-PS are listed in Table 1.

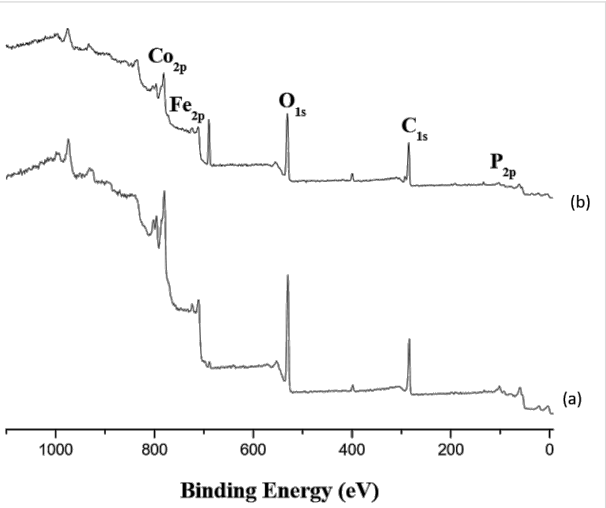

Figure 2: XPS survey spectra of (a) ENP-PS-18, (b) ENP-PS-24.

Table 1: XPS-determined atomic composition of as-prepared $Co_xFe_{3-x}O_4$-CoO nanoparticles (ENP) and PS-based hybrids.

Sample	Elemental atomic composition (%)					
	Fe	Co	O	C	P	Br
ENP ($Co_xFe_{3-x}O_4$@CoO)*	14.5	24.3	40.2	21.0	–	–
ENP-PS-18	7.7	10.5	37.6	41.5	2.3	0.4
ENP-PS-24	7.4	11.6	37.7	41.8	1.2	0.3

*Reproduced in part with permission from [15]. Copyright 2016 The Royal Society of Chemistry.

The C 1s peak prior to functionalization indicates that organic residues (polyol and acetate molecules) are present at the core–shell NP surface. The Co 2p and Fe 2p peaks are much weaker after polymerization due the presence of a significant polymer coating. The decomposition of the C 1s peak for polystyrene (PS) was difficult since there are many sources of organic matter (PS, initiator, residual polyol and acetates); however, unfortunately, styrene contains no other element suitable for XPS analysis. However, IR spectra of PS-decorated ENPs (Figure 3) exhibit several peaks characteristic of polystyrene: 3024 cm^{-1} ($\nu_{as(CH2\_arom)}$), 2950 cm^{-1} ($\nu_{s(CH\_aliph)}$) and 1600 cm^{-1} ($\nu_{C=C}$) when compared to a commercial reference.

Similar to the PMMA-based nanohybrids, the amount of cobalt was found to be higher than that of iron for PS-functionalized ENPs. The mean free paths of 1.5 nm for iron in CoO and 1.4 nm for cobalt in CoO were calculated following the method

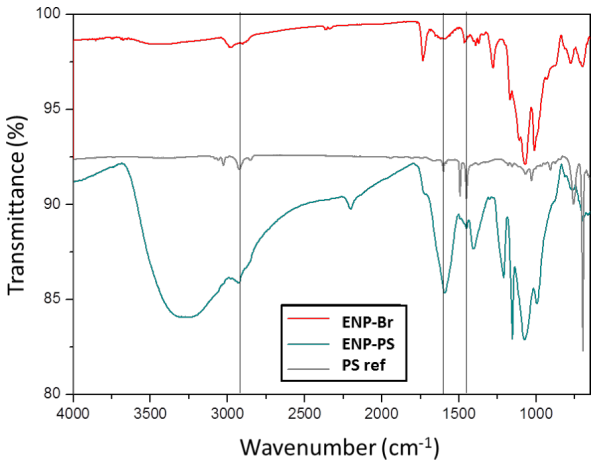

Figure 3: IR spectrum of ENP-PS-18 and those of free PS and ENPs functionalized by the ATRP initiator only (ENP-Br).

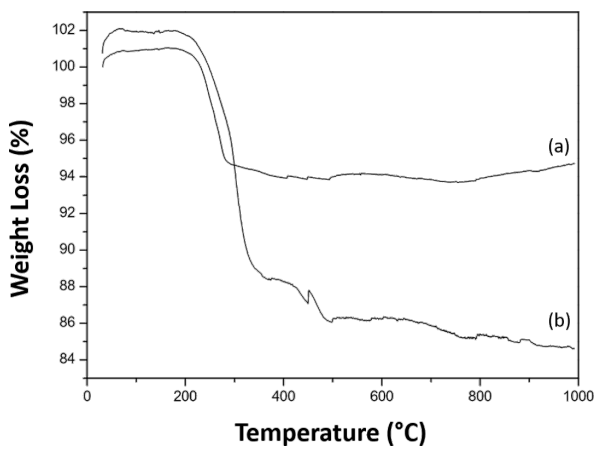

Figure 4: TGA curves of (a) ENP-PS-18 and (b) ENP-PS-20.

described previously [15]. However, electrons pass only through 0.5 nm of the Fe-rich core after having penetrated the 1 nm thick CoO shell, leading to a difference in depth analysis of the core and the shell. Then, we assumed that cobalt and carbon are representative of the CoO shell [30] and the PS brushes, respectively, to determine the PS thickness from the C 1s and Co 2p peaks and their relative intensities. The thicknesses were found to be 2.5 ± 0.5 nm for ENP-PS-18 and 3.0 ± 0.5 nm for ENP-PS-24. However, in the XPS chamber (under ultravacuum conditions), the polymer chains tend to collapse. Therefore, one must consider that XPS measurements do not allow the exact chain length to be determined but that of a polymer in a random coil conformation. Nevertheless, we can conclude that more polystyrene is present around the ENP when the polymerization time increases. TGA thermograms of PS-decorated ENPs are presented in Figure 4. PS is generally decomposed at about 380 °C. It can be seen that, although the polymer is thicker at the ENP surface in the case of PS, the weight losses of PS (6% and 14% for NP-PS-18 and NP-PS-24, respectively) are lower than those of PMMA in ENP-PMMA-1 and ENP-PMMA-3 [15], meaning that PS collapses less than PMMA. This is doubtful due to the presence of aromatic rings.

TEM images presented in Figure 5 depict well-dispersed nanoparticles, although the surface of the grid was not totally covered with ENPs. Similar images have been obtained for the two samples. There are spaces between the ENPs that are close to each other, suggesting that they are separated by PS coatings.

Ligand exchange for improved separation of magnetic NPs

In the previous sections, we demonstrated the feasibility of preparing polymer (PMMA or PS) functionalized magnetic particles with improved polymer chain grafting densities than those previously reported. However, it is still a serious challenge to separate all the particles and avoid a few aggregates. Hence, we replaced the centrifugation of the ENPs after the polyol synthesis by direct ligand exchange between adsorbed polyol molecules and oleic acid (OA) in the reaction mixture (see Experi-

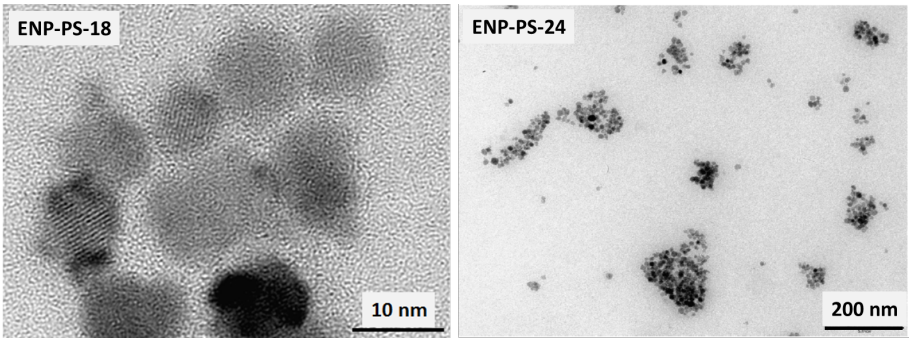

Figure 5: TEM images of ENP-PS-18 (left) and ENP-PS-24 (right).

mental). Oleic acid is known to cap oxide nanoparticles by ionic bonding [24,25]. Moreover, it bears a double bond C=C, inducing a degree of structural rigidity and a kink in the chain, promoting the spacing of the particles during their organization. TEM images (Figure 6) clearly show a better separation of the ENPs previously coated with OA instead of being recovered simply by centrifugation of the polyol mixture.

Figure 7 shows the variation of the size distribution of the magnetic particles as a function of the surface state (with or without oleic acid), determined by dynamic light scattering (DLS) measurements. The distribution is found to be quite polydisperse when ENPs are purified by centrifugation from the polyol and narrower when they are coated with OA. Moreover, the average diameter is found to be ≈100 nm for the former and 25 nm for the latter, which shows that the functionalization by OA through ligand exchange leads to a better separation of exchange-biased magnetic particles. Then, PMMA chains were grown from the surface of ENP-Br by the experimental procedure described previously [15].

Figure 8 presents the TEM images. Better-separated ENPs are recovered when oleic acid is used, and they are, consequently, more adapted for applications in flexible polymer devices.

Assembly of PMMA-decorated magnetic nanoparticles

Finally, we assembled PMMA-functionalized ENPs prepared by the ligand exchange procedure and dispersed in THF. Thin films were prepared by drop casting on silicon wafers and SEM images were recorded. Interestingly, Figure 9 depicts an incomplete monolayer of ENPs (with a scheme presented in the insert).

Then, ENP-PMMA was introduced in a solution of PMMA in THF, where the ENP/PMMA ratio was varied from 1:1 to 1:9. Large aggregates were obtained at higher concentrations of

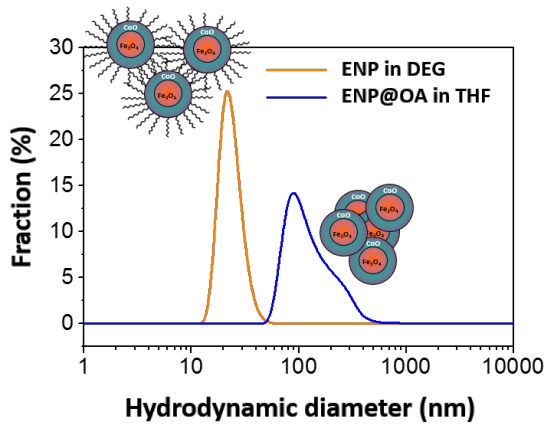

Figure 7: Size distributions of ENPs, in polyol solvent (diethylene glycol) and functionalized by oleic acid, dispersed in tetrahydrofuran solvent (THF), obtained by DLS.

ENPs and small aggregates or isolated ENPs at higher dilutions. SEM images (Figure 10) present well-dispersed ENPs in both cases, suggesting that the ENP-PMMA NPs are very well separated and can be dispersed and assembled in a controlled manner, thanks to the polymer grafted on the ENP surface.

The production of such nanoparticles thus opens the way to various applications such as: (i) the fundamental study of the magnetic properties of the various assemblies of these magnetic ENPs. There is still intensive research to be done on the control of the magnetic properties of magnetic films, either comprised of nanocomposites or not [37], via the spatial ENP orientation [28,38] to be combined with polymer processing [39,40].

As a preliminary result, focusing on these PMMA-decorated ENP assemblies, a net decrease of the blocking temperature value, defined as the critical temperature at the relaxed/blocked magnetic states transition, was observed when the ENP dilution ratio was increased (Figure 11). Such behaviour is

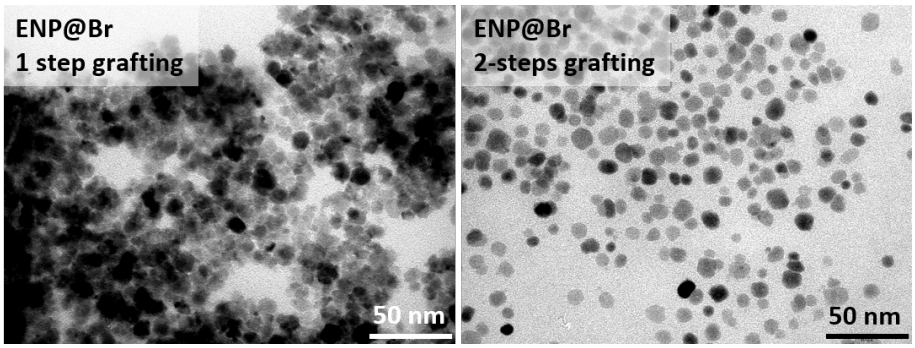

Figure 6: TEM images of a) ENP-Br obtained after centrifugation of as-prepared ENPs and direct grafting of ATRP initiator; b) ENP-Br obtained by two-step ligand exchange by oleic acid followed by grafting of ATRP initiator.

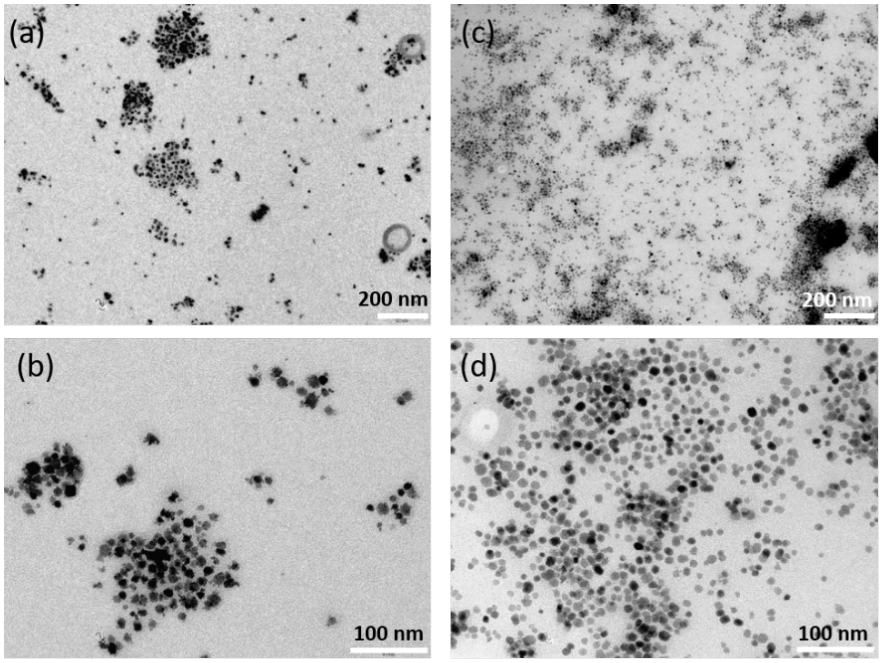

Figure 8: TEM images of magnetic ENPs decorated with PMMA brushes: (a,b) ENP-Br obtained through direct grafting of ATRP initiator after 3 h polymerization; (c,d) ENP-Br obtained by ligand exchange (oleic acid/ATRP initiator) under the same conditions.

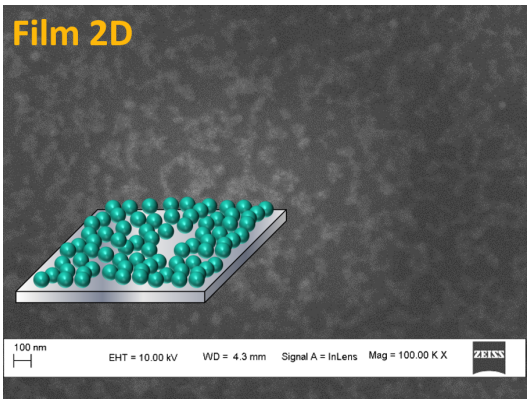

Figure 9: Thin films prepared by drop casting of a suspension of ENP-PMMA in THF.

quite common for superparamagnetic single-domain nanoparticles, and it is here respected in the case of exchange-biased nanoparticles.

It is clear that the material processing approach we proposed here, namely, the controlled surface polymerization of oxide-based ENPs, is able to tune their magnetic properties. Further magnetic measurements are still in progress to fully appreciate the dipolar interaction effect on the exchange bias and the influence of NP assembly on the exchange field.

Conclusion

We described the functionalization of 10 nm exchange-biased $Co_xFe_{3-x}O_4$@CoO core@shell NPs by two different polymers, poly(methyl methacrylate) (PMMA) and polystyrene (PS),

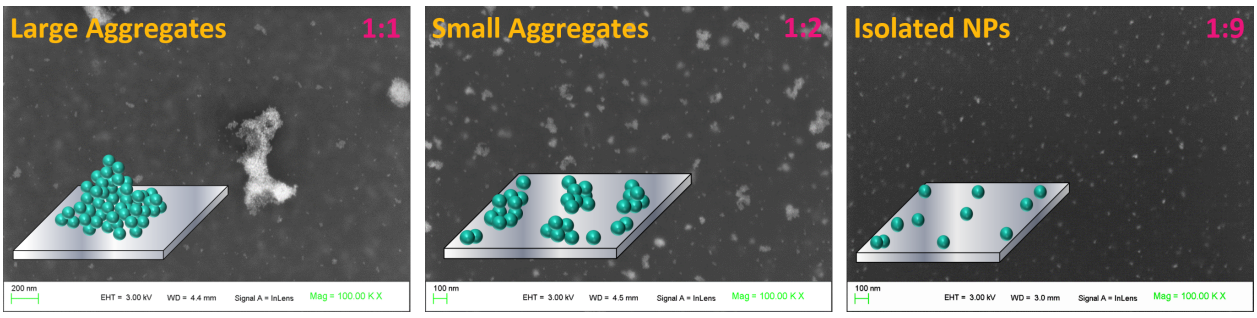

Figure 10: SEM images of various assemblies of ENP-PMMA, obtained by drop casting from THF suspension with ENP/PMMA ratios of 1:1, 1:2 and 1:9.

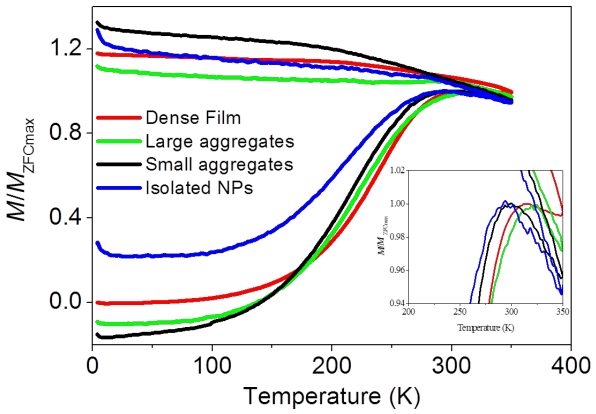

Figure 11: Thermal variation of the normalized dc magnetic magnetization measured in zero-field cooling (ZFC) conditions for the assembled PMMA-decorated ENP sample series (see Figure 10). Details around the maximum of the magnetization is given in the inset.

using radical-controlled polymerization under various processing conditions. We evidenced through TGA, IR spectroscopy and XPS measurements that polymer chains were efficiently grafted onto the nanoparticles using either the direct grafting or the "all in solution" process. In the TEM images we have also observed that very little aggregation occurs. Nevertheless, the alternative two-step strategy leads to better dispersed polymer-decorated magnetic particles, and the resulting nanohybrids can be considered as valuable building blocks for flexible, magnetic polymer-based devices. We also developed various assemblies by varying the dilution of the ENP suspension in THF, where the assemblies varied from small aggregates to isolated ENPs at the surface of silicon substrates. These ENPs allow for the preparation of flexible, functional, hybrid PMMA-ENP films with enhanced properties (e.g., magnetic, mechanical).

Experimental

Hybrid synthesis

PMMA chain growth by ATRP (direct ligand exchange for ATRP initiator grafting) was used as described in [15]: ENPs and 2-phosphonooxy-2-bromo-2-methylpropanoate were introduced in THF and sonicated at room temperature (RT). The resulting nanohybrids were then dispersed in acetonitrile before adding *N*,*N*,*N*′,*N*′,*N*″-pentamethyldiethylenetriamine (PMDTA) methyl methacrylate. The mixture was degassed with argon and mechanically stirred for 1 h. CuBr was added and the solution was heated around 30 °C and sonicated under inert atmosphere. The polymerization time was tuned from 1 to 3 h to influence the length of the polymer chains. The reaction was quenched by opening the system and diluting the solution with THF and hexane. Hairy, hybrid ENPs were recovered by centrifugation and washing with THF. They were referred to as ENP-PMMA-h, where h corresponds to the polymerization time in hours.

PS chain growth (direct ligand exchange for ATRP initiator grafting) proceeded by first dispersing 80 mg of ENP-Br in 37 mL of toluene before adding 8.2 µL of PMDTA, 4.8 mL of styrene and 11.4 mL of malonitrile in order to arrive at the ratio styene/initiator/malonitrile/PMDETA/CuBr 1000:1:4:1:1. The mixture was degassed with argon and mechanically stirred for at least 1 hour. 5.7 mg of CuBr were added and the solution was heated at 90 °C and mechanically stirred under argon. The polymerization time was varied from 18 to 24 h. Finally, the reaction was quenched by opening the system to the atmosphere. The resulting hybrids were referred to as ENP-PS-h, where h corresponds to the polymerization time in hours.

PMMA chain growth (two-step ATRP initiator grafting, ligand exchange by phase transfer) was accomplished using 150 mg of ENPs, dispersed in 45 mL of diethylene glycol, which was added to 75 mL of a solution of oleic acid in toluene (10% v/v) and sonicated for 15 min and left overnight. The OA-functionalized ENPs were recovered from the toluene layer and 375 mg of 2-phosphonooxy-2-bromo-2-methylpropanoate were added to the suspension and sonicated for 24 h. Toluene was then removed and the functionalized ENPs were recovered after several washings with THF.

Hybrid characterization

The different reaction steps were monitored by ATR-FTIR on a Thermo Nicolet 8700 spectrometer equipped with a diamond crystal (50 scans, 4 cm^{-1} resolution). Thermogravimetric analyses (TGA) were performed in air on a Labsys-Evo device with a heating rate of 10 °C min^{-1}. X-ray photoelectron spectroscopy (XPS) measurements were performed on as-prepared and functionalized ENPs using a Thermo VG ESCALAB 250 instrument equipped with a micro-focused, monochromatic Al Kα X-ray source (1486.6 eV) and a magnetic lens. The X-ray spot size was 500 µm (15 kV, 150 W). The spectra were acquired in the constant analyser energy mode with pass energies of 150 and 40 eV for the general survey and the narrow scans, respectively. The samples were fixed on sample holders and out-gassed in the fast entry airlock (2×10^{-7} mbar). The Avantage software package was used for data acquisition and processing. The C 1s line of 285 eV was used as the reference to correct the binding energies. Scanning electron microscopy (SEM) and transmission electron microscopy (TEM) were performed on Supra40 ZEISS FEG-SEM and JEOL-100-CX II TEM microscopes, operating at 5.0 and 100 kV, respectively.

Acknowledgements

The authors would like to thank Dr. Thomas Gaudisson (who designed the $Co_xFe_{3-x}O_4$@CoO ENPs) and Dr. John Lomas for fruitful discussions, Ms. Smina Hammaz for her technical support on polymer brush degrafting, Dr. Philippe Decorse for

the XPS measurements and M. Ludovic Mouton for recording the TEM images.

The ANR (Agence Nationale de la Recherche) and CGI (Commissariat à l'Investissement d'Avenir) are gratefully acknowledged for their financial support of this study through Labex SEAM (Science and Engineering for Advanced Materials and Devices) ANR 11 LABX 086, ANR 11 IDEX 05 02.

References

1. Balazs, A. C.; Emrick, T.; Russel, T. P. *Science* **2006,** *314,* 1107–1110. doi:10.1126/science.1130557
2. Frankamp, B. L.; Boal, A. K.; Tuominen, M. T.; Rotello, V. M. *J. Am. Chem. Soc.* **2005,** *127,* 9731–9735. doi:10.1021/ja051351m
3. Fleutot, S.; Nealon, G. L.; Pauly, M.; Pichon, B. P.; Leuvrey, C.; Drillon, M.; Gallani, J.-L.; Guillon, D.; Donnio, B.; Begin-Colin, S. *Nanoscale* **2013,** *5,* 1507–1516. doi:10.1039/c2nr32117c
4. Dormann, J. L.; Fiorani, D.; Cherkaoui, R.; Spinu, L.; Lucari, F.; D'Orazio, F.; Noguès, M.; Tronc, E.; Jolivet, J. P.; Garcia, A. *Nanostruct. Mater.* **1999,** *12,* 757–762. doi:10.1016/S0965-9773(99)00231-7
5. Fiorani, D.; Testa, A. M.; Tronc, E.; Lucari, F.; D'Orazio, D.; Nogués, M. *J. Magn. Magn. Mater.* **2001,** *226–230,* 1942–1944. doi:10.1016/S0304-8853(00)00680-6
6. Beji, Z.; Smiri, L. S.; Yaacoub, N.; Grenèche, J.-M.; Menguy, N.; Ammar, S.; Fiévet, F. *Chem. Mater.* **2010,** *22,* 1350–1366. doi:10.1021/cm901969c
7. Liu, Y.-W.; Zhan, Q.-F.; Li, R.-W. *Chin. Phys. B* **2013,** *22,* 127502. doi:10.1088/1674-1056/22/12/127502
8. Ghoneim, M. T.; Hussain, M. M. *Electronics (Basel, Switz.)* **2015,** *4,* 424–479. doi:10.3390/electronics4030424
9. Wang, Y.; Teng, X.; Wang, J.-S.; Yang, H. *Nano Lett.* **2003,** *3,* 789–793. doi:10.1021/nl034211o
10. Xu, G.; Wu, W.-T.; Wang, Y.; Pang, W.; Zhu, Q.; Wang, P.; You, Y. *Polymer* **2006,** *47,* 5909–5918. doi:10.1016/j.polymer.2006.06.027
11. Ninjbadgar, T.; Yamamoto, S.; Fukuda, T. *Solid State Sci.* **2004,** *6,* 879–885. doi:10.1016/j.solidstatesciences.2003.11.009
12. Garcia, I.; Zafeiropoulos, N. E.; Janke, A.; Tercjak, A.; Eceiza, A.; Stamm, M.; Mondragon, I. *J. Polym. Sci., Part A: Polym. Chem.* **2007,** *45,* 925–932. doi:10.1002/pola.21854
13. Galeotti, F.; Bertini, F.; Scavia, G.; Bolognesi, A. *J. Colloid Interface Sci.* **2011,** *360,* 540–547. doi:10.1016/j.jcis.2011.04.076
14. Basti, H.; Ben Tahar, L.; Smiri, L. S.; Herbst, F.; Nowak, S.; Mangeney, C.; Ammar, S. *Colloids Surf., A* **2016,** *490,* 222–231. doi:10.1016/j.colsurfa.2015.11.013
15. Ourry, L.; Mammeri, F.; Toulemon, D.; Gaudisson, T.; Delamar, M.; Ammar, S. *RSC Adv.* **2016,** *6,* 49973–49979. doi:10.1039/C6RA06963K
16. Gaudisson, T.; Ourry, L.; Hammoud, H.; Nowak, S.; Menguy, N.; Yaacoub, N.; Grenèche, J.-M.; Mammeri, F.; Ammar, S. *J. Nanopart. Res.* **2014,** *16,* 2359. doi:10.1007/s11051-014-2359-5
17. Baaziz, W.; Pichon, B. P.; Lefevre, C.; Ulhaq-Bouillet, C.; Grenèche, J.-M.; Toumi, M.; Mhiri, T.; Bégin-Colin, S. *J. Phys. Chem. C* **2013,** *117,* 11436–11447. doi:10.1021/jp402823h
18. Chandra, S.; Biswas, A.; Khurshid, H.; Li, W.; Hadjipanayis, G. C.; Srikanth, H. *J. Phys.: Condens. Matter* **2013,** *25,* 426003. doi:10.1088/0953-8984/25/42/426003
19. Weller, D.; Moser, A. *IEEE Trans. Magn.* **1999,** *35,* 4423–4439. doi:10.1109/20.809134
20. Fullerton, E. E.; Margulies, D. T.; Schabes, M. E.; Carey, M.; Gurney, B.; Moser, A.; Best, M.; Zeltzer, G.; Rubin, K.; Rosen, H.; Doerner, M. *Appl. Phys. Lett.* **2000,** *77,* 3806–3808. doi:10.1063/1.1329868
21. Sun, Y.; Ding, X.; Zheng, Z.; Cheng, X.; Hu, X.; Peng, Y. *Eur. Polym. J.* **2007,** *43,* 762–772. doi:10.1016/j.eurpolymj.2006.10.021
22. Ohno, K.; Mori, C.; Akashi, T.; Yoshida, S.; Tago, Y.; Tsujii, Y.; Tabata, Y. *Biomacromolecules* **2013,** *14,* 3453–3462. doi:10.1021/bm400770n
23. Huang, Y.; Ishige, R.; Tsujii, Y.; Ohno, K. *Langmuir* **2015,** *31,* 1172–1179. doi:10.1021/la504429c
24. Fan, Q.-L.; Neoh, K.-G.; Kang, E.-T.; Shuter, B.; Wang, S.-C. *Biomaterials* **2007,** *28,* 5426–5436. doi:10.1016/j.biomaterials.2007.08.039
25. Gravano, S. M.; Dumas, R.; Liu, K.; Patten, T. E. *J. Polym. Sci., Part A: Polym. Chem.* **2005,** *43,* 3675–3688. doi:10.1002/pola.20823
26. Babu, K.; Dhamodharan, R. *Nanoscale Res. Lett.* **2009,** *4,* 1090–1102. doi:10.1007/s11671-009-9365-z
27. Babu, K.; Dhamodharan, R. *Nanoscale Res. Lett.* **2008,** *3,* 109. doi:10.1007/s11671-008-9121-9
28. Mammeri, F.; Le Bras, Y.; Daou, T. J.; Gallani, J.-L.; Colis, S.; Pourroy, G.; Donnio, B.; Guillon, D.; Bégin-Colin, S. *J. Phys. Chem. B* **2009,** *113,* 734–738. doi:10.1021/jp808177y
29. Mutin, P. H.; Guerrero, G.; Vioux, A. *Chimie* **2003,** *6,* 1153–1164. doi:10.1016/j.crci.2003.07.006
30. Daou, T. J.; Begin-Colin, S.; Grenèche, J.-M.; Thomas, F.; Derory, A.; Bernhardt, P.; Legaré, I. P.; Pourroy, G. *Chem. Mater.* **2007,** *19,* 4494–4505. doi:10.1021/cm071046v
31. Huang, C.; Tassone, T.; Woodberry, K.; Sunday, D.; Green, D. L. *Langmuir* **2009,** *25,* 13351–13360. doi:10.1021/la901918v
32. Patil, R. R.; Turgman-Cohen, S.; Šrogl, J.; Kiserow, D.; Genzer, J. *ACS Macro Lett.* **2015,** *4,* 251–254. doi:10.1021/mz5007188
33. Sayed Hassan, R.; Gaudisson, T.; Yaacoub, N.; Grenèche, J.-M.; Menguy, N.; Nedelka, N.; Slawaska-Waniewska, A.; Galmiche, M.; Mammeri, F.; Ammar, S. *Mater. Res. Express* **2014,** *1,* 025035. doi:10.1088/2053-1591/1/2/025035
34. Jiaming, Z.; Rui, L.; Jianying, H.; Jiayan, C.; Xurong, L.; Yutai, L.; Yousi, Z. *J. Polym. Sci., Part A: Polym. Chem.* **2007,** *45,* 4082–4090. doi:10.1002/pola.22217
35. Vergnat, V.; Pourroy, G.; Masson, P. *Polym. Int.* **2013,** *62,* 878–883. doi:10.1002/pi.4435
36. Sunday, D.; Curras-Medina, S.; Green, D. L. *Macromolecules* **2010,** *43,* 4871–4878. doi:10.1021/ma1004259
37. Lim, G.-H.; Lee, J.; Kwon, N.; Bok, S.; Sim, H.; Moon, K.-S.; Lee, S.-E.; Lim, B. *Electron. Mater. Lett.* **2016,** *12,* 574–579. doi:10.1007/s13391-016-6179-x
38. Koo, J.; Kim, H.; Kim, K.-Y.; Jang, Y. R.; Lee, J.-S.; Yoon, S. W.; Suh, B. J.; Yu, T.; Bang, J.; Yoon, K.; Yuan, G.; Satija, S. K. *RSC Adv.* **2016,** *6,* 55842–55847. doi:10.1039/C6RA10026K
39. Ourry, L.; Marchesini, S.; Bibani, M.; Mercone, S.; Ammar, S.; Mammeri, F. *Phys. Status Solidi A* **2015,** *212,* 252–258. doi:10.1002/pssa.201431563
40. Ben Osman, C.; Nowak, S.; Garcia-Sanchez, A.; Charles, Y.; Ammar, S.; Mercone, S.; Mammeri, F. *Eur. Polym. J.* **2016,** *84,* 602–611. doi:10.1016/j.eurpolymj.2016.09.056

BEILSTEIN JOURNAL OF NANOTECHNOLOGY

α-((4-Cyanobenzoyl)oxy)-ω-methyl poly(ethylene glycol): a new stabilizer for silver nanoparticles

Jana Lutze[1], Miguel A. Bañares[2], Marcos Pita[2], Andrea Haase[1], Andreas Luch[1] and Andreas Taubert[*3,§]

Full Research Paper

Open Access

Address:
[1]German Federal Institute for Risk Assessment (BfR), Department of Chemical and Product Safety, Max-Dohrn-Strasse 8-10, D-10589 Berlin, Germany, [2]Instituto de Catálisis y Petroleoquímica, ICP-CSIC, C/ Marie Curie 2, E-29049 Madrid, Spain and [3]Institute of Chemistry, University of Potsdam, Karl-Liebknecht-Str. 24-25, D-14476 Golm, Germany

Email:
Andreas Taubert[*] - ataubert@uni-potsdam.de

* Corresponding author
§ Tel.: +49 331 977 5773; Fax: +49 331 977 5055, web: http://www.taubert-lab.net

Keywords:
cyano anchor group; poly(ethylene glycol); polymer coating; silver nanoparticles

Beilstein J. Nanotechnol. **2017,** *8,* 627–635.
doi:10.3762/bjnano.8.67

Received: 14 October 2016
Accepted: 27 February 2017
Published: 15 March 2017

This article is part of the Thematic Series "Hybrid nanomaterials: from the laboratory to the market".

Associate Editor: M. Stenzel

Abstract

The article describes the synthesis and properties of α-((4-cyanobenzoyl)oxy)-ω-methyl poly(ethylene glycol), the first poly(ethylene glycol) stabilizer for metal nanoparticles that is based on a cyano rather than a thiol or thiolate anchor group. The silver particles used to evaluate the effectiveness of the new stabilizer typically have a bimodal size distribution with hydrodynamic diameters of ca. 13 and ca. 79 nm. Polymer stability was evaluated as a function of the pH value both for the free stabilizer and for the polymers bound to the surface of the silver nanoparticles using ^{1}H NMR spectroscopy and zeta potential measurements. The polymer shows a high stability between pH 3 and 9. At pH 12 and higher the polymer coating is degraded over time suggesting that α-((4-cyanobenzoyl)oxy)-ω-methyl poly(ethylene glycol) is a good stabilizer for metal nanoparticles in aqueous media unless very high pH conditions are present in the system. The study thus demonstrates that cyano groups can be viable alternatives to the more conventional thiol/thiolate anchors.

Introduction

Nanoparticles (NPs), especially metal NPs such as gold and silver NPs (SNPs), are currently among the most popular research subjects and many particles have been suggested for applications in, e.g., electronics or medicine [1-3]. Metallic nanoparticles intended for use in medicine or diagnostics are generally modified with an organic coating designed to prevent

or at least to reduce aggregation in aqueous media [4-13]. A good stabilizing agent is thus essential to obtain and retain stable particle dispersions [11,14-16].

Synthetic particles often have coatings made from polymers such as poly(vinyl pyrrolidone), poly(vinyl alcohol), or poly(ethylene glycol) (PEG). PEG-based coatings are particularly popular [17,18]. This is also due to the high hydrophilicity and biological inertness of PEG, which renders PEG-stabilized NPs water-soluble and less susceptible to opsonization [19,20]. As a result, PEG-coated NPs are often referred to as "stealth" NPs [21,22]. Moreover, PEG coatings often lower the toxicity of otherwise toxic NPs [23,24]. For example, Zhang et al. [25] demonstrated the passivating effect of a PEG/silica hybrid coating on CdSe quantum dots. Thus, there is a growing interest in PEG-based stabilizers for a large variety of applications including catalysis, diagnostics, biology or biomedicine.

There are numerous examples in which the oligomeric or polymeric stabilizer is attached to the particle surface without a specific anchor group [26-30]. The current gold standard for anchoring an organic moiety on the NP surface is the thiol or thiolate group [3,24,31-33]. There are, however, cases where the thiol group may not be desirable (such as situations, where thiols may form thiyl radicals leading to protein degradation and cause diseases such as cancer) [34,35]. Hence, there is an interest in alternative anchoring groups with a similar or better anchoring efficiency. Among the possible candidates are the amine and the cyano groups. Especially the cyano group is interesting because of its relatively high metal binding capability (although lower than that of the thiol group) [36] and its stability in a variety of chemical environments [37]. Yet, the number of reports on stabilizers for metal nanoparticles with a cyano group anchor is limited [36,38-43] and further development of cyano-based stabilizers is of high interest. However, depending on the application, the toxicity of the cyano-based stabilizers will also have to be considered [44].

The current study introduces a new stabilizer, α-((4-cyanobenzoyl)oxy)-ω-methyl poly(ethylene glycol) (CBAmPEG) exploiting the cyano group as an anchor. CBAmPEG is (i) accessible in good yield via a simple one-step synthesis and (ii) provides an efficient stabilization of SNPs in a pH range between 3 and 9. The latter point is important because degradation of the stabilizer may lead to particle aggregation and sedimentation, which is often –for example in a biomedical context [10,11,45] – highly undesirable and must be avoided. The new CBAmPEG introduced here is thus an attractive alternative to other polymeric stabilizers and to the best knowledge of the authors it is the first PEG-based stabilizer for metal nanoparticles with a cyano anchor group.

Experimental

General

4-Cyanobenzoic acid (98%, abcr), 4-(dimethylamino)pyridine (99%, Aldrich), deuterium oxide (99.9 atom % D, Aldrich), hydrochloric acid (37%, lab reagent grade, Fisher Scientific), L-ascorbic acid (≥99%, Roth), *N*,*N'*-dicyclohexylcarbodiimide (99%, Aldrich), poly(ethylene glycol) methyl ether (M_n = 4830 g·mol^{-1}, Aldrich), silver nitrate (≥99%, Sigma-Aldrich), sodium hydroxide (>99%, Roth), and trisodium citrate dihydrate (99.7%, Merck) were used as received. Water with a resistivity of 18.2 MΩ·cm (Milli-Q) was used for particle synthesis and purification.

Synthesis of CBAmPEG

4-Cyanobenzoic acid (0.6 g, 4 mmol), poly(ethylene glycol) methyl ether (5.0 g, 1 mmol, M_n = 4830 g·mol^{-1}) and 4-(dimethylamino)pyridine (DMAP, 50 mg, 0.4 mmol) were dissolved in dichloromethane (DCM, 10 mL). The solution was cooled to 0 °C and *N*,*N'*-dicyclohexylcarbodiimide (DCC, 1.0 g, 5 mmol) in dichloromethane (1 mL) was added slowly. After ten minutes of stirring the reaction mixture was warmed to room temperature and stirred overnight. The precipitate was filtered off and the filtrate was precipitated in *tert*-butyl methyl ether. The product was dissolved in distilled water and insoluble parts were removed by filtration. Lyophilization afforded the pure product as a colorless powder. Yield: 3.8 g (74%). The number of repeating units of CBAmPEG was calculated from the molar mass derived from gel permeation chromatography (GPC) measurements with refractive index (RI) detector.

^{1}H NMR (300 MHz, D_2O) δ 8.05 (m, 4H), 4.53 (m, 2H), 3.67 (m, 488H); ATR-IR (cm^{-1}): 2947 (sh, ν(CH)), 2885 (s, ν(CH)), 2742 (vw, ν(CH)), 2696 (vw, ν(CH)), 1724 (w, ν(C=O)), 1466 (m, δ(CH_2)), 1412 (w, δ(CH_2)), 1358 (w, δ(CH_2), ν(CC)), 1342 (m, δ(CH_2)), 1281 (m, δ(CH_2)), 1242 (m, δ(CH_2)), 1146 (m, ν(C-O)), 1107 (s, ν(C-O)), 1061 (m, δ(CH_2), ν(C-O)), 960 (m, δ(CH_2)), 845 (m, δ(CH_2)), 768 (vw, δ(C=O)), 694 (vw, δ(Ph)), 528 (vw, δ(OCC)); Raman (cm^{-1}): 2953 (sh, ν(CH)), 2934 (s, ν(CH)), 2897 (sh, ν(CH)), 2237 (m, ν(CN)), 1612 (m, ν(Ph)), 1480 (m, δ(CH_2)), 1449 (w, δ(CH_2)), 1306 (m, δ(CH_2)), 1287 (m, δ(CH_2)), 1132 (m, ν(C-O)), 1054 (m, ν(C-O), ν(CC), ν(CH_2)), 854 (m, ν(C-O), ν(CH_2)); GPC: M_n(UV) = 4627 g·mol^{-1}; PDI(UV) = 1.0544; M_n(RI) = 4578 g·mol^{-1}, PDI(RI) = 1.0654; Anal. calcd: C, 54.9; H, 9.0; found: C, 54,8; H, 8.3.

Silver nanoparticle synthesis

Citrate-coated SNPs were synthesized according to a procedure of Qin et al. [46] 4 mL of a 1.2·10^{-3} M aqueous ascorbic acid solution (4.8 μmol) and 4 mL of a 6·10^{-3} M aqueous trisodium citrate dihydrate solution (24 μmol) were combined and the pH

was adjusted to 10.5 with a 0.5 M sodium hydroxide solution. The mixture was heated to 30 °C and a silver nitrate solution (0.1 M, 80 µL, 8.0 µmol) was added under vigorous stirring. After ten minutes stirring at room temperature the mixture was refluxed for two hours, resulting in an orange dispersion, which was allowed to cool to room temperature before adding CBAmPEG (200 mg, 44 µmol) for the ligand exchange reaction. After stirring the mixture overnight at room temperature under the exclusion of light, the dispersion was centrifuged three times at 8000 rpm for 60 min. The sediment was redispersed in DI water or purified by dialysis against water for 24 h (MWCO 100 kDa). Scheme 1 summarizes polymer and nanoparticle synthesis.

Raman (cm^{-1}): 2930 (s, ν(CH)), 2247 and 2237 (m, ν(CN)), 1648 (w, ν(C=C)), 1605(w, ν(Ph)), 1573(m, ν(CO_2), 1508 (w, δ(CH_2)), 1443 (w, δ(CH_2)), 1390 (sh, δ(CH_2)), 1362 (m, ν(CO_2)), 1310 (w, δ(CH_2)), 1285 (sh, δ(CH_2)), 1234 (w, δ(CH_2)), 1170 (s, ν(C-O)), 1128 (vw, ν(CC), δ(CH_2)), 1032 (w, ν(C-O), ν(CC), δ(CH_2)), 1002 (w, ν(C-O), ν(CC), δ(CH_2)), 944 (w, ν(C-O), ν(CC), δ(CH_2)), 889 (vw, ν(C-O), δ(CH_2)), 819 (w, ν(C-O), δ(CH_2)), 773 (w, 1,4-disubstituted aromatic ring bending), 715 (m, δ(CO)), 675 (m, δ(CO)), 659 (sh, δ(CO)), 613 (m, scissoring NO_2), 569 (vw, CN in plane bending), 523 (w, δ(OCC)), 504 (sh, 1,4-disubstituted aromatic ring bending), 396 (vw, δ(CCN), 347 (vw, δ(COC), δ(OCC)), 311 (vw, possibly due to general skeletal vibrations).

Cleavage experiments

For evaluating the cleavage of the pure CBAmPEG polymer, D_2O solutions with a pH value of 3, 6, 9, and 12 were prepared by dissolving an appropriate amount of sodium hydroxide or concentrated hydrochloric acid in D_2O and adjusting the pH with 0.1 M sodium hydroxide or 0.1 M hydrochloric acid. The differences of pH, pD, and pHD values were not considered. CBAmPEG was then dissolved in each of the pH-adjusted D_2O solutions at a concentration of 0.02 mol/L and the mixtures were heated to 37 °C. After 6, 12, 18, and 24 h ^{1}H NMR spectra of each solution were recorded.

Evaluation of the cleavage of the polymer on the silver nanoparticles (CBAmPEG@SNPs) was done as follows: the pH of a dialyzed dispersion of CBAmPEG@SNPs (2.5 mL) was adjusted to 12. This sample and a control sample (dialyzed dispersion without pH adjustment, pH ca. 7) were incubated at 37 °C in the dark for 66 h without stirring. The experiment was repeated three times with three different SNP batches. For the control experiments a change in color from yellow to orange was observed in two of three cases, whereas for the samples with an adjusted pH of 12 a small amount of solid floating at the surface of the reaction vessels could be observed. Samples were removed from the heating bath for DLS and zeta-potential measurements.

Analytical methods

Gel permeation chromatography. GPC measurements were done on two 300 × 8 mm^2 PSS-GRAM (7 µm particles) columns with porosities of 10^2–10^3 Å in *N*-methyl-2-pyrrolidone (NMP + 0.5 wt % LiBr at 70 °C and a flow rate of 0.8 mL/min with simultaneous UV and RI detection. Polyethylene oxide (PEO) standards (PSS, Mainz, Germany) were used for calibration.

Transmission electron microscopy. Samples were centrifuged three times to remove residual polymer not attached to the NP surface. For TEM measurement the samples were diluted and

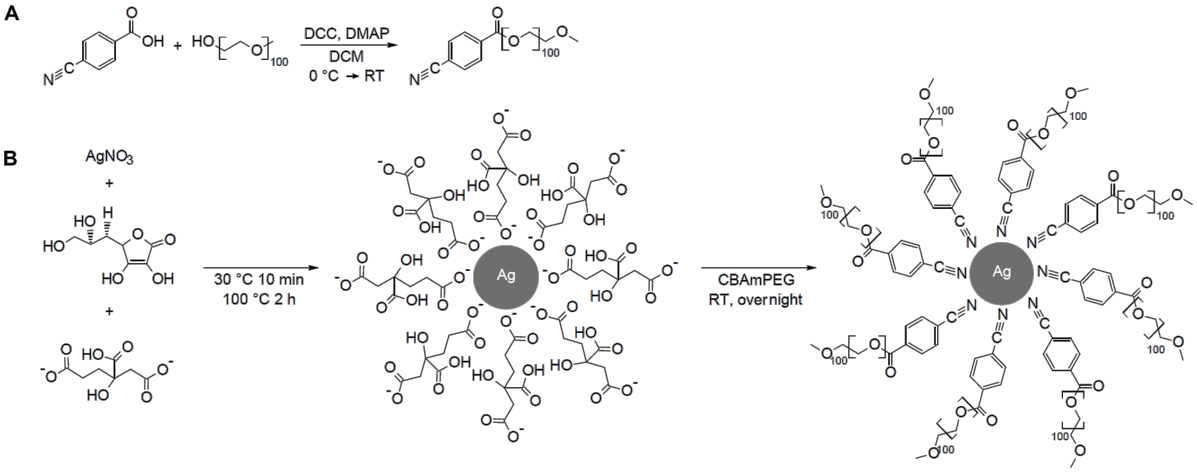

Scheme 1: Synthesis of A) α-((4-cyanobenzoyl)oxy)-ω-methyl poly(ethylene glycol) (CBAmPEG) via Steglich esterification and B) synthesis of CBAmPEG-coated SNPs (CBAmPEG@SNPs). Note that the exchange between citrate and CBAmPEG is not complete (see details below) and the final product is a mixed coating.

dispersed in an ultrasonic bath for 15 min. Afterwards a drop of the diluted and ultrasound-treated sample was deposited on a carbon film coated 200 mesh copper TEM grid (Electron Microscopy Sciences) and allowed to dry. A 200 kV JEOL 2100 transmission electron microscope equipped with an Oxford Instruments EDX analyzer was used for the analysis.

IR spectroscopy. IR spectra were measured with a Thermo Nicolet Nexus FTIR spectrometer with a Thermo Scientific Smart Orbit (Diamond). ATR correction was done with Omnic 8.1.11 from Thermo Nicolet Fischer Scientific. For IR spectroscopy, a few microliters of SNP dispersion were deposited on the ATR crystal and allowed to dry in air for a few minutes. Spectral resolution was 4 cm^{-1} and spectra were acquired from 400 to 4000 cm^{-1}.

Raman spectroscopy. Raman spectroscopy measurements were performed on a Renishaw System 1000 Raman Spectrometer with 514.5 nm tuned solid-state excitation laser and an edge filter to remove elastically scattered light, and a Peltier-cooled CCD detector (−70 °C). Raman spectra were acquired with a laser power of 1 mW on sample; 10 spectra of 6 s were acquired for each sample. Samples were used as obtained from particle synthesis, that is, no dilution or other sample processing was performed prior to Raman analysis.

NMR spectroscopy. ^{1}H NMR spectra were recorded on a Bruker Avance 300 MHz or 500 MHz spectrometer in D_2O with TMS as an internal standard.

Light scattering and zeta potential. The hydrodynamic diameter R_h and the zeta potential of the SNPs were determined with a Zetasizer ZS and the Zetasizer 7.1 Software (Malvern Instruments, UK). For DLS experiments the samples were diluted with DI water (18.2 MΩ) and placed in disposable plastic cuvettes. For each sample five measurements consisting of ten runs of ten seconds each were done. The laser wavelength was 633 nm and data were recorded in backscattering mode 2θ = 173° at a temperature of 25 °C. Electrophoretic mobilities were measured five times for each sample in an automatic mode (10 to 100 runs per measurement) at 25 °C and automatically converted to zeta potentials using the Smoluchowski model.

Results

α-((4-Cyanobenzoyl)oxy)-ω-methyl poly(ethylene glycol) (CBAmPEG)

CBAmPEG was synthesized via Steglich esterification of 4-cyanobenzoic acid and poly(ethylene glycol) methyl ether (M_n = 4830 g·mol^{-1}) as shown in Scheme 1. The ^{1}H NMR and the IR spectra of the product confirm the successful formation of CBAmPEG, Figure 1. The ATR-IR spectra show bands at 2947, 2885, 2742, 2696, 1466, 1412, 1358, 1342, 1281, 1242, 1061, 960, and 845 cm^{-1} that can be assigned to various C–H vibrations (see Experimental section for specific assignments). Bands at 1724, 1146, 1107, and 768 cm^{-1} can be assigned to C=O and C–O vibrations. Finally, a band at 694 cm^{-1} is due to phenyl ring bending vibrations. Signals in the ^{1}H NMR spectra are due to the aromatic protons of the phenyl group (8.05 ppm), the methylene (4.53 ppm, 2 H atoms) protons adjacent to the ester linker unit, and the methylene groups of the PEG chain (3.67 ppm, 488 H atoms). The terminal methyl group of the PEG chain is not visible in the NMR spectra. These data are confirmed by elemental analysis (experimental part) and GPC (Figure 1) proves that the product CBAmPEG has a monomodal molecular weight distribution.

CBAmPEG-modified SNPs (CBAmPEG@SNPs)

Citrate-coated SNPs (citrate@SNP) [46] were reacted with CBAmPEG at room temperature to obtain SNPs coated with CBAmPEG (CBAmPEG@SNP). The particles were characterized with Raman spectroscopy, dynamic light scattering (DLS), and transmission electron microscopy (TEM).

TEM images of citrate@SNP and CBAmPEG@SNP (Figure 2) show spherical to ellipsoidal particles with diameters in the range of 10 to 40 nm with a broad size distribution. Some samples (Figure 2B) show a fair amount of rod-like particles, typical of the synthesis using ascorbic acid. After modification with CBAmPEG, the resulting CBAmPEG@SNP nanoparticles show a halo around each silver core demonstrating that the particles are indeed modified with the polymer coating. The polymer layer is (in the vacuum-induced dry state in the TEM) about 4 nm thick. Further analysis of CBAmPEG@SNP in aqueous dispersion at pH 7 via dynamic light scattering (DLS) yields a hydrodynamic radius R_h of around 60 nm after dialysis; often the samples have a bimodal size distribution (Table 1).

Figure 2C shows Raman spectra of a dispersion of CBAmPEG@SNP and of an aqueous solution of the pure polymer CBAmPEG. The intense signal at 3400 cm^{-1} and a weak broad mode near 1600 cm^{-1} derives from the OH-stretching and bending modes of water, respectively. The signal at 2230 cm^{-1} observed in the cases of the pure polymer and CBAmPEG@SNP but not for citrate@SNP can be assigned to the CN-stretching mode of the nitrile group of the polymer. The blue shift in the spectrum obtained from CBAmPEG@SNP must be related to the polymer being attached to the SNP. Moreover, the clear signal enhancement of the polymer bands in the CBAmPEG@SNP samples prove that the polymer is indeed anchored to the SNP surface. Finally a band at 613 cm^{-1} is due to a scissoring NO_2 vibration, likely from nitrate anions

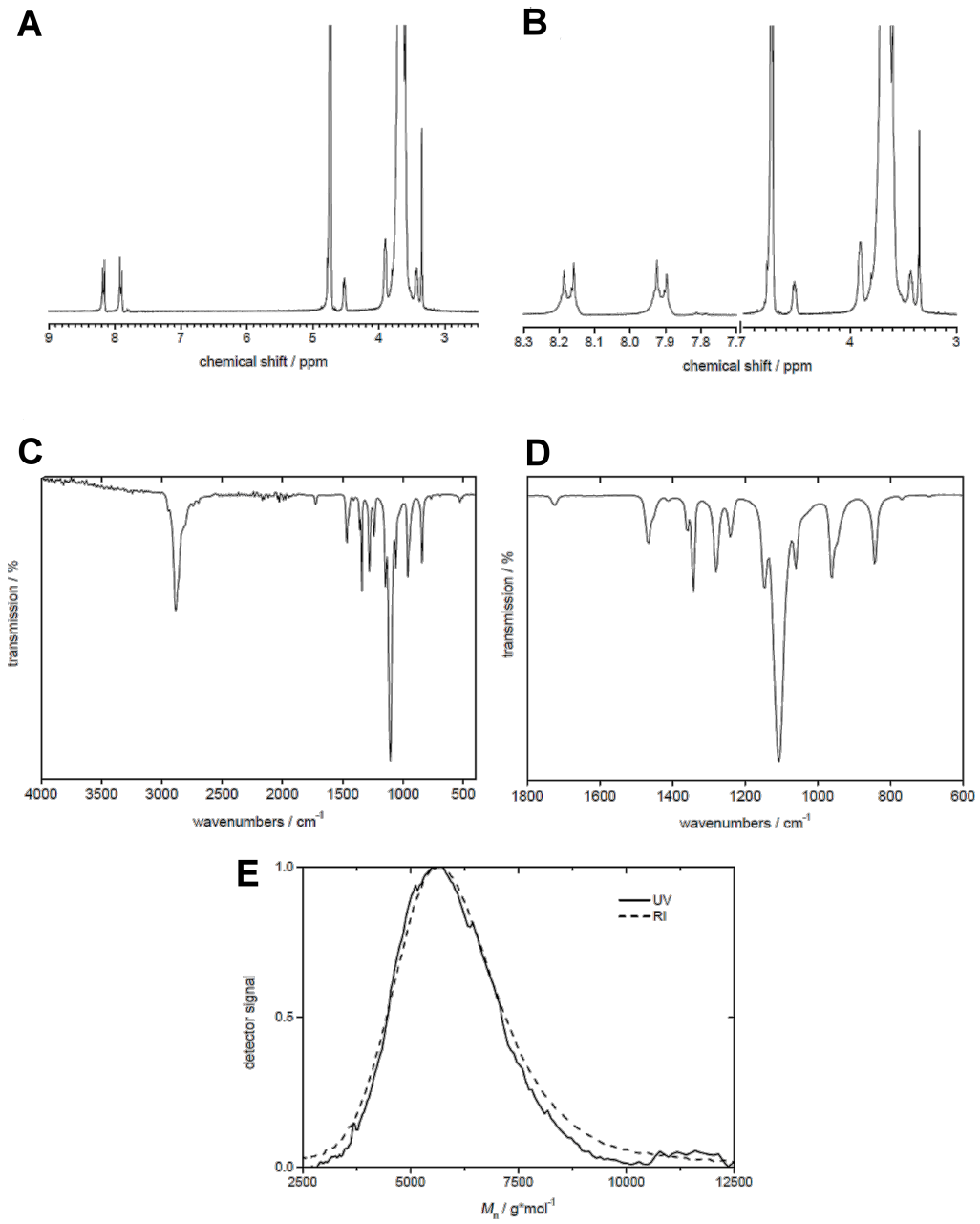

Figure 1: A) ^{1}H NMR spectrum, B) magnified view of the NMR signals, C) overview FTIR spectrum, and D) detailed view of the spectral region with the most intense signals, E) GPC data of CBAmPEG. NMR and IR bands are listed in the Experimental section.

adsorbed on the SNP surface [47]. It must be noted here that at an excitation wavelength of 514.5 nm, the surface enhancement effect is less pronounced than at other wavelengths, but nevertheless is an established approach [48-54].

Figure 2D shows that the UV–vis spectra exhibit significant changes upon treatment of the nanoparticles with the polymer. Initially the samples exhibit a single, rather broad plasmon band at 385 nm. After modification with the polymer, two bands at 393 and 545 nm are visible.

Stability of CBAmPEG in solution and on the SNP surface

One of the most important parameters that affect polymer and particle stability and behavior is the pH value. We have studied the effects of pH variation on polymer degradation both in solution of the pure polymer and on the SNP surface. The least stable functional group in our model system is the ester group linking the PEG chain to the cyanobenzoic acid group. As a result, a cleavage of the ester group is likely the first degradation step.

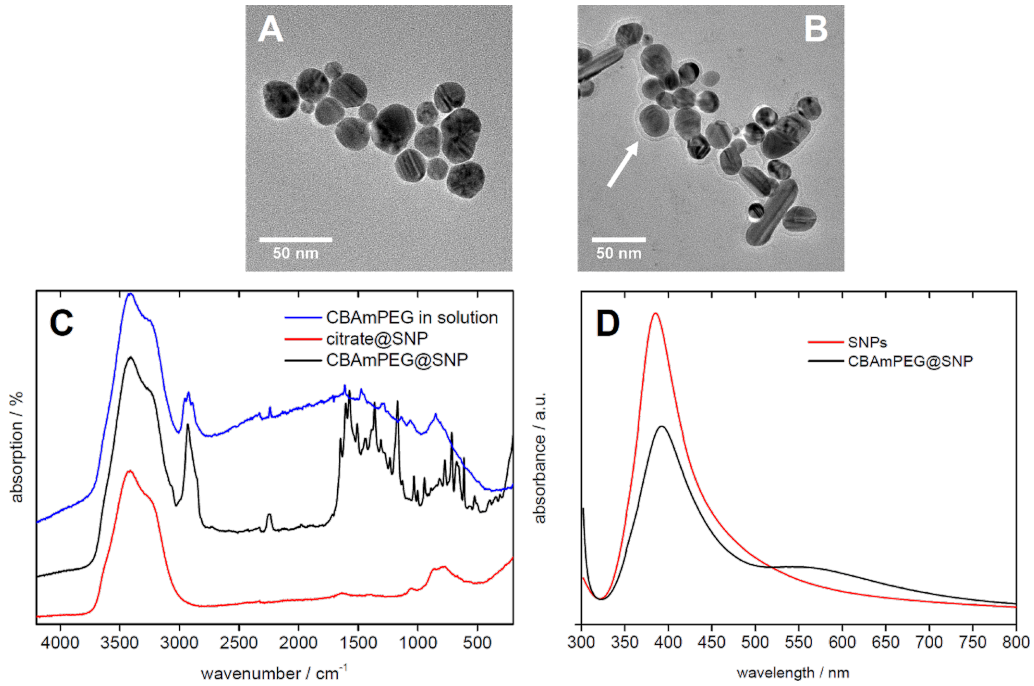

Figure 2: TEM images of A) citrate@SNPs and B) CBAmPEG@SNPs. C) Raman spectra of aqueous solutions or suspensions of CBAmPEG, CBAmPEG@SNPs, and citrate@SNPs. A detailed assignment of the Raman bands is given in the Experimental section. D) UV–vis spectra of SNP without polymer modification and CBAmPEG@SNP.

Table 1: Zeta potential and R_h of CBAmPEG@SNPs incubated at 37 °C for 66 h at pH 7 and pH 12 from three independent experiments.

	zeta potential (mV)		R_h (DLS, nm), peak intensities (%) in brackets			
experiment #	pH 7	pH 12	pH 7	PDI	pH 12	PDI
1	−20(1)	−50(2)	9 ± 3 (6.8%); 68 ± 31 (100%)	0.278	11 ± 3 (4.7%); 68 ± 34 (95.3%)	0.283
2	−21(1)	−42(2)	11 ± 3 (5.9%); 70 ± 29 (94.1%)	0.240	64 ± 28 (100%)	0.244
3	−29(1)	−42(3)	46 ± 14 (100%)	0.221	54 ± 23 (100%)	0.312

To determine the extent of ester cleavage in the pure polymer, CBAmPEG was incubated in D_2O solutions of pH 3, 6, 9, and 12 at 37 °C for 24 h. After different time intervals, aliquots were taken and the samples were directly investigated using ^{1}H NMR spectroscopy (Figure 3).

At pH 3, 6, and 9 no significant change of the polymer was observed and all NMR spectra indicate that CBAmPEG remains intact over the measurement period of 24 h. A small signal at 7.8 ppm indicates that ca. 1% of unreacted cyanobenzoic acid is still present in the samples and could not be removed.

At pH 12, however, changes occur: (i) the signal at ca. 7.8 ppm from the cyanobenzoic impurity becomes slightly more intense and (ii) a new signal is visible at 8.0 ppm. These data show that at pH 12 the polymer is indeed cleaved at the ester moiety. Interestingly, however, the efficiency of the cleavage is rather low and integration of the NMR signals shows that even at pH 12, only ca 12% of the polymer is cleaved.

Finally (iii), the spectra obtained from samples at pH 12 after 24 h are shifted compared to the signals observed for the samples held at pH 3 and the initial sample at pH 12. We currently speculate that this is due to some additional reaction of the nitrile group in the basic environment, but neither IR nor Raman spectroscopy show chemical changes in the –CN group. Overall, NMR spectroscopy shows that the polymer is very stable up to pH 9 and even at pH 12, the ester hydrolysis is only ca. 12 % in 24 h.

As the observation of the polymer degradation using NMR spectroscopy has proven difficult in the case of the polymers

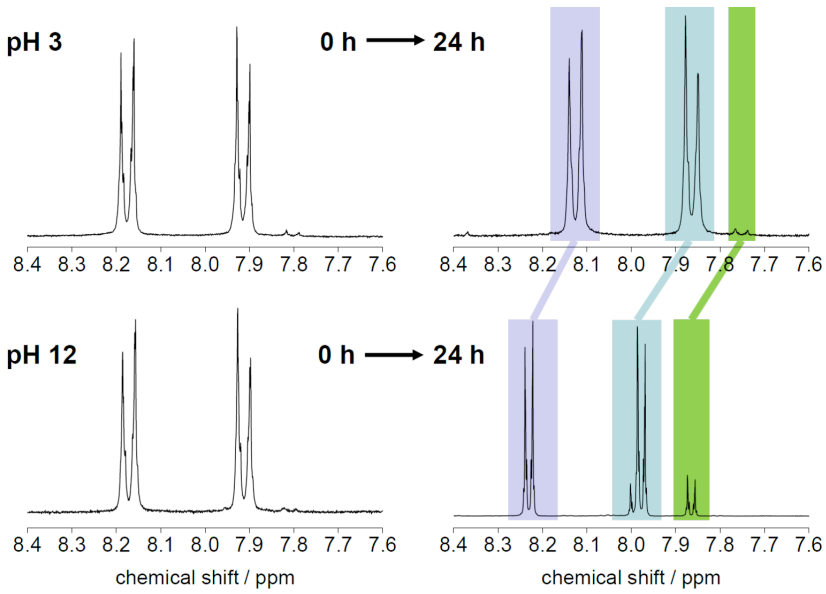

Figure 3: Representative NMR spectra of CBAmPEG after incubation at pH 3 for 0 h (left top) and 24 h (right top) and after incubation at pH 12 after 0 h (left bottom) and 24 h (right bottom). All data are for 37 °C. See Experimental section for signal assignments. Colored areas highlight the corresponding signals that are shifted after treatment at pH 12.

bound to the SNP surface, we have used zeta-potential measurements to evaluate the ester cleavage on the particles. Indeed, these data confirm the hydrolysis of the ester bond in CBAmPEG@SNPs incubated at pH 12 (Table 1). The zeta potentials are shifted towards more negative values (around −40 to −50 mV) for samples incubated in dispersions with a pH of 12. In contrast, the zeta potentials measured for samples treated at lower pH are around −20 to −30 mV.

Unlike the zeta potential, the hydrodynamic radius R_h (as determined by DLS) remains the same at all pH values and over the entire time of incubation, although there is a fairly large batch-to-batch variation. This also applies to samples treated at much longer reaction times up to 66 h. The fact that occasionally two populations with different hydrodynamic radii are observed is assigned to the presence of rather broad particle size distributions. DLS sometimes detects bimodal size distributions and in other cases monomodal but very broad distributions. This is also reflected in the rather large deviations from the mean value of R_h (Table 1) and is consistent with the UV–vis spectra (Figure 2).

Discussion

Stable nanoparticle dispersions are currently of high interest [4,5]. Arguably, the most common stabilizer for gold and silver nanoparticles is PEG and the most common anchor group is the thiol/thiolate group. As stated in the introduction, there may however be situations where the thiol group may be unwanted. The new stabilizer presented here, CBAmPEG, is a viable alternative for at least some cases. The new polymer is easily accessible in good yields. NMR spectroscopy, IR spectroscopy, elemental analysis, and GPC show that the polymer is clean and has a monomodal (although somewhat broad, depending on the PEG used for the reaction) size distribution.

Moreover, the interaction of the cyano group with the silver surface is reasonably strong [36,38-43] and provides a good attachment of CBAmPEG to the NP surface. UV–vis spectroscopy suggests that a smaller fraction of the nanoparticles may aggregate upon modification with the polymer. There is, however, no indication of precipitation. This suggests that the polymer is a viable stabilizer for the SNPs. Finally, CBAmPEG is stable up to pH 9 before some degradation via cleavage of the ester bond is observed.

Consistent with the data on the pure CBAmPEG polymer, zeta-potential measurements show that no ester cleavage occurs up to pH 9, but we do observe a shift in the zeta potential towards more negative values after incubation of CBAmPEG@SNPs at pH 12. This is due to the fact that ca. 12% of the polymers attached to the SNP surface are cleaved at pH 12. This produces a negatively charged carboxylate (from 4-cyanobenzoic acid attached to the SNP surface) and a neutral alcohol (from the free PEG chains released from the surface). The –OH group does not affect the surface charge at pH 12 but the higher number of negative charges from the cleaved benzoic acid units on the SNP surface reduces the zeta potential. As the fraction of cleaved polymer is rather low, we never observed particle

aggregation or sedimentation and the data thus show that the new polymer is a viable stabilizer for SNP over a wide pH range.

The fact that the particles already have a negative zeta potential at the beginning of the experiment is due to the presence of residual citrate and nitrate ions adsorbed on the particle surface that are not removed during CBAmPEG@SNP synthesis. This is confirmed by Raman spectroscopy, which detects carboxylate groups (from citrate) and NO_2 vibrations from residual nitrate ions (from $AgNO_3$), both of which contribute to a negative zeta potential even after polymer grafting but prior to polymer cleavage.

Finally, it is important to note that DLS does not detect a change in the hydrodynamic radius, R_h, upon polymer degradation on the particle surface. In case of large amounts of cleaved polymer on the particle surface, aggregation and a concurrent increase of R_h may be expected. We currently assign the unchanged R_h to the fact that only a small fraction of the polymer chains is cleaved over the course of the reaction. As a result, the polymer shell on the particle surface is still intact and provides adequate steric stabilization. Possibly, the steric effect is further complemented by a contribution from electrostatic repulsion [55,56] as indicated by the zeta potential of the particles, which is shifted to more negative values after ester cleavage.

Overall the data thus demonstrate that CBAmPEG is an efficient stabilizer for silver nanoparticles. At low and neutral pH values it appears to stabilize the particles by a combination of steric repulsion (via the PEG coating) and a contribution from electrostatics arising from residual citrate and nitrate anions that still remain on the SNP surface even after washing. After treatment at high pH values and the corresponding cleavage of some of the stabilizer, the steric contribution is likely less pronounced (as some of the PEG is removed from the surface) and the contribution from electrostatic stabilization is likely somewhat stronger because the negatively charged carboxylate groups (from the cyanobenzoic acid moieties) also contribute to charging the SNP surface.

Conclusion

The current article describes synthesis and performance of α-((4-cyanobenzoyl)oxy)-ω-methyl poly(ethylene glycol), the first polymeric stabilizer for metal nanoparticles based on a cyano rather than a thiol or thiolate anchor group. The polymer is quite stable at different pH conditions and is only cleaved at pH 12 or higher. Even after cleavage of the stabilizer attached to the SNP surface, however, the nanoparticle dispersions remain stable and no flocculation or precipitation is observed. As a result, the study shows that (i) cyanobenzoic acid-based polymeric stabilizers are applicable over a wide pH range and (ii) some stabilizer degradation may take place without causing a subsequent destabilization of the nanoparticle dispersion. The new polymeric stabilizer CBAmPEG may thus be interesting for application in biology, medicine, or diagnostics.

Author Contributions

A.H., A.L., and A.T. conceived and designed the experiments; J.L. performed the experiments; M.B. supervised and discussed the Raman experiments; M.P. performed TEM analyses; J.L., A.H., and A.T. analyzed the data; J.L., A.H., and A.T. wrote the article. All authors reviewed and corrected the final manuscript.

Acknowledgements

We thank M. Gräwert (MPI of Colloids & Interfaces) for GPC measurements, A. Krtitschka and Prof. H. Möller (University of Potsdam) for help with NMR experiments, and U. Koch (FU Berlin/University of Potsdam) for preliminary experiments on nanoparticle synthesis. Funding by the University of Potsdam, BfR – German Federal Institute for Risk Assessment, and COST Action MODENA TD1204 is gratefully acknowledged.

References

1. Daraee, H.; Eatemadi, A.; Abbasi, E.; Aval, S. F.; Kouhi, M.; Akbarzadeh, A. *Artif. Cells, Nanomed., Biotechnol.* **2016,** *44,* 410. doi:10.3109/21691401.2014.955107
2. Zare-Zardini, H.; Ferdowsian, F.; Soltaninejad, H.; Azam, A. G.; Soleymani, S.; Zare-Shehneh, M.; Mofidi, M.; Rafati, R.; Ebrahimi, L. *J. Nano Res.* **2016,** *35,* 55. doi:10.4028/www.scientific.net/JNanoR.35.55
3. Amiens, C.; Ciuculescu-Pradines, D.; Philippot, K. *Coord. Chem. Rev.* **2016,** *308,* 409. doi:10.1016/j.ccr.2015.07.013
4. Majdalawieh, A.; Kanan, M. C.; El-Kadri, O.; Kanan, S. M. *J. Nanosci. Nanotechnol.* **2014,** *14,* 4757. doi:10.1166/jnn.2014.9526
5. Stark, W. J.; Stoessel, P. R.; Wohlleben, W.; Hafner, A. *Chem. Soc. Rev.* **2015,** *44,* 5793. doi:10.1039/C4CS00362D
6. Kangoa, S.; Kaliab, S.; Celli, A.; Njugunad, J.; Habibie, Y.; Kumar, R. *Prog. Polym. Sci.* **2013,** *38,* 1232. doi:10.1016/j.progpolymsci.2013.02.003
7. Sperling, R. A.; Parak, W. J. *Philos. Trans. R. Soc. London, Ser. A* **2010,** *368,* 1333. doi:10.1098/rsta.2009.0273
8. Zhang, N.; Xu, Y.-J. *Chem. Mater.* **2013,** *25,* 1979. doi:10.1021/cm400750c
9. Zhou, J.; Ralston, J.; Sedev, R.; Beattie, D. A. *J. Colloid Interface Sci.* **2009,** *331,* 251. doi:10.1016/j.jcis.2008.12.002
10. Foroozandeh, P.; Aziz, A. A. *Nanoscale Res. Lett.* **2015,** *10,* 221. doi:10.1186/s11671-015-0922-3
11. Lane, L. A.; Qian, X.; Smith, A. M.; Nie, S. *Annu. Rev. Phys. Chem.* **2015,** *66,* 521–547. doi:10.1146/annurev-physchem-040513-103718
12. Li, X.; Lenhart, J. J.; Walker, H. W. *Langmuir* **2012,** *28,* 1095. doi:10.1021/la202328n
13. Sivera, M.; Kvitek, L.; Soukupova, J.; Panacek, A.; Prucek, R.; Vecerova, R.; Zboril, R. *PLoS One* **2014,** *9,* 103675. doi:10.1371/journal.pone.0103675

14. Shen, Z.; Nieh, M.-P.; Li, Y. *Polymers (Basel, Switz.)* **2016,** *8,* 83. doi:10.3390/polym8030083
15. Batista, C. A. S.; Larson, R. G.; Kotov, N. A. *Science* **2015,** *350,* 1242477. doi:10.1126/science.1242477
16. Moore, T. L.; Rodriguez-Lorenzo, L.; Hirsch, V.; Balog, S.; Urban, D.; Jud, C.; Rothen-Rutishauser, B.; Lattuada, M.; Petri-Fink, A. *Chem. Soc. Rev.* **2015,** *44,* 6287. doi:10.1039/C4CS00487F
17. Fang, C.; Bhattarai, N.; Sun, C.; Zhang, M. *Small* **2009,** *5,* 1637. doi:10.1002/smll.200801647
18. Pelaz, B.; del Pino, P.; Maffre, P.; Hartmann, R.; Gallego, M.; Rivera-Fernández, S.; de la Fuente, J. M.; Nienhaus, G. U.; Parak, W. J. *ACS Nano* **2015,** *9,* 6996. doi:10.1021/acsnano.5b01326
19. Grubbs, R. B. *Polym. Rev.* **2007,** *47,* 197. doi:10.1080/15583720701271245
20. Li, S.-D.; Huang, L. *J. Controlled Release* **2010,** *145,* 178. doi:10.1016/j.jconrel.2010.03.016
21. Owens, D. E., III; Peppas, N. A. *Int. J. Pharm.* **2006,** *307,* 93. doi:10.1016/j.ijpharm.2005.10.010
22. Jokerst, J. V.; Lobovkina, T.; Zare, R. N.; Gambhir, S. S. *Nanomedicine* **2011,** *6,* 715. doi:10.2217/nnm.11.19
23. Bhadra, D.; Bhadra, S.; Jain, P.; Jain, N. K. *Pharmazie* **2002,** *57,* 5.
24. Mout, R.; Moyano, D. F.; Rana, S.; Rotello, V. M. *Chem. Soc. Rev.* **2012,** *41,* 2539. doi:10.1039/c2cs15294k
25. Zhang, T.; Stilwell, J. L.; Gerion, D.; Ding, L.; Elboudwarej, O.; Cooke, P. A.; Gray, J. W. *Nano Lett.* **2006,** *6,* 800. doi:10.1021/nl0603350
26. Popa, M.; Pradell, T.; Crespo, D.; Calderón-Morenoa, J. M. *Colloids Surf., A* **2007,** *303,* 184. doi:10.1016/j.colsurfa.2007.03.050
27. Sarkar, A.; Kapoor, S.; Mukherjee, T. *Res. Chem. Intermed.* **2010,** *36,* 411. doi:10.1007/s11164-010-0151-4
28. Polshettiwar, V.; Nadagouda, M. N.; Varma, R. S. *Aust. J. Chem.* **2009,** *62,* 16. doi:10.1071/CH08404
29. Patel, K.; Kapoor, S.; Dave, D. P.; Mukherjee, T. *Res. Chem. Intermed.* **2006,** *32,* 103. doi:10.1163/156856706775372771
30. Sra, A. K.; Ewers, T. D.; Schaak, R. E. *Chem. Mater.* **2005,** *17,* 758. doi:10.1021/cm0484450
31. Harrison, E.; Coulter, J. A.; Dixon, D. *Nanomedicine* **2016,** *11,* 851. doi:10.2217/nnm.16.28
32. Zhao, P.; Li, N.; Astruc, D. *Coord. Chem. Rev.* **2013,** *257,* 638. doi:10.1016/j.ccr.2012.09.002
33. Grzelczak, M.; Pérez-Juste, J.; Mulvaney, P.; Liz-Marzán, L. M. *Chem. Soc. Rev.* **2008,** *37,* 1783. doi:10.1039/b711490g
34. Schöneich, C. *Free Radical Res.* **2016,** *50,* 143. doi:10.3109/10715762.2015.1077385
35. Toyokuni, S. *Front. Pharmacol.* **2014,** *5,* 11. doi:10.3389/fphar.2014.00200
36. Holze, R. *J. Solid State Electrochem.* **2013,** *17,* 1869. doi:10.1007/s10008-013-2076-5
37. Vollhardt, K. P. C. *Organische Chemie;* VCH Verlagsgesellschaft: Weinheim, Germany, 1990.
38. Taubert, A.; Wiesler, U.-M.; Müllen, K. *J. Mater. Chem.* **2003,** *13,* 1090. doi:10.1039/b207895c
39. Barmatov, E. B.; Pebalk, D. A.; Barmatova, M. V. *Langmuir* **2004,** *20,* 10868. doi:10.1021/la048601h
40. Jang, Y. H.; Hwang, S.; Cho, K.; Lim, M.; Joo, T.; Choi, S.; Kim, J.; Joo, S.-W. *Surf. Interface Anal.* **2011,** *43,* 757. doi:10.1002/sia.3626
41. Meli, M.-V.; Lardner, M. J.; Taweel, A. M. *Liq. Cryst.* **2015,** *42,* 497. doi:10.1080/02678292.2014.1002548
42. Lapanik, A.; Rudzki, A.; Kinkead, B.; Qi, H.; Hegmann, T.; Haase, W. *Soft Matter* **2012,** *8,* 8722. doi:10.1039/c2sm25991e
43. Shiraishi, Y.; Sano, S.; Baba, A.; Kobayashi, S.; Toshima, N. *Kobunshi Ronbunshu* **2002,** *59,* 753. doi:10.1295/koron.59.753
44. Veselá, A. B.; Franc, M.; Pelantová, H.; Kubáč, D.; Vejvoda, V.; Šulc, M.; Bhalla, T. C.; Macková, M.; Lovecká, P.; Janů, P.; Demnerová, K.; Martinková, L. *Biodegradation* **2010,** *21,* 761. doi:10.1007/s10532-010-9341-4
45. Sée, V.; Free, P.; Cesbron, Y.; Nativo, P.; Shaheen, U.; Ridgen, D. J.; Spiller, D. G.; Fernig, D. G.; White, M. R. H.; Prior, I. A.; Brust, M.; Lounis, B.; Lévy, R. *ACS Nano* **2009,** *3,* 2461. doi:10.1021/nn9006994
46. Qin, Y.; Ji, X.; Jing, J.; Liu, H.; Wu, H.; Yang, W. *Colloids Surf., A* **2010,** *372,* 172. doi:10.1016/j.colsurfa.2010.10.013
47. Socrates, G. *Infrared and Raman Characteristic Group Frequencies,* 3rd ed.; John Wiley & Sons Ltd.: New York, NY, U.S.A., 2004.
48. Nie, S.; Emery, S. R. *Science* **1997,** *275,* 1102. doi:10.1126/science.275.5303.1102
49. Lee, C.-r.; Bae, S. J.; Gong, M.-s.; Kim, K.; Joo, S.-W. *J. Raman Spectrosc.* **2002,** *33,* 429. doi:10.1002/jrs.873
50. Kim, K.; Kim, K. L.; Shin, D.; Choi, J.-Y.; Shin, K. S. *J. Phys. Chem. C* **2012,** *116,* 4774. doi:10.1021/jp211730r
51. Kneipp, J.; Kneipp, H.; Kneipp, K. *Chem. Soc. Rev.* **2008,** *37,* 1052. doi:10.1039/b708459p
52. Kneipp, K.; Kneipp, H.; Itzkan, I.; Dasari, R. R.; Feld, M. S. *J. Phys.: Condens. Matter* **2002,** *14,* R597. doi:10.1088/0953-8984/14/18/202
53. Efrima, S.; Bronk, B. V. *J. Phys. Chem. B* **1998,** *102,* 5947. doi:10.1021/jp9813903
54. Dieringer, J. A.; Wustholz, K. L.; Masiello, D. J.; Camden, J. P.; Kleinman, S. L.; Schatz, G. C.; Van Duyne, R. P. *J. Am. Chem. Soc.* **2009,** *131,* 849. doi:10.1021/ja8080154
55. de O. Santos, K.; Elias, W. C.; Signori, A. M.; Giacomelli, F. C.; Yang, H.; Domingos, J. B. *J. Phys. Chem. C* **2012,** *116,* 4594. doi:10.1021/jp2087169
56. Pugh, T. L.; Heller, W. *J. Polym. Sci.* **1960,** *47,* 219. doi:10.1002/pol.1960.1204714919

License and Terms

BEILSTEIN JOURNAL OF NANOTECHNOLOGY

First examples of organosilica-based ionogels: synthesis and electrochemical behavior

Andreas Taubert*[1,§], Ruben Löbbicke[1], Barbara Kirchner[2] and Fabrice Leroux[3]

Full Research Paper

Open Access

Address:
[1]Institute of Chemistry, University of Potsdam, D-14476 Potsdam, Germany, [2]Mulliken Center for Theoretical Chemistry, Institut für Physikalische und Theoretische Chemie, Universität Bonn, Beringstraße 4+6, D - 53115 Bonn, Germany and [3]Inorganic Materials, Institut de Chimie de Clermont-Ferrand (ICCF) - UMR 6296, Université Blaise Pascal, Chimie 5, Campus des Cézeaux, 24 avenue des Landais, BP 80026 63171 Aubière Cedex, France

Email:
Andreas Taubert* - ataubert@uni-potsdam.de

* Corresponding author
§ Web: www.taubert-lab.net, Tel.: +49 (0) 331 977 5773;
Fax: +49 (0) 331 977 5059

Keywords:
ionic liquids; ionogels; organosilica; proton conductivity

Beilstein J. Nanotechnol. **2017,** *8,* 736–751.
doi:10.3762/bjnano.8.77

Received: 12 October 2016
Accepted: 07 March 2017
Published: 29 March 2017

This article is part of the Thematic Series "Hybrid nanomaterials: from the laboratory to the market".

Associate Editor: J. J. Schneider

Abstract

The article describes the synthesis and properties of new ionogels for ion transport. A new preparation process using an organic linker, bis(3-(trimethoxysilyl)propyl)amine (BTMSPA), yields stable organosilica matrix materials. The second ionogel component, the ionic liquid 1-methyl-3-(4-sulfobutyl)imidazolium 4-methylbenzenesulfonate, [BmimSO$_3$H][PTS], can easily be prepared with near-quantitative yields. [BmimSO$_3$H][PTS] is the proton conducting species in the ionogel. By combining the stable organosilica matrix with the sulfonated ionic liquid, mechanically stable, and highly conductive ionogels with application potential in sensors or fuel cells can be prepared.

Introduction

Ionic liquids (ILs), that is, substances solely composed of ionic species have been studied for virtually every application from organic synthesis to lubrication and battery technology [1-4]. A particularly promising field of IL-based materials is the general area of advanced energy technology, such as proton-exchange membrane (PEM) or alkaline fuel cells, solar cells, or various battery types [1,5-7]. ILs offer, unlike conventional solvents and substances, easy access to virtually unlimited structural diversity by simple variation of the respective ions. This facilitates the tailoring of their properties, e.g.,

viscosity, ionic conductivity, solubility, or melting and glass points and therefore makes ILs perfect media for task-specific applications [1,4]. Additionally, compared to many systems based on molecular solvents, ILs often offer improved safety of a device by way of their low vapor pressure and low flammability [8].

As a result, ILs have been investigated as advanced electrolytes to replace traditional aqueous or organic electrolytes in batteries and fuel cells [5-7]. Among others, ILs are interesting for intermediate temperature fuel cells operating above ca. 80 °C. At this point, conventional Nafion membranes dry out and lose the ability for proton conduction [9]. Due to their relatively high thermal stability, high ionic conductivity, and low vapor pressure, many ILs can overcome this temperature limit and provide access to proton transporting membranes that can operate in the anhydrous state up to ca. 200 °C [5,10].

However, to use ILs in electrochemical devices such as fuel cells, they need to be immobilized in a viable matrix. Materials resulting from the combination of a support (silica, polymer, colloidal particles, carbon nanotubes, or gelators) and an IL are called ionogels (IGs) or ion-gels [11-13].

Several research groups have put forward approaches towards mechanically stable IGs and studied their electrochemical properties. Gayet et al. made silica/poly(methyl methacrylate)-based IGs using 1-butyl-3-methylimidazolium bis(tri-fluoromethanesulfonyl)imide, [Bmim][NTf_2], to obtain an IG membrane with high ionic conductivity [14,15]. Néouze et al. studied IGs from the same IL and a silica matrix. The IGs exhibit rather high conductivities of up to 10^{-3} S·cm^{-1}. This is close to the conductivity of the pristine IL indicating that the confinement of the IL into a matrix does not significantly affect the conductivity [11,16,17]. Again using the same IL, Martinelli and coworkers have provided a set of interesting studies on how the ion flexibility and dynamics affect the conductivity in silica nanoparticle-based IGs and related systems [18-22]. Horowitz and Panzer synthesized mechanically compliant silica-based IGs. These IGs also showed unusually high IL loadings of up to 94% [23,24].

Delahaye et al. used the sulfonated IL 1-methyl-3-(3-sulfopropyl)-imidazolium *para*-toluenesulfonate, [PmimSO_3H][PTS], and a silica-based matrix to synthesize IGs with conductivities of 10^{-2} and 10^{-3} S·cm^{-1} in the hydrated and anhydrous state, respectively [25]. Negre et al. reported IG-based supercapacitors that can be operated over a 3 V cell voltage window. Moreover, the supercapacitor has a capacitance up to 90 F/g at room temperature [26]. Ameri et al. made IG transistors using graphene [27] for low voltage operation.

Using a slightly different approach, Hesemann and coworkers and Néouze and coworkers incorporated IL-like functionalities into periodic mesoporous organosilicas (PMOs) [28,29] and into silica nanoparticle networks [30-33], respectively. Although no IGs were made from either of these materials, they are quite similar to the organosilica matrix materials used in the current work.

The current article is the first account of organosilica-based IGs. The IGs combine the advantageous (mechanical) properties of organosilica hosts and the IL 1-methyl-3-(3-sulfobutyl)imidazolium *para*-toluenesulfonate, [BmimSO_3H][PTS], which has a high ionic conductivity and can be synthesized in high purity in a very simple reaction at near-quantitative yields. The materials have two main advantages over existing proton-conducting IGs (PIGs). First, the silica matrix shows a better mechanical stability than neat silica due to the organic bridging moieties present in the organosilica host. Second, the organic moiety of these organosilanes contains nitrogen atoms, which can reversibly be protonated and should thus also contribute to the ionic conductivity of the PIGs. A further synthetic advantage is that the organosilanes used here also catalyze silane and silica condensation. There is thus no need for additional catalysts that must to be removed after synthesis.

Experimental

Preparation of the organosilica monoliths. Silica monoliths were made via sol–gel reaction from bis(3-(trimethoxysilyl)propyl)amine (BTMSPA) and tetramethylorthosilicate (TMOS) or methyltrimethoxysilane (MTMS). Reactions were made such that the total silicon concentration in the reaction mixture was always 16.5 mmol (from TMOS or MTMS and BTMSPA combined; note that BTMSPA contributes two moles of silicon for every mole of silane). The amount of water was 82.5 mmol (1.485 mL) and the amount of acetone or methanol used as solvents was 200 mmol (10.8 mL or 6.4 mL, respectively).

In a typical experiment, TMOS (0.488 mL), BTMSPA (2.254 mL), and acetone (10.8 mL), were mixed in a 50 mL plastic tube. All reactants are liquid and fully miscible at room temperature. The reaction vessel was held in a cooling bath (acetone/dry ice) while adding the components to the mixture to minimize gelation during initial mixing. After mixing, the mixture was allowed to warm to room temperature. Subsequently, water was added. After vigorous shaking, the clear solution was poured into a polypropylene mold, sealed with a septum, and covered with parafilm. After 5 min gelation occurred but all samples were allowed 24 h for further condensation. The resulting material was washed extensively by Soxhlet extraction with methanol and was stored in methanol until further use. When acetone was used as solvent, opaque monoliths were obtained

whereas transparent monoliths were obtained when using methanol during synthesis.

Sample nomenclature. Organosilicas made from TMOS and BTMSPA are denoted TBMxx and TBAxx, where xx (fraction of silicon provided by monosilane precursor, not from BTMSPA) = 20, 40, 50, 60. "A" denotes samples made in acetone and "M" denotes samples made in methanol. Samples made from MTMS and BTMSPA are denoted MBMxx and MBAxx using the same assignments as above. For example, TBM20 is a sample made with TMOS and BTMSPA in methanol where 20% of the silicon atoms are provided by TMOS and 80% by BTMSPA.

Preparation of 1-methyl-3-butylimidazoliumsulfonate [25]. 1-Methylimidazole (40 mmol, 3.28 g) and 1,4-butanesultone (40 mmol, 5.45 g) were mixed in a 50 mL round bottom flask. The mixture was heated to 60 °C for 1 h with stirring under nitrogen. Precipitation of the white zwitterionic salt 1-methyl-3-butylimidazoliumsulfonate ($BmimSO_3$) starts after ca. 30 min. As the viscosity of the reaction mixture increases during the synthesis, 10 mL of acetone were added after 30–40 min and the resulting solution was refluxed for 8 h. After filtration, the salt was washed with acetone to remove residues of the starting materials. The white solid was dried overnight at room temperature. $C_8H_{14}N_2SO_3$ (M = 218.27 g/mol); ^{1}H NMR (300 MHz, D_2O, δ in ppm): 1.637 (q, 2H); 1.922 (q, 2H); 2.839 (t, 2H); 3.787 (s, 3H); 4.144 (t, 2H); 7.335 (d, 1H); 7.396 (d, 1H); 8.635 (s, 1H); elemental analysis, found (calculated, %): C 44.02 (43.92); H 6.46 (6.31); N 12.83 (12.78); S 14.69 (14.91).

Preparation of 1-methyl-3-(3-sulfobutyl)imidazolium *para*-toluenesulfonate [$BmimSO_3H$][PTS] [25]. $BmimSO_3$ was mixed with *para*-toluenesulfonic acid (p-TSA) in stoichiometric amounts. The mixture was heated to 60 °C and stirred for 4 h to yield 1-methyl-3-(3-sulfobutyl)imidazolium *para*-toluenesulfonate, [$BmimSO_3H$][PTS]. $C_{15}H_{22}N_2S_2O_6$ (M = 390.47 g/mol); ^{1}H NMR (300 MHz, D_2O, δ): 1.577 (q, 2H); 1.843 (q, 2H); 2.234 (s, 3H); 2.782 (t, 2H); 3.712 (s, 3H); 4.056 (t, 2H); 7.252 (ar, 4H); 7.515 (d, 2H); 8.540 (s, 1H). Elemental analysis: found (calculated, %): C 46.14 (44.18); H 5.68 (5.33); N 7.17 (6.93); S 16.42 (15.72). The reason for the deviations between experimental and calculated values is likely due to a slight mismatch between $BmimSO_3$ and p-TSA from weighing in the starting materials. EA data did vary slightly from batch to batch, which confirms this hypothesis. Excess $BmimSO_3$ or p-TSA can however not be removed.

Ionogel preparation. Silica monoliths filled with methanol (from Soxhlet extraction) were placed in a methanolic solution of [$BmimSO_3H$][PTS]. After 12 h, the silica monolith was removed from the methanol/IL mixture and placed in the pure IL at 50 °C in a vacuum oven to remove the residual methanol. After 24 h, the methanol was removed from the ionogel as the vacuum had reached a constant value.

Ionogel nomenclature. IGs are denoted TBMxxIL, TBAxxIL, MBMxxIL, and MBAxxIL, respectively. For details of organosilica nomenclature see above.

Spectroscopy. Infrared (IR) spectra were recorded using the KBr pellet method or the attenuated total reflection (ATR) mode on a Thermo Nicolet FT-IR Nexus 470 with ATR probe head. Spectra were taken from 500 to 4000 cm^{-1} with a resolution of 2 cm^{-1} and 32 scans per measurement.

Elemental analysis (EA). EA was done on an Elementar Vario EL III elemental analyzer.

Thermal analysis. Simultaneous thermogravimetric analysis-differential thermal analysis (TGA-DTA) experiments were done on a Linseis L81 thermal balance and on a Linseis STA PT-1600 thermal balance in air from 20 to 900 °C with a heating rate of 10 °C/min. Differential scanning calorimetry (DSC) measurements were done on a Netzsch DSC 204. DSC traces were recorded from −150 to 200 °C using liquid nitrogen cooling and a heating rate of 10 °C/min. Isothermal times were 5 min. Samples of ca. 5 mg were placed in aluminum pans with pierced lids. To remove traces of water the samples were heated to 120 °C before the first cooling cycle. Heating and cooling cycles were repeated three times for reproducibility.

Pore analysis. Nitrogen sorption experiments were carried out at 77 K on a Quantachrome Autosorb-1. Prior to measurements the samples were degassed in vacuum overnight at 80 °C. Surface areas were calculated via the Brunauer–Emmett–Teller (BET) method [34]. Determination of average pore diameters was done using the Barrett–Joyner–Halenda (BJH) approach using the desorption branch of the sorption isotherms [35].

X-ray scattering. Small angle X-ray scattering (SAXS) intensities were recorded at room temperature with a Nonius rotating anode instrument (4 kW, Cu Kα) with pinhole collimation and a MARCCD detector (pixel size: 79 μm). The distance between sample and detector was 74 cm, covering a range of the scattering vector $s = 2/\lambda \sin\theta$ = 0.04–0.7 nm^{-1} (θ = scattering angle, λ = 0.154 nm). 2D diffraction patterns were transformed into 1D radial averages of the scattering intensity [36]. The pore sizes of the monoliths were evaluated via SAXS using the Porod approach [37-40] with data obtained from BJH pore analysis [35].

The porosity φ of the samples was calculated from BJH data via Equation 1

$$\varphi = \frac{\text{porevolumeBJH}}{\text{porevolumeBJH} + \frac{1}{\rho}}, \quad (1)$$

where ρ is the density of the silica, 2.1 g/cm.

Electron microscopy. Transmission electron microscopy (TEM) was done on a Philips CM100 electron microscope operated at 80 kV. TEM copper grids were coated with a carbon layer. Samples were ground in an agate mortar and suspended in acetone. One drop of the suspension was deposited on the grid and dried before microscopy. Scanning electron microscopy (SEM) was done on an FEI Phenom desktop electron microscope operated at 5 kV and on a JEOL JSM-6510 with a tungsten filament operated at 15 kV. Energy dispersive X-ray spectroscopy (EDXS) was done with an Oxford Instrument INCAx-act X-ray detector. Prior to measurements the samples were coated with a 100 nm carbon layer using a POLARON CC7650 Carbon Coater.

Electrochemical impedance spectroscopy (EIS). For EIS the dry IGs were contacted with a graphite paper layer and sandwiched between platinum electrodes. The graphite paper layer was used as a sacrificial layer (used one time for one sample) to avoid a direct contact with the platinum electrode. Even though the IGs are rather stable, their surfaces may be slightly sticky; this especially applies at higher temperatures. The roughness between the graphite and ionogel is average as observed by the angle of the Nyquist curve with the *x*-axis in the low frequency domain. The angle is about π/4, which is typically observed for such contact electrodes (the absence of any roughness will result in an angle of π/2). The variation of this angle does not modify the characteristics of the samples, i.e., the conductivity and the dielectric behavior as given by the intercept of the curve with the *x*-axis and in the high frequency domain, respectively.

Conductivity measurements were performed by the complex impedance method carried out with a Solartron 1174 frequency analyzer. The frequency range was from 1 to 10^6 Hz and the temperature cycle was between 258 and 473 K as a cooling/heating/cooling sequence. The customary model using constant phase elements was applied to simulate the impedance spectra. After removal of the geometric capacitance of the cell, the impedance plots were refined by using CPE_p and CPE_s constant phase angle elements, which are related to the dielectric relaxation of the material and electrode phenomena, respectively. Their related impedance is expressed as $CPE_p = K^{-1}(j\omega)^{-n}$ and $CPE_s = Q^{-1}(j\omega)^{-p}$ $(0 \leq (n, p) \leq 1)$.

Computational methodology. The ab initio molecular dynamics (AIMD) simulations in which the forces are calculated from the electronic structure on the fly were carried out as described previously [41] using the cp2k program packages [42]. AIMD simulation was started from a classical molecular dynamics simulation snapshot of 32 ion pairs of [$BmimSO_3H$][PTS] under periodic boundary conditions. The snapshot can be obtained upon request. In the classical MD simulation the system was set up for a density of 1.6 g/cm^3 and NPT simulations were performed resulting in a box size of 2349.41 pm^3. The AIMD simulations we run at 440 K with massive thermostats (parameters as in [41]) for 5 ps. After this the simulation was done in an NVT ensemble to provide 2.5 ps production trajectory at 450 K which was analyzed with the software TRAVIS [43]. A forth-

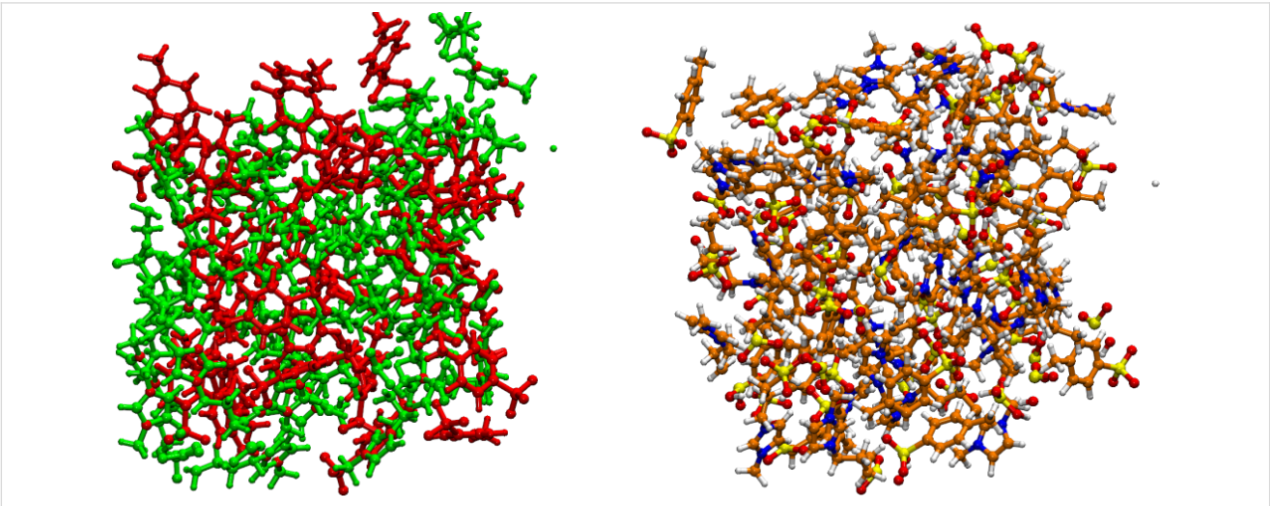

Figure 1: Ball-and-stick representation of the simulation box. Visualized with TRAVIS [43] and vmd [44]. Left: cations in green and anions in red. Right: carbon in orange, sulfur in yellow, oxygen in red, nitrogen in blue, and hydrogen in white.

coming publication will provide more details and longer simulation times. Figure 1 shows the simulation box used for the experiments.

Results

Silica monoliths

As stated in the introduction, mesoporous silica monoliths are often brittle and thus difficult to handle. The first goal of the current study is thus to provide a synthetic protocol towards more robust silica matrix materials suitable for IL incorporation. The second goal is to produce IGs with high proton conductivities.

One viable strategy to obtain mechanically robust silica hosts is the use of organic linkers to provide additional flexibility and stability to the silica network [45,46]. The current study therefore focuses on organosilica monoliths with varying ratios of the silicon alkoxide precursors TMOS and BTMSPA ranging from 20:80, 40:60, 50:50, to 60:40 in two different solvents, methanol and acetone. All monoliths remain intact after Soxhlet extraction, Figure 2. After drying at ambient conditions, the monoliths shrink but again remain intact. The monoliths synthesized in methanol are clear to translucent as long as they are wet, but turn opaque upon drying. The monoliths grown in acetone are opaque already after the sol–gel reaction and Soxhlet extraction.

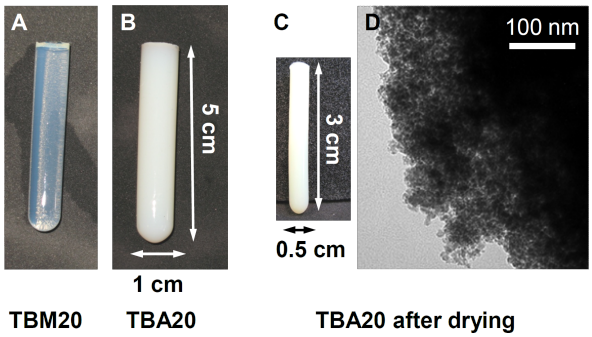

Figure 2: Representative photographs and TEM images of organosilica monoliths. (A) Wet TBM20 after Soxhlet extraction with methanol, (B) wet TBA20 after Soxhlet extraction with methanol, (C) dry TBA20 after drying at ambient conditions, (D) TEM image of TBA20 after drying.

Transmission electron microscopy (TEM, Figure 2) images obtained from ground samples show that the size of the primary silica particles making up the monoliths is around 10 nm. TEM also shows that the materials do not have a periodic order, but contain disordered pores. This observation applies to all organosilica monoliths, regardless of the solvent, the precursors, or the precursor ratios used during synthesis.

Figure 3 shows elemental analysis (EA) data of all organosilica monoliths. Samples made with MTMS have slightly higher carbon and hydrogen contents than the samples made with TEOS. This is partly due to the additional methyl group present in MTMS, possibly also to a slightly higher rate of MTMS incorporation. Generally the content of carbon, hydrogen, and nitrogen decreases as the organosilane fraction (MTMS or BTMPSA, respectively) decreases and the fraction of TMOS (which does not introduce organic moieties) increases. Comparison between samples of the same composition but made in acetone or methanol only shows minor differences, which are within the sample to sample variation typically observed in these reactions.

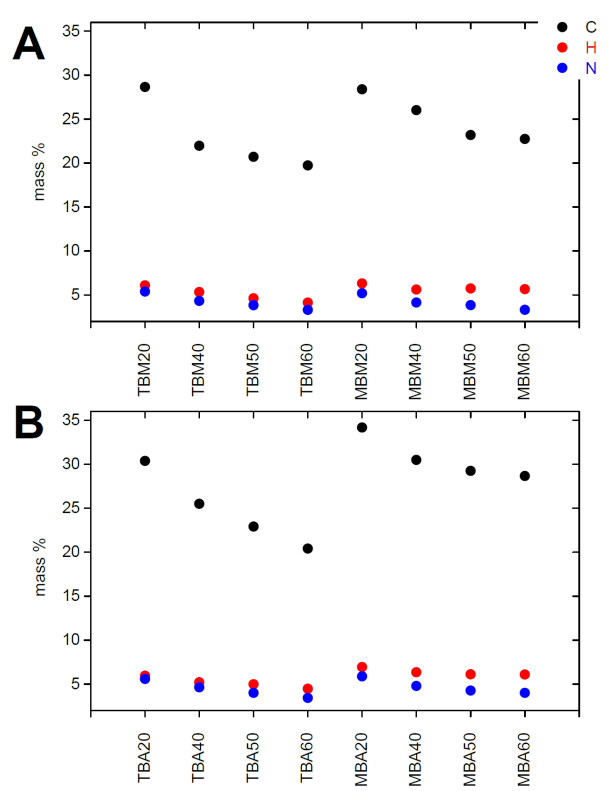

Figure 3: Carbon, hydrogen, and nitrogen contents of silica monoliths made from methanol (A) and acetone (B).

Figure 4 shows representative thermogravimetric analysis (TGA) data of the pure organosilica host materials. All TGA curves exhibit a three-step degradation process. The first step between 35 and ca. 120 °C is due to the loss of surface-bound water. Generally, the monoliths made from TMOS (TBA60 and TBM60) show higher weight losses (up to ca. 5%) in this region than samples made from MTMS, which only show a loss of up to 1.5%. This difference is attributed to the methyl group of MTMS possibly rendering the material slightly more hydrophobic and thus reduces water uptake.

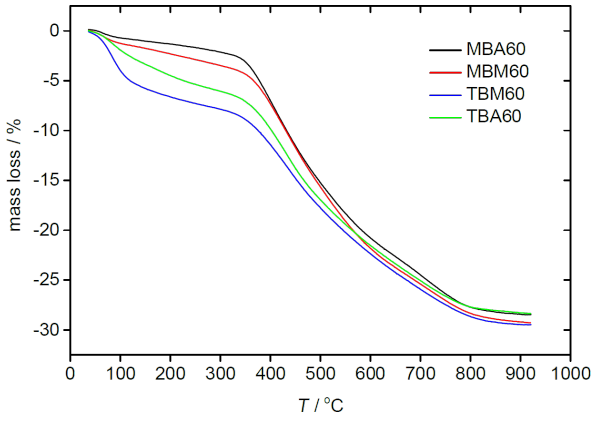

Figure 4: TGA data of pure organosilica monoliths.

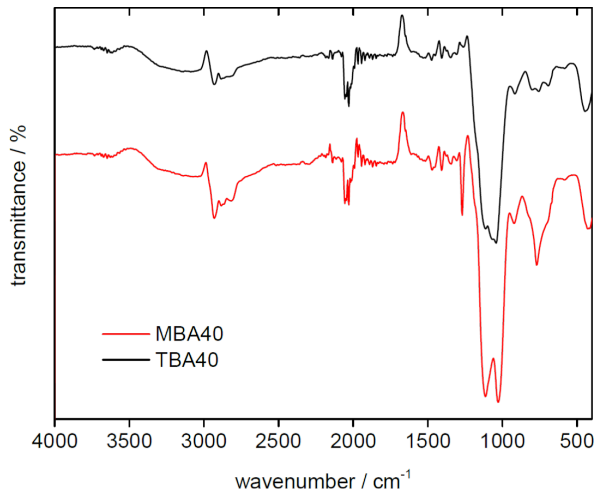

Figure 5: Representative IR spectra of TBA40 and MBA40.

The second weight loss between ca. 120 and 300 °C is assigned to condensation of residual silanol groups and further water evaporation. Possibly this is accompanied by elimination of some organic fragments from the organic linkers. The last weight loss from 300 to ca. 870 °C is largely due to the oxidative elimination of the organic linker [47] and further condensation of the silanol groups. The remaining weight at 900 °C is due to silica and carbon residues.

Figure 5 shows representative ATR-IR spectra of two dried monoliths. The spectra of all samples are virtually identical and exhibit fairly broad bands in all cases. All spectra show C–H bending vibrations at 770, 850, and 950 cm^{-1}. Bands at 900, 1010, and 1080 cm^{-1} are due to asymmetric and symmetric Si–O–Si stretching vibrations and Si–OH silanol groups on the silica surface. Broad bands between 3000 and 3400 cm^{-1} originate from Si–OH, H_2O, C–N, and N–H stretching vibrations. A further characteristic N–H stretching vibration is observed at 2055 cm^{-1} [48].

Figure 6 shows a representative small angle X-ray scattering (SAXS) pattern. All SAXS patterns show a strong scattering signal with a typical q^{-4} behavior indicating an amorphous, mesoporous system with strong phase boundaries and cylindrical pores, but without ordered mesopores [37].

This is confirmed by nitrogen sorption measurements, Figure 6. All monoliths show a type IV isotherm typical of mesoporous solids. The H2 hysteresis loop is due to capillary condensation in the mesopores and is attributed to differences between condensation and evaporation processes occurring in pores with narrow necks and wide cavities often referred to as ink bottle pores. The late onset of significant nitrogen uptake and the parallel adsorption and desorption branches also indicate the

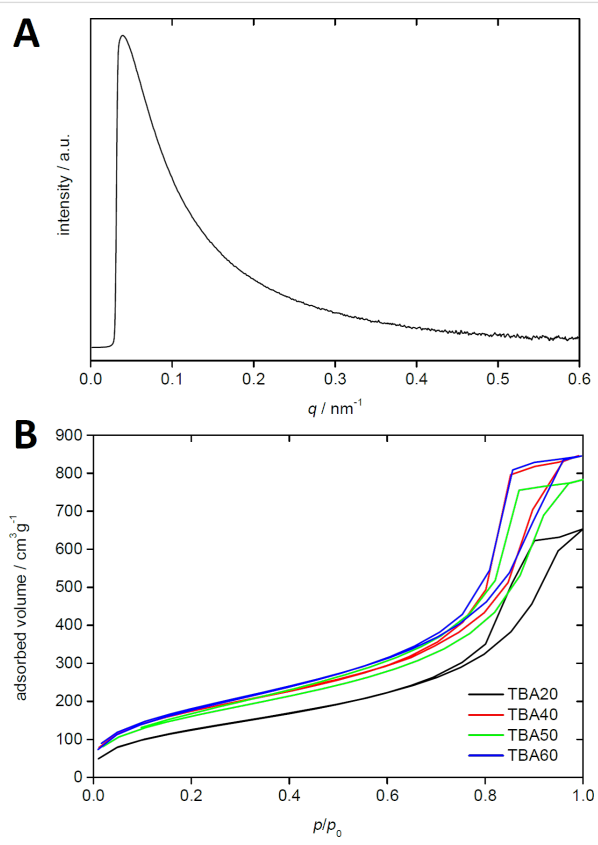

Figure 6: (A) SAXS pattern of TBA40 and (B) nitrogen sorption data of TBA20 to TBA60.

presence of rather small pores and a relatively narrow pore size distribution [37]. Analysis of the SAXS data using the Porod-approach [37-40] confirms this, although pore sizes determined via SAXS are slightly larger than the values determined from BJH analysis, Table 1.

Table 1: Surface areas, pore volumes, porosity, and BJH average pore sizes derived from SAXS and nitrogen sorption (BET).

sample	BET surface area [m^2/g]	BJH pore volume [cm^3/g]	Open pore volume [%]	average pore size radius (BJH) [nm]	average pore size radius (SAXS) [nm]
TBA20	466	0.95	66.5	6.3	8.3
TBA40	634	1.23	72.2	6.2	9.5
TBA50	523	1.14	70.5	6.9	8.2
TBA60	518	1.31	73.4	6.4	8.0
TBM20	506	0.35	42.4	1.9	3.7
TBM40	350	0.19	28.5	1.9	2.5
TBM50	309	0.18	27.4	1.9	2.4
TBM60	752	0.82	63.4	2.1	7.8
MBA20	478	0.66	58.2	3.8	6.2
MBA40	710	1.00	67.8	4.9	8.2
MBA50	746	0.69	59.2	3.2	6.4
MBA60	740	1.14	70.6	5.0	13.5
MBM20	188	0.18	27.8	1.8	3.4
MBM40	383	0.23	32.8	1.9	3.4
MBM50	248	0.17	26.8	1.9	2.9
MBM60	363	0.29	37.7	1.2	3.7

Table 1 summarizes the data obtained from SAXS and nitrogen sorption. All organosilica materials have surface areas between 250 and 750 m^2. In general, silica materials made from acetone have larger surface areas than the materials made from methanol. The surface areas are remarkably high for monolithic silica materials dried under ambient conditions (xerogels) [49,50]. Moreover, many mesoporous systems collapse because of the strong forces applied to the pore walls by the evaporating solvent [49]; this is, however, not the case here. We never observe cracking or other pore collapse. This is likely due to the flexibility of the organic bridges that enable the dry solid to respond to local mechanical stress without breaking or pore collapse.

Table 1 also shows that the pore size and open pore volume strongly depend on the composition of the monolith and the solvent. Monoliths made in methanol have much smaller pore radii (ca. 2 nm) than silica monoliths made in acetone (4 to 6 nm). If made in methanol, the surface area depends on the amount of TMOS or MTMS. TMOS results in surface areas that are about 200 m^2/g higher than surface areas of samples made from MTMS. Overall the open pore volume of these samples is similar and around 30–40%. Moreover, monoliths made from acetone generally have much higher surface areas of 500–750 m^2 than monoliths made from methanol. The synthesis protocol using MTMS and acetone results in the highest surface areas.

Overall, organosilica monoliths prepared with TMOS in acetone shows the highest open pore volumes, the largest pores with 6 to 7 nm in radius, and the highest pore volumes of up to 1.31 cm^3/g. An increasing amount of the linker BTMSPA decreases the pore volume, pore size, and open pore volume. The same observation applies to materials obtained with MTMS instead of TMOS in acetone. High surface areas up to 740 cm^3/g, high open pore volumes of around 60%, and pore sizes between 3 and 5 nm are also obtained in this system.

In contrast, the methanol-based synthesis yields no clear trend in the product characteristics, except for the fact that the pore radius is around 2 nm in all samples. The precursor TMOS results in slightly higher surface areas compared to MTMS. Overall the pore volume are much smaller than those for acetone-based silica.

Ionogels

As stated in the introduction, the goal of the current study is the evaluation of new IGs for proton transport. The following section thus presents the results of IL synthesis and the properties of the IGs resulting from the combination of the IL with the different organosilica host materials.

The synthetic protocol (Scheme 1) is adapted from our previous study [25]. However, as 1,3-propanesultone (which was used in the previous work) has a series of safety issues (see the corresponding MSDS) that make it unattractive for larger scale or commercial application, we have replaced 1,3-propanesultone with 1,4-butanesultone for the current work. Accordingly, the new IL used in this study is 1-methyl-3-(3-sulfobutyl)imidazolium *para*-toluenesulfonate, [$BmimSO_3H$][PTS]. [$BmimSO_3H$][PTS] carries two sulfonate groups, one on the sulfobutyl side chain of the imidazolium ring and one in the

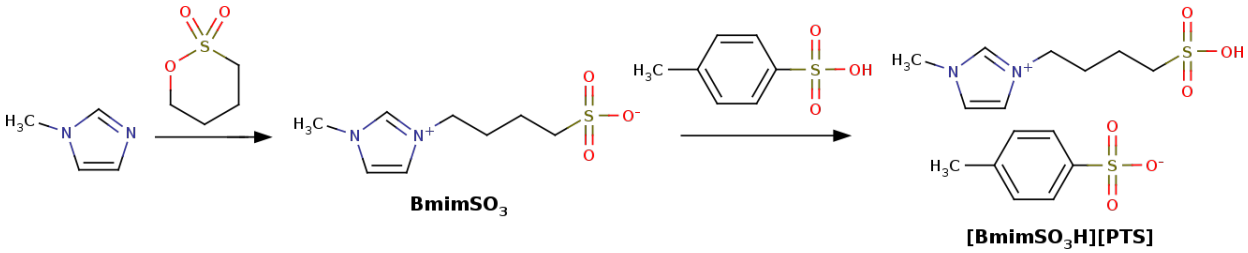

Scheme 1: Synthesis of the IL [BmimSO$_3$H][PTS].

para-toluenesulfonate anion. These two sulfonate groups share a proton and are thus expected to enhance proton conductivity, identical to the previous example [25].

The combination of [BmimSO$_3$H][PTS] with the organosilicas described above yields IGs with the shapes and dimensions of the respective organosilica matrix. In touching the materials they exhibit a rubberlike consistency, but this aspect has not been evaluated here. Figure 7 shows that the IGs are clear and translucent materials. In some cases, they are slightly yellow; the reason for this color is not quite clear because both the neat IL and the monoliths before IG formation are almost colorless. Some monoliths are, however, somewhat off-white or turbid. This could contribute to the slight color change and is mostly observed for IGs obtained via the acetone-based synthesis (TBA and MBA materials).

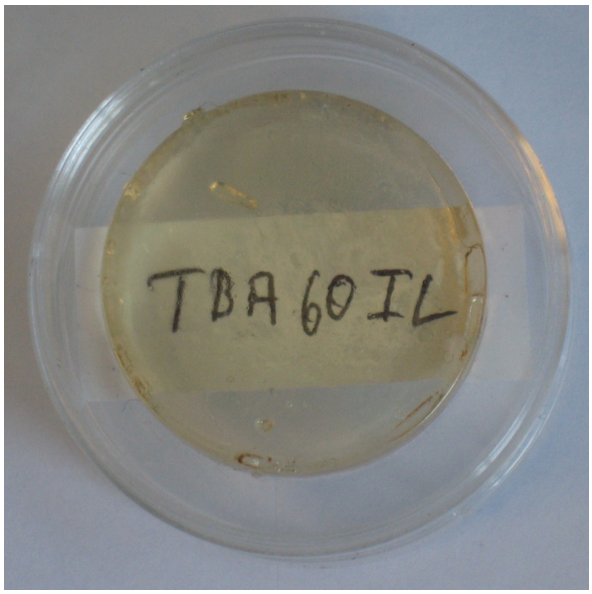

Figure 7: Photograph of an IG resulting from the combination of the TBA60 organosilica matrix and [BmimSO$_3$H][PTS].

The IL is tightly trapped in the organosilica matrix and does not show signs of leakage when stored at ambient conditions over several months. Moreover, the IGs do not show degradation (such as color changes or crack formation) even when stored in a vacuum oven at 250 °C for several days.

Figure 8 shows representative IR spectra of a neat TBA20 monolith, the neat IL, and the TBA20IL ionogel resulting from the combination of the two components. The distinct bands of the IL dominate the IG spectrum and indicate that the IL is the major component of the IG. Bands around 2900 and 2000 cm^{-1} also show the presence of the silica material.

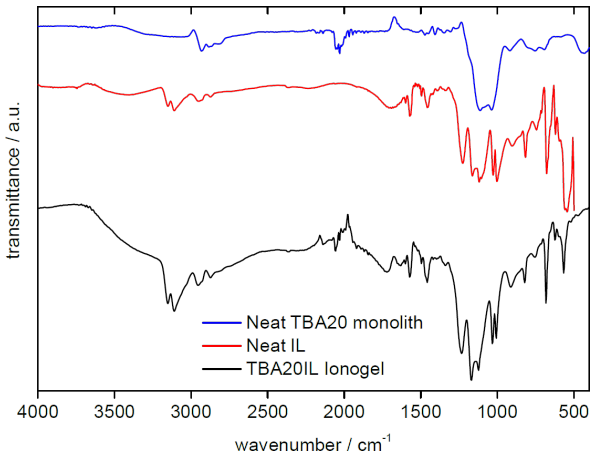

Figure 8: IR spectra of a neat TBA20 monolith, pure IL, and the resulting TBA20IL IG.

In detail, in the spectra of the neat IL [BmimSO$_3$H][PTS], the bands can be assigned to the C–N and C–H stretching vibration modes of the imidazolium ring (3151, 3112, 2957, and 2922 cm^{-1}), CH$_3$–N and CH$_2$–N stretching modes and C–C stretching vibrations of the imidazolium ring (1602, 1573, 1456, and 1229 cm^{-1}), and out of plane C–H bending vibrations (816, 743, and 681 cm^{-1}). The two characteristic bands at 1028 and 1116 cm^{-1} can be attributed to the asymmetric and symmetric

stretching vibrations of the sulfonate group [48]. Between 500 and 1700 cm^{-1} the spectra of the neat IL and the IGs are virtually identical indicating a dominant contribution of the IL to the IR spectra.

Figure 9 shows the results from EA of the IGs. Overall, EA data do not show significant variations between the individual IGs. All IGs based on monoliths made from methanol have carbon contents between 42 and 44%, hydrogen contents between 5 and 7%, nitrogen contents between 6 and 7%, and sulfur contents around 15%. In the case of the IGs based on the monoliths made from acetone, the carbon contents are somewhat more scattered and vary from around 40 to 48%, while the H, N, and S contents are again rather constant at around 5 to 8%, 5 to 8%, and 15 to 17%, respectively.

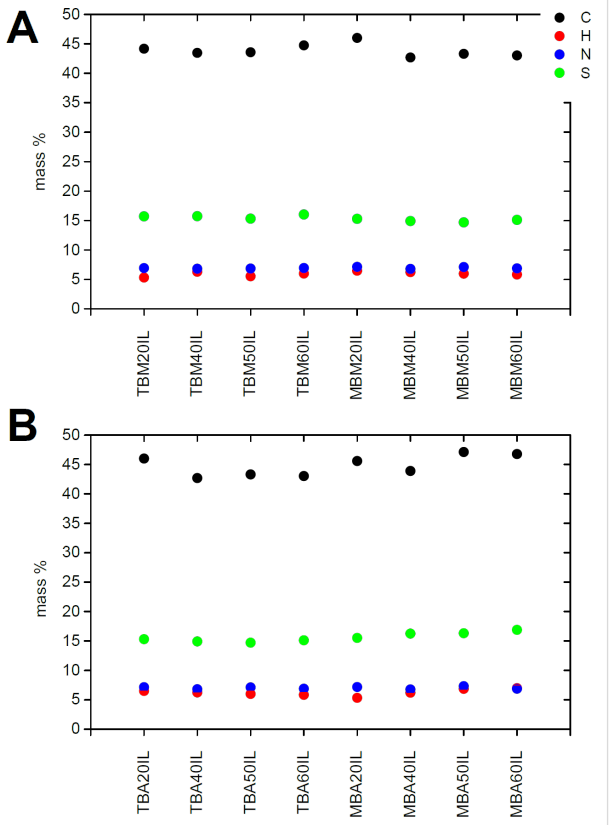

Figure 9: EA data of IGs. Samples shown in panel (A) were made via the methanol-based synthesis and samples shown in panel (B) were made via the acetone-based synthesis of the organosilica. It must be noted here that for reasons described in the Experimental part, there is a slight variation in the IL composition. Moreover, the organisilica composition also slightly varies from batch to batch. As such it is rather difficult to exactly assign compositions from EA data.

Figure 10 shows representative TGA data obtained from the IL and the MBA IGs. If the IGs are dried in vacuum before the TGA experiments, they are stable up to 250 °C with a maximum mass loss of only around 3%. This is presumably due to traces of water in the IL, to condensation of remaining silanol groups, or to traces of organic solvent from the synthesis.

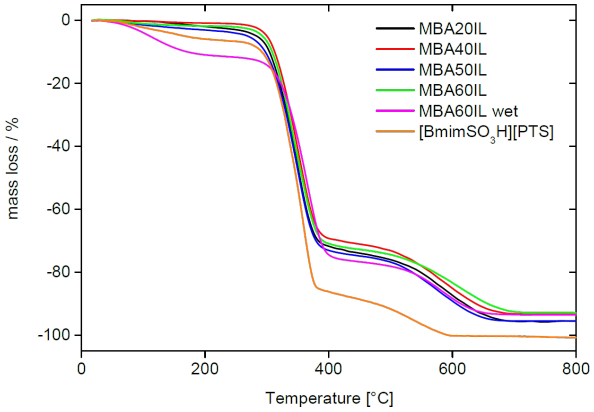

Figure 10: TGA data of MBA20IL, MBA40IL, MBA50IL, and MBA60IL along with TGA trace obtained from wet MBA60IL obtained without drying before TGA, and a TGA trace of the pure IL [$BmimSO_3H$][PTS].

Between 260 and 420 °C a significant mass loss of ca. 70% is observed. It is mainly due to the decomposition of the IL but the decomposition of the organic linker in the organosilica matrix also contributes to this weight loss. The last weight loss of ca. 25% between 500 and 700 °C is assigned to the complete decomposition of the IL and further water release associated with silanol condensation.

Complete decomposition of the neat IL is already achieved at 600 °C. Moreover, a comparison of IGs that were dried before TGA with identical wet IGs directly from the synthesis shows that the overall water uptake of the IG can reach ca. 12% when stored at ambient conditions rather than under vacuum. Even when dried, the IL alone already contains ca. 6% of water. Overall, TGA thus shows that the IGs consist of around 85 to 90% of IL by weight (not considering the contribution of the organic linker moiety in the organosilica host) and 10 to 15% of organosilica matrix.

Figure 11 shows representative DSC traces of the neat IL and the samples TBA20IL to TBA60IL. The neat IL (grey line) exhibits a glass transition at T_g = −11.9 °C. No crystallization or melting peaks are visible in the range of −170 to 150 °C. The fact that the glass transition is less visible in the cooling curves is due to supercooling and indicates rather slow dynamics of the IL due to high viscosity, similar to our previous example [25]. Table 2 shows that the glass transition temperatures do not change significantly by entrapping the IL inside the mesoporous silica networks made from acetone. The variations of T_g

in the host materials made in methanol are somewhat more pronounced but also here T_g remains at around −9 °C.

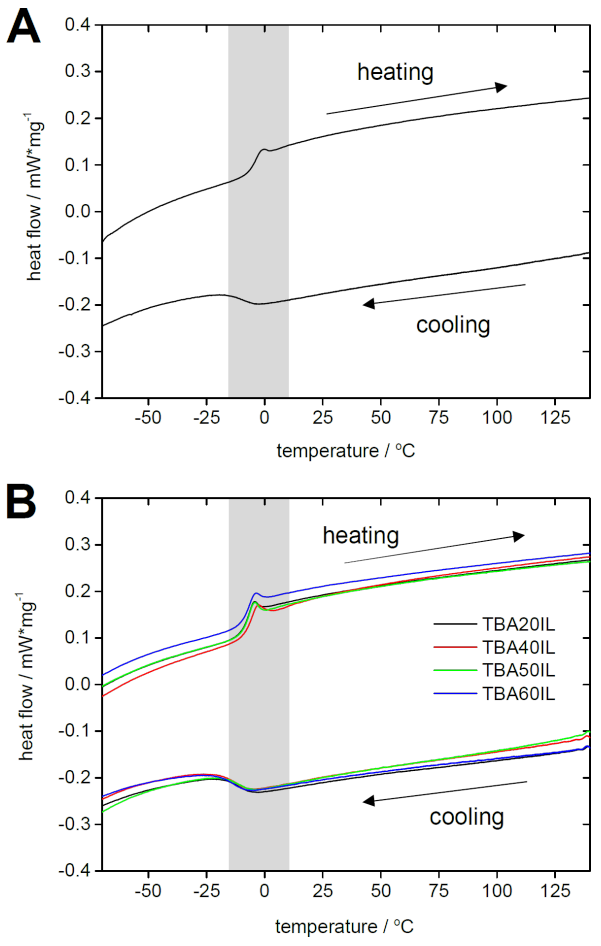

Figure 11: DSC heating traces of (A) [BmimSO$_3$H][PTS] and (B) the resulting TBA IGs. Gray areas highlight the region of the glass transition.

Table 2: T_g values obtained from DSC measurements (second heating cycle). The T_g of the pure IL [BmimSO$_3$H][PTS] is −11.9 °C. n.o. = not observed.

	T_g [°C]			
	TBA	TBM	MBA	MBM
20	−9.8	−10.0	−9.7	−10.4
40	−9.1	−6.2	−10.0	−9.0
50	−9.6	−8.1	−10.2	−8.4
60	−9.9	−9.4	n.o.	n.o.

It has been pointed out by a referee of this manuscript that – because the DSC signals are around 0 °C – water may also be involved in these processes. As detailed in the Experimental section however, the samples underwent a first heating/drying cycle to 120 °C and the subsequent cycles were run up to 200 °C, suggesting that the vast majority of the water possibly present in the IL was removed. Moreover, DSC traces obtained from third and fourth heating cycles are identical to those shown in Figure 11, thus confirming this assumption.

Electrochemical impedance spectroscopy (EIS) was used to evaluate the electrical behavior of the IGs. Figure 12 shows a representative Nyquist plot of TBA20IL, where the imaginary part of the impedance is described as a function of the real part (*Z*'' vs *Z*') in orthonormal basis. Clearly, the impedance depends on the temperature. This is expected because the ion mobility within the sample is activated by temperature. To a first approximation, the intercept of the depressed semi-circle with the *z*'-axis (or the intercept of the straight line with the *z*'-axis) provides information on the resistance of the material. A temperature increase shifts the intercept to lower *z*' values indicating a lower resistance and hence a higher conductivity.

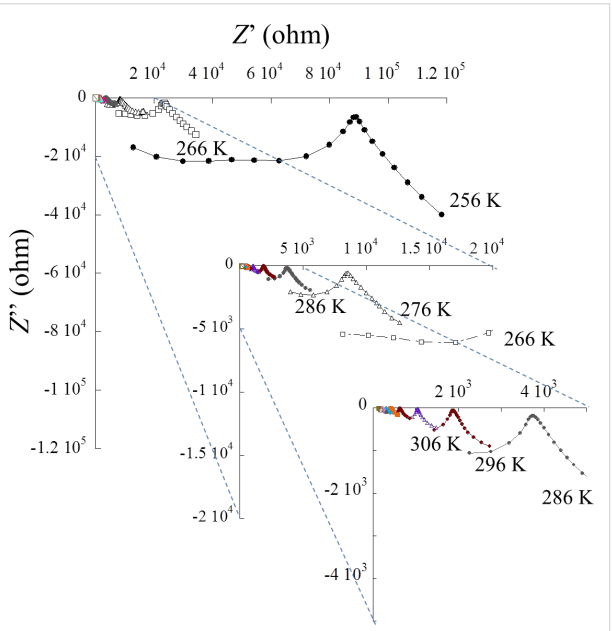

Figure 12: Nyquist curve *Z*''(ω) vs *Z*'(ω) for TBA20IL with zoom-ins to the central areas of the plot vs temperature.

Indeed, the general feature changes drastically with the presence of the depressed semi-circle and the straight line at low temperature, then the depressed semi-circle disappears progressively, and the straight line at higher temperatures becomes more pronounced. This behavior corresponds to the freezing of the ion mobility at lower temperature where the semi-circle represents the inside bulk that fades when increasing the temperature until the presence of polarization and diffusion is only visible by the straight line.

More specifically, the lower frequency response visualized as a straight line is representative of the electrode polarization, while the higher frequency response forming the depressed circle is due to the dielectric properties of the bulk. The first part can be described as a non-ideal capacitor (constant phase element) in series with the interfacial resistance while the second part is fitted with a constant phase element in parallel with the same interfacial resistance. The divergence from ideal behavior (Debye case) at high frequency is displayed by the depressed circle and the fact that the circle does not close on the z'-axis. The related impedance of the capacitor is given in the Experimental part.

For the lower frequency region, the straight line is not parallel to the z"-axis, which should be expected from an ideal capacitor (forming an angle $\pi/2$ from z'-axis). The deviation is due to the roughness of the interface between the sample and the blocking electrode.

The components of the so-called equivalent electrical circuit are refined using the entire frequency domain. The fitted resistances as a function of the temperature are used to determine the conductivity and they are displayed $\log(\sigma \cdot T)$ as a function of the inverse of the temperature ($1000/T$). The points describe a straight line disrupted at one point ($1000/T \approx 3.5$ K^{-1}, i.e., $T = 285$ K, Figure 13).

Surprisingly, for some compositions, especially MBM40IL, MBM60IL, and TBM60IL, a plateau between both linear regions appears. This intermediate regime, suggesting that the mobility is not thermally activated anymore, can be understood as a transient behavior. These two linear variations rather than a slightly curved feature suggest the presence of a thermally activated Arrhenius-type process rather than a Vogel–Tammann–Fulcher (VTF) type process. To ensure the true occurrence of these two linear variations the derivative, $d(\log(\sigma \cdot T)/d(1000/T)$, was analyzed. The derivative forms a stair-type feature indicative of two distinct slopes, i.e., two distinct energies of activation. In contrast, a VTF mechanism would produce an inclined straight line on the derivative. Such a behavior is, e.g., observed for ILs in soft matrices such as polymers [14-16,51].

All samples show an Arrhenius-type behavior with two distinct energies of activation. MBA40 (followed by TBM20 and MBM20) performs the best with $\sigma = 7 \times 10^{-3}$ S·cm^{-1} at 357 K and $\sigma = 3.4 \times 10^{-3}$ S·cm^{-1} at 293 K. This is associated with an activation of energy E_a of 0.6 eV between −20 °C and 20 °C and subsequently with an E_a of 0.45 eV from 20 °C to 80 °C. It shows that the charge-carrier mobility is less activated with temperature when the temperature increases.

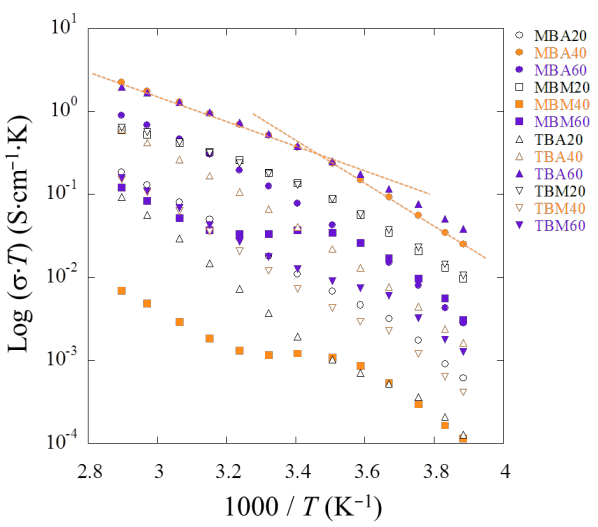

Figure 13: Variation of $\log(\sigma \cdot T)$ versus $1000/T$ for all IGs. The change in the energy of activation likely does not stem from a weight loss process such as a weak dehydration because there is no apparent thermal event below 100 °C. However, data collected by DSC clearly show a transition at around −9 °C. This is reasonably close to 12 °C, i.e., $1000/T = 3.5$ K^{-1}, where the change in E_a occurs. Le Bideau and coworkers performed quasi-elastic neutron scattering experiments to address the presence of a soft transition responsible of the change in the conductive dynamics [52] but as there are no data available for the present system we prefer to not speculate about the details of the kink observed in some of the data. The experiments are, however, highly reproducible.

The conductivities obtained from the measurements are comparable to other IGs where the IL confinement leads to an intermediate state between liquid and solid (conductivity vs mechanical strength, respectively), since $\sigma_{298\ K} = 3.15 \times 10^{-3}$ S·cm^{-1} and $\sigma_{343\ K} = 1.12 \times 10^{-2}$ S·cm^{-1} for one of the best polymer nanocomposite ionogel composed of modified PMMA bearing trimethoxysilane groups and tetraethoxysilane (TEOS) with 76 wt % of 1-butyl-3-methylimidazolium bis(trifluoromethane sulfonyl)imide ([BMIm][NTf2]) [15]. A critical threshold in ionic conductivity around this value of 76% was explained by a transition from a polymer in salt to a quasi-liquid state [14]. It is noteworthy that the IL content in the MBA series is somewhat higher at 85 to 90% as derived from TGA analysis (Figure 10).

Taking one of the better performing IGs, MBA40IL, a further study scrutinizes the dielectric properties to better understand the presence of two E_a. The dissipation factor tan δ (= ε"/ε') is interesting to evaluate since it represents the ratio between the electrical power dissipated in the sample and the total power in the circuit [53]. With increasing temperature a large hump is observed due an increase in the dielectric properties. This signal stems from interfacial phenomena within the bulk of MBA40IL. The peak maximum in intensity ($\omega \cdot \tau = 1$) is the relaxation time (Figure 14a) [54], and their positions are plotted against the inverse of the temperature (Figure 14b). Once again, an Arrhe-

nius-type behavior with the presence of two defined slopes is observed. The associated energy of dielectric relaxation can be obtained as:

$$f = f_0 \cdot e^{-E_r/RT} \text{ and, } \log f = \log f_0 - E_r / RT \cdot \log e.$$

E_r = 0.72 eV in the lower temperature range and E_r = 0.38 eV in the higher temperature window. It is likely that the same charge carriers are responsible for the conductivity and dielectric properties. The slight deviation between the energy of activation and the energy of dielectric relaxation is probably due to the inner structure with the migration in the vicinity of silicate walls compared to the porous structure, as already observed in other composites [55]. The relative ion conductivity considering the physical versus chemical contributions was recently addressed in polymer-ionic liquid pairing [56].

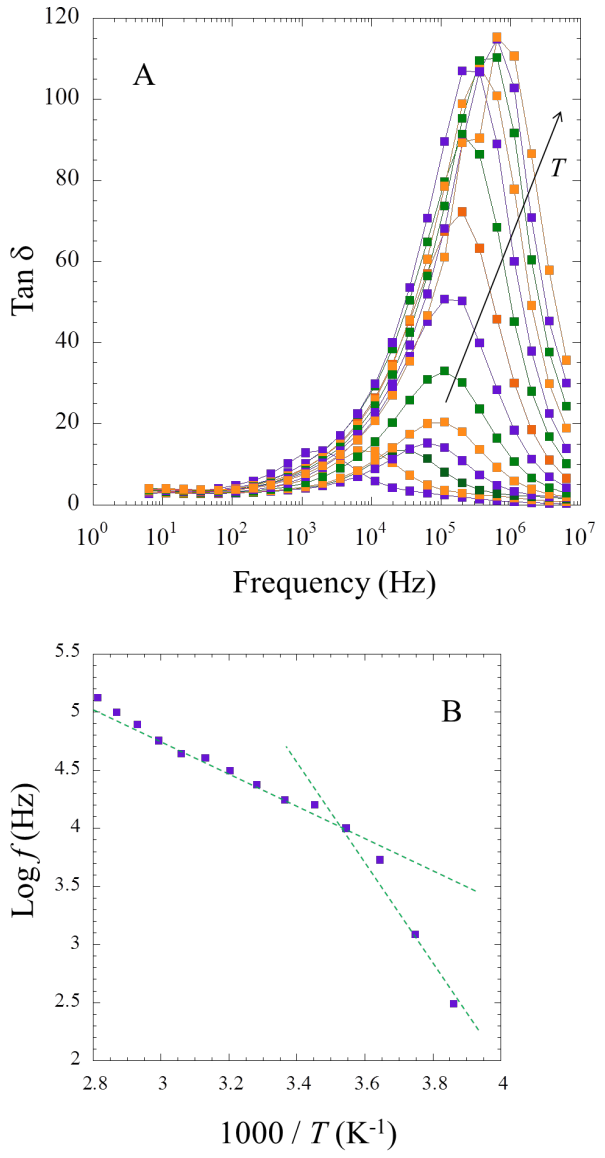

Figure 14: Variation of (A) tan δ vs log *f* and (B) relaxation time vs 1000/*T* for MBA40. The temperature is as follows: 1000/*T* (K^{-1}) = 3.861, 3.745, 3.643, 3.545, 3.452, 3.364, 3.282, 3.204, 3.130, 3.060, 2.994, 2.930, 2.870, 2.813.

To further evaluate the molecular processes occurring in the IGs, we have performed computational studies on the pure IL [BmimSO$_3$H][PTS]. Figure 15 shows that there are three states of the SO$_3$H-proton in its intramolecular O–H bond (the bond is described in [25]). The first state is a tight O–H bond of approximately 100 pm in length. Next there is a more loosely bound (150 pm) state and thirdly we find three protons that fully depart their parent SO$_3$ group of the cation.

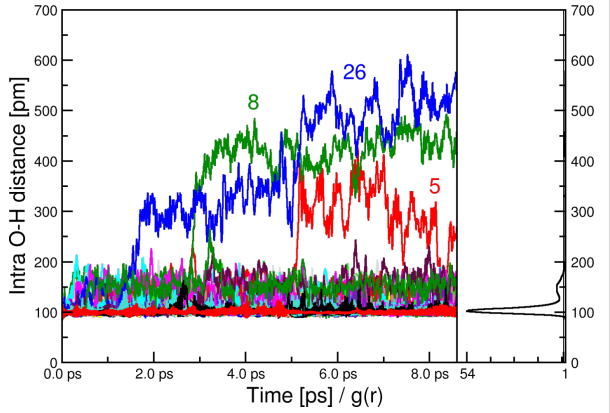

Figure 15: Full temporal development (from equilibrium search to production run) of all 32 intramolecular O–H distances in the SO$_3$H group (left) along with the radial pair distribution function of the same atom pair (right). The numbers refer to the molecules in the simulation box.

To elucidate whether these states are correlated to oxygen atoms of other cations or anions Figure 16 shows three combined distribution functions. These data clearly show that the proton – while normally bound to one oxygen atom – can form very short (150–180 pm) hydrogen bonds to the SO$_3$ group of either other anions or other cations, see red areas in CDFs of Figure 16. If the hydrogen increases the intramolecular bond to approximately 150 pm either a cation SO$_3$ group or one of the tosylate anions is close. A very large O–H distance of a former intramolecular O–H group can correlate with both, a short O–H anion or cation distance.

Moreover, inspection of the trajectory clearly shows that the protons are very mobile and several events can happen. For example, the proton of the SO$_3$H can move to the SO$_3$H group of another cation or to the SO$_3$ group of an anion. This can be supported by a concerted proton transfer from another SO$_3$H group or furthermore it can be supported by a sizeable hydrogen bond

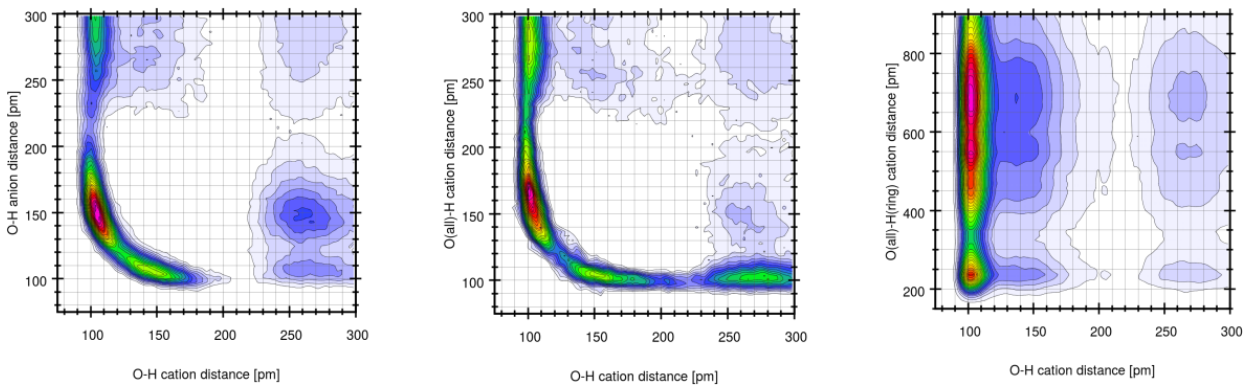

Figure 16: Combined distribution function of the intramolecular O–H distances (including only the bonding oxygen) on the *x*-axis. The *y*-axis is (from left to right) the O(anion)–H distance, the O(cation)–H distance (including all oxygen atoms of the SO_3H group), and the O(cation)–H(ring) distances, respectively.

of the imidazolium ring proton towards the SO_3H group. This is also reflected in Figure 16 (right) where short (<200 pm) H–O(SO_3H) distances are observed while the original O–H intramolecular bond is still intact.

Discussion

IGs are emerging materials with a high application potential [5,12,13]. Among others, silica has attracted interest as an IG matrix. This is due to the fact that silica is highly tunable in terms of the pore sizes, pore volumes, pore organization, and pore wall functionality [45,46]. These parameters enable the tuning of the IL loading, the IL/matrix ratio, and in some cases also the tuning of the IL behavior by tailoring the interactions of the IL with the wall of the silica [36,57]. Indeed, several research groups have provided different approaches towards silica-based IGs [11,16-18,22,24,25]. The main issue with most of these materials is that they cannot withstand mechanical stress and there is thus a need for stabilizing silica IGs for, e.g., flexible devices.

The current article describes new organosilica matrix materials based on silica and an organic linker. The linker provides the matrix with a rubberlike appearance rather than a high stiffness. Although the mechanical properties are still under investigation, the current data show that the organosilica matrix materials exhibit much higher stabilities towards drying and shrinking than conventional silica monoliths. While the latter often break upon drying, the current monoliths do shrink somewhat but remain intact over the whole composition range (Figure 2). This clearly shows that organosilica matrix materials are attractive host materials for the generation of advanced silica-based IGs.

Moreover, analysis of the organosilica materials with EA (Figure 3), TGA (Figure 4), IR spectroscopy (Figure 5), nitrogen sorption (Figure 6 and Table 1), and SAXS (Figure 6 and Table 1) shows that the properties of the organosilica monoliths can be tuned by a careful selection of the precursors, the precursor ratio, and the solvent used for preparation. Monoliths prepared in methanol are colorless and translucent and are therefore potentially interesting for optical devices or spectroscopy. On the other hand, methanol-based monoliths appear slightly softer when touching them and much more turbid in appearance. These materials may therefore be of interest as IL hosts for applications where a more flexible material without specific optical properties is desired, such as batteries or fuel cells.

The IL used in the current study (Scheme 1) is a new IL based on a related example published earlier [25]. The difference between the two ILs is the chain length of the sulfonated side chain attached to the imidazolium ring: while Delahaye et al. used a sulfopropyl chain, the current IL is functionalized with a sulfobutyl chain. The reason is the rather high toxicity of the 1,3-propanesultone precursor used for the synthesis of the previous IL. 1,3-Butanesultone, which was used in the current study has a similar reactivity but is less toxic. Moreover, the current IL, [BmimSO_3H][PTS], has a significant advantage in terms of its thermal behavior because it does not crystallize. In contrast to the propane sultone analogue, which slowly crystallizes after 12 months [25], the longer alkyl chain of [BmimSO_3H][PTS] suppresses crystallization of the IL even after over three years at ambient conditions and DSC data reproducibly show a glass transition at around −14 to −9 °C (Figure 11).

These data indicate that replacing the propyl with a butyl spacer provides two advantages, (i) a less hazardous synthesis protocol and (ii) efficient stabilization of the (highly viscous) liquid phase over extended periods of time. As a result, [BmimSO_3H][PTS] is a viable candidate for use in membranes,

especially when considering the simple, near quantitative synthesis (Figure 7) and the high thermal stability of the IL (Figure 10).

The combination of the organosilica matrix with the IL yields IGs that combine the appearance of the matrix with the conductivity of the IL. All IGs are stable and do not show degradation at ambient condition for over 6 months (Figure 7). IR spectroscopy (Figure 8) shows that the IGs are homogeneous in the sense that all IR spectra of the IGs are a superposition of the spectra of the matrix and the IL. The fact that the IR spectrum of the IL dominates the IG spectrum shows that the IG is mainly composed of the IL and that the matrix is the minority phase. This is confirmed by EA (Figure 9) and TGA (Figure 10). EA detects up to ca. 48% of carbon and TGA finds a residual mass of ca. 10% at 800 °C, indicating that ca. 90% of the material consist of IL and organic linker of the organosilica matrix. High IL loadings in silica IGs are quite common, although ca. 90% of IL is on the higher end of what has been reported so far [23,24]. These data therefore show that all organosilica monoliths yield stable monolithic IGs with high IL loading.

DSC data (Figure 11) and EIS analysis (Figure 12-14) show that (i) the confinement of the IL in the matrix does not affect its physical properties and (ii) that the conductivities in the IGs are comparable to those observed in other IGs [19,23-25,36]. In all cases DSC only finds a glass transition, which is independent both of the matrix type (TBA, TBM, MBA, MBM) and also of the fraction of IL present in the IGs.

EIS analysis (Figure 12-14) always finds an Arrhenius-type temperature dependence associated to high ion conductivity. Indeed an optimized composition, MBA40IL, exhibits an ionic conductivity of almost 10^{-2} S·cm^{-1} at 357 K (84 °C, the upper limit in this study). Figure 12 however shows that 84 °C is not the upper limit for this system. This is relevant for application in energy storage devices. Indeed, there is a correlation between the DSC and the EIS data in the sense that DSC finds a T_g at around −9 °C and EIS finds a change in the Arrhenius behavior at around 10 °C. Although there is a slight difference between these two measurements, the data indicate a change in mobility in the general temperature window between −10 and +10 °C. The difference in the transition temperatures is likely due to the quite different experimental setups, but this will have to be verified with a modified EIS setup in the future.

Possibly, the rather high conductivity of the IGs is also due to the fact that the organic bridging moiety in the organosilica matrix contains a nitrogen atom that may also be protonated because alkylamines have pK_a values between 9 and 10. As a result, we speculate that protons can not only transfer between individual sulfonate groups, but also to amino groups of the linker and on to other sulfonates from there. This effect may contribute to the rather efficient conduction but the details are currently under investigation using solid-state NMR spectroscopy.

The hypothesis of very mobile protons is however qualitatively supported by computer simulations (Figure 15 and Figure 16). The simulation data clearly show that significant proton transfer can occur between many different atoms of both the cations and the anions of the IL. This suggests that other proton-accepting atoms such as the nitrogen atoms in the bridge elements of the silica matrix will also be efficient proton acceptors. In turn, a contribution of these positions will likely also contribute to the overall conductivity of the materials.

These data indicate that in the current IGs, the interaction of the IL with the matrix is weaker than in some previously reported IGs [36,57]. This is surprising, because previous data indicate that an organic modification of a silica host can very strongly affect the behavior of a confined IL in a silica matrix [57]. The reason for this weak interaction in the current materials is not clear, but we speculate that the zwitterionic nature of the [BmimSO$_3$H][PTS] IL will lead to very strong interactions within the IL rather than between the IL and the silica pore wall. The main advantage of this behavior is that the IL is "self-sufficient" as far as the ionic transport is concerned and transport properties will likely not change significantly over extended periods of time because the IL does not crystallize or interact strongly with the surrounding host material.

Overall, the current study shows that the combination of [BmimSO$_3$H][PTS] with a suitable organosilica host provides access to robust and somewhat flexible IGs that may be interesting as membrane materials in electrochemical devices such as sensors, batteries, or fuel cells.

Conclusion

The current article is the first account on organosilica host materials for ionogel fabrication. Compared to pure silica host materials, organosilica hosts offer many advantages such as better mechanical stability, the possibility to tune the composition (and hence possibly the properties), and the possibility to include organic moieties in the host material that may enhance some properties such as proton conduction. Overall, organosilica IGs are therefore interesting materials with a high application potential in various fields.

Acknowledgements

We thank R. Rothe for nitrogen sorption measurements, Y. Linde for elemental analysis measurements, Dr. A. Friedrich

and Dr. M. Neumann for help with TGA, P. Ray for carrying out the classical simulations providing the starting configuration of the AIMD simulation, Dr. O. Holloczki for help with simulation data analysis, Dr. K. Tauer for access to the DSC instrument, and the Max-Planck Institute of Colloids & Interfaces for access to the SAXS instrument. The University of Potsdam, the Max-Planck Institute for Colloids & Interfaces, and the DFG (TA571/2-1, 3-1, 13-1 and KI 768/12-1, DFG SPP 1708, Materials Synthesis near Room Temperature) are thanked for financial support. R. L. acknowledges COST MP1202 for funding an exchange with ICCF in Clermont-Ferrand for EIS measurements.

References

1. Plechkova, N. V.; Seddon, K. R. *Chem. Soc. Rev.* **2008,** *37,* 123–150. doi:10.1039/B006677J
2. Joseph, A.; Żyła, G.; Thomas, V. I.; Nair, P. R.; Padmanabhan, A. S.; Mathew, S. *J. Mol. Liq.* **2016,** *218,* 319–331. doi:10.1016/j.molliq.2016.02.086
3. Amarasekara, A. S. *Chem. Rev.* **2016,** *116,* 6133–6183. doi:10.1021/acs.chemrev.5b00763
4. Liu, B. Y.; Jin, N. X. *Curr. Org. Chem.* **2016,** *20,* 2109–2116. doi:10.2174/1385272820666160527101844
5. MacFarlane, D. R.; Forsyth, M.; Howlett, P. C.; Kar, M.; Passerini, S.; Pringle, J. M.; Ohno, H.; Watanabe, M.; Yan, F.; Zheng, W. J.; Zhang, S. G.; Zhang, J. *Nat. Rev. Mater.* **2016,** *1,* 15005. doi:10.1038/natrevmats.2015.5
6. Osada, I.; de Vries, H.; Scrosati, B.; Passerini, S. *Angew. Chem., Int. Ed.* **2016,** *55,* 500–513. doi:10.1002/anie.201504971
7. Giffin, G. A. *J. Mater. Chem. A* **2016,** *4,* 13378–13389. doi:10.1039/C6TA05260F
8. Guo, F.; Zhang, S. J.; Wang, J. J.; Teng, B. T.; Zhang, T. Y.; Fan, M. H. *Curr. Org. Chem.* **2015,** *19,* 455–468. doi:10.2174/1385272819666150114235649
9. Bakangura, E.; Wu, L.; Ge, L.; Yang, Z. J.; Xu, T. W. *Prog. Polym. Sci.* **2016,** *57,* 103–152. doi:10.1016/j.progpolymsci.2015.11.004
10. MacFarlane, D. R.; Forsyth, M.; Howlett, P. C.; Pringle, J. M.; Sun, J.; Annat, G.; Neil, W.; Izgorodina, E. I. *Acc. Chem. Res.* **2007,** *40,* 1165–1173. doi:10.1021/ar7000952
11. Néouze, M.-A.; Le Bideau, J.; Gaveau, P.; Bellayer, S.; Vioux, A. *Chem. Mater.* **2006,** *18,* 3931–3936. doi:10.1021/cm060656c
12. Le Bideau, J.; Viau, L.; Vioux, A. *Chem. Rev.* **2011,** *40,* 907–925. doi:10.1039/C0CS00059K
13. Taubert, A. *Eur. J. Inorg. Chem.* **2014,** *2015,* 1148–1159. doi:10.1002/ejic.201402490
14. Gayet, F.; Viau, V.; Leroux, F.; Monge, S.; Robin, J.-J.; Vioux, A. *J. Mater. Chem.* **2010,** *20,* 9456–9462. doi:10.1039/c000033g
15. Gayet, F.; Viau, L.; Leroux, F.; Mabille, F.; Monge, S.; Robin, J.-J.; Vioux, A. *Chem. Mater.* **2009,** *21,* 5575–5577. doi:10.1021/cm9027918
16. Néouze, M.-A.; Le Bideau, J.; Leroux, F.; Vioux, A. *Chem. Commun.* **2005,** 1082–1084. doi:10.1039/b416267f
17. Néouze, M.-A.; Le Bideau, J.; Vioux, A. *Prog. Solid State Chem.* **2005,** *33,* 217–222. doi:10.1016/j.progsolidstchem.2005.11.049
18. Martinelli, A.; Matic, A.; Jacobsson, P.; Börjesson, L.; Fernicola, A.; Panero, S.; Scrosati, B.; Ohno, H. *J. Phys. Chem. B* **2007,** *111,* 12462–12467. doi:10.1021/jp0735029
19. Martinelli, A.; Iojoiu, C.; Sergent, N. *Fuel Cells* **2012,** *12,* 169–178. doi:10.1002/fuce.201100098
20. Garaga, M. N.; Nayeri, M.; Martinelli, A. *J. Mol. Liq.* **2015,** *210,* 169–177. doi:10.1016/j.molliq.2015.06.055
21. Martinelli, A. *Eur. J. Inorg. Chem.* **2014,** *2015,* 1300–1308. doi:10.1002/ejic.201402496
22. Nayeri, M.; Nygård, K.; Karlsson, M.; Maréchal, M.; Burghammer, M.; Reynolds, M.; Martinelli, A. *Phys. Chem. Chem. Phys.* **2015,** *17,* 9841–9848. doi:10.1039/C5CP00709G
23. Horowitz, A. I.; Panzer, M. J. *Angew. Chem., Int. Ed.* **2014,** *53,* 9780–9783. doi:10.1002/anie.201405691
24. Horowitz, A. I.; Panzer, M. J. *J. Mater. Chem.* **2012,** *22,* 16534–16539. doi:10.1039/c2jm33496h
25. Delahaye, E.; Göbel, R.; Löbbicke, R.; Guillot, R.; Sieber, C.; Taubert, A. *J. Mater. Chem.* **2012,** *22,* 17140–17146. doi:10.1039/c2jm00037g
26. Negre, L.; Daffos, B.; Turq, V.; Taberna, P. L.; Simon, P. *Electrochim. Acta* **2016,** *206,* 490–495. doi:10.1016/j.electacta.2016.02.013
27. Ameri, S. K.; Singh, P. K.; D'Angelo, A. J.; Panzer, M. J.; Sonkusale, S. R. *Adv. Electron. Mater.* **2016,** *2,* 1500355. doi:10.1002/aelm.201500355
28. Nguyen, T. P.; Hesemann, P.; Moreau, J. J. E. *Microporous Mesoporous Mater.* **2011,** *142,* 292–300. doi:10.1016/j.micromeso.2010.12.014
29. Thach, U. D.; Prelot, B.; Hesemann, P. *Eur. Phys. J.: Spec. Top.* **2015,** *224,* 1669–1674. doi:10.1140/epjst/e2015-02489-4
30. Litschauer, M.; Néouze, M.-A. *Monatsh. Chem.* **2008,** *139,* 1151–1156. doi:10.1007/s00706-008-0916-2
31. Litschauer, M.; Peterlik, H.; Néouze, M.-A. *J. Phys. Chem. C* **2009,** *113,* 6547–6552. doi:10.1021/jp900179f
32. Czakler, M.; Litschauer, M.; Föttinger, K.; Peterlik, H.; Néouze, M.-A. *J. Phys. Chem. C* **2010,** *114,* 21342–21347. doi:10.1021/jp109273d
33. Néouze, M.-A. *J. Mater. Chem.* **2010,** *20,* 9593–9607. doi:10.1039/c0jm00616e
34. Brunauer, S.; Emmett, P. H.; Teller, E. *J. Am. Chem. Soc.* **1938,** *60,* 309–319. doi:10.1021/ja01269a023
35. Barrett, E. P.; Joyner, L. G.; Halenda, P. P. *J. Am. Chem. Soc.* **1951,** *73,* 373–380. doi:10.1021/ja01145a126
36. Göbel, R.; Hesemann, P.; Weber, J.; Möller, E.; Friedrich, A.; Beuermann, S.; Taubert, A. *Phys. Chem. Chem. Phys.* **2009,** *11,* 3653–3662. doi:10.1039/b821833a
37. Polarz, S.; Smarsly, B. *J. Nanosci. Nanotechnol.* **2002,** *2,* 581–612. doi:10.1166/jnn.2002.151
38. Porod, G. *Kolloid-Z.* **1951,** *124,* 83–114. doi:10.1007/BF01512792
39. Porod, G. *Kolloid-Z.* **1952,** *125,* 51–57. doi:10.1007/BF01519615
40. Porod, G. *Kolloid-Z.* **1952,** *125,* 108–122. doi:10.1007/BF01526289
41. Elfgen, R.; Hollóczki, O.; Ray, P.; Groh, M. F.; Ruck, M.; Kirchner, B. *Z. Anorg. Allg. Chem.* **2016,** *643,* 41–52. doi:10.1002/zaac.201600342
42. CP2k developers group under the terms of the GNU General Public License; see http://www.cp2k.org.
43. Brehm, M.; Kirchner, B. *J. Chem. Inf. Model.* **2011,** *51,* 2007–2023. doi:10.1021/ci200217w
44. Humphrey, W.; Dalke, A.; Schulten, K. *J. Mol. Graphics* **1996,** *14,* 33–38. doi:10.1016/0263-7855(96)00018-5
45. Hoffmann, F.; Cornelius, M.; Morell, J.; Fröba, M. *Angew. Chem., Int. Ed.* **2006,** *45,* 3216–3251. doi:10.1002/anie.200503075
46. Hoffmann, F.; Fröba, M. *Chem. Soc. Rev.* **2011,** *40,* 608–620. doi:10.1039/C0CS00076K

47. Li, Z.; Taubert, A. *Molecules* **2009,** *14,* 4682–4688. doi:10.3390/molecules14114682
48. Pretsch, E.; Clerc, T.; Seibl, J.; Simon, W. *Tables of Spectral Data for Structure Determination of Organic Compounds;* Springer: Berlin, Heidelberg, New York, Tokyo, 1983. doi:10.1007/978-3-662-10207-7
49. Kupiec, K.; Konieczka, P.; Namieśnik, J. *Crit. Rev. Anal. Chem.* **2009,** *39,* 60–69. doi:10.1080/10408340802569555
50. Benvenutti, E. V.; Moro, C. C.; Costa, T. M. H.; Gallas, M. R. *Quim. Nova* **2009,** *32,* 1926–1933. doi:10.1590/S0100-40422009000700039
51. Wang, S.-W.; Liu, W. J.; Colby, R. H. *Chem. Mater.* **2011,** *23,* 1862–1873. doi:10.1021/cm103548t
52. Cerclier, C. V.; Zanotti, J.-M.; Le Bideau, J. *Phys. Chem. Chem. Phys.* **2015,** *17,* 29707–29713. doi:10.1039/C5CP04889C
53. Purohit, P. J.; Huacuja-Sánchez, J. E.; Wang, D.-Y.; Emmerling, F.; Thünemann, A.; Heinrich, G.; Schönhals, A. *Macromolecules* **2011,** *44,* 4342–4354. doi:10.1021/ma200323k
54. Leroux, F.; Illaik, A.; Stimpfling, T.; Troutier-Thuilliez, A.-L.; Fleutot, S.; Martinez, H.; Cellier, J.; Verney, V. *J. Mater. Chem.* **2010,** *20,* 9484–9494. doi:10.1039/b926978a
55. Frunza, L.; Schönhals, A.; Frunza, S.; Parvulescu, V. I.; Cojocaru, B.; Carriazo, D.; Martin, C.; Rives, V. *J. Phys. Chem. A* **2007,** *111,* 5166–5175. doi:10.1021/jp0717140
56. D'Angelo, A. J.; Grimes, J. J.; Panzer, M. J. *J. Phys. Chem. B* **2015,** *119,* 14959–14969. doi:10.1021/acs.jpcb.5b08250
57. Göbel, R.; Friedrich, A.; Taubert, A. *Dalton Trans.* **2010,** *39,* 603–611. doi:10.1039/B913482D

License and Terms

BEILSTEIN JOURNAL OF NANOTECHNOLOGY

Recombinant DNA technology and click chemistry: a powerful combination for generating a hybrid elastin-like-statherin hydrogel to control calcium phosphate mineralization

Mohamed Hamed Misbah[1], Mercedes Santos[1], Luis Quintanilla[1], Christina Günter[2], Matilde Alonso[1], Andreas Taubert[3] and José Carlos Rodríguez-Cabello[*1]

Full Research Paper

Open Access

Address:
[1]G.I.R. Bioforge, University of Valladolid, CIBER-BBN, Paseo de Belén 19, 47011 Valladolid, Spain, [2]Institute of Earth and Environmental Sciences, University of Potsdam, D-14476 Potsdam, Germany and [3]Institute of Chemistry, University of Potsdam, D-14476 Potsdam, Germany

Email:
José Carlos Rodríguez-Cabello[*] - roca@bioforge.uva.es

* Corresponding author

Keywords:
calcium phosphate; elastin-like recombinamers; hydroxyapatite; mineralization; SN_A15

Beilstein J. Nanotechnol. **2017,** *8,* 772–783.
doi:10.3762/bjnano.8.80

Received: 27 November 2016
Accepted: 07 March 2017
Published: 04 April 2017

This article is part of the Thematic Series "Hybrid nanomaterials: from the laboratory to the market".

Associate Editor: M. Stenzel

Abstract

Understanding the mechanisms responsible for generating different phases and morphologies of calcium phosphate by elastin-like recombinamers is supreme for bioengineering of advanced multifunctional materials. The generation of such multifunctional hybrid materials depends on the properties of their counterparts and the way in which they are assembled. The success of this assembly depends on the different approaches used, such as recombinant DNA technology and click chemistry. In the present work, an elastin-like recombinamer bearing lysine amino acids distributed along the recombinamer chain has been cross-linked via Huisgen [2 + 3] cycloaddition. The recombinamer contains the SN_A15 peptide domains inspired by salivary statherin, a peptide epitope known to specifically bind to and nucleate calcium phosphate. The benefit of using click chemistry is that the hybrid elastin-like-statherin recombinamers cross-link without losing their fibrillar structure. Mineralization of the resulting hybrid elastin-like-statherin recombinamer hydrogels with calcium phosphate is described. Thus, two different hydroxyapatite morphologies (cauliflower- and plate-like) have been formed. Overall, this study shows that crosslinking elastin-like recombinamers leads to interesting matrix materials for the generation of calcium phosphate composites with potential applications as biomaterials.

Introduction

Combination of the specific properties of two materials is often a key to generating a new material, whose properties are superior to those of its individual components, with improved functional performance that can be used for different applications, such as tissue engineering [1]. This perspective can be applied in one of the hottest current research fields, namely control of

the formation of calcium phosphate (CP) nanostructures for the generation of biomimetic hybrid materials. Among these CP structures, dicalcium phosphate dihydrate (DCPD), hydroxyapatite (HA) and β-tricalcium phosphate (β-TCP) have attracted attention because of their potential applications [2,3]. HA is a stable crystalline phase that forms the main inorganic component of bone and teeth [2,4]. HA has a nanorod morphology in natural bone, with the individual rods being roughly aligned parallel to one another throughout the collagen matrix [5-7]. β-TCP is a resorbable and degradable synthetic material that can be replaced by naturally re-grown bone tissue [2,3]. As a result, HA and β-TCP have already been used in (composite) materials for bone regeneration [2,8]. Due to the correlation between the (crystal) structure and properties of CP, it is important to be able to control its nanostructures [9-11]. For example, hollow and mesoporous CP particles can be used for drug delivery due to their high specific surface area and three-dimensional porous structures. In addition, osteoblast proliferation and apoptosis are affected by the size and shape of CP. Despite this interest, control of the formation of CP nanostructures with specific characteristics remains a challenge. Although dry methods and high temperature methods are able to produce highly crystalline CP, they also produce aggregated products of large crystal size and low phase purity [9,11]. Moreover, these processes cannot control the morphology and size of the CP generated. Similarly, although wet-chemistry methods can be used to control the size and morphologies of CP under mild reaction conditions, it is difficult to control the crystallinity and phase purity of the synthesized CP nanostructures with narrow size distribution [9,12]. Furthermore, the generation of delicate nanostructures, for example neuron-like morphology of amorphous calcium phosphate (ACP) phase [9,12,13] remains a challenge due to the fast nucleation, aggregation and subsequent anisotropic growth of the crystal faces.

Biomineralization-inspired “soft chemistry” routes provide simple and often rather cheap protocols for the synthesis of complex CP-based hybrid materials with a high application potential [14]. Although organic additives can be used to control the CP mineralization process in aqueous solution, their soluble nature restricts their use in potential applications. To overcome this problem, organic chains are introduced as insoluble additives, for example in the case of a templating approach or in a cross-linked state [15-17]. Following this approach, the most common templates used are Langmuir monolayers and self-assembled monolayers. Mineralization in gel phases has also attracted interest because these gels are easily prepared and provide a high level of control over mineralization [18,19], including the potential to hierarchically generate structured hybrid materials that may, for example, resemble bone tissue [20]. Although extensive research has been conducted on the mineralization field, it is a challenge to integrate CP nanocrystals, different in morphology and composition, into the hydrogel matrices [21].

In order to obtain a hydrogel system that can control the formation of CP, it is important to combine different approaches with each other to overcome the challenges inherent to generating materials with the desired properties. Recombinant DNA technology [22,23] and click chemistry [24-26] are two such approaches. Thus, recombinant DNA technology offers advantages such as reduction in production costs, a time reduction in large-scale bioproduction, close control of the biomacromolecules product sequence (size and uniformity) and high yields [22,23]. Moreover, it provides the possibility to achieve structural complexity by using various bio-inspired materials with distinct mechanical, chemical or biological properties. Biomaterials that can be readily controlled using this approach include the so-called elastin-like polymers (ELPs) or recombinamers (ELRs), which are excellent example of materials that exhibit self-assembly and self-organization [27-29].

The majority of ELPs or ELRs consist of simple amino-acid consensus epitopes that are also present in natural elastin, such as (VPGXG)* (see Table 1 for details of sample nomenclature), where the guest amino acid X can be any of the natural or synthetic L-amino acids except L-proline. ELRs exhibit an intrinsic inverse temperature transition (T_t) in aqueous solution. Thus, below T_t, the ELR chains are highly hydrated, which gives rise to well-solvated polymers in a random coil conformation, whereas above T_t, the ELR chains self-assemble into β-turns, which are organized into a fibrillar morphology [27,30]. Changes to the guest residue X modulate T_t, with the key influence being the polarity of the amino acid side-chain in X. As such, ELRs can be designed with different polarities. This variability provides access to a multitude of related, but different, amphiphilic multiblock ELRs with pre-programmed self-assembling capabilities. Moreover, if the guest residue X carries amino or carboxyl groups, for example in lysine or glutamic acid, different post-synthesis reactions can be performed with the ELRs.

As far as polymer bioconjugation is concerned, the thermoresponsivity of ELRs could be exploited to tune the bioactivity of biological components [13,31-34]. According to this idea, the use of recombinant DNA technology [23,35] allows the combination of ELRs with mineralizing domains to be obtained. One of these mineralization-enhancing segments is the SN_A15 (DDDEEKFLRRIGRFG)* peptide from salivary statherin that has negative and positive charges stemmed from the side chains of aspartic (D), glutamic (E), lysine (K) and arginine (R) amino

acids [36]. The addition of specific functional domains further broadens the application potential of ELRs. The SN_A15 domain exhibits a high affinity for CP and is able to nucleate mineral phases from calcium- and phosphate-containing solutions [36,37]. Moreover, its α-helical conformation and distinct charge distribution endows this domain a high affinity for HA [36,37].

The use of click reactions – e.g., cycloadditions – to cross-link hybrid elastin-like-SN_A15 recombinamers synthesized at the gene level, and prepare chemical hydrogels, is considered to be highly successful, since the groups required for cycloaddition – azides and terminal alkynes – are easily introduced [24-26,38]. The reaction conditions for biomedical and pharmaceutical applications are preferably mild and typically performed in water to ensure that the biological structures do not lose their function. Hydrogels can subsequently be synthesized by covalently crosslinking the monomer chains via these azide and cyclooctyne groups by means of a Huisgen [2 + 3] cycloaddition ("click" reaction).

Most of the work performed on ELRs combined with SN_A15 is about studying their behavior in vitro studies [31-34]. For example, ELR membranes with SN_A15 epitopes and/or surface topographies have been conducted on the cell morphology, adhesion, proliferation and differentiation, and their potential for dental and orthopedic implants integration during the mineralization process. Although the mineralization activity of ELRs combined with SN_A15 in soluble state has been investigated so far [13,31], to our best knowledge, there is only one study about the mineralization of ELRs in a hydrogel state [21]. In this study, Li et al. developed mineralized ELR-hydrogels using a polymer induce liquid precursor (PILP) mineralization process where the poly aspartic acids (poly Asp) mimic the role of non-collagenous proteins (NCPs) in biominerals. Although, poly Asp may facilitate the infiltration of ACP into the ELR hydrogel, the interaction of poly Asp with the ELR was not stated. However, to the best our knowledge, the foundations of the impact of SN_A15 on the mineralization activity of ELR in the hydrogel state have not been provided yet.

In light of the above, the main aim of this work was to evaluate the potential of ELR-based hydrogels for CP mineralization. To that end, recombinant DNA technology was combined with click chemistry to synthesize well-formed and cross-linked hydrogels. Crosslinking of hybrid elastin-like-SN_A15 chains bearing lysine as amino acid was achieved by means of a Huisgen [2 + 3] cycloaddition.

Two ELRs were used to produce hydrogels: one is based on a simple ELR chain with no specific moiety and the other one is based on a hybrid elastin-like-SN_A15 recombinamer. In this regard, we are going to focus on the interplay between ELRs, SN_A15 and CP at the molecular level, in order to discuss the following outstanding inquiries: (1) The role of ELRs during mineralization: How do they interact with the mineral? (2) The role of the SN_A15 domain: How does it modulate the mineralization of CP by ELRs?

Experimental

1 Materials

All chemicals were purchased from Aldrich Co. and used as received. ((1*R*,8*S*,9*S*)-Bicyclo[6.1.0]non-4-yn-9-ylmethyl succinimidyl carbonate with a purity of 95% was purchased from SynAffix B.V. (Nijmegen, the Netherlands).

2 ELR bioproduction

The ELR IK24 and the hybrid elastin-like-SN_A15 recombinamer H3AH3, with the composition and amino acid sequence shown in Table 1, were synthesized using recombinant DNA technology as described previously [22,31,39]. Cloning and molecular biology experiments for gene construction were performed using standard methods. ELR production was carried out using cellular systems for genetically engineered protein biosynthesis in *E. coli* and purification was performed with several cycles of temperature-dependent reversible precipitation. After purification, ELRs were characterized using matrix-assisted laser deposition ionization time of flight mass spectrometry (MALDI-TOF-MS), attenuated total reflection infrared spectroscopy (ATR-IR) and nuclear magnetic resonance spectroscopy (^{1}H NMR).

3 Preparation of ELR hydrogels

ELR hydrogels were made by covalent crosslinking of the ELRs via the azide and cyclooctyne groups present in the ELR chains by means of a Huisgen [2 + 3] cycloaddition [24]. The azide and cyclooctyne groups needed for this reaction were introduced directly into the ε-amino group of the L-lysines distributed along the ELR chains. A fraction of the ELR product was functionalized with azide groups as described previously by Lundquist et al. [38]. In this case, all the amino acid groups distributed along the IK24 (25 amine groups) or H3AH3 (31 amine groups) recombinamer chains were modified with an azide group. The other fraction was functionalized with cyclooctyne groups as described previously by González et al. [25]. In this case, 60% of the amine groups distributed along the IK24 or H3AH3 recombinamer chains were modified with a cyclooctyne group.

3.1 Azide derivatization

Briefly, azide groups were introduced by using a diazo-transfer reaction. The reaction was carried out in ultrapure water em-

ploying freshly prepared trifluoromethanesulfonic azide (TA) and $CuSO_4$.

TA preparation: The TA solution was prepared in situ prior to each reaction. NaN_3 (100 equiv) was dissolved in 14 mL ultrapure water followed by the addition of 5.26 g NaN_3/19 mL CH_2Cl_2, yielding a two-phase mixture. Trifluoromethanesulfonic anhydride (Tf_2O) (20 equiv) was then added dropwise with continuous stirring at 4 °C. This solution was kept at 4 °C for an hour, and then at room temperature for another hour. The organic phase was separated and washed with a saturated Na_2CO_3 solution. This organic TA solution was used without further purification.

Amine-Azide interconversion: The ELR was dissolved in ultrapure (Millipore) water at 85 mg/mL and 4 °C. Aqueous Na_2CO_3 (1.5 equiv) and $CuSO_4$ (0.01 equiv) solutions were added. Methanol (2 mL) was added to act as a phase-transfer agent to transfer TA from CH_2Cl_2 to the aqueous phase. The freshly prepared TA solution was added dropwise to the mixture at 4 °C. The azide exchange reaction was performed overnight under an inert atmosphere at room temperature.

The organic solvents were subsequently removed under reduced pressure and the ELR-azide solution was dialyzed against ultrapure water at 4 °C and lyophilized. The product was characterized using ATR-IR spectroscopy, and MALDI-TOF-MS.

3.2 Cyclooctyne derivatization

The amount of (1*R*,8*S*,9*S*)-bicyclo[6.1.0]non-4-yn-9-ylmethyl succinimidyl carbonate required to modify 60% of the amino groups distributed along the recombinamer chain was dissolved in 1 mL of dimethylformamide (DMF). This solution was then added to a solution of the ELR at 25 mg/mL in DMF. The reaction was performed under an inert atmosphere and with continuous stirring at room temperature for 48 hours. The ELR-cyclooctyne product was precipitated by addition of diethyl ether. The white precipitate was washed three times with acetone and dried under reduced pressure. Finally, the ELR-cyclooctyne was dissolved and dialyzed against ultrapure water at 4 °C, lyophilized, and characterized using ^{1}H NMR spectroscopy.

4 ELR-gel formation

ELR-cyclooctyne and ELR-azide samples were dissolved separately in ultrapure water at 4 °C and 50 mg/mL each. Then, 500 µL of each solution was mixed in a cylindrical mold for one hour at 4 °C (since the chains are more soluble at this temperature, and therefore the two solutions will be well-mixed at the molecular level) and a further hour at room temperature, at which the ELRs are covalently cross-linked to generate the ELR gels. These gels were lyophilized for scanning electron microscopy (SEM).

5 Calcium phosphate mineralization

Mineralization was performed by alternative incubation of ELR hydrogels in calcium and phosphate solutions at 37 °C and pH 7.4 for 14 days. Each hydrogel was incubated in 15 mL of a 500 mM aqueous $CaCl_2$ solution for two days, followed by rinsing in ultrapure water. The hydrogels were subsequently incubated in 15 mL of a 300 mM aqueous K_2HPO_4 solution for another two days then once again rinsed with ultrapure water. This sequence was repeated a maximum of seven times (14 days). Salt concentrations are comparable to those used in other studies [40-44]. To evaluate intermediate stages, samples were isolated at different incubation times (4, 8, and 14 days) by removing and rinsing with ultrapure water followed by drying under vacuum at 37 °C.

6 Analysis

6.1 Matrix-assisted laser desorption-ionization time-of-flight mass spectrometry (MALDI-TOF-MS)

The molecular weight (M_w) of the ELRs was determined by MALDI-TOF-MS. Samples were dissolved in ultrapure water at 4 °C. The MALDI-TOF matrix was 2,5-dihydroxyacetophenone (2,5-DHAP). Samples were prepared by dissolving 7.6 mg of 2,5-DHAP in 375 µL of ethanol and mixing with 125 µL of an 18 mg/mL aqueous solution of $C_6H_8O_7{\cdot}2NH_3$. 1 µL of this matrix solution was dispensed onto the MALDI plate along with 1 µL of aqueous ELR solution. The plate was dried in air and mass spectra were recorded using a Bruker autoflex speed instrument with a nitrogen laser (337 nm) operating in positive ion mode with delayed extraction.

6.2 Nuclear magnetic resonance (NMR) spectroscopy

^{1}H NMR spectroscopy was performed using an Agilent 400 MHz spectrometer (Agilent technologies) equipped with an Agilent MR console 400 and one NMR probe. For NMR experiments, 15–20 mg of the ELR sample was dissolved in 600 µL deuterated dimethyl sulfoxide (DMSO-d_6). Chemical shifts (δ) are given in ppm. The DMSO signal at δ = 2.54 ppm was used as internal reference [45].

6.3 X-ray diffraction (XRD)

Dry samples were ground in an agate mortar prior to XRD analysis. Powder XRD patterns were recorded for 2 hours using a Bruker D8 Discover A 25 equipped with a Cu K_α radiation source (λ = 1.5406 Å), a position-sensitive detector (2θ = 5–70°), and a silicon sample holder. Step size was 0.02°. Phase identification was performed using PCPDFWIN (version 2.2 June 2001 JCPDS).

6.4 Attenuated total reflection infrared spectroscopy (ATR-IR spectroscopy)

Dry samples were ground in an agate mortar and placed directly on the ATR crystal for measurement. IR spectra were recorded using a Bruker Tensor 27 USA spectrophotometer with a diamond crystal. For each spectrum, a 128-scan spectrum was collected from 4000 to 500 cm^{-1} with a 2 cm^{-1} resolution. Spectral analysis was performed using OPUS v4.2 (Mattson Instruments, Inc.).

6.5 Thermogravimetric analysis (TGA)

Dry samples were ground in an agate mortar prior to TGA analysis. TGA experiments were performed using a Mettler-Toledo thermo-balance S.A.E instrument with a horizontal furnace and an automatic gas flow controller. Samples were weighed in a 70 µL aluminum oxide crucible and heated at 20 °C/min under N_2 purge (40 mL/min) from 50 to 1000 °C followed by an isothermal step at 1000 °C for 10 min.

6.6 Scanning electron microscopy (SEM)

SEM images of the dry ELR/calcium phosphate composites were obtained using an FEI Quanta Field Emission SEM. Samples were fractured mechanically using tweezers prior to mounting on the SEM stub. Images were recorded in low-vacuum mode (7–15 keV, working distance 7.9–13.2 mm), with water as the auxiliary gas. The Ca/P ratios were obtained by energy dispersive X-ray spectroscopy (EDAX Genesis with an Apollo SDD detector, 10 mm). The energy dispersive X-ray (EDX) spectrometer was calibrated for quantitative analysis using Cu and Al for energy and Mo for energy resolution.

Results

All steps in the production process must be closely controlled to obtain the final hydrogel product with the highest possible yield and correct sequence, and the clickable ELR-based hydrogels studied herein are no exception. This process starts with the gene design, using recombinant DNA technology, and finishes with the final purification steps. The recombinamers are then chemically modified to enable their cross-linking to form a chemical hydrogel.

Elastin-like recombinamer

Two recombinamers were synthesized using recombinant DNA technology and characterized as previously described [31,39]. The amino-acid sequence of the corresponding building blocks (the elastin-like recombinamer IK24 and the hybrid elastin-like-SN_A15 recombinamer H3AH3) are shown in Table 1. IK24 is essentially a 24-fold repetition of the unit $(VPGIG)_2(VPGKG)(VPGIG)_2$ in which the hydrophilic blocks (VPGKG) are distributed among the hydrophobic blocks (VPGIG) [39]. This ELR displays a T_t at about 31.5 °C. The second recombinamer, H3AH3, shows a more complex sequence with T_t of about 27 °C [31]. It has a triblock architecture with two end blocks made of a modified version of IK24 and a central $(VPAVG)_{20}$ block. In addition to the IK24 sequence, the two end blocks bear six SN_A15 epitopes, which are regularly interdispersed along the block chain (Table 1). The main advantage of recombinant DNA technology is the ability to control the distribution of lysines and the SN_A15 bioactive domain along the recombinamer chain.

Elastin-like recombinamer hydrogel formation

Click reactions are a class of reaction that can often also be performed in biological fluids. These reactions are based on pairs of functional groups, for example azide and alkyne, which rapidly and selectively react with one another under mild conditions [24,25,38]. Functional groups such as the ε-amine groups present in the lysine side chains of IK24 and H3AH3 ELRs can be modified to bear two complementary chemical functions. This process is shown in Figure 1 for H3AH3 as an example. Half of the ELR product was functionalized with azide groups by treatment of the amine residues with triflyl azide (TfN_3), as described elsewhere [38] (component 1, Figure 1B). The other half was modified by adding cyclooctyne groups by amidation, with the ε-amino groups of the lysine residues being converted into cyclooctyne bearing an activated carboxyl group (*N*-succinimidyl ester), as described elsewhere [25], to form component 2 (Figure 1B).

Azide derivatization of ELRs is indicated by an increase in their respective M_w in the MALDI-TOF-MS spectra (Supporting Information File 1, Figures S1, S3), and a characteristic absorp-

Table 1: ELRs used in the current study.

ELR	Amino acid sequence[a]	M_w (Da)
IK24	MESLLP[$(VPGIG)_2(VPGKG)(VPGIG)_2]_{24}$V	51996.5 ± 11.3
H3AH3	MESLLP[$(VPGIG)_2(VPGKG)(VPGIG)_2]_2$DDDEEKFLRRIGRFG[$(VPGIG)_2(VPGKG)(VPGIG)_2]_2]_3$ $(VPAVG)_{20}$[$(VPGIG)_2(VPGKG)(VPGIG)_2]_2$DDDEEKFLRRIGRFG[$(VPGIG)_2(VPGKG)(VPGIG)_2]_2]_3$V	71430.7 ± 12.9

[a]Where, D = L-aspartic acid, E = L-glutamic acid, K = L-lysine, F = L-phenylalanine, L = L-leucine, R = L-arginine, I = L-isoleucine, G = glycine, V = L-valine, P = L-proline, M = L-methionine and S= L-serine.

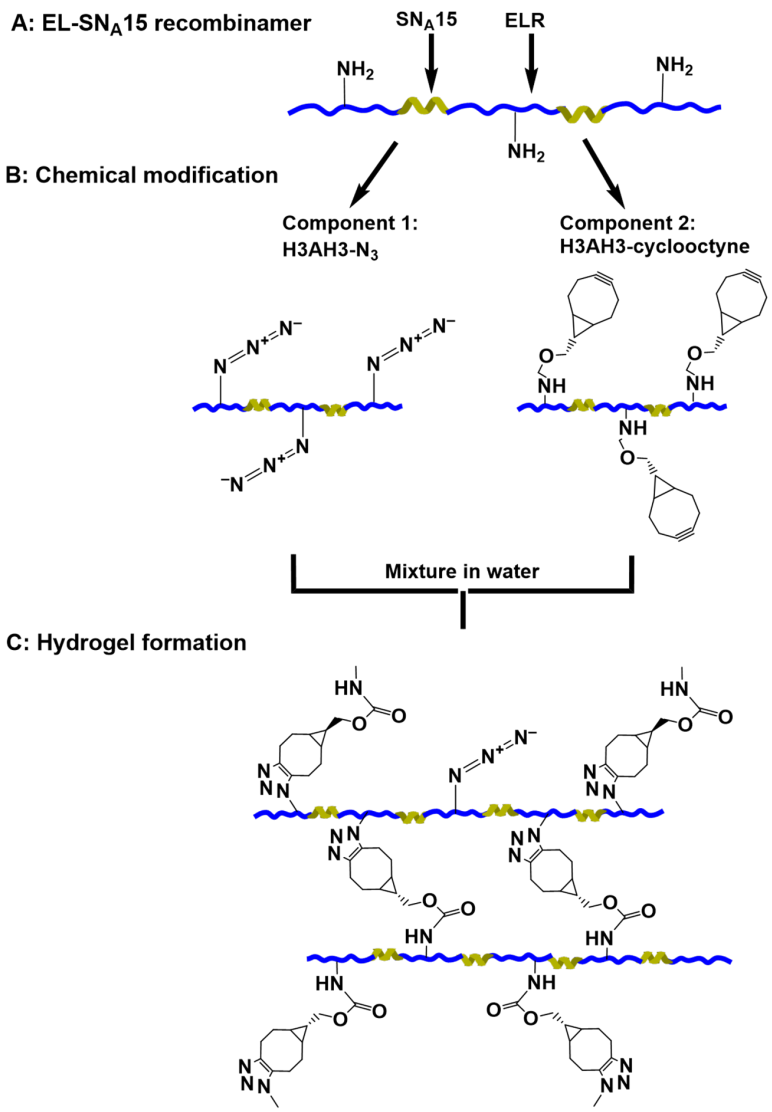

Figure 1: Schematic representation of (A) the H3AH3 recombinamer, (B) azide- (component 1) and cyclooctyne-derivatized H3AH3 (component 2), and (C) formation of the hydrogels via Huisgen [2 + 3] cycloaddition ("click" reaction).

tion band at 2100 cm^{-1} in their ATR-IR spectra (Supporting Information File 1, Figures S2, S4) [46]. Chemical transformation of the ε-amine into the respective cyclooctyne derivative was confirmed by ^{1}H NMR spectroscopy (Supporting Information File 1, Figures S5, S6). The ^{1}H NMR spectra show signals at 2.91, 4.02, and 7.04 ppm, which can be assigned to the methylene group adjacent to the carbamate group, the methylene group adjacent to the cyclopropyl and carbamate groups, and to the proton bonded to nitrogen from the carbamate group, respectively.

The hydrogel was formed by mixing an aqueous solution of the azide-modified ELR (component 1) with an equivolume aqueous solution of the same ELR, but modified with cyclooctyne (component 2). Upon mixing, the ELRs undergo cross-linking via a Huisgen [2 + 3] cycloaddition, thus giving rise to hydrogel formation (Figure 1C).

SEM images of the cross-linked IK24 and H3AH3 ELR-based hydrogels are shown in Supporting Information File 1, Figure S7 and Figure 2, respectively. The high magnification image reveals the existence of a fibrillar morphology. It is known that ELRs undergo hierarchical self-assembly producing a fibrillar structure [27,30,47]. For example, poly(VPGVG) and its analog poly [f_v(VPGVG), f_x(VPGKG)] ($0.1 \leq f_x \leq 0.2$, $f_v + f_x = 1$) interact hydrophobically and self-assemble into nanofilaments that align in parallel, forming fibrillar structure of several hundred nanometres in diameter [47]. Thus, the SEM micro-

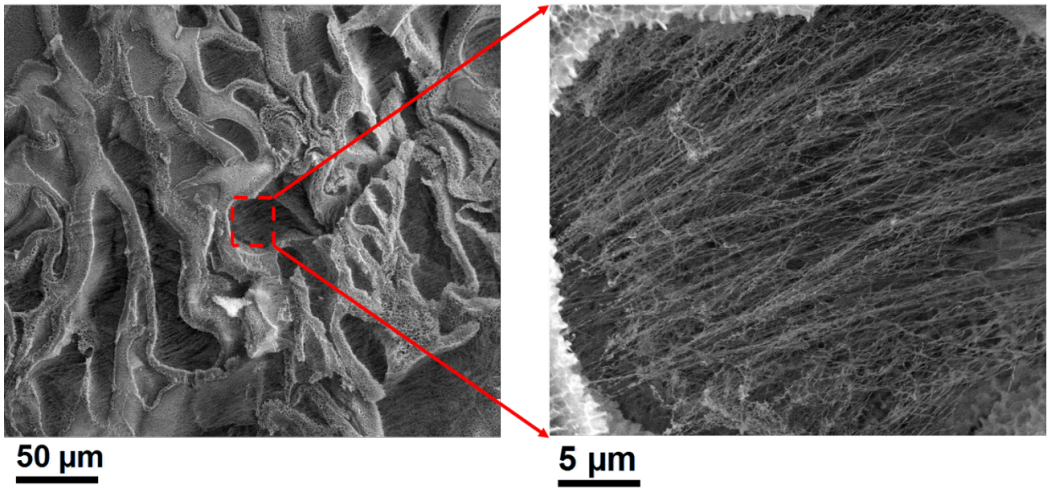

Figure 2: H3AH3 ELR hydrogel morphology observed by SEM. A high magnification image of the red framed area is shown in the micrograph on the right.

graphs (Figure 2 and Supporting Information File 1, Figure S7) clearly show that the chains after cross-linking inside the IK24 and H3AH3 hydrogels are composed of thin, rather homogeneous, fibres that often appear to have some order or, at least, a somewhat parallel organization. This fibrillar structure resembles that of physical elastin-based hydrogels and natural elastin [27,30].

Calcium phosphate mineralization

The solid-state structure of the precipitates obtained from the mineralization reaction was investigated by XRD. Figure 3A shows the XRD patterns obtained from the IK24 ELR-based hydrogel (no SN_A15 domain) after different incubation times. Due to the large fraction of organic matter and the generally rather low order of many CPs, all patterns are rather noisy; this is consistent with the literature [14,48]. After 4 days of mineralization (two days in calcium chloride followed by two days in potassium phosphate solution), the diffraction patterns show reflections at 27.47, 28.43, 29.73, 31.08, 36.14, 37.89, 40.61, 43.45, 50.28, 55.28, and 58.81° 2θ. After 8 days of mineralization, and using the same alternating immersion process, new reflections at 26.05, 31.31, 31.74, 32.20, 49.37, and 53.46° 2θ emerge. After 14 days of mineralization, XRD patterns assigned to the typical pattern of HA (JCPDS 01-072-1243) are found.

Figure 3B shows XRD patterns obtained from the hydrogel H3AH3 (with the SN_A15 domain). After 4 days of mineralization, two peaks at 30.14° and 31.55° 2θ are observed. After 8 days of mineralization, the collected pattern is similar to that obtained for the hydrogel lacking the SN_A15 domain (IK24). After 14 days, XRD indicates the presence of HA (JCPDS 01-072-1243). The broad and rather non-descript signals that

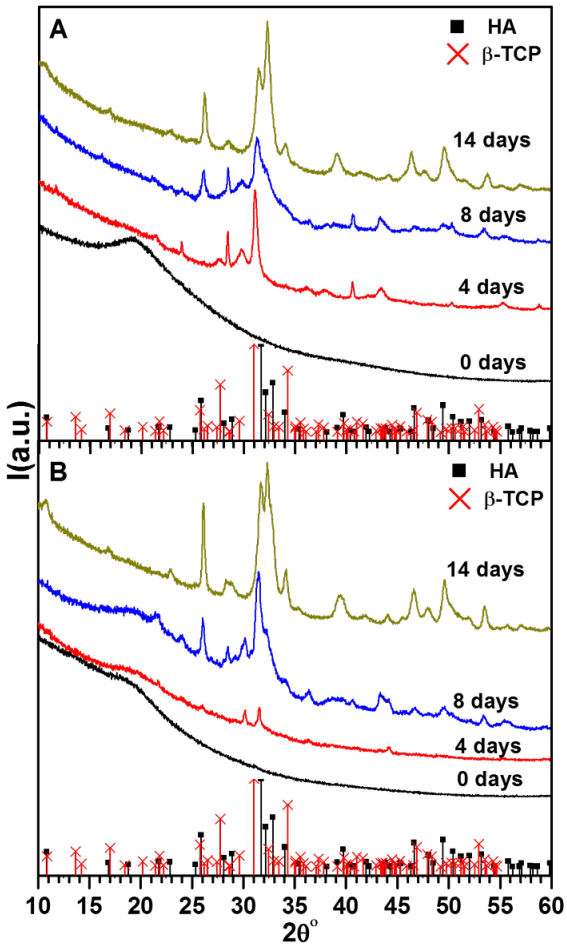

Figure 3: XRD patterns of mineralization products. (A) IK24 hydrogel, and (B) H3AH3 hydrogel after different incubation times. The XRD patterns of HA and β-TCP (bars) have been included for comparison.

are also observed in many samples are presumably due to the presence of the ELR gel phase, which is still present in these materials.

Figure 4 shows the IR spectra of the IK24- and H3AH3-based hydrogels, with the bands at around 1628, 1518, and 1233 cm^{-1} being attributed to amide I (C=O stretching), amide II (mainly C–N stretching), and amide III (N–H in plane deformation) vibrations, respectively [49,50]. In addition, the bands at around 1333 and 1097 cm^{-1} are assigned to δ(CH) and N–$C_α$ vibrations, respectively. The signals between 1400 and 1500 cm^{-1} are attributed to CH_3 asymmetric bending, CH_2 scissoring, and COO^- symmetric stretching vibrations. The band at around 1018 cm^{-1} is assigned to nonstoichiometric apatites containing HPO_4^{2-} ions, whereas the shoulder at around 1084 cm^{-1} is assigned to the $ν_3(PO_4)^{3-}$ vibration in stoichiometric HA [51-53]. The band at around 881 cm^{-1} is assigned to HPO_4^{2-}, most likely due to the presence of DCPD. The bands at around 600 and 550 cm^{-1} are assigned to $ν_4(PO_4)^{3-}$ bending mode.

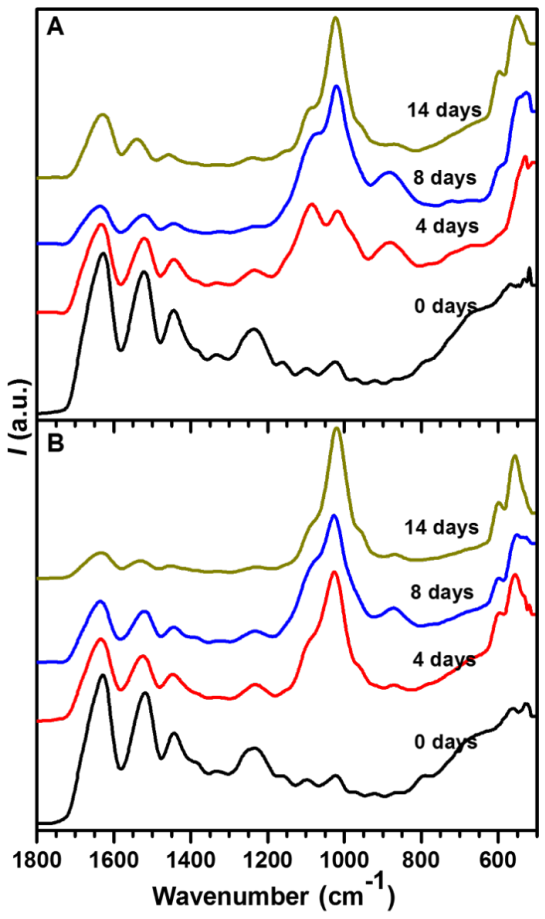

Figure 4: ATR-IR spectra of the mineralized hydrogels: (A) IK24 hydrogel, and (B) H3AH3 hydrogel after different incubation times.

Figure 5 shows the thermogravimetric analysis (TGA) curves obtained for the ELR hydrogels after mineralization and drying. The first weight loss (around 5–15%), which occurs at between around 80 and 150 °C is assigned to water evaporation. The weight loss in the range 250–450 °C can be attributed to ELR degradation and to further water loss from the CP mineral phase. The relative weight concomitant with this process allows an estimation of the final relative CP content in the hydrogels as a function of mineralization time. At 4 days, the relative weight is about 29% and 36% for IK24 and H3AH3 hydrogels, respectively, whereas after 14 days it is about 53% for both ELR hydrogels. This is in contrast to the pure hydrogels before mineralization, which lose 90% of their initial weight up to 1000 °C. The remnant 10% of the pure hydrogel are all decomposed when they are subjected to an isothermal process at 1000 °C. As such, there is no significant difference between the IK24- and H3AH3-based hydrogels.

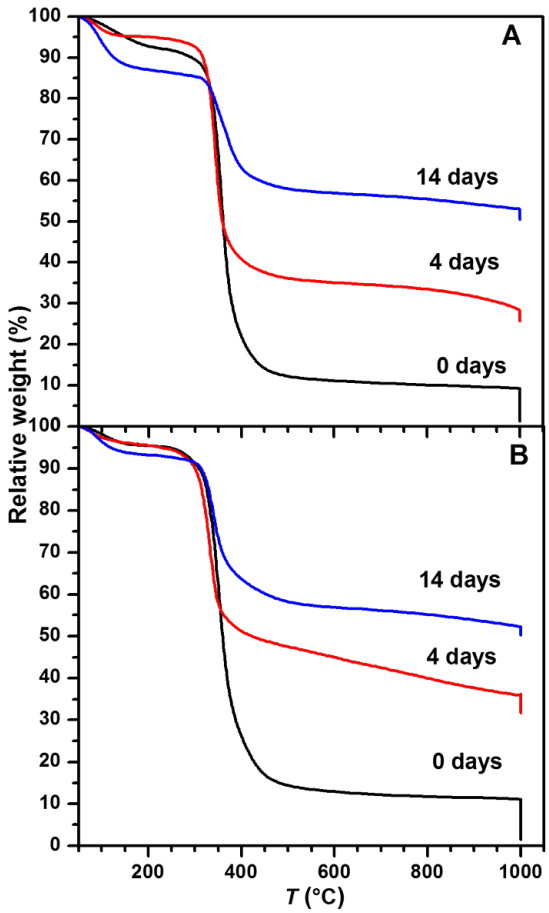

Figure 5: TGA curves for (A) IK24 hydrogels mineralized for 0, 4, and 14 days, respectively, and (B) H3AH3 hydrogels mineralized for 0, 4, and 14 days, respectively.

Figure 6 shows scanning electron micrographs of CP formed within the hydrogels after different mineralization times. After

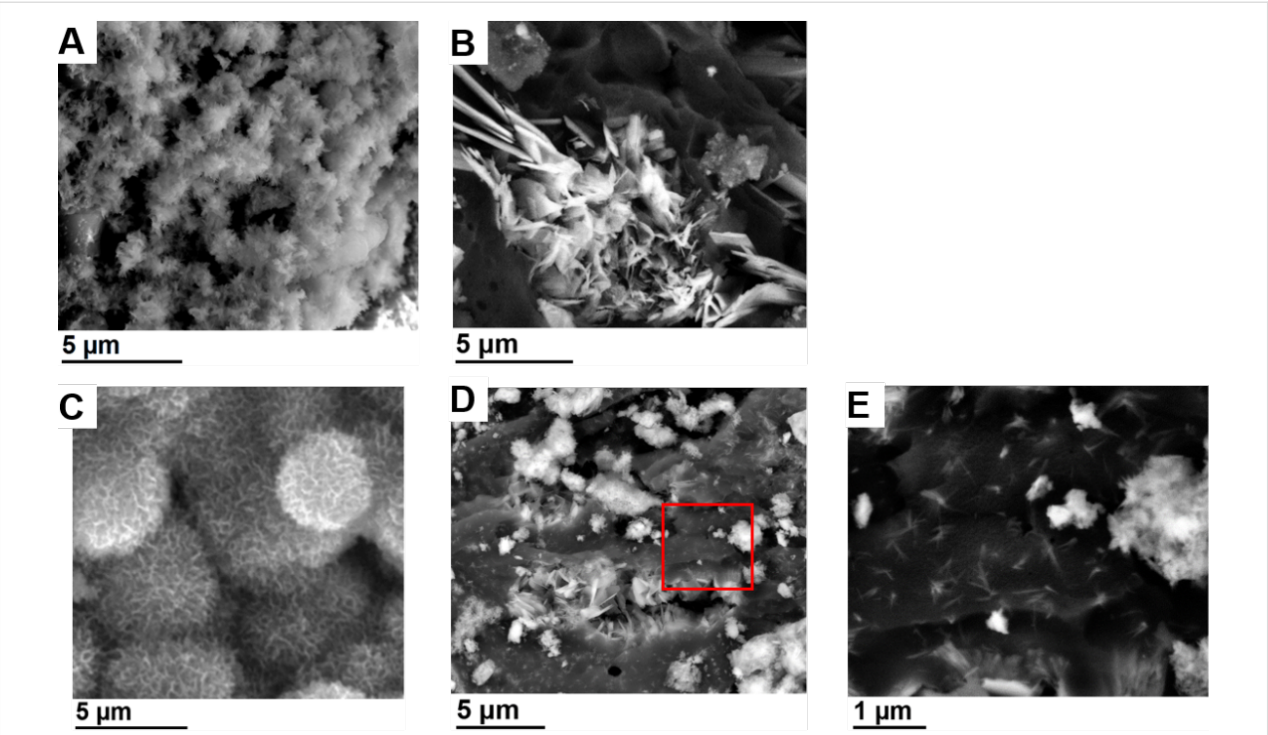

Figure 6: SEM images of the hydrogels after mineralization: (A) IK24 and (B) H3AH3 hydrogels after 4 days of mineralization. (C) IK24 hydrogel after 14 days of mineralization. (D) H3AH3 hydrogels after 14 days of mineralization. (E) High magnification SEM micrograph of the red framed region in D.

4 days of mineralization, IK24-based hydrogels exhibit a spherical structure somewhat resembling a microscale cauliflower morphology (Figure 6A). When the mineralization time increases, the morphology remains the same, but the features increase in size. After 4 days, the individual "cauliflower" is on the order of 1–3 µm, whereas after 14 days their diameter is around 4–8 µm (Figure 6C) and they densely populate the entire material. In the case of the H3AH3 hydrogels, a plate-like morphology is formed after incubation for 4 days (Figure 6B). In addition to the spherical aggregates (Figure 6D and Supporting Information File 1, Figure S8A) generated by the H3AH3-based hydrogels after incubation for 14 days, the calcium phosphate also forms plates (Figure 6D, and Supporting Information File 1, Figure S8B) with lengths of around 1–5 µm. Figure 6E shows, at high magnification, the dispersed plates-like HA that are embedded into the ELR hydrogel matrix and distributed over the entire material, which could result from the interaction of calcium and phosphate ions with SN_A15. These plates are intertwined and strongly clustered (Supporting Information File 1, Figure S8B). As a result, it is difficult to quantify their sizes in detail. As many of these aggregates appear to grow from a central point, they have a petal-like morphology that is clearly different from the previous spherical cauliflower-type precipitates. As such, different morphologies (plate-like and spherical-like structures) are simultaneously generated in the H3AH3 hydrogels.

Energy-dispersive X-ray spectroscopy (EDXS, Supporting Information File 1, Table S1) shows that all samples contain Ca, P, C, O, and also K and Cl impurities from the initial reagents ($CaCl_2$ and K_2HPO_4). In the case of IK24, the Ca/P ratio increases from 1.17 to 1.52 as the incubation time increases from 4 to 14 days. In the case of the H3AH3 hydrogel, the Ca/P ratio also increases from 1.12 to 1.78 as the incubation time increases from 4 to 14 days. Overall, the EDXS data show an increase in the Ca/P ratio with increasing reaction time, irrespective of the type of hydrogel used for mineralization.

Discussion

The combination of two or more materials can give rise to the formation of a multifunctional hybrid system with properties superior to those of each component separately. This combination depends on both the properties of each component and on the way in which they are assembled so that they can work cooperatively. Recombinant DNA technology allows the overall architecture of recombinamers to be controlled, thus making recombinant proteins interesting for a variety of reasons [22]. Among others, their behavior in aqueous media can be adjusted by appropriate design of the amino acid sequence, addition of bioactive domains – e.g., SN_A15 – and by the solution composition. For example, temperature changes are an efficient means of self-assembling and disassembling ELPs and ELRs [27,29]. Recently, the self-assembly properties of ELRs have been

combined with the mineralization capacity of SN_A15 using such a biotechnology approach [13]. In that study, Misbah et al. demonstrated that ELRs cannot control the formation of CP in the absence of SN_A15. In addition, the self-assembly properties of ELRs have a marked influence on the mineralization activity of SN_A15. These complementary functionalities give rise to the formation of fibre- or petal-like HA, in addition to amorphous CP with a neuron-like morphology.

In the ELRs used in this current work (IK24 and H3AH3), the lysine amino acids are distributed in a regular manner along the recombinamer chains. In addition, the nucleating SN_A15 domains in H3AH3 are also distributed along the recombinamer chain, thus giving rise to the formation of hybrid elastin-like statherin recombinamers. The IK24 and H3AH3 chains are cross-linked via the Huisgen [2 + 3] cycloaddition to form a hydrogel matrix containing well-defined calcium phosphate binding domains. The success of this cycloaddition reaction with ELRs is mainly dependent on the success of the recombinant DNA technology used to distribute the lysine amino acid residues along the ELR chain in a regular manner. These lysine amino acid residues are easily modified with cyclooctyne and azide groups (Figure 1, Supporting Information File 1, Figures S1–S6). Moreover, the cross-linking reaction is easily performed in water, which is an important condition for biomedical applications as it avoids problems with toxic reagents.

XRD provides two significant results, indicating that the ELR-based hydrogels affect the CP mineralization process. The first one is the phase-incubation time dependence. After mineralization for 4 days, the peaks observed at 29.73, 31.08, 36.14, 37.89, and 50.28° 2θ can be assigned to β-TCP phase (JCPDS 01-070-2065). β-TCP is normally synthesized at high temperature, although there are a few examples of β-TCP formation under milder conditions. For example, β-TCP can be synthesized at room temperature in methanol from $CaHPO_4$ and ACP precursor phases [54], or in ethylene glycol [55]. Two studies using aqueous solutions also reported the formation of β-TCP. CP nanoparticles prepared in the presence of Aliquat 336 also seem to consist of β-TCP, at least partly [56]. Poly(acrylic acid) hydrogels immersed in a phosphate solution were also calcified by β-TCP [57]. However, the other intense XRD peaks assigned to β-TCP at 32.42 and 34.33° 2θ are not observed. Moreover, the IR band at around 881 cm^{-1} assigned to HPO_4^{2-} [41,58] suggests the presence of DCPD. Since the Ca/P ratio calculated by EDX is around 1.1 for both hydrogels after mineralization for 4 days, DCPD formation cannot be ruled out [14,48]. In order to clarify this point, other mineralization conditions and characterization techniques are being studied. With increasing the incubation time to 8 days, new reflections at 26.05, 31.31, 31.74, 32.20, 49.37, and 53.46° 2θ indicate the HA formation (JCPDS 01-072-1243). Therefore, the mineralization is kinetically driven where a transient phase β-TCP is formed and eventually transformed into HA. It is worthwhile mentioning that CP precipitation in collagen matrices is also kinetically driven, with transient precursors such as ACP, octacalcium phosphate (OCP), and even TCP [5-7].

The second observation is the SN_A15-functionality dependence, where the CP phases formed after 4 days of incubation show clear difference between the two hydrogels (see XRD patterns in Figure 3). The CP phase shows stronger reflections in the case of the IK24 hydrogel than in the H3AH3 hydrogel (functionalized with SN_A15), suggesting that SN_A15 inhibits the spontaneous transformation of ACP into the crystalline phase. This behavior may be related to the CP morphologies generated by this family of ELRs at soluble state. In a previous study [13], the building block H3 [$(IK)_2$-SN_A15-$(IK)_2$] inhibits the transformation of ACP into the crystalline phase in solution, thus giving rise to the formation of a neuron-like morphology. In the confined state (IK24 and H3AH3 hydrogels in the current work) this effect seems to be observed after incubation for 4 days, with formation of the HA phase being supressed and other CP phases being generated. Nevertheless, after incubation for 14 days the CP formed gives rise to the formation of spherical- or petal-like HA. Moreover, not only the phases and morphologies of the CP can be controlled, but also the mineral content. According to Figure 5, after 4 days, mineralized hydrogel matrices with poorly crystalline CP show a mineral content of about 29% and 36% for IK24 and H3AH3 hydrogels, respectively. After 14 days, mineralized hydrogel matrices with HA of different morphologies and high mineral content (about 53%) are achieved for both hydrogels.

The present work shows the merit of using the in situ-inhibition CP approach, where SN_A15 moieties are regularly distributed along the hydrogel matrix for controlling the CP mineralization process. The combination of the self-assembly properties of ELRs with the mineralization capacities of SN_A15 gives rise to the formation of plate-like HA, different from the spherical cauliflower morphology formed by IK24. Surprisingly, the ELR H3AH3 at the insoluble state controls the formation of the plate-like of crystalline CP phase (HA), whereas its building block H3 controls the formation of neuron-like morphology of ACP phase at the soluble state [13].

The approach used in this work, which avoids the need for substances that may harm the human body (methanol, ethylene glycol, surfactants) [54-56], shows the merit of controlling the generation of hybrid materials for potential biomedical applications. At the same time, these materials, at the insoluble state,

have the ability to control the formation of CP in terms of both phase and morphology, different from the ones formed at the soluble state.

Conclusion

The present work shows the merit of using the in situ-inhibition CP approach, via the hybrid elastin-like-SN_A15 recombinamer hydrogel matrix. This merit depends on the combination of ELRs properties with the CP binding capacities of SN_A15, and on the integration of two synthesis approaches (recombinant DNA and click chemistry) to form advanced biocompatible soft and hybrid materials. Recombinant DNA technology allows the distribution of lysine amino acids and the SN_A15 domains along the recombinamer chain to be carefully controlled. Cyclooctyne and azide groups can then be introduced successfully by functionalizing these lysine groups. The resulting functional groups are easily cross-linked via click chemistry in an aqueous medium to form a hydrogel matrix. This hydrogel matrix has a marked impact on the mineralization of calcium phosphates. In absence of the SN_A15 nucleation inhibitor, cauliflower-like HA is formed. In contrast, plate-like HA grows in the presence of SN_A15. The soluble state of the ELRs shows the merit of generating delicate nanostructures, such as neuron-like morphology [13]. Yet, their soluble nature could restrict their applications for tissue engineering as compared to its hydrogel state. When hydrogel matrices are used, different HA morphologies are obtained after incubation for 14 days (spherical or plate-like) that are not easy to obtain in the soluble state.

In conclusion, the combination between recombinant DNA and click reaction approaches has resulted in the generation of well-programmable and controlled ELR hydrogels to regulate the formation of calcium phosphate nanostructures.

Supporting Information

Supporting Information File 1

MALDI-TOF spectra, NMR spectra, ATR-IR spectra, SEM micrographs, EDXS analysis are presented.
[http://www.beilstein-journals.org/bjnano/content/supplementary/2190-4286-8-80-S1.pdf]

Acknowledgements

We thank D. Hentrich (University of Potsdam) for useful discussion. The authors are grateful for funding from the European Commission (NMP-2014-646075, HEALTH-F4-2011-278557, PITN-GA-2012-317306 and MSCA-ITN-2014-642687), the MINECO of the Spanish Government (MAT2013-42473-R and MAT2013-41723-R) and the Junta de Castilla y León (VA244U13, VA313U14 and GRS/516/A/10), Spain. The Deutsche Forschungsgemeinschaft (DFG, TA571/11-1), and the University of Potsdam are thanked for financial support.

References

1. Cobo, I.; Li, M.; Sumerlin, B. S.; Perrier, S. *Nat. Mater.* **2015,** *14,* 143–159. doi:10.1038/nmat4106
2. Murugan, R.; Ramakrishna, S. *Compos. Sci. Technol.* **2005,** *65,* 2385–2406. doi:10.1016/j.compscitech.2005.07.022
3. Abdel-Fattah, W. I.; Elkhooly, T. A. *Biomed. Mater.* **2010,** *5,* 035015. doi:10.1088/1748-6041/5/3/035015
4. Reznikov, N.; Shahar, R.; Weiner, S. *Acta Biomater.* **2014,** *10,* 3815–3826. doi:10.1016/j.actbio.2014.05.024
5. Jiao, K.; Niu, L.-N.; Ma, C.-F.; Huang, X.-Q.; Pei, D.-D.; Luo, T.; Huang, Q.; Chen, J.-H.; Tay, F. R. *Adv. Funct. Mater.* **2016,** *26,* 6858–6875. doi:10.1002/adfm.201602207
6. Nudelman, F.; Lausch, A. J.; Sommerdijk, N. A. J. M.; Sone, E. D. *J. Struct. Biol.* **2013,** *183,* 258–269. doi:10.1016/j.jsb.2013.04.003
7. Olszta, M. J.; Cheng, X.; Jee, S. S.; Kumar, R.; Kim, Y.-Y.; Kaufman, M. J.; Douglas, E. P.; Gower, L. B. *Mater. Sci. Eng., R* **2007,** *58,* 77–116. doi:10.1016/j.mser.2007.05.001
8. Dorozhkin, S. V. *Acta Biomater.* **2012,** *8,* 963–977. doi:10.1016/j.actbio.2011.09.003
9. Sadat-Shojai, M.; Khorasani, M.-T.; Dinpanah-Khoshdargi, E.; Jamshidi, A. *Acta Biomater.* **2013,** *9,* 7591–7621. doi:10.1016/j.actbio.2013.04.012
10. Shi, Z.; Huang, X.; Cai, Y.; Tang, R.; Yang, D. *Acta Biomater.* **2009,** *5,* 338–345. doi:10.1016/j.actbio.2008.07.023
11. Lin, K.; Wu, C.; Chang, J. *Acta Biomater.* **2014,** *10,* 4071–4102. doi:10.1016/j.actbio.2014.06.017
12. Lin, K.; Liu, P.; Wei, L.; Zou, Z.; Zhang, W.; Qian, Y.; Shen, Y.; Chang, J. *Chem. Eng. J.* **2013,** *222,* 49–59. doi:10.1016/j.cej.2013.02.037
13. Misbah, M. H.; Espanol, M.; Quintanilla, L.; Ginebra, M. P.; Rodríguez-Cabello, J. C. *RSC Adv.* **2016,** *6,* 31225–31234. doi:10.1039/C6RA01100D
14. Bleek, K.; Taubert, A. *Acta Biomater.* **2013,** *9,* 6283–6321. doi:10.1016/j.actbio.2012.12.027
15. Song, R.-Q.; Cölfen, H. *CrystEngComm* **2011,** *13,* 1249–1276. doi:10.1039/c0ce00419g
16. Hentrich, D.; Junginger, M.; Bruns, M.; Börner, H. G.; Brandt, J.; Brezesinski, G.; Taubert, A. *CrystEngComm* **2015,** *17,* 6901–6913. doi:10.1039/C4CE02274B
17. Tarasevich, B. J.; Chusuei, C. C.; Allara, D. L. *J. Phys. Chem. B* **2003,** *107,* 10367–10377. doi:10.1021/jp027445p
18. Phadke, A.; Zhang, C.; Hwang, Y.; Vecchio, K.; Varghese, S. *Biomacromolecules* **2010,** *11,* 2060–2068. doi:10.1021/bm100425p
19. Cha, C.; Kim, E.-S.; Kim, I. W.; Kong, H. *Biomaterials* **2011,** *32,* 2695–2703. doi:10.1016/j.biomaterials.2010.12.038
20. Roveri, N.; Falini, G.; Sidoti, M. C.; Tampieri, A.; Landi, E.; Sandri, M.; Parma, B. *Mat. Sci. Eng. C* **2003,** *23,* 441–446. doi:10.1016/S0928-4931(02)00318-1
21. Li, Y.; Chen, X.; Fok, A.; Rodriguez-Cabello, J. C.; Aparicio, C. *ACS Appl. Mater. Interfaces* **2015,** *7,* 25784–25792. doi:10.1021/acsami.5b07628

22. Rodríguez-Cabello, J. C.; Pierna, M.; Fernández-Colino, A.; García-Arévalo, C.; Arias, F. J. Recombinamers: combining molecular complexity with diverse bioactivities for advanced biomedical and biotechnological applications. In *Biofunctionalization of Polymers and their Applications;* Nyanhongo, G. S.; Steiner, W.; Gübitz, G., Eds.; Advances in Biochemical Engineering / Biotechnology, Vol. 125; Springer: Berlin, Germany, 2011; pp 145–179. doi:10.1007/10_2010_94
23. Girotti, A.; Orbanic, D.; Ibáñez-Fonseca, A.; Gonzalez-Obeso, C.; Rodríguez-Cabello, J. C. *Adv. Healthcare Mater.* **2015,** *4,* 2423–2455. doi:10.1002/adhm.201500152
24. Xi, W.; Scott, T. F.; Kloxin, C. J.; Bowman, C. N. *Adv. Funct. Mater.* **2014,** *24,* 2572–2590. doi:10.1002/adfm.201302847
25. González de Torre, I.; Santos, M.; Quintanilla, L.; Testera, A.; Alonso, M.; Rodríguez Cabello, J. C. *Acta Biomater.* **2014,** *10,* 2495–2505. doi:10.1016/j.actbio.2014.02.006
26. Tasdelen, M. A.; Kiskan, B.; Yagci, Y. *Prog. Polym. Sci.* **2016,** *52,* 19–78. doi:10.1016/j.progpolymsci.2015.09.003
27. Misbah, M. H.; Quintanilla, L.; Alonso, M.; Rodríguez-Cabello, J. C. *Polymer* **2015,** *81,* 37–44. doi:10.1016/j.polymer.2015.11.013
28. Roberts, S.; Dzuricky, M.; Chilkoti, A. *FEBS Lett.* **2015,** *589,* 2477–2486. doi:10.1016/j.febslet.2015.08.029
29. Urry, D. W. *J. Phys. Chem. B* **1997,** *101,* 11007–11028. doi:10.1021/jp972167t
30. Muiznieks, L. D.; Keeley, F. W. *Biochim. Biophys. Acta, Mol. Basis Dis.* **2013,** *1832,* 866–875. doi:10.1016/j.bbadis.2012.11.022
31. Prieto, S.; Shkilnyy, A.; Rumplasch, C.; Ribeiro, A.; Arias, F. J.; Rodríguez-Cabello, J. C.; Taubert, A. *Biomacromolecules* **2011,** *12,* 1480–1486. doi:10.1021/bm200287c
32. Li, Y.; Chen, X.; Ribeiro, A. J.; Jensen, E. D.; Holmberg, K. V.; Rodriguez-Cabello, J. C.; Aparicio, C. *Adv. Healthcare Mater.* **2014,** *3,* 1638–1647. doi:10.1002/adhm.201400015
33. Tejeda-Montes, E.; Smith, K. H.; Rebollo, E.; Gómez, R.; Alonso, M.; Rodriguez-Cabello, J. C.; Engel, E.; Mata, A. *Acta Biomater.* **2014,** *10,* 134–141. doi:10.1016/j.actbio.2013.09.001
34. Tejeda-Montes, E.; Klymov, A.; Nejadnik, M. R.; Alonso, M.; Rodriguez-Cabello, J. C.; Walboomers, X. F.; Mata, A. *Biomaterials* **2014,** *35,* 8339–8347. doi:10.1016/j.biomaterials.2014.05.095
35. Rodríguez-Cabello, J. C.; Girotti, A.; Ribeiro, A.; Arias, F. J. Synthesis of Genetically Engineered Protein Polymers (Recombinamers) as an Example of Advanced Self-Assembled Smart Materials. In *Nanotechnology in Regenerative Medicine;* Navarro, M.; Planell, J. A., Eds.; Methods in Molecular Biology, Vol. 811; Springer: Berlin, Germany, 2012; pp 17–38. doi:10.1007/978-1-61779-388-2_2
36. Raj, P. A.; Johnsson, M.; Levine, M. J.; Nancollas, G. H. *J. Biol. Chem.* **1992,** *267,* 5968–5976.
37. Schwartz, S. S.; Hay, D. I.; Schluckebier, S. K. *Calcif. Tissue Int.* **1992,** *50,* 511–517. doi:10.1007/BF00582164
38. Lundquist, J. T., IV; Pelletier, J. C. *Org. Lett.* **2001,** *3,* 781–783. doi:10.1021/ol0155485
39. García-Arévalo, C.; Pierna, M.; Girotti, A.; Arias, F. J.; Rodríguez-Cabello, J. C. *Soft Matter* **2012,** *8,* 3239–3249. doi:10.1039/c2sm06893a
40. Izawa, H.; Nishino, S.; Maeda, H.; Morita, K.; Ifuku, S.; Morimoto, M.; Saimoto, H.; Kadokawa, J.-i. *Carbohydr. Polym.* **2014,** *102,* 846–851. doi:10.1016/j.carbpol.2013.10.080
41. Abdel-Fattah, W. I.; Reicha, F. M.; Elkhooly, T. A. *Biomed. Mater.* **2008,** *3,* 034121. doi:10.1088/1748-6041/3/3/034121
42. Hutchens, S. A.; Benson, R. S.; Evans, B. R.; O'Neill, H. M.; Rawn, C. J. *Biomaterials* **2006,** *27,* 4661–4670. doi:10.1016/j.biomaterials.2006.04.032
43. Sinha, A.; Guha, A. *Mat. Sci. Eng. C* **2009,** *29,* 1330–1333. doi:10.1016/j.msec.2008.10.024
44. Yokoi, T.; Kawashita, M.; Ohtsuki, C. *J. Asian Ceram. Soc.* **2013,** *1,* 155–162. doi:10.1016/j.jascer.2013.04.003
45. Gottlieb, H. E.; Kotlyar, V.; Nudelman, A. *J. Org. Chem.* **1997,** *62,* 7512–7515. doi:10.1021/jo971176v
46. Lummerstorfer, T.; Hoffmann, H. *J. Phys. Chem. B* **2004,** *108,* 3963–3966. doi:10.1021/jp049601t
47. Urry, D. W.; Okamoto, K.; Harris, R. D.; Hendrix, C. F.; Long, M. M. *Biochemistry* **1976,** *15,* 4083–4089. doi:10.1021/bi00663a026
48. Schweizer, S.; Taubert, A. *Macromol. Biosci.* **2007,** *7,* 1085–1099. doi:10.1002/mabi.200600283
49. Barth, A. *Biochim. Biophys. Acta, Bioenerg.* **2007,** *1767,* 1073–1101. doi:10.1016/j.bbabio.2007.06.004
50. Kong, J.; Yu, S. *Acta Biochim. Biophys. Sin.* **2007,** *39,* 549–559. doi:10.1111/j.1745-7270.2007.00320.x
51. Koutsopoulos, S. *J. Biomed. Mater. Res.* **2002,** *62,* 600–612. doi:10.1002/jbm.10280
52. Garskaite, E.; Gross, K.-A.; Yang, S.-W.; Yang, T. C.-K.; Yang, J.-C.; Kareiva, A. *CrystEngComm* **2014,** *16,* 3950–3959. doi:10.1039/c4ce00119b
53. Gadaleta, S. J.; Paschalis, E. P.; Betts, F.; Mendelsohn, R.; Boskey, A. L. *Calcif. Tissue Int.* **1996,** *58,* 9–16. doi:10.1007/BF02509540
54. Bow, J.-S.; Liou, S.-C.; Chen, S.-Y. *Biomaterials* **2004,** *25,* 3155–3161. doi:10.1016/j.biomaterials.2003.10.046
55. Tao, J.; Pan, H.; Zhai, H.; Wang, J.; Li, L.; Wu, J.; Jiang, W.; Xu, X.; Tang, R. *Cryst. Growth Des.* **2009,** *9,* 3154–3160. doi:10.1021/cg801130w
56. Singh, S.; Bhardwaj, P.; Singh, V.; Aggarwal, S.; Mandal, U. K. *J. Colloid Interface Sci.* **2008,** *319,* 322–329. doi:10.1016/j.jcis.2007.09.059
57. Furuichi, K.; Oaki, Y.; Ichimiya, H.; Komotori, J.; Imai, H. *Sci. Technol. Adv. Mater.* **2006,** *7,* 219–225. doi:10.1016/j.stam.2005.10.008
58. Victoria, E. C.; Gnanam, F. *Trends Biomater. Artif. Organs* **2002,** *16,* 12–14.

License and Terms

BEILSTEIN JOURNAL OF NANOTECHNOLOGY

The role of 2D/3D spin-polarization interactions in hybrid copper hydroxide acetate: new insights from first-principles molecular dynamics

Ziyad Chaker, Guido Ori*, Mauro Boero and Carlo Massobrio

Letter

Open Access

Address:
Université de Strasbourg, CNRS, Institut de Physique et Chimie des Matériaux de Strasbourg, UMR 7504, F-67034 Strasbourg, France

Email:
Guido Ori* - guido.ori@ipcms.unistra.fr

* Corresponding author

Keywords:
first-principles molecular dynamics; hybrid material; magnetic properties; pressure; spin polarization

Beilstein J. Nanotechnol. **2017,** *8,* 857–860.
doi:10.3762/bjnano.8.86

Received: 19 September 2016
Accepted: 23 March 2017
Published: 12 April 2017

This article is part of the Thematic Series "Hybrid nanomaterials: from the laboratory to the market".

Guest Editor: A. Taubert

Abstract

The magnetic properties response of the layered hybrid material copper hydroxide acetate $Cu_2(OH)_3CH_3COO{\cdot}H_2O$ is studied as a function of the applied pressure within first-principles molecular dynamics. We are able to elucidate the interplay between the structural properties of this material and its magnetic character, both at the local (atomic) level and at the bulk level. We performed a detailed analysis of the intralayer spin configurations occurring for each value of the imposed projection along the *z*-axis for the total spin and of the applied pressure. The transition from an antiferromagnetic to a ferromagnetic state at high pressure (above 3 GPa) goes along with a vanishing difference between the spin polarizations pertaining to each layer. Therefore, at high pressure, copper hydroxide acetate is a ferromagnet with no changes of spin polarization in the direction perpendicular to the inorganic layers.

Introduction

Copper hydroxide acetate $Cu_2(OH)_3CH_3COO{\cdot}H_2O$ (CuOHAc) is the precursor of a whole class of hybrid organic–inorganic materials that are made of inorganic sheets separated by alkyl chains (such as alkyl sulfates and carboxylates) or conjugated molecules (such as fluorene phosphonates) [1-3]. The interest in $Cu_2(OH)_3X$ systems stems from their tunable magnetic properties, strongly dependent on the nature of the organic ligands. Based on experimental evidence, CuOHAc exhibits (when seen as a bulk material) 3D antiferromagnetic (AF) interlayer character and (within each layer) a weak ferromagnetic (F) intralayer (2D) character. The use of pressure is a valuable and practical tool to tune the magnetic behavior of this lamellar hybrid material [4]. In our previous studies, first-principles molecular dynamics (FPMD) approaches combined with density functional theory (DFT) have been useful to complement the missing structural information on the atomic positions obtained

experimentally [5]. We also provided an exploratory insight into CuOHAc bonding and magnetic properties changes in response to an applied external pressure [6,7]. Recently, Banerjee et al. [8,9] with a similar approach by means of first-principles calculations showed a cooperative spin-state transition upon application of pressure for a hybrid metal–organic framework perovskite. Both the transition pressure and the width of the hysteresis have found to be strongly dependent on the nature of the organic molecular component.

Motivated by an updated set of the atomic coordinates for CuOHAc, recently proposed on the basis of a single-crystal X-ray experiment [10], we refine here the study of the effect of pressure on the structural and 2D/3D magnetic character of CuOHAc. With respect to previous theoretical studies, we consider a supercell four times larger and a wider range of pressures (0–17 GPa) as well as magnetization states for three different values of the spin multiplicities. Overall, this novel set of calculations allowed us to achieve a better agreement with the experimental findings in terms of the AF-to-F transition pressure. We also elucidate in greater detail the role of spin polarization in driving the AF-to-F transition, thereby making available an atomic-scale rationale for the change of magnetic nature.

Computational Methods

We employ a first-principles molecular dynamics (FPMD) approach in the framework of Kohn–Sham density functional theory (DFT) with a generalized gradient approximation according to Becke [11] for the exchange energy and according to Lee, Yang and Parr [12] (BLYP) for the correlation functional. The valence electrons are treated explicitly, whereas norm-conserving pseudo-potentials generated following the scheme of Trouiller and Martin [13] are used to account for the core–valence interaction. Nonlinear core corrections (NLCC) are used for Cu atoms according to the prescription of Louie and co-workers [14]. The present calculations are performed on a system made of 288 atoms (32 Cu, 96 O, 32 C, and 128 H) applying periodic boundary conditions. Such a supercell is the result of doubling the primitive cell of 72 atoms along the *x*- and *y*-directions. The original lattice parameters a = 5.5776 Å, b = 6.0733 Å, c = 18.5134 Å and β = 91.802°, and symmetry group $P2_1$ are those recently proposed by Svarcova and co-workers [10] based on a single-crystal X-ray diffraction study. The wave functions are expanded at the Γ point of the supercell in a plane-wave basis set with an energy cutoff of 90 Ry. Following our previous works [6,7], in order to produce a set of distinct electronic ground states differing in the local spin densities, we assigned different initial random values to the fictitious electronic degree of freedom. In particular, we performed 17 initial randomization per pressure and per magnetization state. More details about the procedure employed can be found in [5]. This procedure allows us to explore the multiple-minima landscape resulting from the existence of different spin configurations for a given value of the imposed multiplicity. Each multiplicity corresponds to a total value S for the projection along the z-direction of the total spin. In this way one obtains different local intralayer spin configurations and associated values Σ (Σ = 0 or Σ ≠ 0) corresponding to an identical multiplicity for the whole system. Herein, we consider both limiting cases of total spin multiplicity $2S + 1$ corresponding to values equal to 1 (S = 0) and 33 (S = 16) as well as one intermediate case such as 17 (S = 8). The spin density is defined as

$$\rho_s(x) = \rho_\alpha(x) - \rho_\beta(x) = \sum_i \left(\left|\psi_i^\alpha(x)\right|^2 - \left|\psi_i^\beta(x)\right|^2 \right),$$

where α and β indicate, respectively, the up- and down-spin components, and $\psi_i^{\alpha,\beta}(x)$ are the Kohn–Sham orbitals of the system. The systems under pressure are obtained by reducing the dimensions of the model on the three crystallographic directions. This has been done by following the experimental changes of the lattice parameters reported in [4]. For each system the pressure is then computed by fitting the total energy E of the system as a function of the volume V of the simulation cell following the definition $P_{ext} = dE/dV$.

Results and Discussion

Figure 1a shows the total energy of the systems as a function of their volume for three different magnetization states with total spin multiplicities equal to 1 (S = 0), 17 (S = 8), and 33 (S = 16). In the absence of any external pressure, the S = 0 configuration corresponds to the ground state. In particular, this configuration is approx. 0.1 eV and approx. 0.25 eV more stable than the systems with S = 8 and S = 16, respectively. This energy difference between the states S = 0, S = 8, and S = 16 reduces significantly with increasing the pressure. The configuration with S = 8 becomes more stable than the one with S = 0 for pressures of ca. 3 GPa (Figure 1b), in fair agreement with the experimental findings (ca. 1.2 GPa) [4].

Notably, the AF-to-F transition pressure is closer to the experimental value than the one found in previous theoretical investigations (ca. 7.5 GPa) [7]. From a structural point of view, upon compression both Cu–O and Cu–Cu interatomic distances decrease and Cu–O–Cu angles are affected in order to adjust to the compression, in line with what reported in our previous theoretical works [7].

We report in Figure 2 the 2D spin configuration as a function of the pressure. In particular, we analyze the spin distribution in

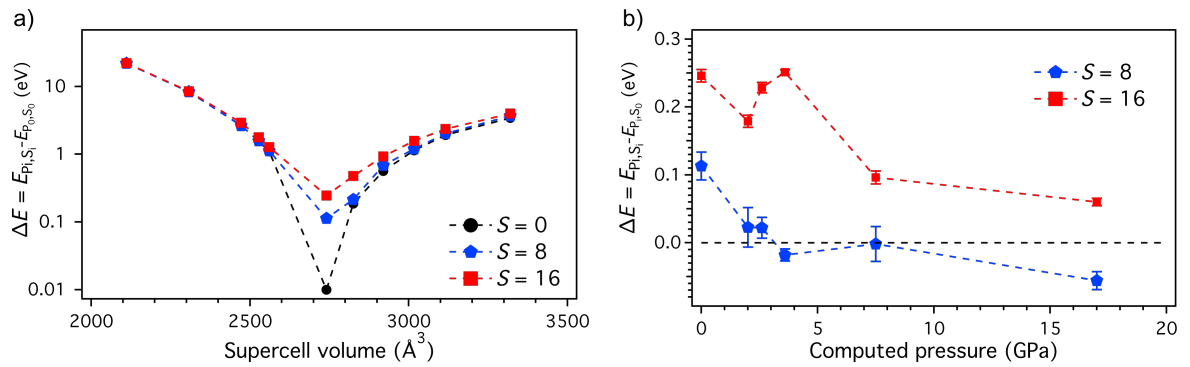

Figure 1: (a) Total energy of the simulated systems as a function of their volumes. We show the data for the three magnetization states: $S = 0$ in black circles, $S = 8$ in blue pentagons, and $S = 16$ in red squares. The data is normalized with respect to the energy of the ground state, found for the system with $S = 0$ at $P = 0$ GPa. (b) Relative stability of the systems with $S = 8$ and $S = 16$ shown in terms of total energy difference ($\Delta E_{P_i} = E_{P_i,S_i} - E_{P_i,S_0}$) with respect to the $S = 0$ state (black dashed line) as a function of the applied pressure.

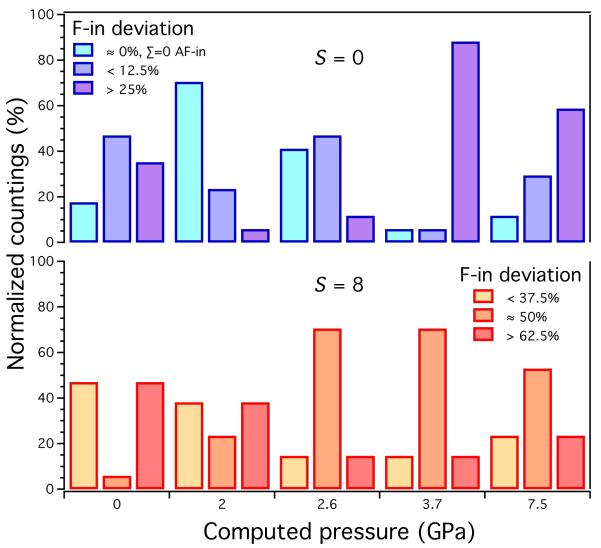

Figure 2: Distribution of the intralayer spin configurations for the systems with $S = 0$ (top) and $S = 8$ (bottom) as a function of pressure. For each pressure we split the spin distributions showing percentages of deviation with respect to the in-layer $\Sigma = 0$ case. For $S = 0$ we show deviations corresponding to one (i.e., 12.5%) and two or more (i.e., >25%) up(down)-spin of difference between the two layers. For $S = 8$ we show F-in corresponding to three or less (i.e., <37.5%), four (i.e., 50%), and five or more (i.e., >62.5%) up(down)-spin of difference between the two layers. Note that F-in deviation of 50% corresponds to an equal distribution between the two layers of the total spin for $S = 8$.

terms of the intralayer deviation (F-in) from the case $\Sigma = 0$. To this purpose the spin distributions are shown by highlighting the different values taken with respect to this reference value (i.e., 0%) and the maximally spin polarized layer case (i.e., 100% F-in). Typical examples of the obtained spin distributions are shown in Figure 3 for $S = 0$ and $S = 8$ at 0 GPa and 7.5 GPa. By looking at the partial populations with different F-in deviation, the following tendencies can be observed. For $S = 0$, the pressure induces a decrease of the spin distributions with $\Sigma = 0$ whereas the content of spin distributions with a large 2D spin polarization (F-in > 25%) increases significantly. Conversely, for $S = 8$, an opposite trend can be noticed, with a decrease of the 2D spin polarized distributions (F-in > 62.5%) with pressure and, simultaneously, an increase of the populations with a lower polarization (F-in = 50%).

Following the same scheme, by plotting the difference of interlayer spin $\Delta\Sigma^S_{l_1 l_2} = \Sigma^S_{l_1} - \Sigma^S_{l_2}$ we can estimate the degree of 3D spin polarization couplings of the system (Figure 4). For $S = 0$ the difference $\Delta\Sigma^S_{l_1 l_2}$ increases upon compression whereas for $S = 8$ the difference $\Delta\Sigma^S_{l_1 l_2}$ decreases. The cross-linking between these two trends, at about the AF-to-F transition pressure, suggests that the driving force to induce this transition is the tendency of the system to acquire equal values of finite spin polarization on each layer. Eventually, the most stable system under pressure features $S = 8$ as resulting from equal contributions of $S_1 = 4$ and $S_2 = 4$ on each layer. This spin configuration is the best suited to optimize the overall ferromagnetic character of this compound.

Conclusion

We show that in $Cu_2(OH)_3CH_3COO{\cdot}H_2O$ the net effect of an external pressure is to affect both the structural properties as well as the intra- and inter-layer magnetic interactions of the inorganic layers. The novel set of results reported in the present study allows us to estimate a AF-to-F transition pressure upon compression in better agreement with the experimental findings than the previously reported. We found that the driving force underlying the magnetic transition is the trend toward a uniform spin polarization across the layers, ensuring an overall optimal ferromagnetic character.

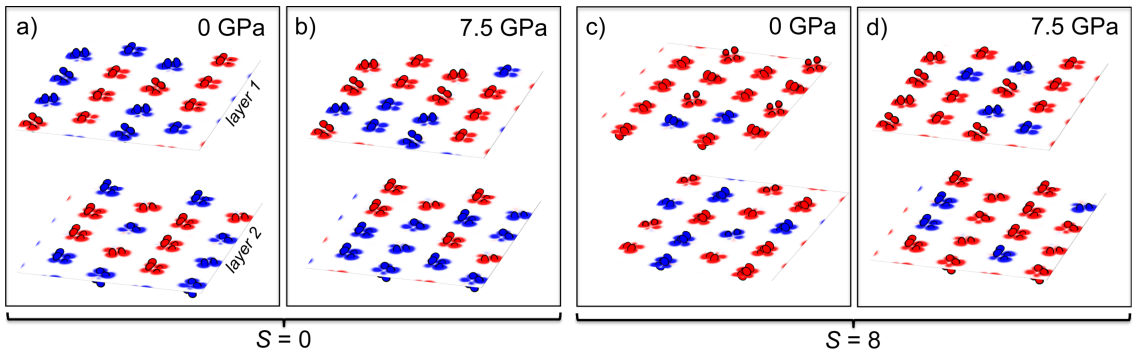

Figure 3: Volume-slice representations of the local spin configurations for the systems with $S = 0$ and $S = 8$ at pressure 0 GPa and 7.5 GPa. Volume slices centered along the two copper hydroxide planes per system, named layer 1 (L_1) and layer 2 (L_2). For each layer, the number of up- and down-spins are specified in the following: a) L_1: 8 (up-spin)-8 (down-spin); L_2: 8-8; b) L_1: 10-6; L_2: 6-10; c) L_1: 2-14; L_2: 6-10; d) L_1: 4-12; L_2: 4-12. These representations correspond to F-in deviations of ca. 0% (a) and >25% (b) for $S = 0$ and >62.5% (c) and ca. 50% (d) for $S = 8$, respectively.

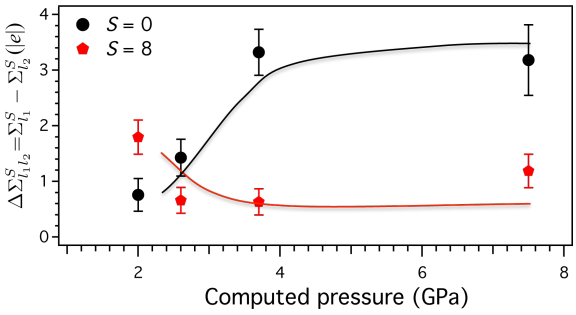

Figure 4: Difference of spin density between the two inorganic layers per system for $S = 0$ (black circles) and $S = 8$ (red pentagons) as a function of the pressure. Solid lines are guides to the eye.

Acknowledgements

We acknowledge computational facilities provided by HPC Equipe@MESO at the University of Strasbourg and the Idex Unistra program "Investissements d'Avenir" (2015–2016) managed by the French National Research Agency.

References

1. Rabu, P.; Drillon, M.; Agawa, K.; Fujita, W.; Sekine, T. Hybrid Organic-Inorganic Multilayer Compounds: Towards Controllable and/or Switchable Magnets. In *Magnetism: Molecules to Materials II: Models and Experiments;* Miller, J. S.; Drillon, M., Eds.; Wiley-VCH: Weinheim, Germany, 2001; pp 357–395. doi:10.1002/3527600590.ch11
2. Rogez, G.; Massobrio, C.; Rabu, P.; Drillon, M. *Chem. Soc. Rev.* **2011,** *40,* 1031–1058. doi:10.1039/c0cs00159g
3. Rabu, P.; Delahaye, E.; Rogez, G. *Nanotechnol. Rev.* **2015,** *4,* 557–580. doi:10.1515/ntrev-2015-0017
4. Suzuki, K.; Haines, J.; Rabu, P.; Inoue, K.; Drillon, M. *J. Phys. Chem. C* **2008,** *112,* 19147–19150. doi:10.1021/jp807636u
5. Yang, F.; Boero, M.; Massobrio, C. *J. Phys. Chem. C* **2010,** *114,* 20213–20219. doi:10.1021/jp1043249
6. Yang, F.; Boero, M.; Rabu, P.; Massobrio, C. *C. R. Chim.* **2012,** *15,* 202–208. doi:10.1016/j.crci.2011.09.007
7. Yang, F.; Massobrio, C.; Boero, M. *J. Phys. Chem. C* **2014,** *118,* 18700–18705. doi:10.1021/jp503489g
8. Banerjee, H.; Chakraborty, S.; Saha-Dasgupta, T. *Chem. Mater.* **2016,** *28,* 8379–8384. doi:10.1021/acs.chemmater.6b03755
9. Banerjee, H.; Kumar, M.; Saha-Dasgupta, T. *Phys. Rev. B* **2014,** *90,* 174433. doi:10.1103/PhysRevB.90.174433
10. Švarcová, S.; Klementová, M.; Bezdička, P.; Łasocha, W.; Dušek, M.; Hradil, D. *Cryst. Res. Technol.* **2011,** *46,* 1051–1057. doi:10.1002/crat.201100262
11. Becke, A. D. *Phys. Rev. A* **1988,** *38,* 3098. doi:10.1103/PhysRevA.38.3098
12. Lee, C.; Yang, W.; Parr, R. G. *Phys. Rev. B* **1988,** *37,* 785. doi:10.1103/PhysRevB.37.785
13. Troullier, N.; Martins, J. L. *Phys. Rev. B* **1991,** *43,* 1993. doi:10.1103/PhysRevB.43.1993
14. Louie, S. G.; Froyen, S.; Cohen, M. L. *Phys. Rev. B* **1982,** *26,* 1738–1742. doi:10.1103/PhysRevB.26.1738

License and Terms